

**E-BOOK**  
**Clean energy**  
**&**  
**functional materials**  
**(CenMAT)**

Gdańsk 2023



# Preface

I have a pleasure to present the e-book for PhD students containing the most important topics presented by the lecturers during three schools under the main subject '*Clean energy and functional materials*'. During the schools the foreign PhD students had possibilities not only to listen to the lectures but also visit laboratories at the Institute of Fluid Flow Machinery (IMP PAN) in Gdańsk and at the Research Center of the Polish Academy of Sciences – Energy Conversion and Renewable Resources (KEZO) in Jabłonna as well as Lubań Living Lab in Kashubian district.

The schools were realised in the frame of the project '*Clean energy and functional materials*' (CenMAT) funded by Polish National Agency for Academic Exchange (NAWA), as part of the SPINAKER programme – Intensive International Education Programs.

The program is financed from the non-competition project No. POWR.03.03.00-00-PN16/18 'Supporting the institutional capacity of Polish universities through the creation and implementation of international study programs' under the Knowledge Education Development Operational Program.

The IMP PAN (the project Beneficiary) was founded in 1956 and now is the leading scientific unit of Polish Academy of Sciences in the Northern Poland and the second largest in the country. The research and innovation at the IMP PAN is related to a various of subjects from the mechanical engineering discipline. It covers the area of material degradation processes, diagnostics (structural health monitoring and enhanced non-destructive techniques) fluid flows with heat transfer, flows with chemical reactions and mi-

crostructure, mikro and nano flows, plasma and laser techniques, material development for energetic application, designing a prototypic solutions for energy conversion application, additive manufacturing techniques. The motto of the Institute is as follow: Combination of basic and applied research. In 2016, KEZO, the branch of the IMP PAN was opened in Jabłonna. Nowadays, the Research Center is one of the largest scientific and research complexes dedicated to topics related to renewable energy sources (RES) and equipped with the most modern, top-class research equipment in Europe.

The results of the project will be implemented at the educational program of the Tricity Doctoral School the Polish Academy of Sciences (TSD PAN). The TSD PAN was established in 2019 and is run jointly by the IMP PAN (leader), the Institute of Hydro-Engineering of the Polish Academy of Sciences (IBW PAN) and the Institute of Oceanology of the Polish Academy of Sciences (IO PAN). The Doctoral School offers education in three disciplines: Mechanical Engineering, Civil Engineering and Transportation, and Earth and Environmental Science.

The e-book is divided into three parts with subject related to the particular summer/ winter school. As a separated part lectures in subjects related to a research career development as well as presenting the history and culture of Poland and the beauty of Gdańsk (the IMP PAN main headquarter) were attached. Additionally, statistics information related to the whole project and each school are presented together with the list of lecturers and brief program of each school.

DSc PhD Eng. Magdalena Mieloszyk, assoc. prof. IMP PAN  
Director of the Tricity Doctoral School,  
Polish Academy of Sciences

# Contents

<b>I</b>	<b>Intelligent materials...</b>	<b>8</b>
<b>1</b>	<b>The first School...</b>	<b>10</b>
<b>2</b>	<b>Structural Health Monitoring</b>	<b>19</b>
<b>3</b>	<b>FBG sensors</b>	<b>28</b>
3.1	Fibre optic techniques . . . . .	29
3.1.1	Structure of a fibre optic . . . . .	29
3.1.2	Principle of operation of optical sensors . . . . .	31
3.2	Optical sensors for SHM application . . . . .	32
3.3	FBG sensors . . . . .	34
3.3.1	Methods of manufacturing FBG sensors . . . . .	38
3.3.2	Principle of operation . . . . .	39
3.4	FBG sensors application for SHM . . . . .	44
<b>4</b>	<b>THz spectroscopy</b>	<b>48</b>
4.1	Introduction . . . . .	49
4.2	Principle of operation . . . . .	50
4.3	Examples of the NDT method applications . . . . .	56
4.3.1	GFRP samples . . . . .	56
4.3.2	Complex sample . . . . .	58
4.3.3	AM sample . . . . .	59
<b>5</b>	<b>Guided waves for SHM</b>	<b>61</b>
5.1	Introduction . . . . .	62
5.2	Elastic waves . . . . .	62

5.3	Wave generation and sensing . . . . .	64
5.3.1	Excitation signals . . . . .	65
5.3.2	Elastic wave generation . . . . .	66
5.3.3	Elastic wave sensing . . . . .	66
5.4	SHM system . . . . .	68
5.4.1	Transducer network . . . . .	69
5.4.2	Signal generation/acquisition . . . . .	71
5.4.3	Signal processing and post-processing . . . . .	74
5.5	Influence of external factors on SHM . . . . .	77
5.6	Summary . . . . .	78
<b>6</b>	<b>Laser vibrometry</b>	<b>80</b>
6.1	History . . . . .	81
6.2	Principles of operation . . . . .	82
6.3	LDV types . . . . .	85
6.4	Advantages and limitations . . . . .	89
6.5	Applications . . . . .	91
<b>7</b>	<b>Lubań Living Lab</b>	<b>97</b>
<b>II</b>	<b>Intelligent distributed generation</b>	<b>104</b>
<b>8</b>	<b>The second School...</b>	<b>106</b>
<b>9</b>	<b>Methods of experimental...</b>	<b>115</b>
9.1	Tabular methods . . . . .	116
9.2	Graphical methods . . . . .	118
9.3	Analytical methods . . . . .	121
<b>10</b>	<b>Measurements of...</b>	<b>147</b>
10.1	Pressure measurements . . . . .	148
10.2	Flow velocity... . . . .	156
<b>11</b>	<b>Heat pumps...</b>	<b>177</b>
11.1	Introduction . . . . .	178
11.2	Heat pump basics . . . . .	179
11.3	Use of air source heat pumps . . . . .	180

11.4	Division of ASHP . . . . .	182
11.5	Refrigerators and EU restrictions . . . . .	185
11.6	Bivalent point . . . . .	187
11.7	Noice . . . . .	189
11.8	Methods of defrosting . . . . .	190
11.9	Summary . . . . .	192
<b>III</b>	<b>Clean energy</b>	<b>194</b>
<b>12</b>	<b>The third School...</b>	<b>196</b>
<b>13</b>	<b>Wind tunnel</b>	<b>206</b>
<b>14</b>	<b>Introduction to thermal...</b>	<b>226</b>
14.1	Introduction . . . . .	227
14.2	Turbine cycles – basics . . . . .	228
14.2.1	Brayton cycle . . . . .	229
14.2.2	Clausius-Rankine cycle . . . . .	232
14.3	Turbine stage – basics . . . . .	235
14.4	Classification of turbines . . . . .	238
14.4.1	Flow direction . . . . .	238
14.4.2	Compressibility . . . . .	239
14.4.3	Number of stages . . . . .	240
14.4.4	Steam turbines classification . . . . .	241
14.4.5	Steam turbine classification based on size . . . . .	243
14.4.6	Other classification methods . . . . .	245
14.5	Engineering approach... . . . .	246
14.6	Principle of operation... . . . .	248
14.7	Industrial applications... . . . .	253
14.7.1	Power generation . . . . .	253
14.7.2	Co-generation or combined heat and power . . . . .	254
14.7.3	Waste-to-energy plants . . . . .	254
14.7.4	Renewable energy integration . . . . .	255
14.7.5	Conclusion . . . . .	255
<b>15</b>	<b>Thermodynamic analysis...</b>	<b>256</b>
15.1	Introduction . . . . .	257

15.2	Energy balance . . . . .	257
15.3	Entropy balance . . . . .	258
15.3.1	Exergy Balance . . . . .	260
15.3.2	Detailed calculations and optimisation. . . . .	263
15.4	Summary . . . . .	270
<b>16</b>	<b>An effect of hydrogen. . . . .</b>	<b>273</b>
16.1	Introduction . . . . .	274
16.2	Diffusion . . . . .	275
16.3	Effect of hydrogen on ductility . . . . .	279
16.4	Effect of hydrogen on tensile strength . . . . .	281
16.5	Effect of hydrogen on a damage behaviour . . . . .	283
16.6	Summary . . . . .	284
<b>17</b>	<b>Phase change materials . . . . .</b>	<b>286</b>
17.1	Introduction . . . . .	287
17.2	PCMs characteristic . . . . .	290
17.3	PCMs Applications . . . . .	298
17.4	Summary . . . . .	302
<b>18</b>	<b>Renewable energy. . . . .</b>	<b>303</b>
<b>IV</b>	<b>Other . . . . .</b>	<b>316</b>
<b>19</b>	<b>A researcher's perspective . . . . .</b>	<b>317</b>
19.1	Introduction . . . . .	318
19.2	Academic life . . . . .	319
19.3	Dos and Don'ts . . . . .	322
19.4	Conclusion . . . . .	327
<b>20</b>	<b>Poland . . . . .</b>	<b>329</b>
<b>21</b>	<b>Gdańsk . . . . .</b>	<b>336</b>
21.1	Golden Gdańsk . . . . .	337
21.2	Gdańsk in 21th century . . . . .	338
<b>22</b>	<b>Schools in numbers . . . . .</b>	<b>349</b>

## Part I

# Intelligent materials, diagnostics & structural analyses



# Introduction

I have a pleasure to present the first part of the e-book for PhD students. It contains materials related to the first school in the subject of '*Clean energy and functional materials*', with a subtitle '**Intelligent materials, diagnostics & structural analyses**'.

The school was realised in the form of blended learning at IMP PAN in Gdańsk, 27.09.2022 – 07.10.2022. The presented knowledge is linked with the intelligent diagnostics (structural health monitoring (SHM), non-destructive testing (NDT)) based on elastic wave propagation, fibre Brag grating sensors, THz spectroscopy, etc.

In the frame of the school the PhD students had also possibilities to visit Lubań Living Lab that is also shortly presented in the part of the e-book.

I would like to warmly thank the people who co-created this e-book, especially the authors of individual subchapters:

- ✉ Magdalena Mieloszyk – Chapter 2, Chapter 3, Chapter 4
- ✉ Tomasz Wandowski – Chapter 5
- ✉ Maciej Radzieński – Chapter 6
- ✉ Eco-Construction Ltd. – Chapter 7

Magdalena Mieloszyk, DSc PhD Eng., assoc. prof. IMP PAN  
Director of the Tricity Doctoral School,  
Polish Academy of Sciences

## Chapter 1

# The first School information & statistics

The first school was realised in the blended learning form, in days 27.09.2022 – 07.10.2022.

Hour		Online			Weekend	Hour		at IMP PAN, Gdańsk					
		Day 1	Day 2	Day 3		Day 4	Day 5	Day 6	Day 7	Day 8			
08:00	08:15	W			Travel to Gdańsk	08:00	09:00	R	Luban Living Lab				
08:15	09:00	L1	L9	L17		09:00	09:45	L1	L11	L21	L25		
09:00	09:45	L2	L10	L18		09:45	10:30	L2	L12	L22	L26		
09:45	10:00	CB	CB	CB		10:30	10:45	CB	CB	CB	CB		
10:00	10:45	L3	L11	L19		10:45	11:30	L3	L13	L23	L27		
10:45	11:30	L4	L12	L20		11:30	12:15	L4	L14	L24	L28		
11:30	11:45	CB	CB	CB		12:15	13:45	LB	LB	LB	LB		
11:45	12:30	L5	L13	L21		13:45	14:30	L5	L15	L29			
12:30	13:15	L6	L14	L22		14:30	15:15	L6	L16	L30			
13:15	14:00	LB	LB	LB		15:15	15:30	CB	CB	CB			
14:00	14:45	L7	L15	L23		15:30	16:15	L7	L17	L31			
14:45	15:30	L8	L16	L24		16:15	17:00	L8	L18	L32			
15:30	15:45		CB	C		17:00	17:15	CB	CB	C			
15:45	18:45		LaP			17:15	18:00	L9	L19				
						18:00	18:45	L10	L20				

W – welcome, C – closing, R – registration, CB – coffee break, LB – lunch break, L – lecture, LaP – lecture about Poland, GT – Gdańsk guided walking tour

The school included lectures:

- ① online
  - 🏠 3 days at own place
  - 📎 24 hours of substantial lessons
  - 📎 3 hours of Polish culture and history
- ② onsite
  - 📍 5 days at IMP PAN, Gdańsk
  - 📎 32 hours of substantial lessons (including laboratory shows)
  - 📎 8 hours at Lubań Living Lab
  - 📎 4 hours of Gdańsk guided walking tour

The lectures were given by lecturers from:

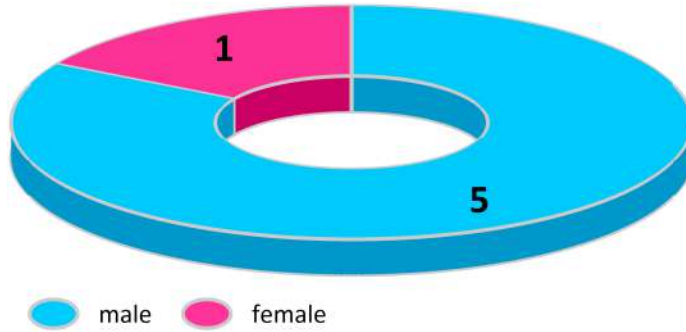
- ✓ 1 person from Lithuania
- ✓ 1 person from Spain
- ✓ 2 persons out of IMP PAN (Kraków, Warszawa)
- ✓ 10 persons from IMP PAN

## Lecturers:

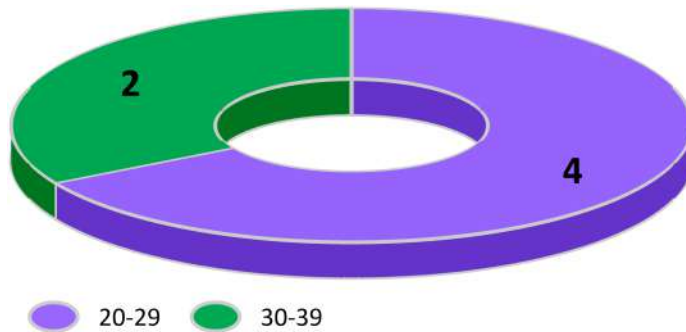
- prof. ANTONIO FERNÁNDEZ-LÓPEZ  
Universidad Politécnica de Madrid, Spain
- prof. RŪTA RIMAŠAUSKIENĖ  
Kaunas University of Technology, Lithuania
- dr hab. inż. ADAM MARTOWICZ  
AGH University of Science and Technology in Kraków, Poland
- mgr inż. JAKUB KORYCIŃSKI  
INTERLAB Warszawa, Poland
- dr hab. MAREK KOCIK  
Institute of Fluid-Flow Machinery Polish Academy of Sciences, Poland
- dr hab. inż. ALICJA KRELLA  
Institute of Fluid-Flow Machinery Polish Academy of Sciences, Poland
- dr hab. inż. MAGDALENA MIELOSZYK  
Institute of Fluid-Flow Machinery Polish Academy of Sciences, Poland
- dr hab. inż. MACIEJ RADZIŃSKI  
Institute of Fluid-Flow Machinery Polish Academy of Sciences, Poland
- dr hab. inż. TOMASZ WANDOWSKI  
Institute of Fluid-Flow Machinery Polish Academy of Sciences, Poland
- dr inż. ŁUKASZ BREŃKACZ  
Institute of Fluid-Flow Machinery Polish Academy of Sciences, Poland
- dr inż. ANDRZEJ KRUPA  
Institute of Fluid-Flow Machinery Polish Academy of Sciences, Poland
- dr inż. TOMASZ PRZYBYLIŃSKI  
Institute of Fluid-Flow Machinery Polish Academy of Sciences, Poland
- dr inż. ROHAN SOMAN  
Institute of Fluid-Flow Machinery Polish Academy of Sciences, Poland
- dr inż. JANUSZ TELEGA  
Institute of Fluid-Flow Machinery Polish Academy of Sciences, Poland

The PhD students, who took a part in the school, at the recruitment stage, filled out an application forms. In the first school edition 6 persons were participating. Based on their submitted application forms, the following statistical data was obtained:

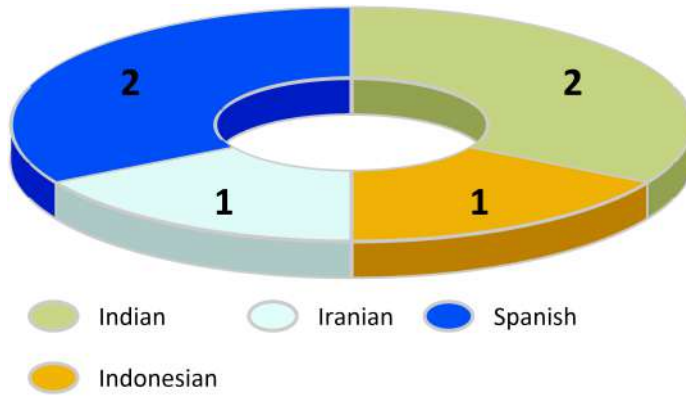
☆ PhD students' gender



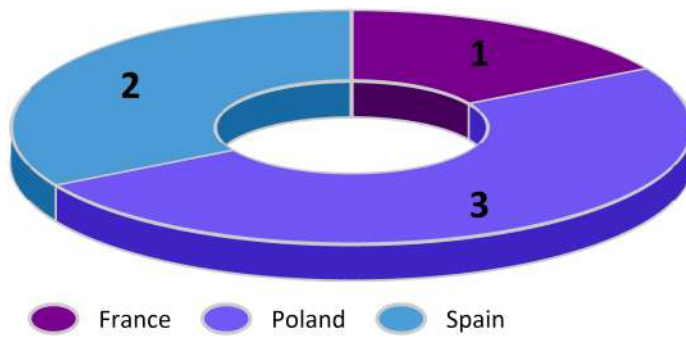
☆ PhD students' age



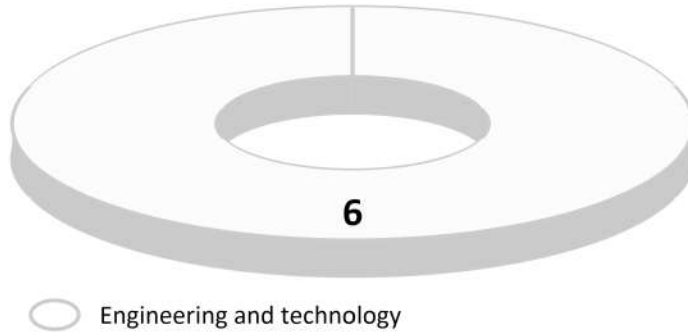
## ☆ PhD students' citizenship



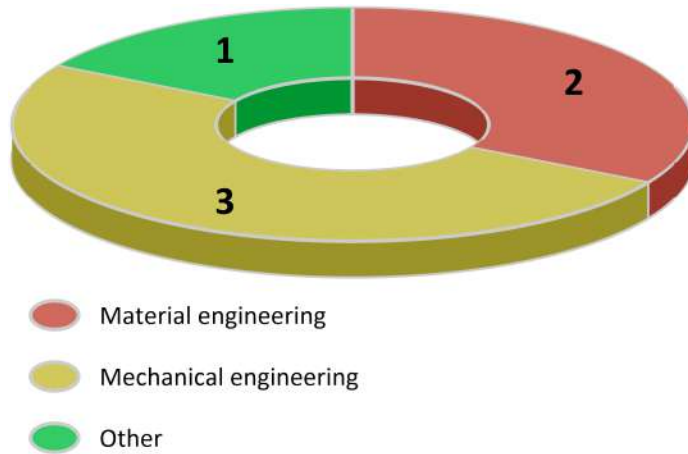
## ☆ PhD students' education country



☆ PhD students' field of PhD thesis

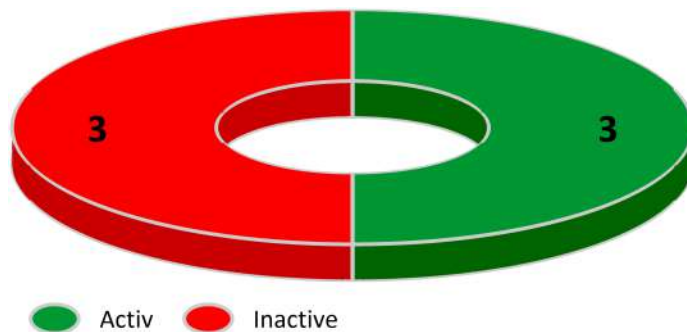


☆ PhD students' discipline of PhD thesis

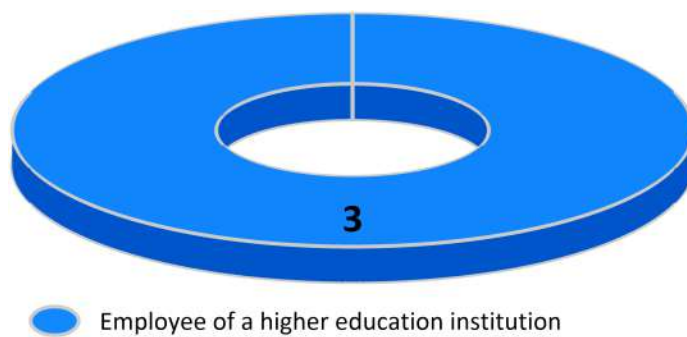




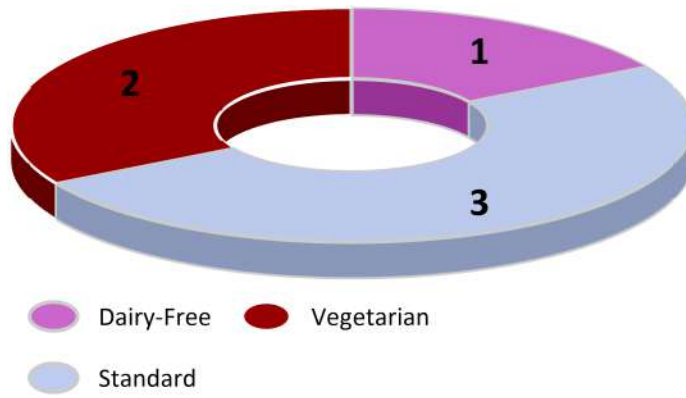
☆ PhD students' status on the labour market



☆ active PhD students' profession



☆ PhD students' diet



*Katarzyna Majewska*

## Chapter 2

# Structural Health Monitoring

Structural Health Monitoring (SHM) is a field of science that aims to obtain reliable data related to the structural integrity. SHM allows for optimal planning the number of necessary technical inspections of the structure, significant reduction of financial outlays while increasing the safety of people working on the structure and reducing the ecological risk.

An SHM system layout and principle of operation was inspired by the human nervous system, consisting of the peripheral nervous system formed by spinal roots and peripheral nerves, and the central nervous system, which includes the brain and spinal cord. The task of the nervous system is to ensure constant contact of the body with the external environment and the integration of internal organs. The task of the peripheral nervous system is to register all information and conduct through nerve impulses to the central nervous system, and then to the executive organs (muscles, endocrine glands). The central nervous system registers and analyses the information coming from the peripheral system and ensures the body's proper response to these stimuli. An SHM system works in a similar way. On the basis of the measurement data obtained from various types of sensors located on the structure and embedded into the structural elements material, a decision is made to continue the operation of the structure or to discontinue it for the period of reparation, or to completely withdraw it from operation.

Tab. 2.1: Comparison of SHM and nervous systems

Feature	Biology	Engineering
Amount of sensors	as many as possible	as few as possible
System complexity level	low	high
Data rate	low	high
Number of backup sensors	large	small
Sensor(s) ability to relocate	no possibility	possible

A comparison between SHM and nervous systems is presented in Tab. 2.1. The nervous system consists of many relatively primitive sensors (receptors), the number of which far exceeds the need for performing a proper decision related to avoid a potential danger. For example to perform a decision about appropriate time of exposition a hand to particular temperature. A large number of sensors is associated with their limited repairability and the inability to change their location and configuration. In contrast to the nervous system, SHM systems aim to minimise the number of sensors, while at the same time making them very complicated. It results in high cost of the sensors themselves as well as the measuring systems units connected to them. Due to this, the number of spare sensors is minimised. There is a possibility to change the configuration of the sensor system on the structure, but in practice it is rarely used due to the possibility of damage to the sensors and the related uncertainty of the correctness of further measurements.

In typical SHM system four main components can be distinguished:

- measurement array containing sensors, cables and measurement units
- data recording, transmission and storage systems
- data post-processing algorithms
- systems assessing the technical condition of the structure

Sensors used in SHM systems can be divided into two groups depending on the measured parameters related to:

- structure (e.g. strain, stress, displacement or acceleration)
- external parameters (e.g. wind speed, temperature)

Sensors can be also divided as mounted on the structure or embedded in the elements material.

In SHM systems, various types of sensors are used during the registration of technical parameters of structures. Sensors are placed at selected points in the structure where damage is the most possible to occur (e.g. stress concentration points). The sensors measure specific parameters in real time. Data is stored and analysed for possible changes in the values of the measured parameters.

An example of a complex SHM system is the Wind and Structural Health Monitoring System (WASHMS) that is installed on the Tsing Ma Bridge in Hong Kong (China). Among many others, this system contains strain gauges, optical sensors, GPS-based position sensors, accelerometers [16]. Another example of complex SHM systems is Composite Hull Embedded Sensor System (CHESS). Such system was installed on the HnoMS Skjold prototype patrol boat. The purpose of this system was to monitor the technical condition of the composite hull and collect information on its actual loads. The sensor locations were chosen, for detection of and discrimination between the following moments and forces: vertical bending (hogging/sagging), horizontal bending, torsion (twisting moment), vertical shear force and longitudinal compression force [117]. SHM systems (similar to CHESS) are currently standard equipment of the Royal Norwegian Navy catamarans hulls [39, 111].

In the SHM method the following diagnostic levels can be distinguished:

1. detection – detection of existing damage
2. location – determination of the damage location
3. identification – damage type classification (size or type)
4. prediction – determination of time of the structure safe work
5. self-healing – reaction to damage by removing its effects

Detection is related to answer a question about any damage occurrence in the structure. In the case of the damage detection, the next step is related to determination its location. For the purpose of better understanding the procedure, those levels are presented on an example of offshore wind turbine physical model equipped with an array of sensors divided into three groups linked with the legs (L1, L2 and L3). The damage detection and localisation based on operational modal analyses with excitation of artificial waves with assumed parameters. The experimental investigation was performed on a water basin. For the damage detection purpose, a damage index (DI) was determined and calculated for all sensors (AL). When damage occurrence was confirmed (DI value above the threshold)

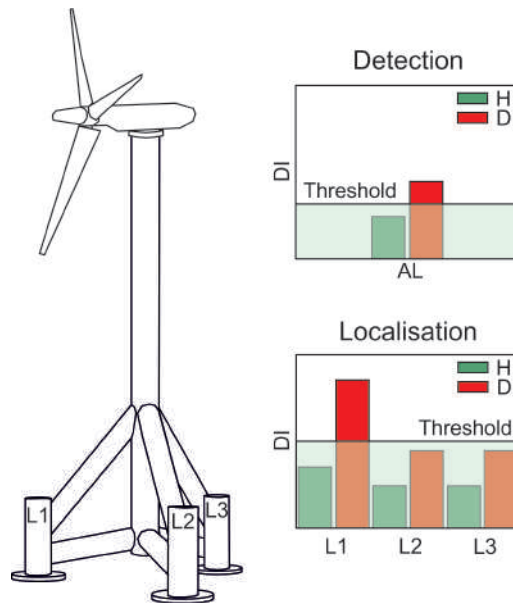


Fig. 2.1: An example of the SHM procedure for the first and the second diagnostic levels.

the next step was to determine the damage localisation with accuracy to the tripod leg. It was observed that leg L1 was damaged. For the leg the DI value was above the threshold. The details of the procedure are presented in paper [78]. The purpose of the next SHM level, identification, is to classify the type of damage, i.e. to determine whether it is a crack, delamination, debonding, corrosion, etc., or to determine the size of the damage. Photographs of selected damage types are presented in Fig. 2.2.

The prediction level is related to determination the time of further safe operation of the analysed structure with damage. For this purpose information about the structure loading conditions, material properties as well as the damage location and type are taken into consideration.

Self-healing is the last, currently developed level of the SHM method available for a chosen structures, only. It based on the appropriate modification of the structure material in such a way that any crack

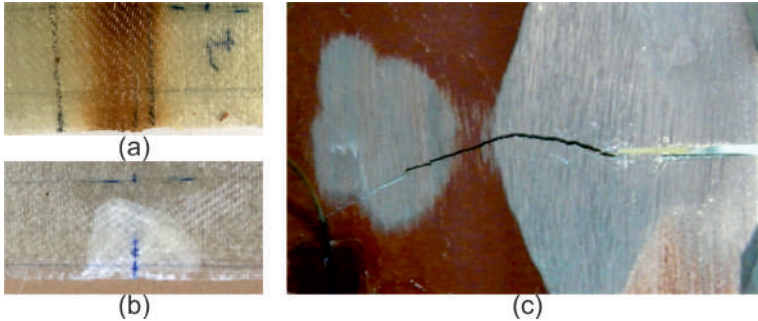


Fig. 2.2: Damage examples: a) burning, b) delamination, c) crack.

propagation initiates the repair mechanism. For example, a polymeric material may contain additional bonds joining polymer chains that break under assumed load and then allow the polymer chain to re-form due to heating. However, this method requires prior detection and localisation of damage. Another method of autonomous self-healing based on placing microcapsules with an activator in a composite material. The propagating crack breaks a microcapsule with the active ingredient, starting a chemical reaction to repair the structure in the damage location.

During the application of the SHM method on a structure four typical steps can be defined:

- development a theoretical model of the structure
- selection of the type, number and locations of sensors on the structure
- defining acceptable levels of measured parameters (threshold)
- analysis of the collected data measured during the operation of the structure.

The numerical tests performed on the structure are used to determine its responses on assumed loadings. Numerical analysis based on finite element method (FEM) are a standard procedure during designing a new solution of a structure and to determine variants that will be then analysed experimentally (prototypes) to compare their responses with the theoretical ones. FEM analyses allow iden-



tification potential critical zones on the structure, such as areas of stress concentration or maximum deformation. Based on the above-described analysis, sensors (types, number and locations) are selected to be mounted on or embedded into structural elements. At this stage, it is important to select appropriate type(s) of sensor(s) taking into consideration measured parameter and the operational environment.

The numerical and experimental tests performed on the structure under typical loads are used to determine the structure standard responses and the threshold values. Exceeding the threshold value results in starting a diagnostic procedure as it could mean both overloading as well as a damage occurrence. Determination of acceptable levels of measured parameters for SHM system usually based on the previously conducted theoretical analysis and measurements performed on the structure during its normal operation. It is worth mentioning that SHM systems can be installed both on new structure (e.g. offshore support structure [78]) and structure that has been in operation for some time (e.g. sailing ship *Dar Młodzieży* [60]). For the second type of structures, the threshold values are usually determined based on experimental analyses. The main reason of such approach is the existence of structural changes in the elements being an effect of loading and environmental conditions during the whole period of the operational time. The last and the most difficult stage of the SHM method is the analysis of measured quantities for the purpose of determination technical condition of the structure at the particular moment in time. This stage is related to data selection, storage and post-processing.

For better understanding the process of the structural changes that occurs in a structure and their influence on parameter values measure by the sensors a particular example was presented. The analysed structure is a composite fast patrol boat with an array of fibre Bragg grating (FBG) sensors embedded into its hull [77]. The strain levels after four selected stages are presented in Fig. 2.3. It is easily observable that at the beginning of the embedding process (EF) the strain determined by all sensors was almost 0. Then the embedding process (EF) results in a tension occurrence – a residual strains

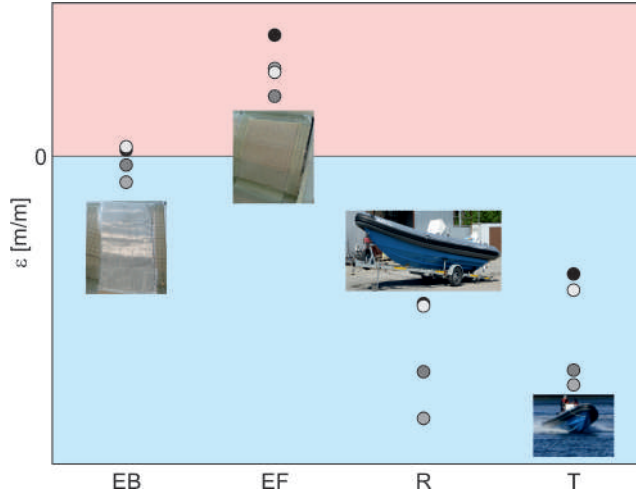


Fig. 2.3: An example of strain level changes for a fast patrol boat after selected stages: EB – beginning of the manufacturing process, EF – finished manufacturing process, R – finished boat structure, T – after operation on the sea.

after the composite curing process. The next step of the construction process was related to adding all necessary elements, including deck, engine, etc. to achieve a finished boat (R). It results in compression at the sensors location. Then the boat was transported to harbour. The transport did not influence the structure. During its operation on the sea, the bow of the boat rises above the sea surface and then hits it. Such impact loadings result in consecutive changes in the strain levels determined by the sensors. Therefore, the strain levels change in time so the threshold levels have to be determined recursively in a combination with a non-destructive testing (NDT) (e.g. visual inspection or infrared thermography) for damage detection and localisation purposes. An example of strain levels after some operational time (T) shows an influence of the mechanical and environmental loadings on the boat hull structure.

One of the most important and the most difficult parts of the SHM system is the correct interpretation of the recorded measurement data originated from a various types of sensors mounted in different

locations on the structure. During the interpretation the technical data (e.g. materials used, their physical properties, geometrical parameters of the structural elements, etc.) related to the structure are applied. As a consequence, this process leads to determining the technical condition of the structure at a given moment. The diagnostic algorithms use both the technical data, the sensors measurements and information about the previous condition of the structure (e.g. about damage location, types). In this part of the SHM system, artificial neural networks and genetic algorithms are very often used. Another important function of SHM systems is their ability to notify about existing damage in the structure (cracks, delaminations, debonding, etc.) online, as well as the prediction of the damaged structure operation time related to the degradation processes that occurs in the structural material.

## Chapter 3

# Fibre Bragg grating sensor

### 3.1 Fibre optic techniques

Optical fibres can be divided into fibre and planar optical fibres (Fig. 3.1). Fibre optics are very thin dielectric fibres, most often made of silica glass, used e.g. for transmitting optical signals over long distances. Optical fibres of this type are now commonly used in telecommunications. Flat optical fibres are thin dielectric layers currently used in the structures of integrated optics [61].

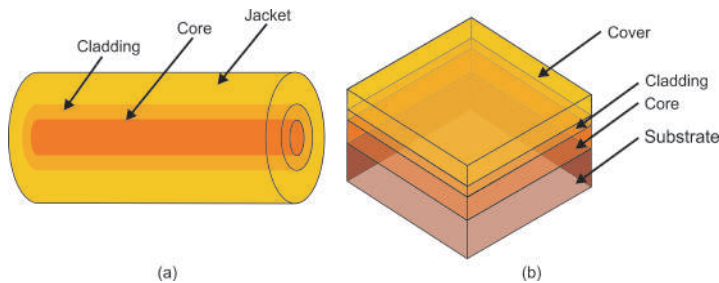


Fig. 3.1: Types of optical fibres: a) fibre, b) planar.

Optical fibres appeared at the beginning of the 20th century. The theory of circular optical fibre was described by Hondoros and Debye in 1910 [36] while the theory of elliptical optical fibre was presented in 1962 by Yeh [124].

The first optical fibres were characterised by very high attenuation of the order of 1000 dB/km. The development of optical fibre techniques started at the end of the 20th century, when in 1970 Corning Glass Works produced an optical fibre with attenuation of 20 dB/km. In 1979, a single-mode optical fibre with attenuation of 0.2 dB/km (wavelength range of 1550 nm) was made in Japan [61].

#### 3.1.1 Structure of a fibre optic

Fibre optics are dielectrics that enable the transmission of a light signal. Such elements consist of three components: core, cladding, and jacket (Fig. 3.1(a)). For sensing purposes, optical fibres with core and cladding made of silica glass are typically used. The refractive index of the cladding is lower than that of the core. Typically,

the difference is less than 1% [89]. The refractive indexes values are chosen in such a way that Snell's law of total internal reflection is satisfied [52]. The light during transmission through the fibre is reflected from the boundaries between core and cladding. Because the core is surrounded by a cladding along the entire length of the fibre, all light introduced into the fibre transmits only through the core of the optical fibre [52].

The first optical fibres were manufactured in the 1920s and did not contain cladding. In this case, the role of the cladding was played by air. The use of a jacket was firstly described by Baird [8] in 1928.

Taking into consideration their internal structure, fibre optics can be divided into single-mode and multi-mode. In single-mode optical fibres, only one light ray (called basic mode) is transmitted [61]. On contrary to this, in multimode optical fibres, many modes (rays) of light are transmitted at different angles to the fibre cladding. Both types of optical fibres have the same outer (jacket) diameter of  $125\ \mu\text{m}$ , while the core diameter for single-mode fibres is  $6.5\text{-}9.5\ \mu\text{m}$ , and for multimode  $62.5\ \mu\text{m}$  [89]. Single-mode optical fibres allow data transmission over longer distances, without the use of a signal amplifier [41]. Multimode optical fibres are used only for data transmission while optical sensors are manufactured by modifying single-mode optical fibres. The main reason is related to the transmitted signal distortion. In multimode fibres the signal is more distorted than when transmitting in a single mode [61].

The outermost layer of an optical fibre, called a jacket, is usually made of polymer. Its task is to ensure proper stiffness of the fibre as well as to protect it against damage [52]. In some sensing application, the jacket material is selected to increase the sensitivity of the sensor on the measured parameter or adapt to the tested structure [52], [89].

Optical fibres can also be divided according to the core material into: glass fibres and polymer fibres. Glass optical fibres (most commonly used) are made of silica glass doped with  $\text{GeO}_2$  and F [69]. In glass optical fibres three telecommunication data transmission windows that correspond to the following wavelengths: 850 nm, 1300 nm and 1550 nm [61] can be distinguished. In such optical fibres the low-

est attenuation (ca. 0.2 dB/km) is related to the third transmission window [69]. Polymer optical fibres have lower stiffness than glass optical fibres. They are very sensitive to deformation, temperature and humidity. Additionally, higher signal attenuation for polymer than for glass fibre optics is observed. The smallest value (50 dB/km) is observed for the visible light range [61].

### 3.1.2 Principle of operation of optical sensors

Optical fibres that transmit light from one point to another undergo geometrical and optical changes under the influence of various external factors. When fibre optics are used in telecommunications, the latter phenomenon is unfavourable, and thus is minimised. However, the same changes in optical properties are used in optical sensors to measure chosen parameters of the external environment or structures. Even small changes in temperature, deformation or the appearance of an electric field are closely correlated with changes in light parameters such as: amplitude (intensity), phase, frequency, wavelength or polarization.

Fibre optic sensors are mostly parametric (passive) sensors. This means that they respond to changes in environmental or structural parameters but cannot be used as an excitation source. A good example of active sensors (transducers) are piezoelectric sensors applied for diagnostic methods based on elastic waves propagation.

The light signal transmitted over the optical fibre can be used on sensors to measure physical parameters (e.g. strain, natural frequencies, temperature). Optical fibres covered by additional material can be sensitive to changes in chemical composition, e.g. formation of corrosion products [9].

There are many ways to classify optical sensors. The first one is based on the light parameters (e.g. intensity, wavelength, phase, polarization) affected by the measured parameter. Another method is related to the area where light modification occurs, i.e. inside or outside the fibre. Optical sensors are also classified in terms of placement as local, quasi-distributed or distributed [52]. This classification is the most popular. Local sensors measure parameters at

selected points on the structure, only. The principle of operation of distributed sensors based on the analysis of changes in the light propagating in the optical fibre caused by the appearance of discontinuities in the tested object. In such case whole optical fibre is treated as a sensor. Quasi-distributed sensors combine the properties of both types described above. Typical quasi-distributed sensors are fibre Bragg grating (FBG) sensors – optical sensors with Bragg diffraction grating. Due to their small dimensions (length typically in a range of 1-25 mm (10 mm for strain measurement application) and  $125\mu\text{m}$  (diameter of a single-mode fibre)), they can be treated as local sensors. However, their multiplexing capabilities, results in manufacturing a line containing many sensors on a single fibre that allows the use of a large part the optical fibre as a sensor. This feature is similar to those observed for distributed sensors.

## 3.2 Optical sensors for SHM application

The advantages of optical sensors make them a very interesting tool in Structural Health Monitoring (SHM) systems used on structures made out of various types of materials: metal (isotropic) [60] and composite (orthotropic) [77]. It results in their wide diagnostic applicability in many branches of industry: marine [60, 77], aviation [109], civil engineering [30, 101].

The beginning of the optical fibre based monitoring techniques is 1970s, when optical fibre was used for the first time for data transmission [108]. Eight years later, Butter and Hocker [13] observed the effect of strain on the transmitted light signal and described the first optical fibre strain sensor. In 1978, FBG sensors were firstly described by Hill et al. [35]. The first successful application of FBG sensors for strain and temperature measurements on a real structure (Beddington Trail Bridge in Calgary, Canada) was performed in 1993 [5].

Optical sensors have many advantages compared to the most commonly used electrical sensors (strain gauges). A comparison of FBG strain sensors and strain gauges are collected in Tab. 3.1.



Tab. 3.1: Comparison of FBG strain sensors and strain gauges.

Feature	FBG sensors	Strain gauges
EMI	immune	sensitive
Electric conductivity	no	yes
Explosive safety	yes	no
Multiplexing	yes	no
Zero drift	no	yes
Weight	low	high (cables)
Calibration	not needed	needed
Corrosion resistance	high	low
Fatigue resistance	high	low
Temperature	high sensitivity	low sensitivity
Thermal compensation	required	required

Optical fibres on which FBG sensors are manufactured are dielectrics, and therefore they are resistant to electromagnetic field interference (EMI) and can work in places inaccessible to electrical sensors. In addition, these sensors are characterised by a non-electrical output signal [41]. A comparison of EMI influence on both FBG sensors and strain gauges was described for a ship with composite hull. The agreement between measurements from both techniques was very good but the data from conventional strain gauges were influenced by the electromagnetic field [117].

Sensors with a fibre core made of silicon glass can be used to measure temperature in the range from  $-200^{\circ}\text{C}$  to  $800^{\circ}\text{C}$  with an accuracy of  $0.1^{\circ}\text{C}$  [52]. The maximum measurement temperature is limited by the glass transition temperature in the material of the optical sensor. Due to their high sensitivity to ambient temperature changes, optical sensors can be used as temperature sensors.

In optical sensors, the transmitted light signal does not depend on the conditions of the external environment. Optical fibres (opti-

cal sensors) are made of materials (usually silicon glass) with high durability and high corrosion resistance. Therefore, they have a long lifetime – estimated to ca. 25 years.

An additional advantage of optical sensors is the possibility of their application in flammable, explosive or chemically aggressive environments [41]. Due to the fact that optical fibres are resistant to sea water, they can be used in SHM systems installed on offshore structures (e.g. oil platforms, wind turbines) [79] or marine vessels [60, 77]. After one year strain gauges installed on oil platform were damaged by the corrosive influence of sea water while FBG sensors worked properly [91].

Thanks to the light weight and geometric dimensions, optical fibers can be embedded in the structure without significant influence on the structure material strength [72]. Additionally, small size of fibre optics allows them to be applied for measurements on small-size elements. Another advantage of optical fibres (optical sensors) is their flexibility. They can be mounted on surfaces with complex geometry and in hard-to-reach places (e.g. around the circumference of a round element, sharp corners or welds).

### 3.3 FBG sensors

One of the sensors types that can be permanently integrated with composite structures and used as a part of SHM system are FBG sensors. Their chosen features are presented in Tab. 3.2.

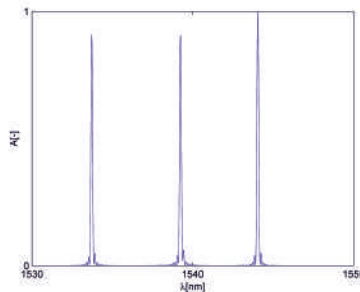


Fig. 3.2: Multiplexing capabilities of FBG sensors.

Tab. 3.2: Advantages and disadvantages of FBG sensors.

Feature	Description
Advantages	
small size & light weight	diameter 0.125 mm length 1-25 mm
installation properties	attaching to structure or embedding in structure
multiplexing capabilities	high dozens of sensors on one fibre
no calibration requirements	no zero drift
no measurement distance limit	low optical signal attenuation
immunity to EMI	optical signal
high resistance to aggressive environment	silica glass
Disadvantages	
brittleness	silica glass
passive elements	read-only
cross sensitivity on strain & temperature	temperature compensation required

FBG sensors made on a single optical fibre can simultaneously measure several different parameters (e.g. longitudinal strain, temperature, acceleration, displacement). The measured parameter in this case depends on the method of attaching the sensor. Multiplexing reduces the amount of cabling required and the complexity of powering the sensors. The FBG sensors utility is also linked with the possibility of manufacturing many diffraction gratings (sensors) with different diffraction grating constants along one fibre. An example of responses from three FBG sensors manufactured on one optical fibre is presented in Fig. 3.2. The sensors are distinguished based on their Bragg wavelengths – wavelengths related to the max-

imal amplitude of the signal. Thanks to this procedure, each sensor is clearly defined by its Bragg wavelength. Such method of identifying FBG sensors is typically used in interrogators – units used for measurements using FBG sensors.

Additionally, due to small attenuation of the signal transmitted by optical fibre a long distance between sensors location and the measurement unit can be designed. For example, the distance between FBG sensors array located on the foremast of the sailing ship *Dar Młodzieży* and the interrogator (the measurement unit) located in a room was ca. 30 m. The distance between the sensors location on the mast and the ship deck was ca. 26 m [60].



Fig. 3.3: Sailing Ship *Dar Młodzieży* – FBG sensors location marked by an arrow.

The main disadvantage of optical sensors is brittleness of the optical fibre material. However, the influence of such feature on the applicability of the optical sensors is nowadays significantly smaller than ca. 20 years ago. At that time, the brittleness was a very big problem because optical fibres broke during packaging, transport and even installation on the tested structure. The problem of core and

cladding brittleness was mostly solved by changing the proprieties of jacket. Nowadays, problems related to the brittleness of optical fibres occurs mostly for embedded optical fibres in the area of their input/output part from the structure. Examples of the input/output parts for two samples is presented in Fig. 3.4. In many cases, it is impossible to repair if the optical fibre is broken at the entrance or exit of the optical sensor. Optical sensors need special protection in such locations. In addition, this protection ensures adequate light transmission, as light transmission may disappear in a bent fibre.

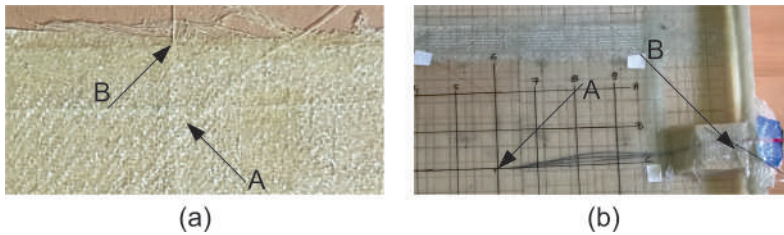


Fig. 3.4: Examples of the input/output part for: (a) thin composite sample, (b) thick sandwich element.

Optical sensors arrays mounted on structures are protected against mechanical and environmental influences on the used adhesive degradation processes. For real structures, e.g. sailing ship, such protection based on epoxy layers that prevent both the sensors array and the metal structure of the foremast against negative marine environment corrosion influence.

Optical sensors can be mounted on elements made of a various of materials, for example metal [16, 44, 60], composite [15, 48, 77] and concrete [11, 49]. Effective operation of the sensor requires an appropriate mechanical connection between the fibre and the tested structure in order to ensure proper transfer of measured values to light signals.

The overall process of mounting FBG sensors on a structure is similar all structural materials (e.g. metal, concrete or fibre reinforced composites) and consists of the following steps:

- mark the sensor position on the structure

- cleaning and degreasing the place where the sensor will be attached
- covering the gluing area by thin layer of adhesive
- sensor placement at the selected location
- adding an appropriate covering material (applied for real structures)

The other possibility of mounting FBG sensors is their embedding in the element material. In such method FBG sensors are placed in appropriated locations during the manufacturing process of the structure. Therefore, the procedure strongly depends on the particular fabrication process.

### 3.3.1 Methods of manufacturing FBG sensors

FBG sensors are manufactured by affecting the fibre core with an ultraviolet laser beam of selected intensity and interference pattern. There are two main techniques: the phase mask method and the interferometric method. Schematic description of both methods is presented in Fig. 3.5.

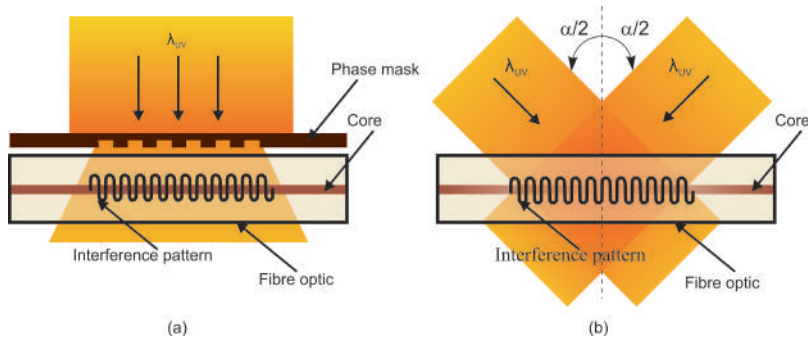


Fig. 3.5: FBG sensors manufacturing methods: (a) phase mask, (b) interferometric.

The first method (Fig. 3.5(a)) uses a phase mask (a special diffraction grating made on a glass plate) as a diffraction element to create interference pattern in a fibre core positioned directly behind and parallel to the phase mask. In the phase mask method, the fi-

bre core is irradiated with laser light directly through the phase mask. The method is very popular due to its low complexity and high process stability. The optical fibre is usually placed close to the mask and therefore the influence of mechanical vibrations is minimal. The main disadvantage of this method is limitation of using one phase mask to produce FBG sensor with particular Bragg wave, only. Therefore, producing a variety of FBG sensors (different Bragg wavelengths) require having the same number of phase masks as the FBG sensors types [41].

In the second method (Fig. 3.5(b)), the laser beam is divided into two equal parts, which, using the optical system, interfere with each other. The image of interference fringes affects the fibre core [41]. In the interferometric method, the periodicity of modulation of the refractive index in the fibre core with respect to the ultraviolet wavelength of the source ( $\lambda_{UV}$ ) depends on the angle between the ultraviolet light beams ( $\theta$ ). Therefore it is possible to manufacture FBG sensor with selected Bragg wavelength by changing the angle value. Unfortunately, because of mechanical vibration it is difficult to obtain a stable interference pattern throughout the sensor fabrication process [71].

### 3.3.2 Principle of operation

FBG sensors (Fig. 3.6) are filters using the Bragg reflection principle. The Bragg diffraction grating is a group of closely spaced parallel lines marked on the fibre core at precisely defined distances. The distance between the lines is the diffraction grating constant. Some light of a certain wavelength is reflected from the Bragg diffraction grating. The rest is transferred along the fibre [52].

A Bragg grating is a permanent periodic modulation of the refractive index in the core of a single-mode optical fibre. A typical configuration is a wavelength-selective mirror having maximum reflectivity at the Bragg wavelength  $\lambda_B$ , which is given by the following equation:

$$\lambda_B = 2n_{eff}\Lambda \quad (3.1)$$

where  $n_{eff}$  is the effective refractive index of the mode propagating

in the optical fibre, and  $\Lambda$  is the grating period.

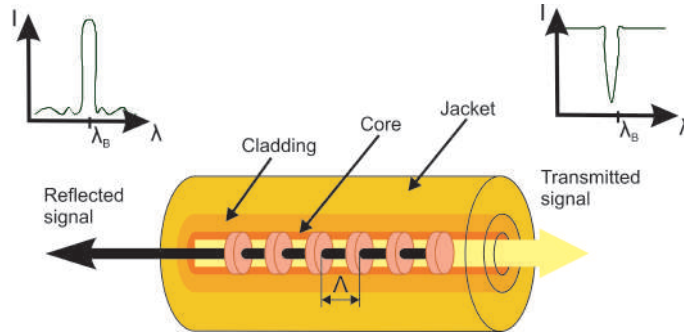


Fig. 3.6: Scheme of FBG sensor.

FBG sensors are sensitive to changes of strain and temperature. The changes in the Bragg wavelength are linearly proportional to the change of those measured parameters. Due to their directional properties, the strongest influences are related to the longitudinal strain (strain in the main axis of the sensor). In the case of strain measurements, a thermal compensation is required.

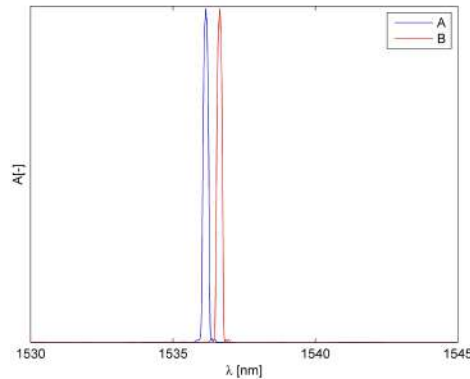


Fig. 3.7: An example of the reflected spectrum – principle of operation of FBG sensor.

Fig. 3.7 presents the principle of operation of FBG sensor. The first spectrum (A) was measured for the undeformed FBG sensor – a base



state. The deformation of the sensor resulting from the application of a tensile load increases the distance between the mirrors of the diffraction grating (increasing the diffraction grating constant  $\Lambda$ ). This process is observed as an increase of the Bragg wavelength. This change is observed as a shift of the main maximum of the spectrum (B) towards larger values of the wavelength. In the case of compressive strains, the principle of operation of the sensor is analogous. As a result of compression, the distances between mirrors in the diffraction grating decrease (the diffraction grating constant  $\Lambda$  decreases). Therefore, the main maximum of the spectrum shifts towards lower wavelength values. Similar behaviour of the measured spectra is observed for temperature measurement.

The standard measurement procedure related to FBG sensors for strain measurement assumes that the spectrum reflected from the sensor contains a single main peak (maximum) only. This assumption is true only when the length of the sensor is sufficiently small so that the strain is constant along the whole length of the grating.

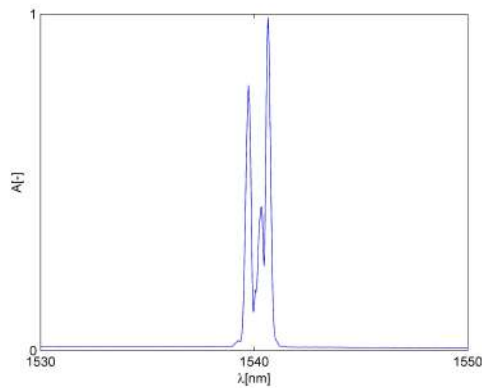


Fig. 3.8: An example of the reflected spectrum distortion – split to spectrum with two maxima.

Another spectrum distortion example is presented in Fig. 3.8. Such distortion of the spectrum can be caused by the compression of the optical fibre in the transverse direction. This changes the cross-section shape of the fibre from circular to ellipsoidal. Due to this

fact, two polarization modes appear. This effect can also be observed on FBG sensors embedded in composite structural elements that are not under load. In this case, it is caused by residual strains in the composite material originated from the embedding process [77].

Fig. 3.9 shows the distortion of the spectrum from the sensor caused by the mismatch of the length of the sensor (diffraction grating) to the strain field in its location. In this case, the tensile load acts only on a part of the diffraction grating. Due to the fact that there is a non-uniform strain field on the sensor, the main maximum cannot be determined in the spectrum reflected from the sensor. For this reason, it is difficult to extract the Bragg wavelength  $\lambda_B$  for the sensor that change is related with the strain of the structure measured by the sensor. The sensor behaviour is similar to a group containing several sensors with similar Bragg wavelengths  $\lambda_B$ . Such kind of spectrum can be observed for embedded FBG sensors under some load conditions [77].

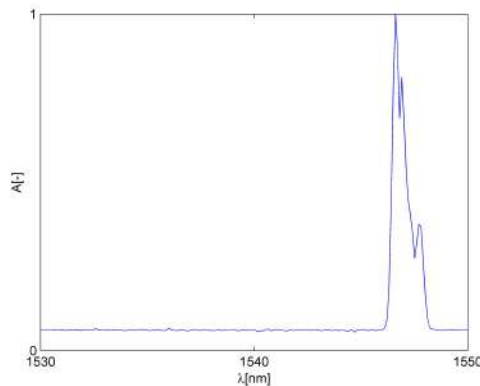


Fig. 3.9: An example of the reflected spectrum distortion – a few maxima with decreasing amplitude values.

Changes in the shape of the reflected spectrum, associated with the appearance of non-uniform deformation of the FBG sensor, are also used in the detection of damage in composite elements.

In SHM systems FBG sensors are mostly applied for strain [122],

and temperature [17] measurements. Changes in these two parameters are linearly proportional to changes in the measured wavelength [113]. The relative change in the Bragg wavelength  $\lambda_B$  due to both temperature and strain is expressed using the followed equation:

$$\Delta\lambda_B = \lambda_B(\alpha + \xi)\Delta T + \lambda_B(1 - \rho_\varepsilon)\varepsilon \quad (3.2)$$

where  $\Delta T$  denotes the change in temperature;  $\varepsilon$  is the longitudinal strain acting within the sensor;  $\alpha$  is the thermal expansion coefficient;  $\xi$  is the thermo-optic coefficient; and  $\rho_\varepsilon$  is the effective photoelastic constant of the fibre core material [62]. Longitudinal strains act on the periodicity of the perturbation (photoelastic effect), whereas temperature affects both the refractive index (thermo-optic effect) and the periodicity of the perturbation (thermoelastic effect) [113]. For silica optical fibres at a Bragg wavelength of  $1550\text{nm}$ , the FBG sensors have a measured sensitivity of  $11\text{ pm}/^\circ\text{C}$  and  $1.3\text{ pm}/\mu\text{m}$  [72]. An example of strain measured on real structure (sailing ship) is presented in Fig. 3.10.

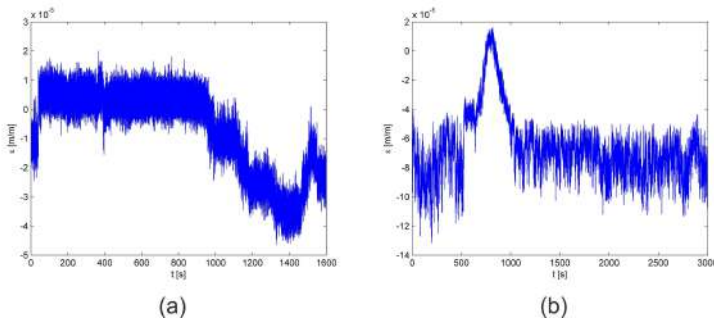


Fig. 3.10: An example of strain measurements on sailing Ship Dar Młodzieży during manoeuvres: (a) setting the sails, (b) wearing the ship.

The FBG sensors advantages, like small dimension and weight, multiplexing capability allow them to embedded into composite structures, e.g. composite hull of a fast patrol boat [77]. Due to the mechanical and geometrical properties of FBG sensors, their influence on material durability is limited.

FBG sensors are applied to monitor the fibre reinforced polymer composites curing process (monitoring strain changes during the entire manufacturing process. Such measurements can be also performed during fabricating elements using additive manufacturing techniques. In both cases the FBG sensors are embedded in the material.

### 3.4 FBG sensors application for SHM

FBG sensors, are applied in SHM systems installed in a various structures, e.g. bridges [30], marine vessels (e.g. fast patrol boat [77] or yacht [20] hulls) or wind turbine blades [55]. Below, some interesting examples of the application of FBG sensors type are presented.

Examples of bridges with SHM systems based on FBG sensors are the Tsing Ma Bridge (Hong Kong, China) and the West Mill Bridge in the UK. On the Tsing Ma Bridge, a system of 40 FBG sensors are mounted on the suspension rope, the rocker bearing and on a the bridge truss. This is part of the entire SHM system called WASHM. The strain measured by the sensors originated from of the bridge loading due to typical car and rail traffic [16].

On the West Mill composite bridge a system of 37 FBG sensors installed. The sensors were embedded into the structure of the bridge. Optical sensors were selected due to their resistance to moisture and high durability, which allowed for the designing a long-term SHM system. Based on the strain values measured by FBG sensors, it is possible to determine the type, direction and speed of each vehicle crossing the bridge [45].

Another structures are wind turbines. SHM system based on FBG sensors was installed on 4.5 MW wind turbine (type E112) located at a wind farm in Wilhelmshaven (Germany). The system based on FBG sensors embedded in the composite material of the rotor blade. In this case, electrical sensors (strain gauges) could not be used due to the high probability of damage caused by the aggressive environment as well as the environmental conditions of the turbine operation. The durability of the SHM system was tested during a year of real-world load measurements of the wind turbine [102].

SHM systems based on FBG sensors can be also installed on buildings. The 16th century historic church of Santa Casa da Misericórdia in Aveiro (Portugal) is an example of this. The SHM system was installed after observing cracks in the building, when it became necessary to assess the stability of the structure. The system was installed on the front facade of the church, therefore one of the most important requirements of the system was invisibility and minimal influence on the historic building. The sensors were installed on both flat and non-planar areas. The sensors allowed determining strain changes related to thermo-mechanical processes in the structure. Additionally, the SHM system recorded the occurrence of an earthquake in February 2007. The collected data are applied for planing restoration and conservation works of the church [54]

SHM systems based on FBG sensors are also installed on marine structures. The SHM system based on FBG sensors was installed on the HnoMS Skjold prototype patrol boat. The purpose of this system was to determine the technical condition of the composite hull and collect information on its actual loads. One of the important applications of the results collected by this system was the verification of the assumed strength of the structure. It was concluded that FBG sensors could be applied for measurements of low-frequency, high-amplitude strains related to the hull bending, as well as high-frequency vibrations occurring in the propulsion system. Based on the data obtained from the SHM system, significant changes were made to the design of the boat [117]. Currently, similar SHM systems are installed on ships of the Norwegian Navy [111].

Tests related to utility of FBG sensors for SHM system on foremast was performed on sailing ship *Dar Młodzieży*. The main goal of the research was to determine the strain/stress level of the foremast during her normal operation. To achieve this goal during the research special attention was paid to responses of sensors during the ship manoeuvres, e.g. setting the sails, taking in the sails, wearing the ship [60].

Another structures are oil platforms subjected to long-term, high-amplitude cyclical loads originated from continuous wave action, cumulative ice floe impacts, submarine earthquakes, and acciden-

tal collisions. In addition, they are exposed to constant corrosion, erosion and flaking. These phenomena accelerate the degradation processes and increasing size of any damage. Applications of electrical sensors (strain gauges) on oil platforms are significantly limited because of occurrence of thermal errors, zero drift, problems with repeatability of readings as well as the sensitivity of these devices to moisture/humidity and the corrosive influence of the sea, etc. as it was mentioned earlier, such problems do not occur for FBG sensors.

On example of such structures is CB271 steel drilling platform located in the Bohai Sea (East China). FBG sensors were used to measure strain and temperature on the lower part of the platform support. The SHM system determined the responses of the structure (its strain) caused by the impact of ocean waves and waves generated by passing heavy ships. It was concluded that the influence of load caused by strong ocean waves to platform durability can be similar to collision with a large vessel. Additionally, the sensitivity of FBG sensors and strain gauges was compared after one year after installation of both arrays on the structure. In the case of optical sensors, no decrease in their sensitivity was observed. However, the strain gauges were damaged by the corrosive action of sea water. [91]



Fig. 3.11: Photographs of fast patrol boat with FBG sensors location area marked by an arrow.

Optical sensors can be also embedded into material of a structure. For example, FBG sensors were embedded into a hull (sandwich structure) of fast patrol boat. Photographs of the boat and the sensors location is presented in Fig. 3.11. The experimental investigations performed on the hull were related to the whole embedding process of FBG sensors as well as the boat construction. The influences of the boat manufacturing on the sensors responses (strain measurements and spectra shapes) were analysed. The utility of designed FBG sensors array for the boat hull was tested during impact tests at dry dock and sea trials. The sensors were applied for strain measurements [77].

Another large-scale application of FBG sensors is aviation. In aircraft structures, their weight is important. It translates directly into the operating costs of aircraft related mainly to fuel costs. This is related to the currently growing interest in the use of composite materials in the construction of aircraft. An important requirement in relation to the aircraft structure is the diagnostics of its structural integrity using non-destructive testing techniques. Ultrasonic methods and thermography, which are successfully used to assess damage in composite structures, are not suitable for use in flight. Measuring systems based on FBG sensors do not have these disadvantages [109].

## Chapter 4

# THz spectroscopy



## 4.1 Introduction

Fibre reinforced polymers (FRP) are recently popular in many industrial branches (e.g. aviation [42], marine [28, 118] or civil engineering [30, 51]). Due to wide variety of applicability FRP elements are working under different environmental and loading conditions. Therefore, to ensure their reliability and guarantee safety of people and ecosystems a variety of non-destructive techniques is developed.

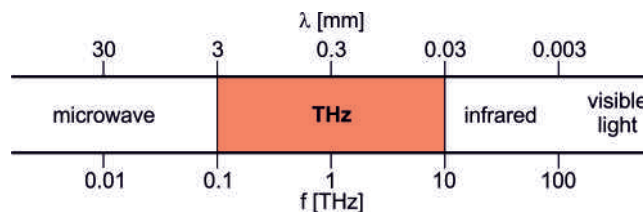


Fig. 4.1: Electromagnetic wave spectrum with marked frequency and wavelength ranges related to THz spectroscopy method.

Many of NDT methods used electromagnetic radiation (Fig. 4.1). One of them is THz spectroscopy. The range of THz electromagnetic waves is typically from 0.1 THz to 10 THz. The THz technique can be used for inspection of internal structures of elements manufactured from non-conductive materials (e.g. tissues [121], paper [87], polymers [81]). In the case of conductive materials whole THz signal is totally reflected from element's surface. Therefore, the applicability of the technique for carbon fibre reinforced polymer (CFRP) materials is limited to their surfaces [76]. However, THz spectroscopy can be applied for examining glass fibre reinforced polymer (GFRP) elements for detection, localisation and determination shape and types of damage (e.g. debonding [73], delamination [100, 104]) as well as inclusion (e.g. Teflon [127], water [74], optical fibres [75]).

Selected advantages and disadvantages of THz spectroscopy method are presented in Tab. 4.1. Very important advantages of the method are low power of the THz beam and non-ionising character of the radiation. Such features allow to perform measurements on sensitive materials, e.g. drying leaves [80].

Tab. 4.1: Advantages and disadvantages of THz spectroscopy.

Feature	Description
Advantages	
low energy	below 1 $\mu\text{W}$
non-ionising radiation	neutral to human body
ability of detection of small discontinuities in material	
Disadvantages	
inspection of non-conductive materials only	cannot be applied for metal or CFRP
water is strong absorber	humidity should be removed from measurement area

## 4.2 Principle of operation

The principle of operation of THz spectroscopy will be presented on TPS Spectra 300 THz Pulsed Imaging and Spectroscopy from TerraView. The measurement equipment is at the IMP PAN laboratory. The unit contains two parts presented in Fig. 4.2.

In the first part (Fig. 4.2(a)) the measurements are performed in one point in transmission mode only. The aim of the system is to determine material parameters (e.g absorption coefficient, refractive index) in the THz wave range. Refractive index is related to the velocity of the THz wave travelling throughout a particular material. Having information about this material parameter is possible to calculate thickness of material and to determine location of a damage hidden inside a sample. Absorption coefficient is linked with the signal attenuation while travelling throughout material.

The second part, called Gantry module (Fig. 4.2(b)), contains two heads that can be arranged in transmission or reflection modes. The system allows to create images of samples with maximal dimension of 700 mm x 700 mm. The Gantry system contains three

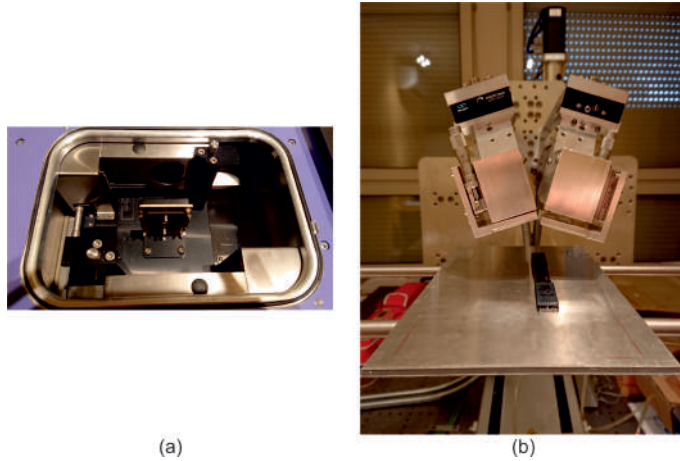


Fig. 4.2: THz spectrometer parts: (a) transmission module, (b) Gantry module in reflection mode.

axis, each of them is controlled using separated engine.

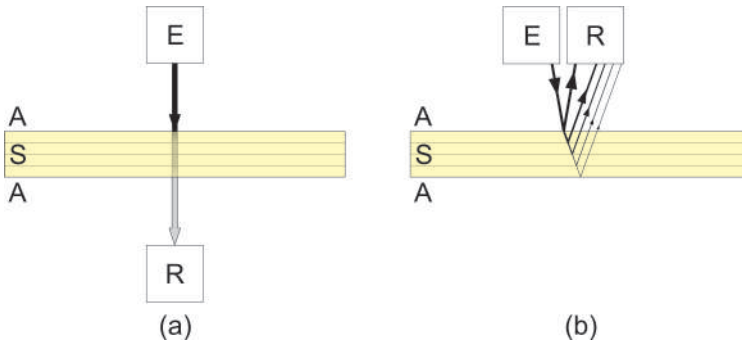


Fig. 4.3: Schema of THz spectrometer modes: (a) transmission, (b) reflection, E – emitter, R – receiver, A – air, S – sample.

The schematic presentation differences between transmission and reflection modes are presented in Fig. 4.3. In both modes, signal goes from the emitter to the receiver. In transmission mode the heads (emitter and receiver) are located on opposite sides of a sample. The registered signal contains information about the media throughout which the THz wave was travelling. In reflection

mode, the heads are arranged in an angle of  $22^\circ$  between them. The THz waves, that reach receiver, are reflected from all boundaries between media, for example air/sample and boundaries between consecutive layers in laminate.

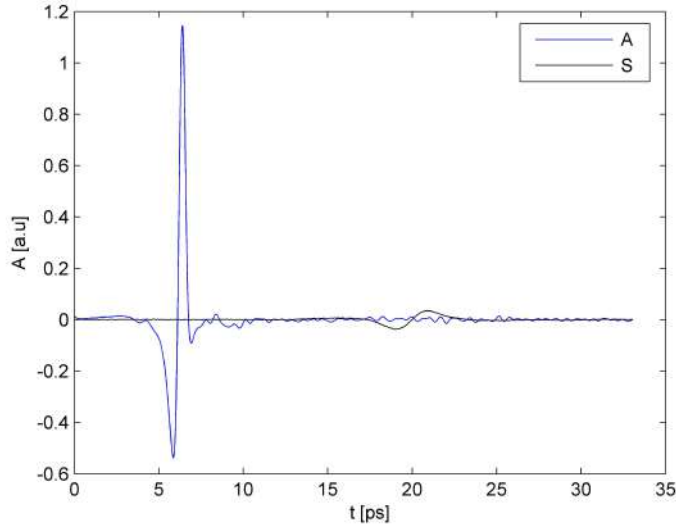


Fig. 4.4: Comparison of THz signals in transmission mode.

For a purpose of better understanding differences between the modes, the THz signals measured for both heads arrangement will be presented. A comparison of two signals measured in reflection mode in the same point without sample (denoted as A) and with sample (denoted as S) is presented in Fig. 4.4. The refractive index of the sample material is higher than the air refractive index. It results in longer time required for the wave to travel throughout the same distance between heads. Therefore the maximum for signal S is observed after a longer time than for signal A. The absorption coefficient of the sample results in attenuation of the signal. It is observed as the decrease of the maximal amplitude of the signal. In the analysed case, the maximal amplitude of signal S is equal to ca. 10% of analogical amplitude in signal A.

In reflection mode, the THz waves are reflected from all boundaries

between media, for example air/sample and boundaries between consecutive layers in laminate. An example of THz signal in reflection mode is presented in Fig. 4.5. It is possible to distinguish parts related to sample and boundaries air/sample, sample/air and air/metal. Reflections from discontinuities hidden inside sample, like boundaries between layers in laminate, delamination, inclusion (e.g. fibre optic, Teflon) are visible as additional maxima in the part of the signal related to the sample.

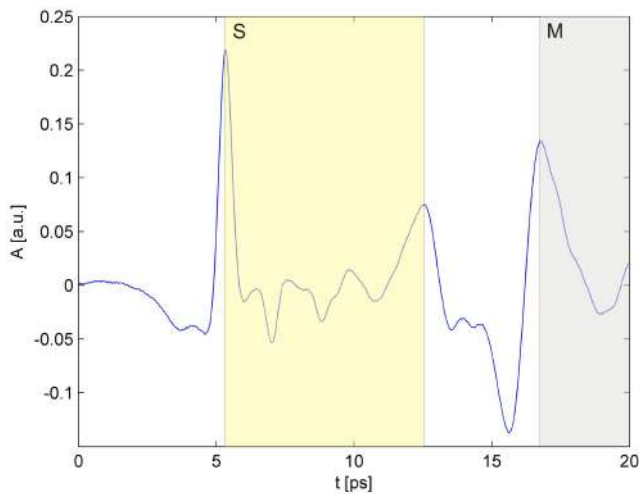


Fig. 4.5: An example of THz signal in reflection mode, S – sample, M – metal.

The THz spectroscopy, similarly like the other imaging techniques, allows presenting the measured data in the following forms: A-scan, B-scan, and C-scan. A-scan is a graph showing the time-domain signal measured at one point and contains information about all THz wave interactions with the analysed material structure. Examples of A-scans for transmission and reflection modes were presented in Fig. 4.4 and Fig. 4.5, respectively. B-scan (Fig. 4.6) is a visual presentation of a set of waveforms measured for points (A-scans) lying on a selected line. Such image presents chosen cross-section of the analysed sample. Performing measurements in few consecutive lines it is possible to create a 3D matrix containing waveforms for

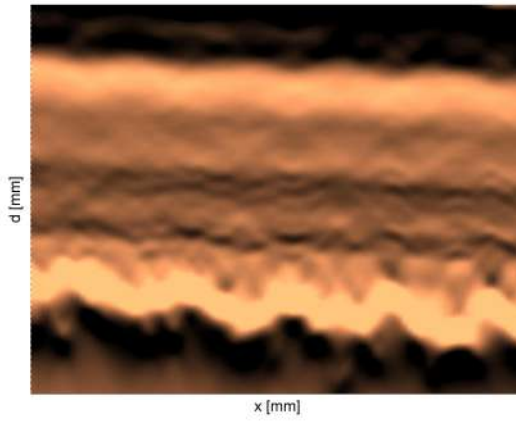


Fig. 4.6: An example of B-scan in reflection mode.

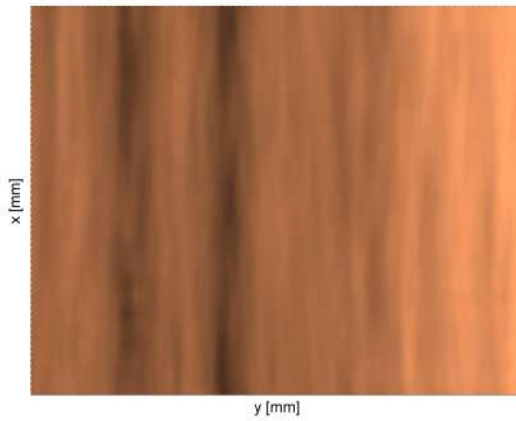


Fig. 4.7: An example of C-scan in reflection mode.

all points on a measured area. Choosing one time, it is possible to create C-scan – a map presenting signal amplitudes for all points for the selected time delay. An example of C-scan in reflection mode is presented in Fig. 4.7. It shows the internal structure of a sample.

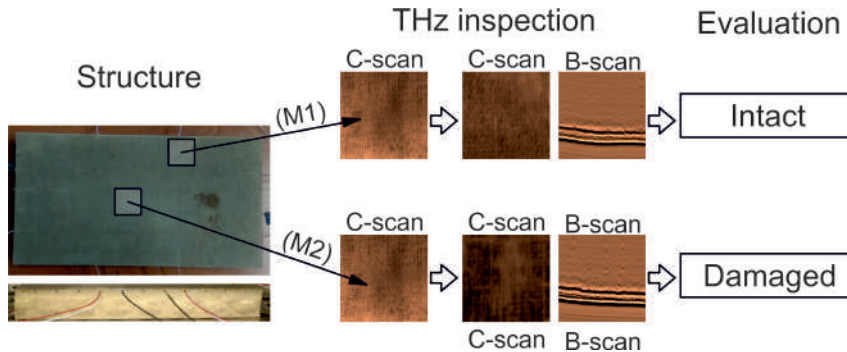


Fig. 4.8: Scheme of THz inspection procedure.

THz radiation can be used in analysis of materials discontinuities or damage types that affects on refractive index, absorption coefficient or can result a THz wave scattering. The schematic procedure of THz spectroscopy application for evaluation of internal structure of element is presented in Fig. 4.8. The analysed structure was a sandwich panel containing two GFRP skins and foam fulfilment. The inspection was focused on the bonding area between skin and fulfilment. The damage was chosen as it is not observable on the sample surface. For NDT inspection, the sample was virtually divided into sections with the same dimensions. In the scheme, a comparison of two them is presented. In the area denoted as M1 the skin and fulfilment are perfectly connected while in the area denoted as M2 a debonding was observed. Because of the type of the damage C-scans for the sample surface are similar for whole sample. Such C-scans are presented in the first column in the scheme for both analysed cases. The second C-scans were created for the boundary between the core and the skin. The lighter area in the middle of second C-scan for M2 is the damaged area. B-scan are created for the sample in chosen line (the middle part of analysed area M1 or M2). In the sample cross-sections, the consecutive parts of the sample are visible. It is also possible to determine the size of the debonding in the particular cross-section.

### 4.3 Examples of the NDT method applications

The THz spectroscopy can be applied for analysing the internal structures of different elements manufactured from non-conductive materials. Examples of three different structure types are presented in Fig. 4.9. The analysed elements are GFRP laminates, sandwich sample and additive manufactured (AM) polymeric samples.

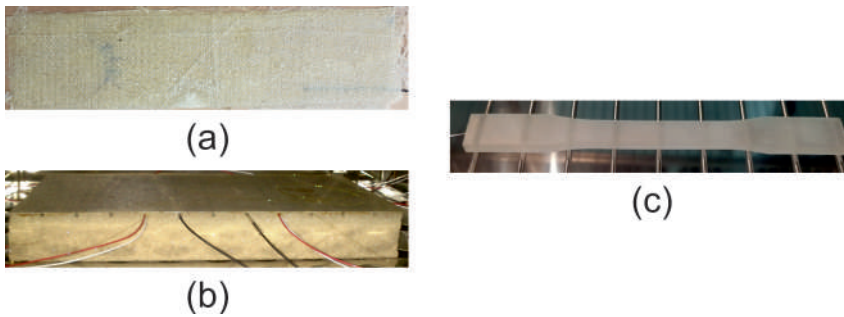


Fig. 4.9: Examples of three samples: (a) GFRP sample, (b) complex sample, (c) polymeric sample.

#### 4.3.1 GFRP samples

The presented GFRP samples were laminates manufactured using infusion method from a glass textile. THz spectroscopy was applied for non-destructive inspection of GFRP material and to determine the thickness of consecutive layers in the laminates as well as to detect an localise different damage and inclusion types. The analysed samples thickness vary from 1 mm to 2 mm.

One of the most typical and dangerous damage for GFRP laminate is delamination. Such damage can be an effect of e.g. impact load. In many cases the surface remain intact. An example of B-scan with two delaminations is presented in Fig. 4.10. THz spectroscopy can be applied for detection only an open delamination. In such case additional boundary between material and air is detected. Sometimes it is observed as a locally thicker boundary between layers



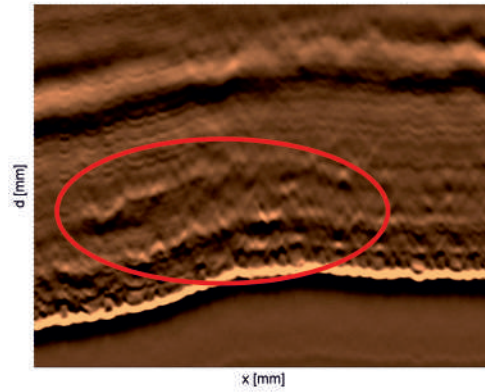


Fig. 4.10: B-scan of GFRP material with delamination.

in laminate. In the case of delamination, THz spectroscopy allows detection its occurrence, determine its location in the thickness direction as well as its size.

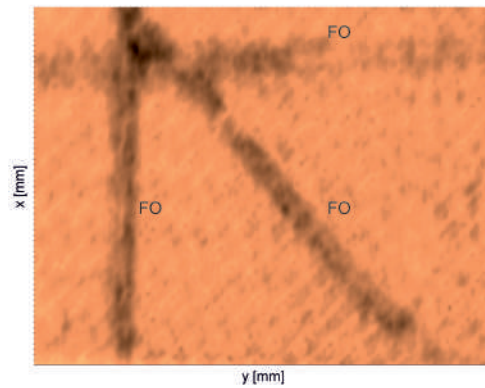


Fig. 4.11: C-scan of GFRP material with embedded optical fibres, FO – optical fibre.

Another type of object that can be detected and localised are inclusions. One of them is water embedded in material due to malfunc-

tion of the production process. Water can be detected because of its high absorption coefficient. In such case a disadvantage, listed in Tab. 4.1, became un useful feature. The details of this application of THz method is presented in paper [74]. A different type of inclusion is optical fibre. Such fibres are embedded in GFRP elements during manufacturing process and then used as a part of structural health monitoring system. An example of C-scan determined for the layer containing optical fibre rosette embedded in the laminate is presented in Fig. 4.11. Optical fibres and glass fibres in GFRP have similar material properties. Additionally optical fibres are very thin. However, the manufacturing method of the element results in scattering of the THz waves on circular shape of the fibres. Detailed explanations are presented in the paper [75].

### 4.3.2 Complex sample

Another structure is a sandwich sample with embedded optical fibres and piezoelectric transducers. The element contains GFRP skins and polyurethane foam fulfilment. The sample thickness was equal to 26 mm. The sample components were joined using epoxy adhesive. The foam contains a structural groves. In some of them piezoelectric transducers and fibre optics were embedded.

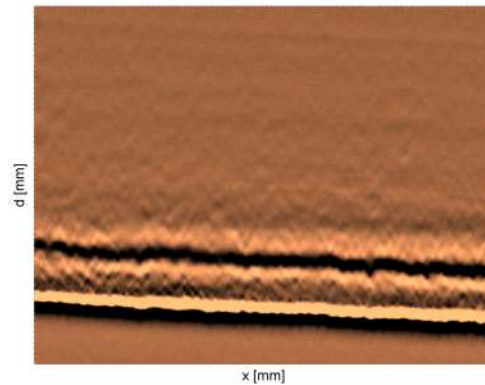


Fig. 4.12: B-scan of the complex sample.

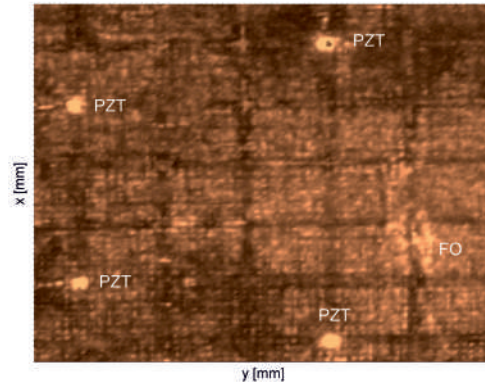


Fig. 4.13: C-scan of complex sample with fulfilment structure as well as embedded transducers (PZT) and optical fibres (FO).

THz spectroscopy allowed to determine the quality of adhesive joint between GFRP and polyurethane. Due to the absorption coefficient value of the foam the THz signal is completely attenuated during its travelling throughout the foam. Therefore, it is not possible to evaluate whole sample thickness during measurements performed from one side of the element. An example of a B-scan of the sample is presented in Fig. 4.12. The NDT method allowed detection and localisation embedded transducers and optical fibres. C-scan of the sample showing the fulfilment structure as well as embedded transducers and optical fibres is presented in Fig. 4.13. Details of the analyses are presented in paper [73].

### 4.3.3 AM sample

Another structure was polymeric sample manufactured using 3D printer. The sample was manufactured from UV cured photopolymer using Multi-jet printing (MJP) manufacturing method. In the method two materials are used: polymer as a structural material and wax as a supporting material. The minimal thickness of one printed layer is be  $16 \mu\text{m}$ . Therefore, the method can be applied for manufacturing elements with high accuracy. Additionally,

the highest temperature that occurs during the AM process is in the range from 30°C to 38°C what is comparable with the human skin temperature. Therefore, the problems related to shrinkage as dimensional stability and residual strain occurrence is limited.

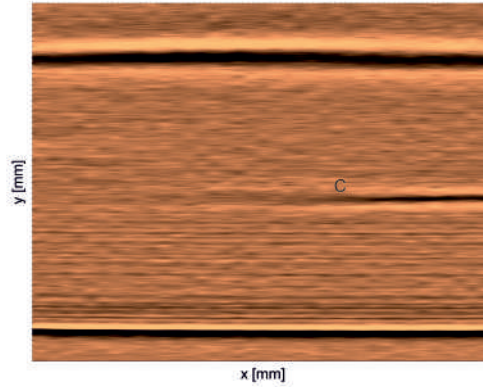


Fig. 4.14: B-scan of the sample with embedded optical fibre.

The analysed elements were dog bone shaped and contained optical fibres. The fibres were embedded in the middle of each sample located parallelly to its main axis. The polymer material properties allowed inspection the sample structure throughout its whole thickness. The B-scan of the sample is presented in Fig. 4.14. During the embedding process of optical fibre some contamination was introduced into the material and it was observed in the sample cross-section. The details about the THz spectroscopy application for AM polymeric structure are presented in paper [72].

## Chapter 5

# Elastic-guided waves generation and sensing for SHM

## 5.1 Introduction

The exploitation of many mechanical structures is related to its periodic damage assessment process. Hidden damage with unnoticed growth could be a source of total collapse of the structure therefore this is important to detect the damage in an early state of evolution just after its initiation. This could be realised using non-destructive testing (NDT). In the NDT very often hand-held measurement devices are utilised. Very popular is the ultrasound testing (UT) method based on heads equipped with transducers that generate and receive diagnostic signals. The NDT methods are utilised periodically and very often they need additional preparation of the structure for the testing and also the exclusion from the usage. Therefore, more and more interesting are methods that allow for continuous structural assessment. Such an approach is called Structural Health Monitoring (SHM). In the SHM the network of actuators and sensors permanently joined with the structure are utilised for the generation and sensing of diagnostic signals. The whole idea of SHM comes from the nervous system of human where the nerves work as sensors and the brain collect and process the data from the sensing system. The main advantage of SHM is its utilisation during the normal exploitation of structure without additional preparation for the testing. Different diagnostic methods could be utilised for the purpose of SHM: vibration-based, strain-based, or guided wave-based. In this chapter, the author will focus on guided wave propagation-based SHM.

## 5.2 Elastic waves

Elastic wave is the motion of the particles of elastic medium where the restoring forces act on the medium particles. In solid structures propagation of longitudinal (L) and shear (S) waves could be observed. In the case of longitudinal waves, the particle displacement is along the direction of the propagating wave. In the case of shear waves the displacement is perpendicular to the wave propagation direction. Such both types of waves propagating in the volume of a solid are called bulk waves. In the thin solid structures due to mul-

multiple internal reflections of L and S waves new types of waves called guided waves could be observed. In the plate-like structures, shear horizontal (SH) waves and Lamb waves could propagate. Mathematical fundamentals of propagation of Lamb waves were formulated by Horace Lamb. Lamb waves can be divided into symmetric and anti-symmetric modes depending on the symmetry of the displacement field. The number of propagating modes depends on the product of wave frequency and thickness of the plate. At least two fundamental symmetric ( $S_0$ ) and anti-symmetric ( $A_0$ ) modes propagate. Higher modes ( $A_1, A_2, \dots$ ) or ( $S_1, S_2, \dots$ ) propagate above the cut-off frequency which could be extracted from the dispersion curves. The waves with different wavelengths propagate at different velocities which is called the dispersion effect. In Fig. 5.1 Lamb wave dispersion curves for steel plate were presented. This plot presents the dependency of the group velocity of Lamb wave modes  $C_g$  in the function of the product of wave frequency and plate thickness  $f \cdot d$ . Propagation of fundamental  $A_0$  and  $S_0$  modes is possible only up to cut-off value  $f \cdot d \sim 1.5 \text{ MHz} \cdot \text{mm}$ . Above this value, propagation of higher-order modes is possible.

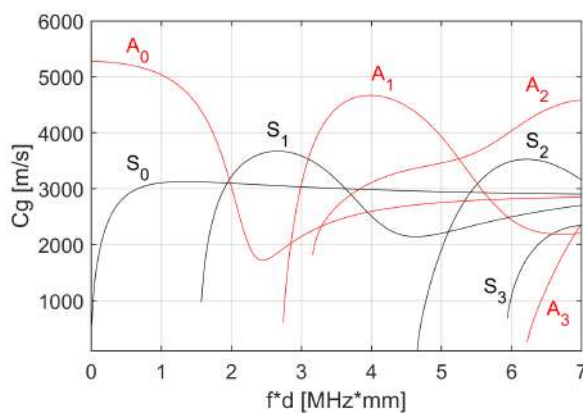


Fig. 5.1: Lamb waves dispersion curves for steel plate.

The phenomenon of elastic wave propagation could be utilised for damage detection. This is caused by the fact that any kind of discontinuity in the medium where the wave propagates is a source

of changes in wave propagation. These changes could be registered as wave reflections, changes in amplitude, changes in velocity/wavelength, or mode conversion. Damage is the source of change of stiffness and sometimes also the mass of the structure that causes discontinuity in the structure. In Fig. 5.2 example of a registered elastic wave signal in a simple panel is presented. The first wave packet is related to generated elastic wave. The last one is related to wave reflection from panel edges. The wavepacket between is related to damage reflected waves. Based on the time of propagation of the damage reflected wave called the time-of-flight (ToF) it is possible to determine the distance of damage from the transducer. This fact is utilised in SHM.

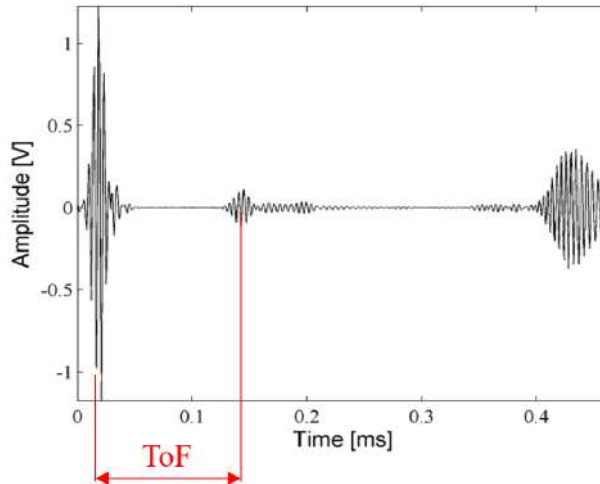


Fig. 5.2: Example of elastic wave signal.

### 5.3 Wave generation and sensing

For the purpose of elastic wave generation and sensing very often piezoelectric materials are utilised. A transducer based on piezoelectric material could work as a wave generator (actuator) as well as a sensor. This is due to the direct and inverse piezoelectric effect. In the case of direct effect, the mechanical energy is converted to



electrical energy. Elastic wave propagation in the structure is related to time-varying strain distribution. Due to electromechanical coupling (piezoelectric transducer bonded to the structure) strains generate the charges on the electrodes of the transducer. They can be converted to voltage signals based on the capacity of the transducer and the load impedance of measurement devices. These electrical signals are related strictly to the propagating elastic waves in the structure. In the case of the inverse piezoelectric effect, the voltage applied to the transducer electrodes causes the strain and deformation of the transducer. In the case of the transducer coupled with the structure strains from the transducer are transferred to the structure. This allows for elastic wave generation based on the electrical signals applied to the transducer.

### 5.3.1 Excitation signals

In the purpose of elastic wave generation, the tone-burst excitation signal is utilised. This signal is based on sine function with amplitude modulation. This signal allows to generate the wave packages. Due to the dispersion phenomenon and multimodal propagation of Lamb waves in the plate-like structures parameters of the wave generation signal need to be chosen carefully. The first parameter is the carrier frequency of the signal. Signal frequency has an influence on the frequency of generated elastic waves. Frequency below cut-off value allows for the generation of only fundamental modes. Multimodal propagation of Lamb waves makes the process of signal analysis difficult therefore it is desired to generate only the fundamental modes and even one desired mode.

To reduce the dispersion effect narrow frequency band signals need to be utilised for wave generation. In the case of wave propagation at long distances, the dispersion causes the deformation of the wave packet which is undesirable from the point of view the signal processing. The width of the frequency band of tone-burst signal is controlled by the number of cycles of the sine function and the type of modulation function. In the case of guided wave propagation signal in the form of a few cycles of sine modulated by Hanning window is frequently utilised. The Hanning window allows for smooth

modulation of the sine function at the beginning and the end of the window which reduced the bandwidth. There are also popular window functions like Gauss and Hamming. In the case of a rectangular window due to the sharp change of modulation function amplitude at the beginning and end time instance, the bandwidth will be much wider. Number of cycles is very often in the range of 3-10, however the most common is 5.

Mentioned type of excitation signal is crucial in the ToF-based SHM systems. In such an approach the time of propagation of the wavepackage (e.g reflected from damage) is utilised in signal processing. However, there could be also broadband frequency signal analysis methods utilised in SHM. In the last case, the excitation signals in the form of a short-time pulse, sweep or chirp could be utilised. Such signal excites many elastic wave modes and the frequency spectrum of the wave signal is broad.

### 5.3.2 Elastic wave generation

In the case of wave generation most popular are piezoelectric transducers. Very often piezoceramic transducers in the form of thin discs/wafers are utilized. Piezoceramic material is very brittle therefore in some cases elastic transducers based on piezoelectric wires embedded in epoxy are utilised. An example of such transducers is Macro Fibre Composite (MFC).

Besides the piezoelectric transducers electromagnetic acoustic transducers (EMATs) are also utilised. They use the magnetostrictive effect to generate elastic waves. They can be applied to structures made of metallic and/or ferromagnetic materials.

### 5.3.3 Elastic wave sensing

Elastic wave sensing is also very often based on sensors made out of piezoelectric material. In such an approach the same transducer can work as a sensor or as an actuator. The most popular are piezoceramic sensors but in some applications like curved panels or pipes flexible sensors are utilised which are based on MFC or PVDV material.

For the purpose of wave sensing more and more fibre Bragg grating (FBG) based strain sensors are utilised. Initially, FBG sensors were utilised for sensing static or quasi-static strain like conventional strain gauges. Further, they were applied for vibration (standing waves) sensing in vibration-based damage assessment methods. Nowadays they are utilised also for elastic wave propagation measurements. The main advantage of the application of FBGs is the lack of use of electrical signals because they work exclusively based on optical signals. Due to this fact, they can be utilised in explosion hazard areas. Moreover, the optical signal could be transmitted through the optical fibre on large distances and one optical fibre could have many FBG sensors that are multiplexed during measurements.

It needs to be underlined here that there is a popular and very useful technique that allows for non-contact elastic wave sensing and visualisation of its propagation. Such a technique is based on scanning laser Doppler vibrometry (SLDV). An example of such equipment is POLYTEC PSV-400 3D scanning vibrometer. This equipment allows for collecting the wave signal from a large area of the structure. This in consequence allows for visualisation of wave propagation and its interactions with the structural elements as well as damage. Such a measurement approach is called full wavefield. Besides the animation of wave propagation, it is possible to perform wave mode filtering. This technique allows to remove the propagation of chosen wave mode from the wavefield. This is helpful in damage imaging. It needs to be underlined that it allows also for wavenumber-frequency analysis which is helpful for the analysis of propagating wave modes. Moreover, it allows to determine the dispersion curves using experimental techniques. This is a very helpful method for structures with unknown properties (e.g. layered composite structures) where the extraction of dispersion curves based on numerical models will cause large errors.

This technique is very helpful for the analysis of wave propagation phenomena in complex structures (thickness change, stiffeners, bolted/riveted/bonded joints). The SLDV is very useful in laboratory conditions during the prototyping stage of the SHM system.

There are solutions using SLDV in the field measurements of the real engineering structures. This is rather NDT approach than SHM.

## 5.4 SHM system

The whole idea of SHM is presented in Fig. 5.3. The key part of the system is the transducer network which delivers diagnostic signals. Acquired signals are the next processed to obtain the information about a structural state of structure. This information is presented in graphic form as a damage map as a result of signal post-processing.

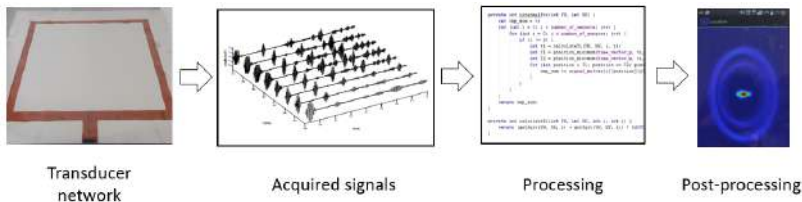


Fig. 5.3: Idea of SHM system.

There are different levels of damage identification in SHM: detection, localisation, determination of size/shape, and determination of type. The SHM system can work in passive mode (only listening to the signals) or in active mode (generation and sensing of the signals). In the passive system elastic waves are generated due to the initiation of the damage (material cracking) or impact. The system only registers the signals related to elastic wave propagation in the structure and can detect and localise the source of waves. An example could be impact detection and localisation system. More interesting is the active system where the elastic waves are generated by actuators and registered by sensors. Damage in the structure acts like a reflector for elastic waves. Focusing on the active SHM system, it consists of the following general sub-systems: transducer network, signal generation/acquisition, signal processing and signal post-processing.

### 5.4.1 Transducer network

The key part that has a direct influence on the work of SHM system is the transducer network. The aim of this network is the generation and sensing of elastic waves. The manner of design of this network will influence the damage sensitivity of the whole system.

Transducers are coupled with the structure to transfer the strain between them. Transducers could be bonded to the structure or embedded in the structure. The process of transducer embedding could be realised in polymer-based structures manufactured in an autoclave in the case of fibre-reinforced polymer composite or the very popular nowadays additive manufacturing process. For this purpose, especially fibre optic sensors could be used due to their very small diameters.

Very important is the type of transducer, its shape, its dimensions, the size of Bragg gratings, and the possibility to attach to the curved parts. The dimensions of the transducer will influence the sensitivity to different elastic wave modes. By choosing the excitation frequency we can control the effectiveness of the transducer for generation and sensitivity of sensor to a particular elastic wave mode. This is caused by relation of sensor dimension to mode wavelength.

An important factor is also the generation/sensing angular characteristic of the transducer. In the case of FBG sensors, they are more sensitive to the elastic wave that propagates in the direction along the sensor. The same situation could be observed in the case of MFC transducers.

However, the most important is the manner of transducer placement on the investigated structures. This is the main aim of transducer network optimisation. The crucial is the decision of how many sensors should be used and where they should be placed. This could be based on structural analysis which could give information about the location of stress concentration. For this purpose also the analysis of elastic wave propagation in complex structures based on numerical simulations could be performed. For this purpose finite element method, FEM or spectral element methods SEM in time/frequency domains could be utilised.

There could be different configurations of transducers: distributed (Fig. 5.4a)), concentrated (Fig. 5.4b)), and mixed (Fig. 5.4c)) depending on transducer distribution on the investigated structure.

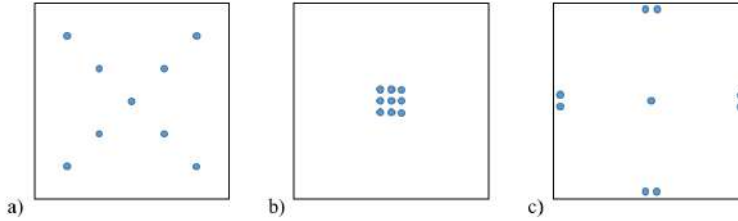


Fig. 5.4: Configurations of transducer networks: a) concentrated, b) distributed, c) mixed.

The state of the transducer network should be also monitored. The transducer can fail as well as can debond from the structure. Transducer could be damaged mechanically or as a result of lightning strikes. Therefore it is important to check if all sensors are coupled with the structures and properly work. In the case of piezoelectric transducers electromechanical impedance method could be utilised. This method allows us to determine the resonant characteristics of the transducer based on measurements of the electrical parameter of the transducer coupled with the structure.

It should be underlined that the electric transducer needs to be connected using shielded coaxial cables in order to prevent the generation of electromagnetic interferences (EMI) during the wave excitation. This allows also to reduce the noise level during the sensing. Shielded cables allow for reducing the cross-talk effect between cables attached to the actuator (voltage up to a hundred volts) and sensors (single mV). Long and not shielded cables or with damaged shields will work as antennas generating and sensing EMI. Moreover, the length of the cables needs to be the aim of analysis. This is because parameters of long cables in high frequencies could cause resonant effects and electromagnetic wave-related phenomena. There is a lack of such electrical problems in the case of FBG sensors and optical fibres transferring signals because they are not influenced by EMI.

### 5.4.2 Signal generation/acquisition

Starting from the problem of signal generation and in consequence elastic wave generation the utilised devices/equipment will be presented. This part will be related only to piezoelectric transducers. The first step in the wave excitation process is the generation of a signal that will drive the transducer. For this purpose signal generator need to be used. Nowadays digital signal generators are utilised. They can be in the form of laboratory equipment as arbitrary waveform generators. Examples of such devices are TTI TGA1241 (one channel, 15 MHz bandwidth, 12 bit resolution with RS232/GPIB communication) or RIGOL DG4062 (2 channels, 60 MHz bandwidth, 14 bits resolution, with USB and LAN communication). Signal generators could be also specially designed as embedded solutions based on direct digital synthesis devices (DDS) or/and programmable units (microcontroller, field programmable gate arrays FPGA). In the case of arbitrary waveform generators on the output, the analog signal used to drive the transducer is obtained. There could be also used an arbitrary waveform generator in the form of a card that could be installed directly in the PC (via PCI, PCI Express) or through the special chassis with communication ports (e.g. National Instrument PXIe chassis). This allows to connect such a card even to a notebook (via USB, Thunderbolt). An example of such a card is PXIe-5413 waveform generator (20 MHz Bandwidth, 16 bits, 2 channels, signals from -12 V to +12 V). In the case of an embedded solution digital to analog converter (DAC) is needed to convert the digital signal form obtained from the microcontroller to the analog signal.

A signal generator could not be utilised for the direct drive of the transducers because they are not designed in order to deliver large electrical power and the output voltage could be too low. Due to this fact signal amplifiers need to be used. This allows using more electrical current/higher voltage. It needs to be underlined that in the case of a piezoelectric transducer due to its capacitive electrical load character proper amplifiers should be used. Examples are EPA 104 Piezo Linear Amplifier (voltage  $\pm 200$  Vpp, current  $\pm 200$  mA, frequency DC to 250 kHz, designed to drive higher capacitive – low

impedance loads) and Krohn Hite 7500 amplifier (voltage 140 Vrms, frequency DC to 1 MHz, voltage gain: 0 dB to 40 dB). Capacitive load is problematic for amplifiers because it could cause the instability of the amplifier resulting in oscillations (it works as a generator). As it was mentioned previously connections of the amplifier with transducers should be performed using shielded cables.

In the case of signal acquisition depending on the transducer it is possible to measure signal from the transducer using an oscilloscope. Examples are LECROY Waverunner LT264 (1 GS/s sampling, 350 MHz bandwidth, 8 bit resolution, 4 channels, with LAN, GPIB communication) and RIGOL DS2302A (2 GHz/s sampling rate, 300 MHz bandwidth, 12 bits resolution, 2 channels, 8" LCD, with LAN, USB, GPIB communication). This could be utilised in the laboratory during the prototyping phase due to the presentation of signals on the large screen of oscilloscopes and the possibility of fast signal analysis (statistical parameters, frequency spectrum, mathematical functions). The second option is to use the data acquisition (DAQ) card with analog to digital converter (ADC) like for example PXIe-5105 (60 MHz, 12 bits, 60 MS/s, 8 channels). The third option could be based on embedded solutions based on programmable devices (microcontrollers, FPGA) with the use of the ADC module. In the case of oscilloscopes, the resolution of ADC is very often equal to 8 bits (LECROY Waverunner LT264). Nowadays, modern oscilloscopes allow to achieve higher resolution like 12 bits (mentioned RIGOL DS2302A). In the acquisition cards and embedded solutions, higher resolutions could be achieved.

However, it needs to be mentioned that very often signal level from the piezoelectric transducer will be not enough to register it directly by oscilloscope/acquisition card. There needs to be an amplifier connected between the transducer and the acquisition unit. In the case of piezoelectric transducer charge amplifiers need to be used. Piezoelectric transducer does not deliver directly the voltage as a response to the deformations (strains) but electrical charges are accumulated at the electrodes of the transducer. Due to the capacitance of the transducer and the input impedance of the acquisition unit, the charges are converted to the voltage signal. However,



the measurement of signals from piezoelectric transducers is only possible if the input impedance of the measurement device is very large. Sometimes its value is not enough to register a signal from piezoelectric transducer and in such a case charge amplifier need to be used. Charge amplifier has a very large input impedance, larger than the input channel of acquisition device. Charge amplifier generates a voltage signal which is proportional to the integrated value of the delivered charges or electrical current and therefore is called charge to voltage converter. It needs to be underlined that the use of the charge amplifier has some additional advantages. Its gain depends only on the feedback capacitance and is not affected by input capacitance like in the case of a typical voltage amplifier. Moreover, the influence of the capacitance of the cable does not influence the gain. This removes the problem of different lengths of cable or the manner of its leading in the structure. Besides the amplification of the signal important is the application of a low-pass filter in the input to the measurement device and correct sampling frequency according to the Nyquist law. The low-pass filter will stop the high-frequency components that are above the bandwidth coming from the sampling theorem (anti-aliasing filter).

It is worth to mention about the equipment needed for the elastic wave sensing based on FBG sensors. In this case most important is a tunable laser source that allows control of the optical wavelength. An example is APEX AP1000 (4 independent tunable laser sources with 1 pm wavelength setting resolution, in the wavelength range of 1526 nm to 1567 nm). It needs to be emphasized that in order to use many FBG sensors in one optical wire they need to have different characteristic wavelength resulting from the different Bragg gratings dimension. Due to the different optical wavelengths of FBGs, it is possible to distinguish different sensors. The tunable laser allows setting the wavelength that is in the linear part of the slope of reflectivity characteristic of FBG sensor. This is utilised in edge filtering elastic wave measurement approach. The laser source is connected to FBG via the circulator. The circulator is three port device whose aim is to send the optical signal separately via two paths: from the laser (port 1) to FBG (port 2) and from FBG (port 2) to the photodetector (port 3). Circulator do not al-

low sending optical signals directly from port 1 to port 3 (laser to the photodetector). The photodetector converts optical to electrical signal (voltage). The electrical signal could be acquired by the oscilloscope, DAQ card or embedded system similarly to the case of piezoelectric sensors.

Finally, data from measurements need to be collected and stored for further processing. In this purpose, two general options could be considered. The first one is based on PC, laptop or very popular nowadays single board computers (SBC) like Raspberry PI and Orange PI. In this case, measurement data need to be sent using a chosen type of data transfer interface. This could be realised by PCI/PCI Express/USB/LAN/WIFI in the case of PC or by USB, LAN, WIFI, or UART in the case of notebook/SBC. The second approach is to use the embedded solution based on a microcontroller/FPGA where the data controlled by this device is stored temporarily in SRAM memory and then transferred further to the host (server) computer or processed in the system if it has sufficient computational power.

### 5.4.3 Signal processing and post-processing

This is a very important part of the whole SHM system. Due to signal processing, it is possible to detect the changes in the signals related to changes in elastic wave propagation. Further, it will allow to detect the damage and determine its location and growth.

Signal processing algorithms can work in real time or they can post-process the registered data. Real-time processing is still a challenge despite very fast growing electronic/computer technology. Multiple channel systems, with high sampling frequency rates, will give a huge amount of data which very often could not be processed in real-time. In such a case data is stored and further post-processed with signal processing algorithms. Real-time processing is utilised in audio systems where the sampling frequencies are significantly lower than for elastic wave-based SHM. However, it needs to be emphasized that in the SHM there is no need to process the data in real-time. Recorded data sets could be simply post-processed just after the acquisition. Even two separate subsystems could be

utilised: one for data acquisition and the second (independent) for processing of data stored in the server.

The first task of signal processing is the filtration of signals. Besides the low-pass filter at the input of the measurement device, additional filters could be utilised to extract some narrower band data or just to remove the noises. For this purpose low-pass, band-pass or high-pass filters could be utilised depending on the need. Such filters could be used in the digital form included in the code. In the case of elastic wave propagation very often narrow frequency band excitation signals are utilised therefore the application of a band-pass filter with the frequency band the same as the excitation signal allows to the removal of the noises out of the band of generated waves. However, damage initiated in the structure could be a source of nonlinearities which are sources of new frequency content in the registered signals. These frequency components have a frequency that was not in the band of excitation signals. Such a phenomenon could be utilised in SHM and in such a case band pass filter could not be used.

Besides filtering, important is data analysis which allows to extraction the damage-related features in signals. Such processing could be based on simple signal subtractions (for different structural states) and the calculation of mathematical indicators of changes in the signal. In this approach, signals gathered in different states of structure (at different time instants) are compared. Mathematical indicators could be for example root mean square deviation (RMSD). However, there could be also a baseline-free approach utilised. In this case, there is a lack of signal subtractions but other methods based on the symmetry of structures and similarity of signals could be utilised.

Signals from the time domain could be transformed to the frequency domain based on Fourier transform and then the change of frequency content could be related to damage. Changes in the signals allow for damage detection. Extraction of signal envelopes and amplitudes allows for determination of the ToF which could be utilised based on signals from different locations for damage localisation. In order to extract the damage localisation very often signals from the sensing network are processed by delay and sum algorithms. Besides

the damage imaging methods based on algorithms connected with conventional programming, there are methods of machine learning (ML). In the ML we have a data model of the system created based on a learning process performed on this data. There could be a supervised or unsupervised learning approach. In the first approach data with labels (damaged/not damaged) is used for learning. In this case, training data is utilised for learning of the model. The second algorithm needs to distinguish changes in the data without labels. ML performs the clustering, classification, or regression process. There are different methods utilised in the frame of ML like decision trees, sported vector machines (SVM), k-nearest neighbors, and k-means clustering. Data processing could be also based on conventional artificial neural networks and networks with a complex architecture called deep neural networks (DNNs). The deep learning approach requires very large data sets for the purpose of the training process.

The aim of data processing and post-processing is the visualisation of the state of the structure. In this purpose, simple damage index could be utilised. However, very often damage imaging algorithm based on damage indices calculated for many locations on the structure is utilised. The last approach allows the creation of the damage influence maps indicating the damage localisation. Such a damage map could also indicate the changes related to damage growth. Results of damage imaging could be presented on the screen of a computer/notebook or LCD screens of embedded devices Fig. 5.5.

Nowadays, when very popular are the Internet of Things (IoT) solutions more and more attention is related to the connection of IoT with the SHM. Measurement dataset stored in the server could be accessed via LAN/WIFI in order to share it with other computers/devices. Such measurement data from the served could be the processes with such a device like smartphones. In Fig. 5.6 example of a damage map created by an Android application whose aim is access to the measurements database and processing of the data based on delay and sum algorithm. Currently, available smartphones are equipped with very powerful microprocessors with multiple cores and graphic processing units (GPU). Such modern ar-

chitecture allows even for the use of trained deep learning models (image classification, voice recognition application).

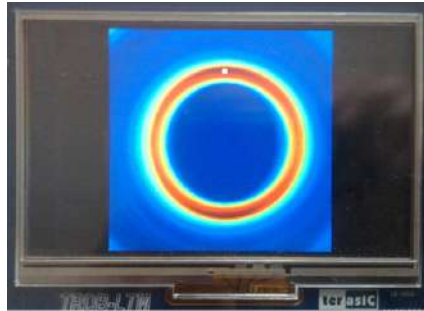


Fig. 5.5: Damage map presented on LCD screen of FPGA based post-processing system.

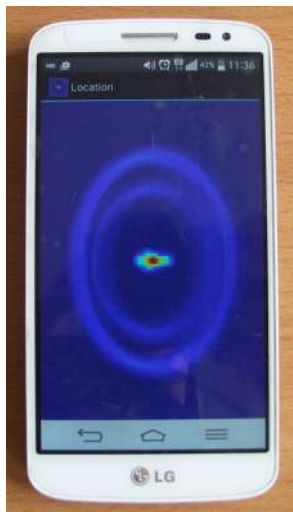


Fig. 5.6: Example of Android application for signal post-processing.

## 5.5 Influence of external factors on SHM

The main idea of SHM is based on a comparison of signals recorded at different time instances (states of structure). Changes in the struc-

tural state will follow with the changes in the signals. As it was mentioned that damage is the source of changes in wave propagation noticed as the changes in gathered wave signals. However, not only the damage could cause changes in the signals and in wave propagation. The first factor that influences wave propagation is the varying ambient temperature. Change in temperature influences the material properties (structure and transducer) and is noticed in wave propagation signals. Temperature change influences elastic wave propagation velocity. The second factor is the load applied to the structure. There could be static load, quasi-static or dynamic. The static load will also influence wave propagation. The dynamic load will result in the vibration of the structure which could influence also the wave signals. Due to much lower frequencies of vibration in comparison to the frequency of excitation of elastic waves changes in the form of low-frequency signal fluctuation can be observed.

A harsh chemical environment or high temperatures can influence the transducer network. It can have the influence on transducer electrodes, bonding layers, cables, and connectors. High temperatures can damage the piezoelectric transducer (Curie temperature). Slow physico-chemical degradation of the transducer network could be also seen in the form of signal changes.

Such mentioned changes in signals due to external influences will be treated by the SHM system like damage. Therefore additional algorithms for compensation of temperature or load influence need to be developed. Otherwise, such external influences will cause false alarms in the SHM system.

## 5.6 Summary

In this chapter basic information about elastic wave propagation-based SHM was given. The author discussed the elastic wave propagation phenomena from the point of view of structural assessment. Moreover, the typical structure of the SHM system with consideration of main subsystems for wave generation/sensing, signal acquisition, and signal processing/post-processing was presented. The au-

thor also gives examples of equipment that could be utilised for elastic wave generation and sensing. This chapter could be used as a basic guide in the process of SHM system development.

## Chapter 6

# Laser vibrometry - fundamentals and applications



## 6.1 History

The theoretical foundation of laser vibrometry can be traced back to the work of Christian Doppler, an Austrian physicist, in 1842. He described how the frequency of waves (including light) changes when the source and observer are in relative motion. The effect was initially studied in the context of acoustics and later applied to electromagnetic waves. In the early 20th century researchers began exploring ways to measure vibrations non-contactingly. The concept of measuring vibrations without physical contact was first explored using methods like the photoelectric effect and optical lever techniques. However, these early methods had limited sensitivity and were not as accurate as needed for many applications.

The invention of the laser in 1960 by Theodore H. Maiman marked a crucial development in the field of optics. Lasers provided coherent and monochromatic light sources, which became instrumental in various scientific and engineering applications, including laser vibrometry. The first laser vibrometer was reported by Yeh and Cummins at Columbia University in 1964. They used it in fluid velocity measurements.

The technology behind laser vibrometry continued to advance in subsequent years, with several researchers and companies contributing to its development. Laser vibrometers were initially large and expensive, making them mainly suitable for research and specialized industrial applications. In the 1970s, heterodyne techniques were introduced to enhance the performance of laser vibrometers. Heterodyne laser vibrometers use two laser beams with slightly different frequencies. These beams interacted with the vibrating surface, and the difference in frequencies was used to extract vibration information with higher accuracy and sensitivity.

An other milestone in laser vibrometry development came in 1979, when Celestion company developed the first scanning Doppler laser vibrometer (SLDV). This has opened up new areas of application for this type of measurement equipment. SLDV was commercially introduced in 1986 by Ometron.

In the 1980s the advancements in laser technology and the miniaturization of components allowed laser vibrometers to become more compact and affordable. This made them more accessible to a wider range of applications and industries. In the next decade laser vibrometry found widespread use in various fields, including aerospace, automotive, civil engineering, and biomechanics. The technology became an essential tool for assessing structural integrity and performing non-destructive testing.

In recent years, laser vibrometry has continued to evolve with advances in optics, electronics, and signal processing. Digital signal processing techniques and improvements in photodetectors have enhanced the accuracy and speed of data acquisition and analysis. Vibrometers became more compact, portable, and capable of measuring vibrations over a broader frequency range. Today, laser vibrometry remains an essential tool in various industries and research fields. It continues to contribute to the understanding of dynamic behavior, structural integrity testing, and the development of more reliable and efficient engineering systems.

## 6.2 Principles of operation

A laser vibrometer, also known as a laser Doppler vibrometer (LDV), is an optical instrument used to measure the vibrations of a surface without physically contacting it. Instead, the laser beam is pointed at the structure's surface and its reflection is registered. It is based on the principle of the Doppler effect, which is the change in frequency (or wavelength) of light reflected from a moving surface. This frequency shift  $\Delta f$  can be expressed as:

$$\Delta f = 2\cos(\alpha)\frac{V}{\lambda} \quad (6.1)$$

where:  $V$  is the velocity of the measured object relative to a reference (observation) point,  $\alpha$  is the angle between the laser beam and the velocity vector of the measured surface, and  $\lambda$  is the wavelength of the emitted wave. To determine the velocity of the object under test, the Doppler frequency change of the electromagnetic wave is

measured at a known wavelength and a fixed angle of incidence of the laser beam:

$$V = \frac{\Delta f \lambda}{2 \cos(\alpha)} \quad (6.2)$$

In laser vibrometry, the process of measuring the change in frequency of a light wave is carried out by a laser interferometer. In this case, two coherent light beams overlap. As a result, the light intensity is not simply the sum of the individual beam intensities, but their interference. The intensity  $I$  of such light is expressed by the formula:

$$I = I_1 + I_2 + 2\sqrt{I_1 I_2 \cos(2\pi \frac{r_1 - r_2}{\lambda})} \quad (6.3)$$

where  $I_1$  and  $I_2$  are the light intensity of the individual beams,  $r_1$  and  $r_2$  are the distance travelled by the corresponding light beams. If the difference in paths travelled is a multiple of the wavelength of the light emitted by the laser, the total light intensity increases by a factor of four. If the difference in paths travelled differs by half the wavelength, the light intensity becomes zero.

The schematic shown in Fig. 6.1 presents the construction and principle of operation of LDV.

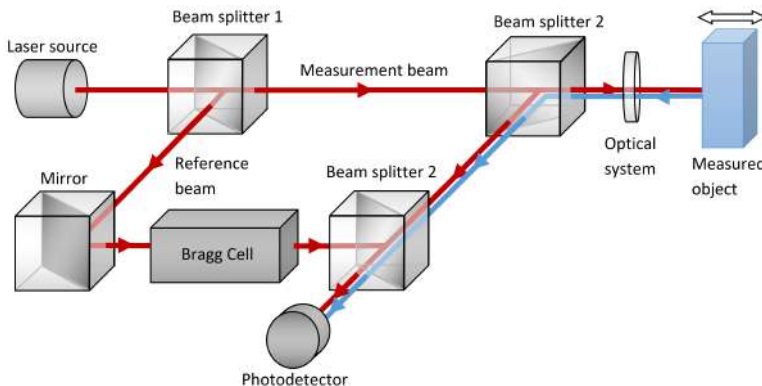


Fig. 6.1: Basic components of laser vibrometer.

A beam from a laser (usually a helium-neon laser or a laser diode) with a frequency  $f_L$  is split by beam splitter 1 into a measurement beam and a reference beam. The former, after passing through the beam divider 2, is focused through the optical system on the object under test. The measurement laser beam is reflected by the measured structure surface. It experiences the Doppler effect due to the motion of the vibrating surface. If the surface moves towards the vibrometer, the frequency of the reflected light will increase. Conversely, if the surface moves away from the vibrometer, the frequency of the reflected light will decrease. The amount of frequency shift is proportional to the velocity of the surface motion (Eq. 6.1). After being reflected measurement beam enters back into the measurement system, where it is directed through beam splitter 2 towards the photodetector. The reference beam directed through the mirror passes through a system that raises (or lowers) its frequency by a known value  $f_b$ . Both beams pass through beam splitter 3, where two beams overlap and hit the photodetector creating an interference pattern.

Since the interference pattern appearing on the photodetector would be the same if the object moved both in the direction of the vibrometer and in the opposite direction, a constant shift of the frequency of one of the beams by a known value – usually 40 MHz – is used. Most commonly, an optical-acoustic modulator, called a Bragg cell, is used for this purpose. This allows the velocity of the object under test to be determined from the signal obtained, based on the modulation frequency of the signal from the photodetector. As a result, a frequency-modulated signal is obtained on the photodetector with a carrier frequency corresponding to the frequency change on the Bragg cell system  $f_b$  and a modulation frequency depending on the velocity vector of the moving sample and resulting from the Doppler effect  $\Delta f$ . In the final stage, the resulting signal is demodulated and the time-domain component of the velocity of the measured point, with a direction parallel to the beam, is obtained. It is also possible to measure displacement with LDV directly. In such a case the signal from the photodetector is not frequency demodulated, but the dark and light fringes are counted.

In general velocity measurements are more suitable for higher frequencies where usually velocities are higher and displacements are smaller, while displacement measurements are more suitable for low frequencies (in the sub Hz range).

Laser vibrometers are highly sensitive and can measure both the velocity and displacement of vibrations with great accuracy. They are widely used in various industries, including aerospace, automotive, structural engineering, and material testing, to study vibrations and assess the structural integrity of components and systems.

### 6.3 LDV types

Laser vibrometers come in different types, each designed for specific applications and with varying levels of complexity and capabilities. Common types of laser vibrometers are shown in Fig. 6.2 and described in this point.

- Single-point LDV

Single-point LDVs are the most basic vibrometers allowing for the velocity or displacement measurement of tested objects at one point in one direction. They can be manually pointed to other points. They form the basis for constructing the remaining types of vibrometers.

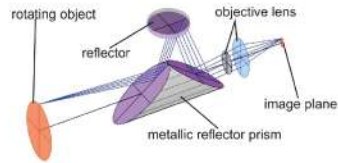
- Differential vibrometers

Differential vibrometers are a type of laser vibrometer that use a differential measurement technique to enhance sensitivity and reduce noise in vibration measurements. Unlike traditional single-point LDVs, which use one laser beam to measure vibrations at a single point on an object's surface, differential vibrometers utilize two or more laser beams that are directed at the same vibrating point on the object's surface. The laser beams may be spatially overlapped or separated, depending on the specific design of the vibrometer. They are designed to measure small vibrations with high accuracy, making them suitable for applications where precise and sensitive measurements are essential.

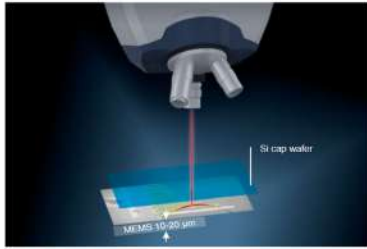
### Single point LDV



### Derotator



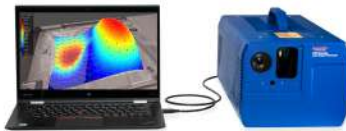
### Microscopic LDV



### Multipoint LDV



### Scanning LDV



### 3D SLDV

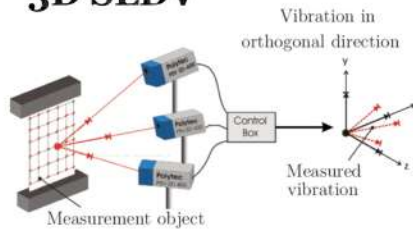


Fig. 6.2: Laser Doppler vibrometer types.

- Rotational LDV

In addition to linear vibration measurements, some laser vibrometers can also measure rotational vibrations or vibrations around a rotational axis. The laser vibrometer is equipped with an optical setup that allows the laser beam to follow the rotation of the object being measured. This can be achieved using a rotating mirror or a rotating prism that reflects the laser beam onto the rotating surface. The rotation of the mirror or prism is synchronized with the rotation of the object. This ensures that the laser beam always strikes the same point on the rotating surface, even as it moves due to the rotation. Derotators are also available on the market, enhancing LDVs and SL DVs to be able to work in this configuration.

The rotational vibration data obtained from the laser vibrometer can be analysed to understand the behaviour of the rotating system, identify potential issues or imbalances, and optimize the performance of rotating components. Rotational vibration measurement with a laser vibrometer provides valuable insights into the dynamics of rotating machinery, such as turbines, motors, fans, and rotors.

- Microscopic laser vibrometers

A microscopic LDV is a specialized laser vibrometer that is designed for measuring vibrations at the microscale or nanoscale level. It offers high sensitivity and precision, allowing researchers and engineers to study and analyse the vibrational behaviour of small and delicate structures, such as microelectromechanical systems (MEMS), nanoscale devices, biological cells, and micro-scale mechanical components. Due to their specialized design and sensitivity, microscopic laser Doppler vibrometers play a crucial role in advancing micro/nanoscale research, precision engineering, and various emerging technologies that involve miniature structures and devices.

- Multibeam LDV

In multi-beam LDV laser beam is directed towards a beam splitter, which divides it into multiple measuring beams. The number of beams generated depends on the design of the multi-beam LDV, and it can range from a few to several dozen beams. A multi-point laser vibrometer allows for the simultaneous measurement of

vibrations at multiple points on an object's surface. Unlike traditional single-point laser vibrometers, which measure vibrations at one specific location at a time, a multipoint laser vibrometer can collect vibration data from multiple points in a single measurement. Moreover, the relative phase between measurement locations can be utilized to instantly generate modal vibration patterns. This ability surpasses the capabilities of single-beam scanning methods and becomes crucial when capturing temporally non-stationary responses during the examination. An other notable benefit, in contrast to single-beam scanning methods, is the quicker inspection time provided by the multi-beam LDV system.

- Scanning LDV

The scanning LDV is equipped with a mechanism to steer the laser beam across the target surface. This mechanism is usually based on a pair of galvanometer mirrors or acousto-optic deflectors (AOD). Galvanometer mirrors consist of small, highly reflective mirrors that can be precisely controlled using electromagnetic coils. AODs use sound waves to control the diffraction angle of the laser beam. Most of the SLDV systems also contain a digital camera. This makes it possible to define a grid of measuring points by indicating on the monitor screen the selected area of the surface to be measured. The advantage of such a system is that a large number of precisely defined points can be measured automatically.

- Continuous scan laser Doppler vibrometry – CSLDV

Continuous-scan Laser Doppler Vibrometry (CSLDV) is a specific technique within the field of laser vibrometry that enables continuous and rapid scanning of the laser beam across the surface of the vibrating object. Unlike traditional point-by-point scanning methods, where measurements are taken at discrete points one at a time, CSLDV allows for continuous measurement of vibrations along a continuous line or area in real time.



- 3D scanning LDV

3D scanning laser Doppler vibrometry (3D SLDV), measures vibrations on the surface of an object in three dimensions. It uses multiple laser beams directed at the target surface from different angles. Separate photodetectors detect the reflections from each laser beam and convert them into electrical signals. With information about the spatial orientation of a structure and laser sources, these signals are processed to extract vibration data along three orthogonal axes (X, Y, and Z). The combined data provides a comprehensive 3D vibration map of the object's surface, allowing to analyse its dynamic behaviour in three dimensions. For complex structures, a 3D SLDV system may be combined with an industrial robot to automate the repositioning of scanning heads. This opens up the possibility of scanning the examined object from different sides.

## 6.4 Advantages and limitations

The LDV offers several advantages compared to traditional contact-based methods and other non-contact techniques. The key advantages of LDVs are given below:

- Non-contact measurement: LDVs provide non-contact vibration measurement, eliminating the need for physical contact with the target surface. It can be directed at targets that are too small, too hot or too fragile to attach a physical transducer.
- No mass loading: LDVs measure vibrations without physically attaching any mass to the target, making them particularly suitable for delicate structures and MEMS devices that could be affected by additional mass.
- High sensitivity: LDVs are highly sensitive and can detect even small-amplitude vibrations with great accuracy. They are capable of measuring micro-vibrations and subtle structural responses, which may not be feasible with other methods.

- High precision: LDVs offer high precision in vibration measurements, providing accurate and reliable data for both amplitude and frequency of vibrations.
- Wide frequency range: LDVs can measure vibrations over a broad frequency range, from extremely low frequencies (e.g. sub-Hertz) to very high frequencies (e.g. several megahertz).
- Full-field vibration mapping: Scanning LDVs enable full-field vibration mapping, providing a comprehensive view of the dynamic behaviour of a structure. This capability allows for a visualization of complex vibration patterns and mode shapes on large surfaces with very high spatial resolution.
- Remote sensing: Some LDVs can perform remote sensing, allowing measurements of vibrations from a distance. This feature is valuable for assessing vibrations in hazardous or hard-to-reach areas, such as industrial machinery or aerospace components.

While laser Doppler vibrometers offer numerous advantages, they also have some limitations and disadvantages. The key limitations of LDVs are:

- Cost: LDVs can be relatively expensive compared to traditional contact-based vibration measurement methods or other non-contact vibration sensors. The initial investment and maintenance costs may be prohibitive for some applications.
- Line of sight requirement: LDVs require a direct line of sight between the laser beam and the target surface. This limitation can be challenging in scenarios where the target is obstructed or has complex geometries, making it difficult to achieve measurements at certain locations.
- Sensitivity to surface properties: LDVs work best with reflective surfaces as they rely on the reflection of the laser beam for measurement. Non-reflective or absorptive surfaces may not provide sufficient feedback, limiting the applicability of LDVs in some cases.

- Environmental interference: Environmental factors, such as ambient light or vibrations from external sources, can interfere with LDV measurements, affecting accuracy and reliability.
- Calibration: LDVs require regular calibration to maintain accuracy and reliability. The calibration process can be complex and time-consuming, especially for multi-beam or scanning LDVs.
- Complexity: The technology behind LDVs, especially multi-beam and scanning variants, involves intricate optics, electronic components, and data processing algorithms. This complexity may require specialized knowledge and training for proper operation and maintenance.

Despite these disadvantages, LDVs remain valuable tools for vibration analysis and testing in various industries and research fields. Careful consideration of the specific application and target characteristics can help mitigate these limitations and maximize the benefits of using LDVs for measurements.

## 6.5 Applications

Laser Doppler vibrometers find a wide range of applications across various industries and research fields due to their non-contact, high-sensitivity measurement capabilities. Some of the primary applications of LDVs include:

- Structure dynamics

The most common application of LDVs is structure dynamic measurement. This technique is used in structural engineering to study the vibrations of buildings, bridges, and other structures. It is used to assess structural integrity, identify potential weak points, and monitor the behaviour of structures under different loads or environmental conditions.

In the aerospace industry, LDVs are used to analyse the dynamic behaviour of aircraft components, such as wings, propellers, and engines. They play a crucial role in ensuring the safety and performance of aircraft by detecting any undesirable vibrations.

LDVs are also extensively used in the automotive industry for vibration measurement of chassis, suspension systems, braking systems, and a variety of electric drives, to mention a few. This helps improve ride comfort, stability, and overall vehicle performance.

Nowadays LDVs have become a standard tool for speaker design, and have also been used to diagnose the performance of musical instruments. They are valuable tools in acoustic studies and noise control applications.

Equipped with fibre-optic probes laser vibrometers are used for measuring vibrations in micro- and nano-scale systems, such as micro-electromechanical systems (MEMS) and nanoscale devices. These applications are crucial in the development of miniaturized technologies. Overall, the versatility and precision of LDVs make them indispensable tools for engineers and researchers for structure dynamics measurement seeking to improve the design and optimization of various mechanical systems, structures, and components across different industries.

- Non-destructive testing and condition monitoring

LDVs are used for continuous monitoring and maintenance testing of the structural integrity of buildings, bridges, aircraft, and other critical structures. They can detect changes in vibration patterns and identify potential damage or defects.

The principle of this operation is based on analysing the dynamic response of the system. The occurrence of damage leads to changes in the system's dynamics and, therefore, changes in its modal parameters (natural frequencies, mode shapes, modal damping), and its frequency response function. Tracking these changes allows for monitoring the technical condition of the object. An example of damage detection is presented in Fig. 6.3, where the measured mode shape is processed using signal analysis methods to create a damage map.

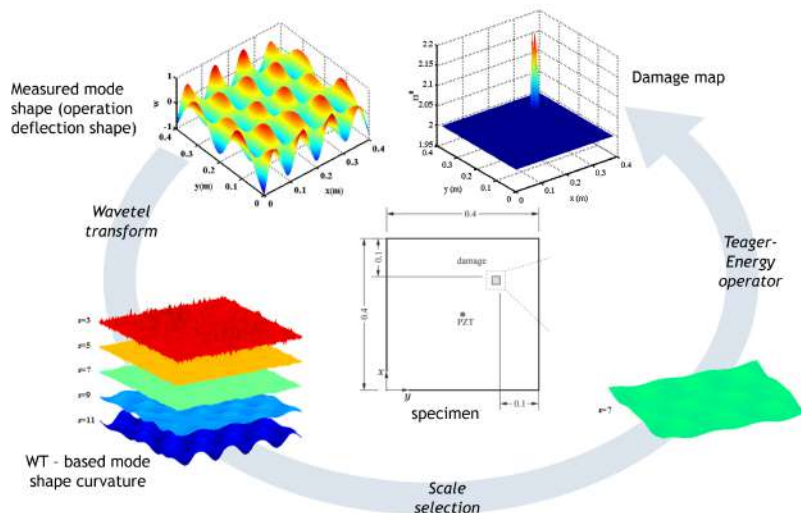


Fig. 6.3: Mode shape-based NDT.

LDVs are also employed in industrial settings for condition monitoring of rotating machinery, such as turbines, motors, and pumps. They can detect early signs of mechanical faults, imbalance, misalignment, or wear manifested in vibration changes, helping to prevent costly breakdowns and unplanned downtime. Similar techniques are used in quality control inspections on the production lines, in which defects, cracks, and material irregularities can be detected.

An other interesting non-destructive testing technique that utilises measurement by SLDV is based on the elastic wave propagation phenomenon. Those waves can travel long distances in structures and are sensitive to changes in the material's properties. The analysis of this phenomenon allows for the detection, localization and assessment of various types of damage in structural elements. An example of a damage mapping technique based on elastic wave analysis is presented in Fig. 6.4.

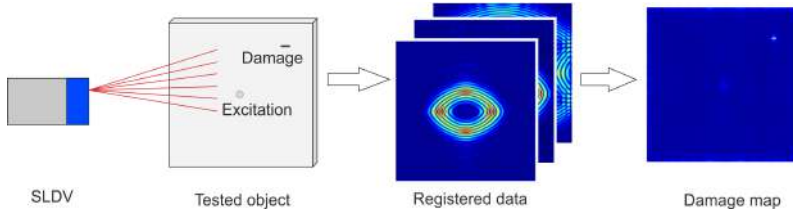


Fig. 6.4: Elastic wave-based NDT.

- Material characterization

LDVs are utilized in materials science to study the mechanical properties and behaviour of various materials. They can be used to determine the mechanical properties of materials, such as their Young's modulus, Poisson's ratio, and damping coefficients, by analysing the resonant frequencies and mode shapes of test specimens. Additionally, SLDVs can be used to register full-field signals of elastic wave propagation. These waves carry information about the materials' internal structure and properties and can be used for material characterization.

- Medical and biological applications

Laser vibrometry has also been found to be a valuable tool for medical research, diagnosis, and treatment evaluation. Its ability to measure subtle mechanical movements in biological systems offers unique insights into various physiological processes and aids in the development of advanced medical technologies.

LDV measurements are used to assess the mechanical properties of bones and joints, as well as to aid in designing prosthetics and optimizing rehabilitation treatments. They are also used to study the vibrations of the middle ear and the cochlea, aiding in research related to hearing function and disorders. They help in understanding the mechanics of sound transmission and can assist in diagnosing hearing impairments.

In dentistry, laser vibrometers are used to analyse the vibrations of teeth and dental structures as well as dental scalers. They are helpful in studying the behaviour of dental implants, prosthetics,

and the effects of various dental treatments on oral tissues and enhancing the quality of vibration of dental tools.

In ophthalmology, measurements of corneal and ocular surface vibrations are performed with LDVs. They are useful in studying eye movements, assessing ocular biomechanics, and evaluating the effects of intraocular pressure on the eye.

Laser vibrometers are used in respiratory research to measure chest wall and lung vibrations. They assist in understanding respiratory mechanics and diagnosing respiratory disorders.

In biomechanics research, they are used to analyse human movements, study gait patterns, and understand the dynamics of musculoskeletal systems.

- Laser microphone

A laser Doppler vibrometer may be used as a laser microphone. When equipped with an infrared laser it can be used to eavesdrop with minimal chance of exposure.

The principle of operation of a laser microphone is based on the fact that propagating sound, such as human speech, can cause objects it encounters to vibrate. Recording these vibrations allows for the reproduction of the sound waves that triggered them. Depending on the laser light the vibration can be registered through the glass (e.g. window) or from its surface.

- Sound wavefield visualization

LDV can also be utilized to visualize the propagation of sound waves in the air. When a sound wave travels in the air, it causes density variations, resulting in local changes in the air refractive index. By measuring the variation of the optical path, which directly depends on the refractive index, the Vibrometer enables the direct visualization of the propagating sound field in the air. This method has been employed in various fields, including loudspeaker design, musical instrument analysis, and transportation. An example of an acoustic field generated by an acoustic transmitter measurement is presented in Fig. 6.5.

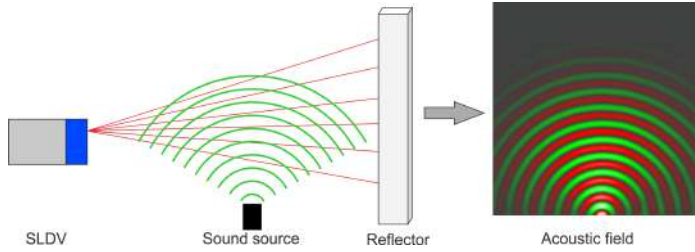


Fig. 6.5: Acoustic field measurement.

Laser Doppler vibrometers have evolved into a powerful and indispensable tool for researchers, engineers, and technicians in various industries, providing valuable insights into the dynamic behaviour of mechanical systems and helping to improve the design, performance, and safety of a wide range of products and structures in all scales starting from nano-scale up to building size scale. As technology advances and innovations emerge, laser vibrometry will continue to play a vital role in advancing scientific research, engineering applications, and our understanding of vibrations in the world around us.



## Chapter 7

# Pomeranian Eco Energy Centre in Lubań



Lubań, Eco Energy concept. source: Eco-Construction Ltd.

The Lubań Living Lab is located in the Kashubian village of Lubań (Kashubian: Lëbòniô) the history of which dates back to the middle-ages (first mentioned in 1280). The population of the rural community in 2019 was about 2000 inhabitants. In XVIII century the mansion was owned by the mother of Józef Wybicki, Polish politician who authored the Polish national anthem. Till the end of the II World War the village was a grange with a XIX century mansion and an extension housing distillery, surrounded by a historical park. The complex, holding during the communistic regime, status of the state-owned farm was a renowned Regional Agricultural Innovation Center ensuring work services for over 3 000 people, along with the village church and shops. Already at the beginning of 90ties village was equipped with an independent sewerage system and a district heating grid supplying heat and domestic hot water to the housing quarters, the grange, the mansion and the Pomeranian Agricultural Advisory Center (PODR) adopting the former agricultural school buildings. The system was powered by a culm-fueled boiler house located in the old distillery. Later, two 900 kW coal boilers were located in an adjacent building. The historical heritage of this place had been significantly damaged, which was the common fate for most manor estates nationalised after 1945. After the system changes of 1989, over many years, Lubań was an example of the slow degradation and depopulation of rural areas, hopelessly waiting for a public development strategy.

In 2012, the Institute of Fluid-Flow Machinery Polish Academy of Sciences (IMP PAN) supported by the Energy Department at the Marshal Office in Gdańsk, initiated cooperation with the PODR, for development and promotion of new technologies in the field of distributed energetics for rural areas. The PODR Center, the largest employer in the region, actively supports both agricultural innovation and the energy prosumer ideas in rural areas. Nowadays, Lubań is known mainly for the Kashubian Agricultural Autumn Fair, gathering up to 50 000 people every year, since 1992.



The XI Kashubian Agricultural Autumn Fair in Lubań, held annually since 1992. source: PODR

In 2015 in active cooperation between the IMP PAN, the Gdańsk University of Technology (GUT) and the private Eco-Construction company, the first microbiogas plant was built as a new educational infrastructure on the PODR plot. This pilot installation of the project *Integrated Technologies for Fuel and Energy Production from Biomass, Agricultural Waste, etc.* in the *Strategic program – Advanced Energy Technologies* of Polish National Centre for Research and Development (NCBR), was used as a Living Lab for subsequent investigations and biogas promotion by scientific institutions and the PODR till 2020. Gradual improvements have led to the changes both in technical and socio-economical domains.

During the interaction and discussions with the local community and the main public-sector stakeholders (esp. PODR), the team of Eco-Construction Ltd., recognized the significance and the high potential of this historical yet degraded village. Its revitalization can be an exemplary subject of energy transition in rural areas. As early as 2015, the company therefore designed (in cooperation with the IMP PAN) a new, energy plus PODR headquarters, while the PODR decided to move its headquarters from Gdańsk. The design included a 40 kW solar installation on a field (executed on and connected to the grid), a solar parking (a concept), a 40 kW wind turbine and 140 kW ground source heat pumps (already executed, supplying two PODR office buildings). In July 2017, a new (totally refurbished) PODR Centre was opened.

In the meantime, a series of interactions and discussion with local citizens and activists led to the development of plans for revitalization of the entire village, including the mansion with the distillery and an energy supply system. In 2016, as the first step, Eco-Construction Ltd. initiated the Revitalisation Living Lab activities aimed at energy transition towards an energy plus village, which involved development of plans in cooperation with the residents, the local administration and IMP PAN participation. The revitalization plan included a solar parking (Fig. 7.1.A), the renovated mansion house with a historical park and the educational path (Fig. 7.1.B), a new private housing estate (Fig. 7.1.C), a new 250 kW biogas plant exploiting the biowaste available locally (i.e. pig, cattle and poultry manure, grass and municipal biowaste) (Fig. 7.1.D), a 40 kW photovoltaic micro-installation and a windmill (Fig. 7.1.E), the Education and R&D Centre (Fig. 7.1.F) and an innovative, low temperature, 4th generation district heating system with a boiler house (located in the old distillery, in the left wing of the mansion). Meanwhile, as a part of the preparation, Eco-Construction Ltd. invested in and bought an old dilapidated distillery, where the new innovative heating system is being designed, including a green energy fueled boilers, supported with PV installation, solar panels and air heat pumps; it should replace the oversized 900 kWt boilers fueled by highly polluting culm (coal waste).



Fig. 7.1: Areal photo 2019 of Lubań and the village revitalization concept, with the Pomeranian Energy Cluster infrastructure designed by Eco-Construction Ltd. From the top left: (A) solar parking in front of PODR headquarter (B) renovated mansion house with historical park and the educational path (revitalization finished in 2020), (C) private housing estate. From the lower left: (D) biogas installation, the wind mill tubin, (E) a 40 kW photovoltaic micro-installation and a windmill, (F) the Education and R&D Centre. Source: Eco-Construction Ltd.

The Revitalisation Living Lab activities included a series of meetings related to:

1. design plan of energy cluster – in cooperation with IMP PAN and GUT – developed by Eco-Construction Ltd.
2. presentation of the design plan during several meetings with local citizens and activists, the municipality and the PODR administration, as well as members of the Polish Parliament

3. development of the LTDH idea with participation of Lubań citizens and the Lubanianka housing cooperative
4. signing of a Letter of Intent with the local cooperative, in order to refurbish a common heating system
5. presentation of a design plan during various project meetings with companies, regional and national authorities, and lobbying with the decision makers
6. development of an Educational Path as part of the Living Lab on RES and waste management

These activities led to the signing of a Letter of Intent (LoI) related to the Pomeranian Energy Cluster (located in Lubań), between local authorities, the GUT, the IMP PAN, and Eco-Construction Ltd. (2016). In 2017, Eco-Construction Ltd. presented the first draft of the revitalization plan for Lubań, developed in cooperation with IMP PAN and local activists, with emphasis on RES (Fig. 7.1). Wide promotion of the Revitalisation Living Lab and the plan designed began.

In 2019, PODR built the designed micro PV farm (40 kWp). Simultaneously, the activities aiming at replacement of the old, oversized coal boiler house supplying the heating to the Lubanianka Housing Cooperative (LHC) began. After the thermomodernization, the heat demand for houses should drop drastically and the heating systems should work more efficiently when it is matched to the heat demand. However, the existing boiler house is equipped with 2 large 900 kW coal boilers, although the average heat demand is a maximum of 350 kW in winter and drops to 60 kW during summer. It has been estimated that the yearly average efficiency of the system approaches 50% and drops to 20% during summer, when only domestic hot water is in demand.

The assessment results were presented to the LHC administration and during a housing cooperative gathering. After a series of meetings and clarifications, an LoI was signed in May 2020 between the LHC, Eco-Construction Ltd. and IMP PAN which has opened the road towards the LTDH system implementation in Lubań. A new on-line energy monitoring system has been designed and imple-

mented by Eco-Construction Ltd. as a part of doctoral work which enables continuous analysis of parameters of the existing grid and boiler house. It takes into account the possibility of heat supply for new housing estates, hotels and restaurants in an Education and R&D Centre (Fig. 7.1), implementation of various RES, including heat-storage systems enabling appropriate heat-demand response. This would be one of the first LTDH systems in a Polish rural area and a benchmark for similar systems.

The municipality of Nowa Karczma (which includes the village of Lubań) strongly supports the concept of the Lubań revitalization. In the years 2016-2022, the municipality designed and implemented a new street plan in Lubań, taking into account the revitalization plans. Additionally, in 2020 as part of the Wasteman project of South Baltic Program, the municipality implemented an educational path, as part of the Revitalisation Living Lab – designed by Eco-Construction Ltd. and the IMP PAN, in relation to waste management and RES.

## Part II

# Intelligent distributed generation




# Introduction

I have a pleasure to present the second part of the e-book for PhD students. It contains materials related to the second school in the subject of '*Clean energy and functional materials*', with a subtitle '**Intelligent distributed generation**'.

The school was realised in the online learning at IMP PAN in Gdańsk, 20.02 – 24.02.2023. The presented knowledge is linked with cogeneration systems, heat and energy production, optimization of systems in terms of savings and efficiency, measurements of fluid flow parameters, etc.

I would like to warmly thank the people who co-created this e-book, especially the authors of individual subchapters:

 Aleksander Olczyk – Chapter 9, Chapter 10

 Tomasz Przybyliński – Chapter 11

Magdalena Mieloszyk, DSc PhD Eng., assoc. prof. IMP PAN  
Director of the Tricity Doctoral School,  
Polish Academy of Sciences

## Chapter 8

# The second School information & statistics

The second school was realised in the online learning form, in days 20.02.2023 – 24.02.2023.

Hour		Online				
		Day 1	Day 2	Day 3	Day 4	Day 5
08:00	08:15	W/R				
08:15	09:00	L1	L9	L17	L25	L33
09:00	09:45	L2	L10	L18	L26	L34
09:45	10:00	CB	CB	CB	CB	CB
10:00	10:45	L3	L11	L19	L27	L35
10:45	11:30	L4	L12	L20	L28	L36
11:30	11:45	CB	CB	CB	CB	CB
11:45	12:30	L5	L13	L21	L29	L37
12:30	13:15	L6	L14	L22	L30	L38
13:15	14:00	LB	LB	LB	LB	LB
14:00	14:45	L7	L15	L23	L31	L39
14:45	15:30	L8	L16	L24	L32	L40
15:30	15:45		CB	CB	CB	C
15:45	17:15		LaP	GT		
17:15	18:45					

W – welcome, C – closing, R – registration, CB – coffee break, LB – lunch break, L – lecture, LaP – lecture about Poland, GT – Gdańsk virtual guided tour

The school included lectures:

- ① online
  - ✎ 40 hours of substantial lessons
  - ✎ 3 hours of Polish culture and history
  - ✎ 2x1.5 hours of virtual Gdańsk guided tour

The lectures were given by lecturers from:

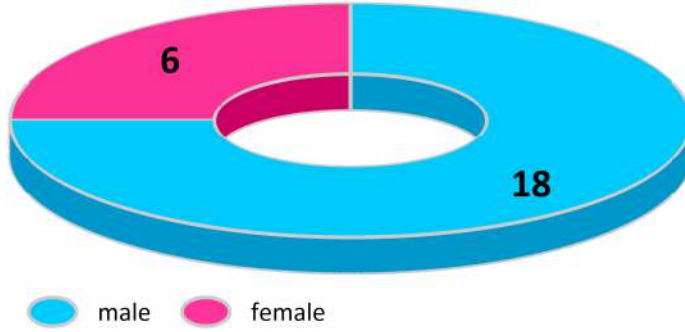
- ✓ 1 person from Spain
- ✓ 1 person from The Netherlands
- ✓ 4 persons out of IMP PAN (Kraków, Łódź)
- ✓ 6 persons from IMP PAN

## Lecturers:

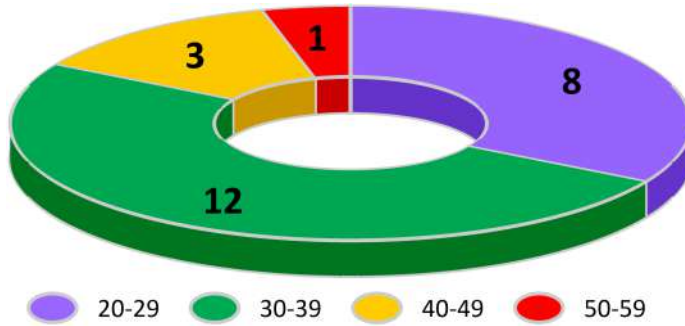
- ALICIA CRESPO  
Universitat de Lleida, Spain
- dr inż. ARTUR POZARLIK  
University of Twente, The Netherlands
- dr hab. inż. PAWEŁ MADEJSKI  
AGH University of Science and Technology in Kraków, Poland
- dr hab. inż. ADAM MARTOWICZ  
AGH University of Science and Technology in Kraków, Poland
- dr hab. inż. ALEKSANDER OLCZYK  
Łódź University of Technology, Poland
- dr inż. KIRILL KABALYK  
Łódź University of Technology, Poland
- dr hab. inż. PIOTR LAMPART  
Institute of Fluid-Flow Machinery Polish Academy of Sciences, Poland
- dr inż. ŁUKASZ BREŃKACZ  
Institute of Fluid-Flow Machinery Polish Academy of Sciences, Poland
- dr inż. KSAWERY KULIGOWSKI  
Institute of Fluid-Flow Machinery Polish Academy of Sciences, Poland
- dr inż. TOMASZ KACZMARCZYK  
Institute of Fluid-Flow Machinery Polish Academy of Sciences, Poland
- dr inż. TOMASZ PRZYBYLIŃSKI  
Institute of Fluid-Flow Machinery Polish Academy of Sciences, Poland
- dr inż. ROHAN SOMAN  
Institute of Fluid-Flow Machinery Polish Academy of Sciences, Poland

The PhD students, who took a part in the school, at the recruitment stage, filled out an application forms. In the second school edition 24 persons were participating. Based on their submitted application forms, the following statistical data was obtained:

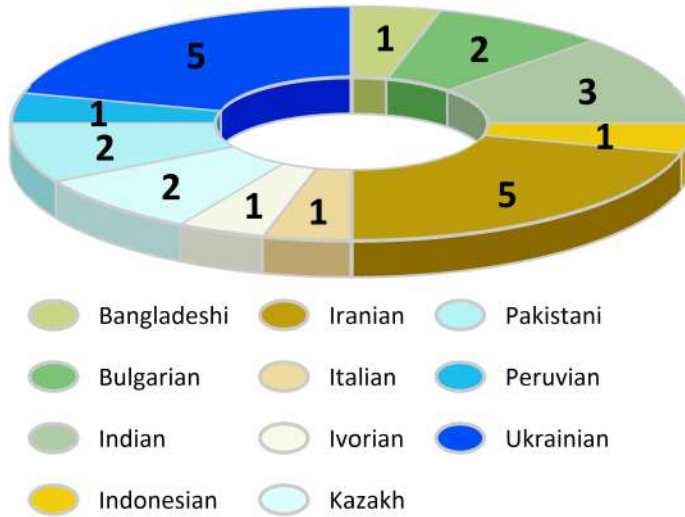
☆ PhD students' gender



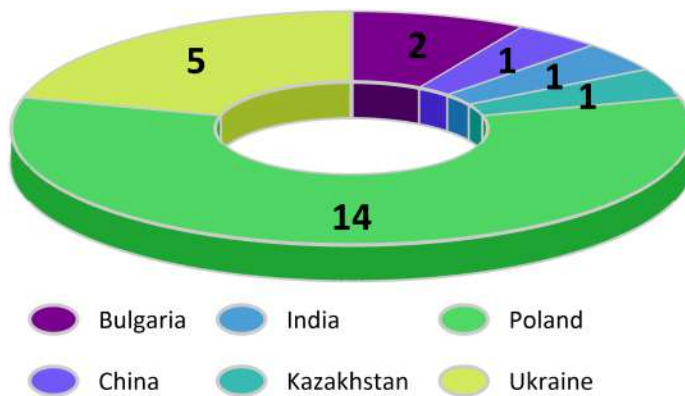
☆ PhD students' age



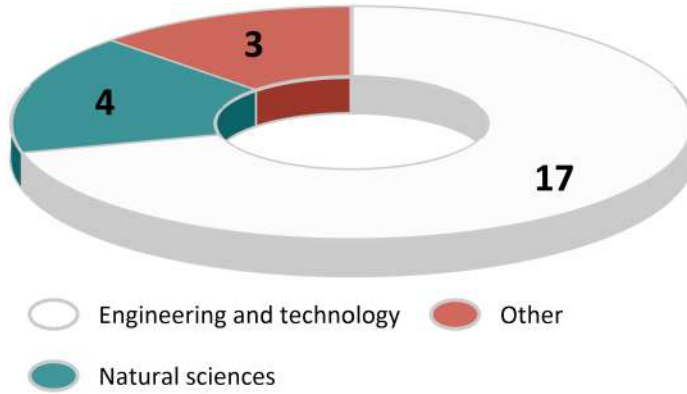
☆ PhD students' citizenship



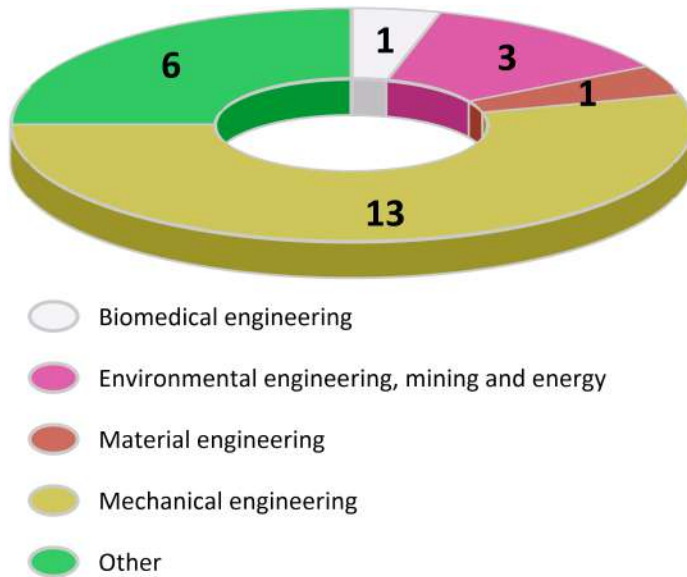
☆ PhD students' education country



## ☆ PhD students' field of PhD thesis

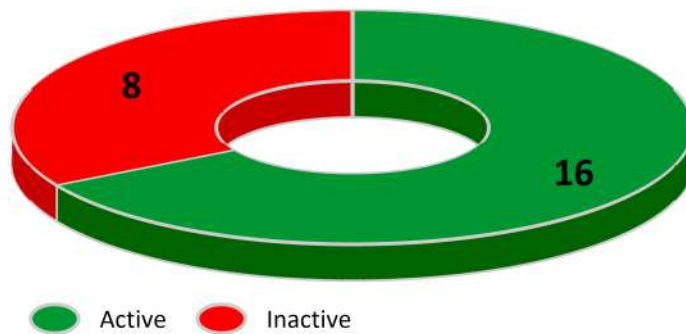


## ☆ PhD students' discipline of PhD thesis

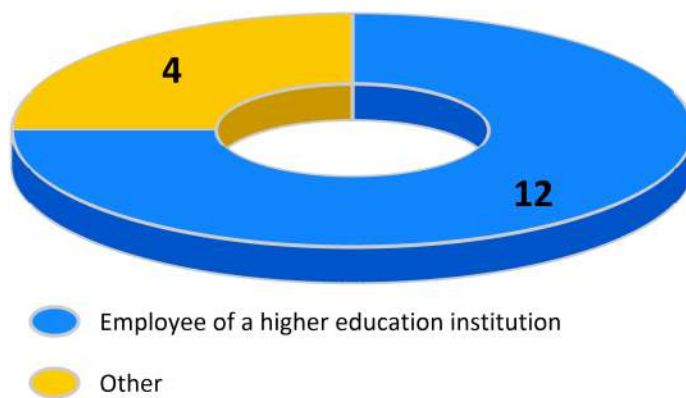




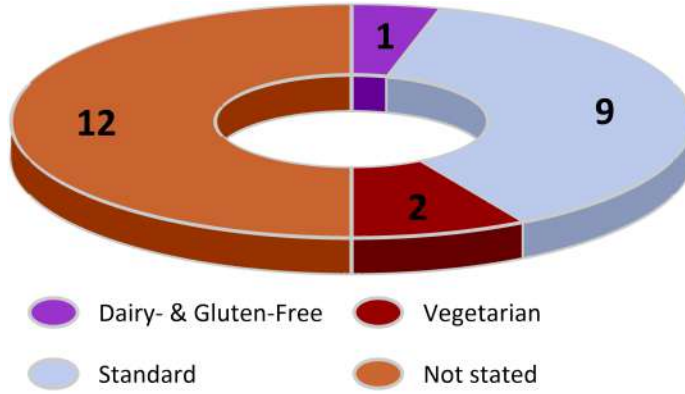
☆ PhD students' status on the labour market



☆ active PhD students' profession



## ☆ PhD students' diet



*Katarzyna Majewska*

## Chapter 9

# Measurements of fluid flow parameters & experimental data handling

Methods of experimental data presentation

In general, we can distinguish 3 methods of presentation of experimental data:

- Tabular methods
- Graphical methods
- Analytical methods

## 9.1 Tabular methods

The table (chart) contains measurement or calculation data recorded in columns and rows. It can be made in a classical form of a paper sheet (measurement sheet) in electronic form (spreadsheet). Usually the table contains raw data. If we use a spreadsheet, further columns may be defined for necessary calculations.

	alpha[X]	V[Y]	Lin3[Y]	Lin6[Y]
	[deg]	[m <sup>3</sup> /s]		
1	0	0	0	0
2	15	2,14	2,28	2,325
3	30	4,55	4,56	4,65
4	45	6,75	6,84	6,975
5	60	9,14	9,12	9,3
6	75	11,65	11,4	11,625
7	90	13,99	13,68	13,95

raw data
operations on columns

Fig. 9.1: An example of table chart

One of the numerical procedures performed on tabular data is interpolation. It allows determination of the value of a function when its analytical description is unknown and we only have the function values at characteristic points (nodes).

### Example

In case of pressure measurements hydrostatic manometers are often used and density of the manometric fluid must be known.

The density  $\rho$  [kg/mm<sup>3</sup>] depends on temperature  $t$  [°C] and usually

is expressed in tabular form as below:

t	0	5	10	15	20	25	30
$\rho$	806.25	802.04	797.82	793.58	789.32	785.04	780.73

The above data are shown in Fig. 9.2.

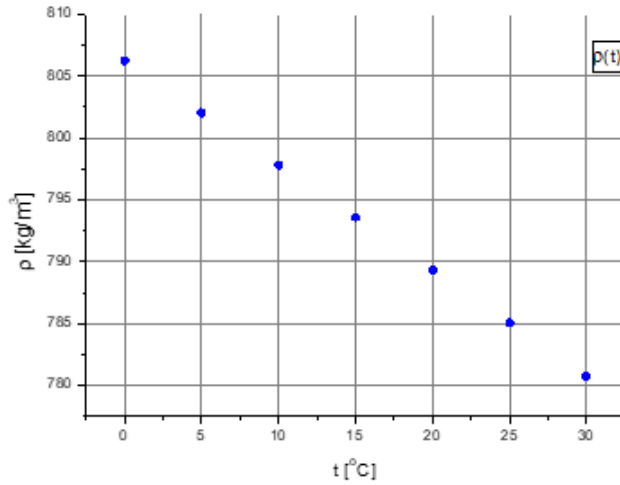


Fig. 9.2: Graphical representation of data.

The most common task is to determine unknown density  $\rho_x$  for given temperature  $t_x$ , different from those given in the table (for example  $t_x = 22^\circ\text{C}$ ).

In order to determine unknown density  $\rho(x)$ , the similarity condition of triangles ABC and AxD can be used (Fig. 9.3):

$$\frac{\rho_A - \rho_B}{t_B - t_A} = \frac{\rho_A - \rho_x}{t_x - t_A} \quad (9.1)$$

by rearranging the equation:

$$\rho_A - \rho_x = \frac{\rho_A - \rho_B}{t_B - t_A} (t_x - t_A) \quad (9.2)$$

We obtain:

$$\rho_x = \rho_A + \frac{t_x - t_A}{t_B - t_A}(\rho_B - \rho_A) \quad (9.3)$$

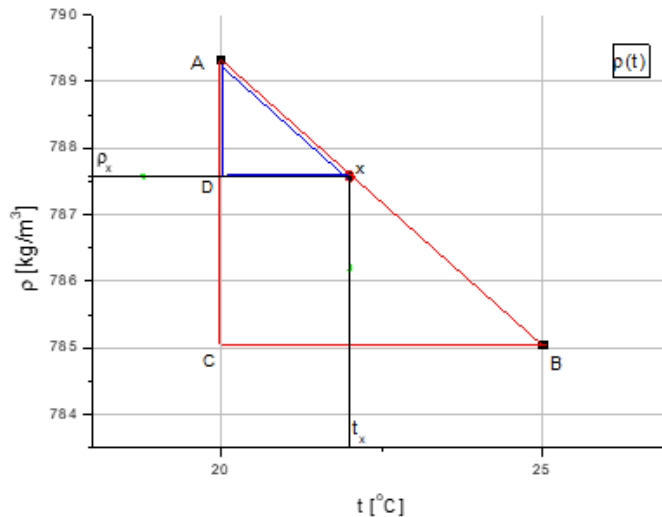


Fig. 9.3: Interpolation of density values for a given temperature.

To solve will require coordinates of two adjacent nodes A and B – Fig. 9.3. Using the data from table above we obtain:

$$A \rightarrow t_A = 20^\circ\text{C}, \rho_A = 789.32 \text{ kg/m}^3;$$

$$B \rightarrow t_B = 25^\circ\text{C}, \rho_B = 785.04 \text{ kg/m}^3;$$

And using the Eq. 9.3 we can calculate density  $\rho_x$ :

$$\begin{aligned} \rho_x &= \rho_A + \frac{t_x - t_A}{t_B - t_A}(\rho_B - \rho_A) = 789.32 + \frac{22 - 20}{25 - 20}(785.04 - 789.32) = \\ &789.32 - 0.4 \cdot 4.28 = 787.61 \text{ kg/m}^3 \end{aligned}$$

## 9.2 Graphical methods

Graphical methods are based on the representation of experimental data in a graph. The most common type of graphs is diagram in Cartesian coordinates  $xy$ .

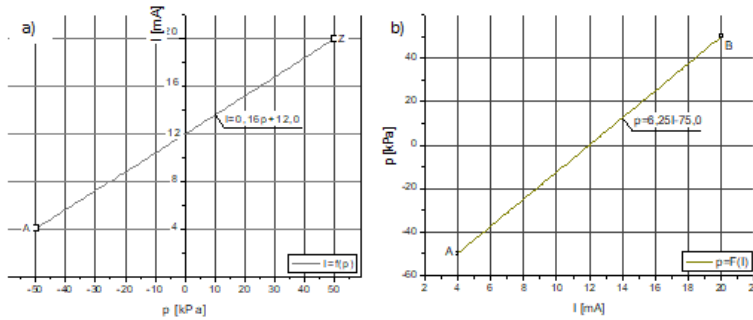


Fig. 9.4: Example charts in Cartesian coordinates.

The diagram in Cartesian coordinates is composed of two axes:

- x (horizontal one) – called abscissa axis
- y (vertical one) – called ordinate axis

Representing the function  $y=f(x)$  we place independent variable values on x axis (horizontal one) and dependent variable values (the function values) on y axis (vertical one).

#### Example

Let's take a pressure transducer having pressure signal  $p$  [kPa] at the inlet and current signal  $I$  [mA] at the outlet (Fig. 9.5).

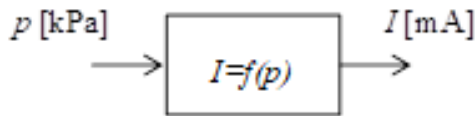


Fig. 9.5: Pressure-to-current conversion scheme.

We can express its static characteristics as the function  $I = f(p)$  (outlet vs. inlet signal – cf. Fig. 9.4a) or as the inverse function  $p = F(I)$  (inlet vs. outlet signal – cf. Fig. 9.4b). In case of linear function, inverse function is also linear (in case of non-linear function, the inverse function may not exist).

There are some important recommendations concerning scales and grid lines. Graduation of scales should satisfy the condition  $1 \cdot 10^n$ ,  $2 \cdot 10^n$ ,  $5 \cdot 10^n$ . Sometimes every second value in the axis description can be omitted (cf. Fig. 9.6).

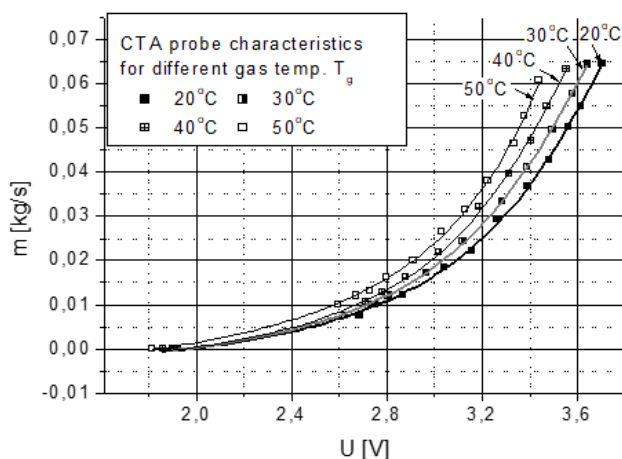


Fig. 9.6: Graphical presentation of data – graduation of scales.

#### Placing the data on the chart

It's very important to distinguish two data sets, that are typically placed on drawing:

1. Measurement data – these are points described by two coordinates  $P(x_i, y_i)$

To indicate measurement points we use geometrical symbols (some examples are given below).

+   ×   ⊕   ⊗   •   ·   ◇   ▽

The points must be large and clear and leave no doubt in the interpretation of the diagram. Most graph drawing software offers the choice of such symbols.

2. Approximation curves – these curves correspond to functions used in the approximation procedure – see analytical methods (Sec. 9.3). They don't have to pass exactly through measuring points!



## 9.3 Analytical methods

Analytical methods consist describing a set of measurement data with an equation. The equation represents an approximation curve.

The approximation procedure is always carried out in two steps:

1. selection of the type of function
2. determination of the coefficients of the chosen equation

Ad. 1.

This step is very important for the final result of approximation. Selected curve should represent correctly the layout of the measuring points and be consistent with the physics of described phenomenon.

In the procedure for selecting the type of function, the following should be taken into account:

- layout of measuring points
- existing theoretical models describing the phenomenon under investigation
- earlier research results on the phenomenon in question

If there is not any guidance, we can choose any type of equation, provided that it describes the layout of the measurement points correctly.

Some examples of functions often used for the analytical description of phenomena are given below:

$y = a_0 + a_1x$	linear function
$y = a_0 + a_1x + a_2x^2 + \dots + a_nx^n$	polynomial function
$y = a_0 + a_1x^{a_2}$	power function
$y = a_0 + a_1a_2^x$	power-law function
$y = a_0 + a_1e^{a_2x}$	exponential function
$y = a_1\ln(x - a_2)$	logarithmic function
$y = a_0 + \frac{a_1}{(a_2+x)}$	rational function
$y = A\sin(2\pi nt - \varphi)$	Wave form (sine curve)

Ad. 2.

In the second step we determine coefficients of selected equation using one of two methods below:

- A. method of selected points
- B. method of least sum of squares

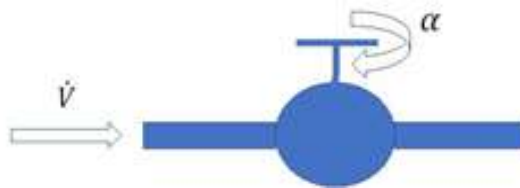
Ad. A.

In this method we select as many measurement points as there are coefficients in the equation to be determined and we guide the curve precisely through the selected points.

#### Example 1

In order to determine the characteristics of the control valve, the value of the water volume flow rate  $\dot{V}$  was determined for successive valve openings  $\alpha$ , obtaining the following results:

i		1	2	3	4	5	6	7
$\alpha$	[°]	0	15	30	45	60	75	90
$\dot{V}$	[l/min]	0	2.14	4.55	6.75	9.14	11.65	13.99



Assuming a linear form of the valve characteristics:  $\dot{V} = a\alpha$ , determine the value of the coefficient  $a$ .

---

The measuring points corresponding to the valve characteristics are shown in Fig. 9.7. The position of points justifies the assumption of a linear form of the characteristics.

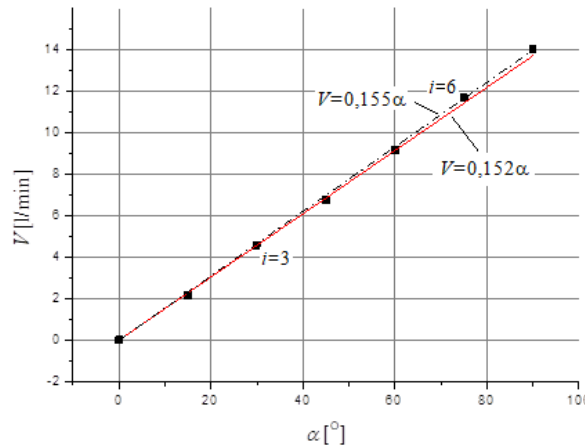


Fig. 9.7: Measurement points and approximation by means of linear function.

As the equation adopted has one coefficient (directional coefficient  $a$ ) only one point is necessary to determine the equation of characteristics. The method does not impose how the points should be selected – their choice is completely arbitrary. In fact we can select any point (except of the first point (0;0) which would not give any solution).

Taking the point  $i = 3$  whose coordinates are:  $\alpha = 30^\circ$ ,  $\dot{V} = 4.55$  l/min and passing the line through it we obtain:

$$\dot{V}_3 = a_3 \alpha_3$$

whence:

$$a_3 = \frac{\dot{V}_3}{\alpha_3} = \frac{4.55 \frac{l}{min}}{30^\circ} = 0.152 \frac{l}{^\circ min}$$

So the equation obtained will be:  $\dot{V} = 0.152 \alpha$  (cf. Fig. 9.7).

Taking another point – for example  $i = 6$  whose coordinates are:  $\alpha = 75^\circ$ ,  $\dot{V} = 11.65$  l/min and passing the line through this point we obtain:

$$\dot{V}_6 = a_6 \alpha_6$$

whence:

$$a_6 = \frac{\dot{V}_6}{\alpha_6} = \frac{11.65 \frac{l}{min}}{75^\circ} = 0.155 \frac{l}{^\circ min}$$

This time, the equation obtained will be:  $\dot{V} = 0.155\alpha$  (cf. Fig. 9.7) and it can be easily seen, that both equations are slightly different.

---

This simple example shows that the method of selected points is ambiguous. It does not give one and only solution, but a number (a field) of solutions.

It has also limited precision, as we use only a small fraction of experimental data – not all of them (some points do not participate in the procedure of determining of unknown coefficients).

Practically, the method of chosen points is applied only for linear equations and it can be use as a first approach having limited precision. However it is worth noting, that this method is very fast, what makes it attractive in certain applications.

In case of linear equation with 2 coefficients:

$$y = a_0 + a_1 x \tag{9.4}$$

2 points should be selected, for example:  $A(x_A, y_A)$  and  $B(x_B, y_B)$ .

The line will pass through these points, so the system of 2 equations should be satisfied:

$$\begin{cases} y_A = a_0 + a_1 x_A \\ y_B = a_0 + a_1 x_B \end{cases} \tag{9.5}$$

Coefficients  $a_0$  and  $a_1$  are the unknowns for this system.

Fig. 9.8 shows the sample result of linear approximation with 2 coefficients for given set of data points. It can be clearly seen, that

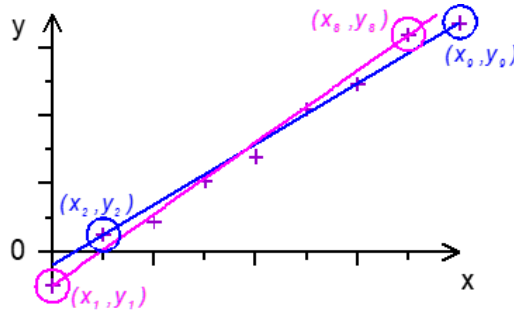


Fig. 9.8: Approximation by means of the chosen points method.

approximation lines for the pairs of point (1;8) and (2;9) are different (ambiguity).

Ad. B.

The method of least sum squares is based on the assumption that the approximating curve should pass as close as possible to all measurement points, but not necessarily through these points. This assumption makes the method accurate (it uses all measuring points) and unambiguous (it gives exactly one solution).

Let's take a look at the scheme presented in Fig. 9.9.

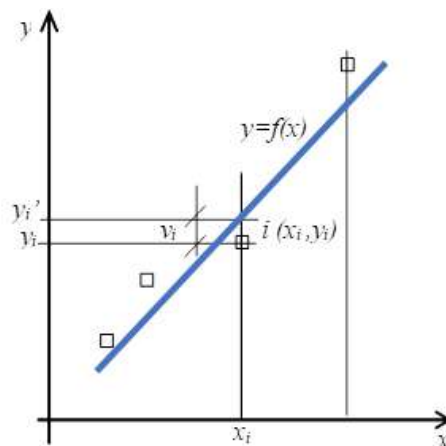


Fig. 9.9: The scheme illustrating the least squares method.

When the approximation is done we have always two elements:

- a set of data points (represented on the scheme by the point  $i(x_i, y_i)$ )
- a curve  $y = f(x)$ , whose general equation has been previously adopted according to the type of function selected

As the curve  $y = f(x)$  does not pass through the point  $i$  (it may happen in some circumstances, but this is not the assumption of the method), the difference between ordinates appear:

- $y_i$  – ordinate of the point  $i(x_i, y_i)$
- $y'_i = f(x_i)$  – ordinate of the point on the curve  $y = f(x)$  for the same abscissa  $x_i$  (in other words: value of the approximating function  $y = f(x)$  for given abscissa  $x_i$ )

This difference can be written as:

$$v_i = y'_i - y_i = f(x_i) - y_i \quad (9.6)$$

Mathematically, the least squares method condition can be written as:

$$\sum_{i=1}^n v_i^2 = \min \quad (9.7)$$

Let's try to see how it works:

### Example 2

Using the least squares method, find the expression for the coefficient  $a$  of the function  $y = ax$ .

---

For the given function we get:

$$y'_i = f(x_i) = ax_i \quad (9.8)$$

$$v_i = f(x_i) - y_i = ax_i - y_i \quad (9.9)$$

The condition of least squares method:

$$\sum_{i=1}^n v_i^2 = \sum_{i=1}^n (ax_i - y_i)^2 = \min \quad (9.10)$$

The condition above is not an equation that could be solved directly, but only a condition for a function to reach a minimum.

This function can be denoted as:

$$G(a) = \sum_{i=1}^n v_i^2 = \sum_{i=1}^n (ax_i - y_i)^2 \quad (9.11)$$

In fact  $(x_i, y_i)$  are constants (as the coordinates of measuring points) and the only variable is coefficient  $a$  (depending on its value, the function  $f(x)$  will pass closer or further to the measurement points).

The condition  $G(a) = \min$  is satisfied when  $\frac{dG(a)}{da} = 0$ , so we can write:

$$\frac{d}{da} \sum_{i=1}^n v_i^2 = \frac{d}{da} \sum_{i=1}^n (ax_i - y_i)^2 = 0 \quad (9.12)$$

and further:

$$\sum_{i=1}^n \frac{d}{da} \underbrace{(ax_i - y_i)}_{G(a)}^2 = 0 \quad (9.13)$$

$$2 \sum_{i=1}^n \underbrace{(ax_i - y_i)}_{G(a)} \frac{d}{da} \underbrace{(ax_i - y_i)}_{G(a)} = 0 \quad (9.14)$$

As  $\frac{d}{da}(ax_i - y_i) = \frac{d}{da}(ax_i) - \frac{d}{da}(y_i) = x_i - 0 = x_i$

We obtain finally:

$$\sum_{i=1}^n (ax_i - y_i)(x_i) = 0 \quad (9.15)$$

And further:

$$\sum_{i=1}^n (ax_i^2 - y_i x_i) = 0 \quad (9.16)$$

$$\sum_{i=1}^n ax_i^2 = \sum_{i=1}^n y_i x_i \quad (9.17)$$

And finally:

$$a = \frac{\sum_{i=1}^n y_i x_i}{\sum_{i=1}^n x_i^2} = \frac{A}{B} \quad (9.18)$$

The expression above defines one and only value of the coefficient  $a$ , that allows the curve  $y = ax$  to pass as close as possible to given set of measuring points.

Coming back to the Example 1 we can determine the coefficient  $a$  for our valve.

Posing:

$$\dot{V} = y, \alpha = x$$

We obtain:

$$a = \frac{\sum_{i=1}^n y_i x_i}{\sum_{i=1}^n x_i^2} = \frac{\sum_{i=1}^n \alpha_i \dot{V}_i}{\sum_{i=1}^n \alpha_i^2} = \frac{A}{B} \quad (9.19)$$

In order to calculate expressions in the numerator and denominator of a fraction above, we can create simple spreadsheet containing data points and appropriate coordinate combinations:

Substituting the values of the corresponding sums:

$$a = \frac{A}{B} = \frac{\sum_{i=1}^n \alpha_i \dot{V}_i}{\sum_{i=1}^n \alpha_i^2} = \frac{3153.9}{20475} = 0.154 \frac{l}{min^\circ}$$

We obtain finally:

$$\dot{V} = 0.154\alpha$$



$i$	$\alpha_i$	$\dot{V}_i$	$\alpha_i \dot{V}_i$	$\alpha_i^2$
1	0	0	0	0
2	15	2.14	32.1	225
3	30	4.55	136.5	900
4	45	6.75	303.75	2025
5	60	9.14	548.5	3600
6	75	11.65	873.75	5625
7	90	13.99	1259.1	8100
$\Sigma$			$A = \sum_{i=1}^n \alpha_i \dot{V}_i$ $= 3153.9$	$B = \sum_{i=1}^n \alpha_i^2$ $= 20475$

Let's see now, how we proceed if the approximating function contains more than one constant.

### Example 3

Using the least squares method, find the expression for the coefficient  $a$  of the function

$$y = a_0 + \frac{a_2}{x^2} \quad (9.20)$$

In this case we have 2 coefficients in our approximating equation:  $a_0$  and  $a_2$ .

For a given set of measuring data points  $(x_i, y_i)$  we will have:

$$y'_i = f(x_i) = a_0 + \frac{a_2}{x_i^2}$$

and:

$$v_i = f(x_i) - y_i = a_0 + \frac{a_2}{x_i^2} - y_i$$

The condition of least squares method can be written as:

$$\sum_{i=1}^n v_i^2 = \sum_{i=1}^n \left( a_0 + \frac{a_2}{x_i^2} - y_i \right)^2 = \min$$

As the approximation curve contains 2 coefficients: ( $a_0$  and  $a_2$ ), the sum  $\sum_{i=1}^n v_i^2$  becomes the function of two variables:

$$g(a_0, a_2) = \sum_{i=1}^n v_i^2 = \sum_{i=1}^n \left( a_0 + \frac{a_2}{x_i^2} - y_i \right)^2$$

In this case we will obtain the system of two equations containing partial derivatives of the function  $g(a_0, a_2)$ :

$$\begin{cases} \frac{\partial}{\partial a_0} \sum_{i=1}^n v_i^2 = 0 \\ \frac{\partial}{\partial a_2} \sum_{i=1}^n v_i^2 = 0 \end{cases}$$

It's worth noting here, that the method allows to create as many equations as there are unknown coefficients in the approximating equation. It's also important to understand that differentiation variables are unknown coefficients ( $a_0, a_2$ ).

Posing:

$$v_i = a_0 + \frac{a_2}{x_i^2} - y_i$$

We obtain:

$$\begin{cases} \frac{\partial}{\partial a_0} \sum_{i=1}^n \left( a_0 + \frac{a_2}{x_i^2} - y_i \right)^2 = 0 \\ \frac{\partial}{\partial a_2} \sum_{i=1}^n \left( a_0 + \frac{a_2}{x_i^2} - y_i \right)^2 = 0 \end{cases}$$

And then:

$$\begin{cases} \sum_{i=1}^n \frac{\partial}{\partial a_0} \underbrace{\left( a_0 + \frac{a_2}{x_i^2} - y_i \right)^2}_{G(a)} = 0 \\ \sum_{i=1}^n \frac{\partial}{\partial a_2} \underbrace{\left( a_0 + \frac{a_2}{x_i^2} - y_i \right)^2}_{G(a)} = 0 \end{cases}$$

Differentiating the equations:

$$\begin{cases} \sum_{i=1}^n 2 \underbrace{\left(a_0 + \frac{a_2}{x_i^2} - y_i\right)}_{G(a_0, a_2)} \frac{\partial}{\partial a_0} \underbrace{\left(a_0 + \frac{a_2}{x_i^2} - y_i\right)}_{G(a_0, a_2)} = 0 \\ \sum_{i=1}^n 2 \underbrace{\left(a_0 + \frac{a_2}{x_i^2} - y_i\right)}_{G(a_0, a_2)} \frac{\partial}{\partial a_2} \underbrace{\left(a_0 + \frac{a_2}{x_i^2} - y_i\right)}_{G(a_0, a_2)} = 0 \end{cases}$$

We obtain:

$$\begin{cases} 2 \sum_{i=1}^n \left(a_0 + \frac{a_2}{x_i^2} - y_i\right) (1) = 0 \\ 2 \sum_{i=1}^n \left(a_0 + \frac{a_2}{x_i^2} - y_i\right) \left(\frac{1}{x_i^2}\right) = 0 \end{cases}$$

And finally:

$$\begin{cases} na_0 + \sum_{i=1}^n \left(\frac{a_2}{x_i^2}\right) = \sum_{i=1}^n (y_i) \\ \sum_{i=1}^n \left(\frac{a_2}{x_i^2}\right) + \sum_{i=1}^n \left(\frac{a_2}{x_i^4}\right) = \sum_{i=1}^n \frac{(y_i)}{x_i^2} \end{cases}$$

Placing coefficients  $a_0$ ,  $a_2$  in front of appropriate sums:

$$\begin{cases} na_0 + a_2 \sum_{i=1}^n \left(\frac{1}{x_i^2}\right) = \sum_{i=1}^n (y_i) \\ a_0 \sum_{i=1}^n \left(\frac{1}{x_i^2}\right) + a_2 \sum_{i=1}^n \left(\frac{1}{x_i^4}\right) = \sum_{i=1}^n \frac{(y_i)}{x_i^2} \end{cases}$$

And posing:  $C_1 = \sum_{i=1}^n \left(\frac{1}{x_i^2}\right)$ ,  $C_2 = \sum_{i=1}^n (y_i)$ ,  $C_3 = \sum_{i=1}^n \left(\frac{1}{x_i^4}\right)$  and  $C_4 = \sum_{i=1}^n \left(\frac{y_i}{x_i^2}\right)$ , we obtain the set of equations:

$$\begin{cases} na_0 + C_1 a_2 = C_2 \\ C_1 a_0 + C_3 a_2 = C_4 \end{cases}$$

Where the unknowns of the system are coefficients  $a_0$ ,  $a_2$ .

The system of equations can be solved by the determinant method.

Subsequent determinants will be:

$$W = \begin{vmatrix} n & C_1 \\ C_1 & C_3 \end{vmatrix}, W_{a_0} = \begin{vmatrix} C_2 & C_1 \\ C_4 & C_3 \end{vmatrix} \text{ and } W_{a_2} = \begin{vmatrix} n & C_2 \\ C_1 & C_4 \end{vmatrix}$$

And finally coefficients  $a_0, a_2$  can be calculated as:

$$a_0 = \frac{W_{a_0}}{W} \text{ and } \frac{W_{a_2}}{W}$$

Some aspects of approximation using non-linear functions.

In case of non-linear approximation, some important features of approximating curve must be taken into account.

#### Example 4

During the calibration of 3 hot wire probes, experimental data as given below were obtained. Choose the appropriate approximating function taking into account different approximation criteria.

	U1[X]	mA1[Y]	U2[Y]	mA2[Y]	U3[Y]	mA3[Y]
	[M]	[kg/s]	[M]	[kg/s]	[M]	[kg/s]
1	3,677	0	3,434	0	3,81832	0
2	5,005	0,00672	4,671	0,00671	5,78266	0,00519
3	5,155	0,00951	4,903	0,00827	5,92943	0,00734
4	5,432	0,01263	5,061	0,01011	6,042	0,009
5	5,594	0,01562	5,324	0,01391	6,18462	0,0104
6	5,816	0,02066	5,405	0,0176	6,35165	0,01165
7	6,045	0,02555	5,693	0,02385	6,46691	0,0138
8	6,152	0,0299	5,851	0,02908	6,61636	0,01734
9	6,323	0,03582	5,986	0,03341	6,81514	0,02034
10	6,44	0,0402	6,095	0,03804	6,92259	0,02326
11	6,556	0,04541	6,162	0,04286	7,14652	0,02932
12	6,581	0,04858	6,311	0,04571	7,35507	0,0356
13	6,691	0,05274	6,399	0,05208	7,50574	0,04165
14	6,768	0,05658	6,544	0,05876	7,6735	0,0479
15	6,855	0,06244	6,611	0,06318	7,84518	0,05621
16	6,951	0,06614	6,69	0,06602	8,07912	0,06796
17					8,25861	0,07886
18						

Hot wire (and hot film) probes are used for gas velocity measurements.

Very thin wire (in typical applications tungsten wire with a diameter of a few millimetres) is used as a sensing element. Electric



current passing through the wire makes it hot and on the other hand flowing gas receives the heat from the wire. When the flow velocity increases, the intensity of heat exchange increases as well, what influences the parameters of electrical circuit.

Calibration characteristics of hot wires are relationships between the voltage  $U$ [V] (output signal from electrical circuit of the probe) and either mass flow rate  $\dot{m}$ [kg/s] or flow velocity  $\nu$ [m/s] or sometimes specific mass flow rate  $\varphi_m = \frac{\dot{m}}{A} = \rho\nu$ [kg/s·m<sup>2</sup>].

In our example, the inlet signal is mass flow rate  $\dot{m}$ [kg/s]

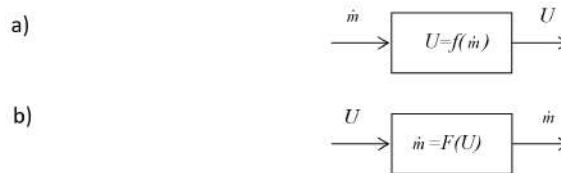


Fig. 9.10: The diagram explaining the difference between static and inverse static characteristics of hot wire.

If we look at the scheme (Fig. 9.10a)) we can observe that hot wire converts mass flow rate  $\dot{m}$ [kg/s] into voltage signal  $U$ [V].

Measurement properties of hot wire probe can be represented as its static characteristics  $U = f(\dot{m})$  or inversed static characteristics  $\dot{m}=F(U)$ .

Raw data for 3 tested hot wires are presented in Fig. 9.11.

Static characteristics of hot wire probes are usually approximated by means of classical King's equation:

$$U^2 = \dot{A} + \dot{B}\dot{m}^n$$

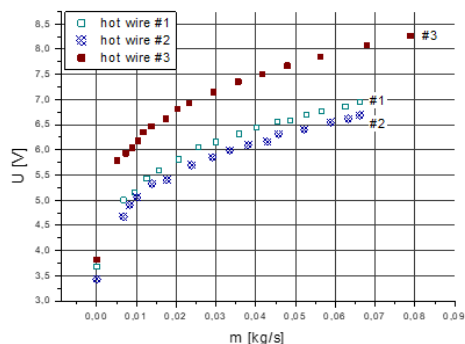


Fig. 9.11: Raw data of hot wire probes characteristics.

The result of such approximation for the probe #1 is shown in Fig. 9.12.

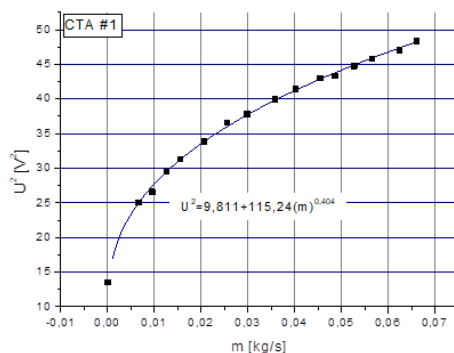


Fig. 9.12: Approximation of hot wire probe characteristics by means of King's equation.

However the King's equation give good results of approximation in the most cases, it's practical application is problematic. During measurements we need to know the inversed static characteristics  $\dot{m}=F(U)$ , as we need co calculate mass flow rate from recorded voltage signal. The form of King's equation does not give such possibility, as the inversed function for the King's equation does not exist.

Therefore, in practice, the procedure of approximation is done on inversed characteristics (cf. Fig. 9.13).

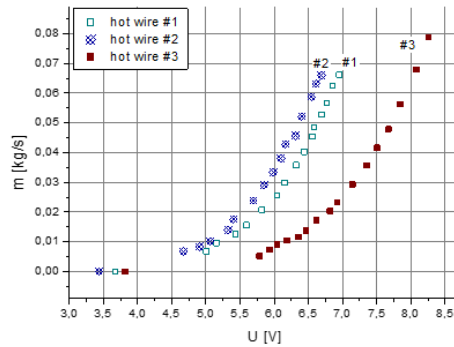


Fig. 9.13: Raw data of hot wire inversed characteristics.

Before we start the procedure of approximation it's good to define some criteria of its quality. To assess the quality of the approximation, some parameters are used.

If we mark:

$x_i, y_i$  – coordinates of measuring point  $i$ ;

$\hat{y}_i = f(x_i)$  – the ordinate resulting from the assumed equation of the approximating function for given abscissa  $x_i$ ;

$n$  – the number of measuring points;

Following parameters can be defined:

$SSE = \sum_{i=1}^n (y_i - \hat{y}_i)^2$  – Sum of Squared Errors (Residual Sum of

Squares);  $SST = \sum_{i=1}^n (y_i - \bar{y})^2$  – Total Sum of Squares;

with:  $\bar{y} = \frac{1}{n} \sum_{i=1}^n y_i$

The most commonly used parameter describing the quality of approximation is the coefficient of determination  $R^2$  defined as:

$$R^2 = 1 - \frac{SSE}{SST}$$

The perfect approximation would take place if  $SSE=0$  (approximating curve passes exactly through all measuring points) and  $R^2=1$ . The approximation is found to be very good if  $R^2>0.95$ .

The coefficient of convergence is also sometimes used (rarely):

$$\varphi^2 = 1 - R^2$$

Dividing the SSE by the number of measuring points we obtain the Mean Squared Error:

$$MSE = \frac{SSE}{n}$$

Sometimes the Root Mean Squared Error:

$$RMSE = \sqrt{MSE}$$

Is also used.

Let's come back to the approximation of our hot wire characteristics and let's use the 3<sup>rd</sup> degree polynomial as the approximation function.

The approximation equation will be:

$$\dot{m} = A_0 + A_1U + A_2U^2 + A_3U^3$$

Applying the method of least squares, the coefficients  $A_0, \dots, A_3$  can be determined:

	$A_0$	$A_1$	$A_2$	$A_3$
	$[\frac{kg}{s}]$	$[\frac{kg}{sV}]$	$[\frac{kg}{sV^2}]$	$[\frac{kg}{sV^3}]$
CTA #1	-0.1961	0.1342	-0.0311	0.0025
CTA #2	-0.0920	0.0737	-0.0202	0.0019
CTA #3	-0.1653	0.1041	-0.0218	0.00155

And the result of approximation is shown in Fig. 9.14.



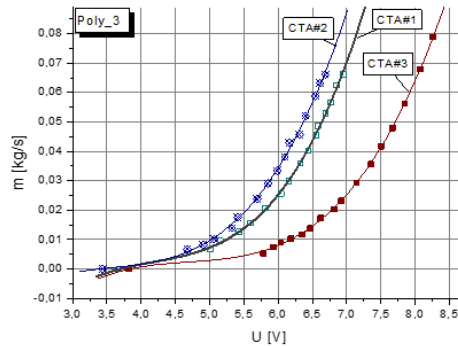


Fig. 9.14: The results of approximation (the 3<sup>rd</sup> order polynomial).

Approx. Polynomial 3 <sup>rd</sup> order			
	CTA#1	CTA#2	CTA#3
SSE	$3.71 \cdot 10^{-4}$	$2.50 \cdot 10^{-5}$	$4.89 \cdot 10^{-5}$
MSE	$2.32 \cdot 10^{-5}$	$1.57 \cdot 10^{-6}$	$2.88 \cdot 10^{-6}$
RMSE	$4.82 \cdot 10^{-3}$	$1.25 \cdot 10^{-3}$	$1.70 \cdot 10^{-3}$
SST	0.00663	0.00691	0.00869
$R^2$	0.9440	0.9964	0.9944
$\phi^2$	$5.5 \cdot 10^{-2}$	$3.6 \cdot 10^{-3}$	$5.6 \cdot 10^{-3}$

The initial evaluation of quality of approximation is good. Approximating curves reproduce well the arrangement of the points. The  $R^2$  value is very close to 1 for CTA#1 and CTA#2 and close to 0.95 for CTA#3.

In case of the approximation of static characteristics of measurement devices, it is also important to analyse the shape of the approximating curve taking into account:

- ambiguity of the approximating function
- the presence of inflection points

The ambiguity appears, when one ordinate (function value) corre-

sponds to two (or more) different abscissas (like shown in Fig. 9.15). In case of measurement device (transducer) it corresponds to a situation in which the same output signal corresponds to more than one input signal value. In other words, the static characteristics must be always monotonic (increasing or decreasing) cf. Fig. 9.16. The easiest way to verify this, is to examine the first derivative of approximating curve. If the first derivative passes by zero (what corresponds to the extremum of a function – cf. Fig. 9.16b), it means that the characteristics is ambiguous.

The result of approximation is shown in Fig. 9.15.

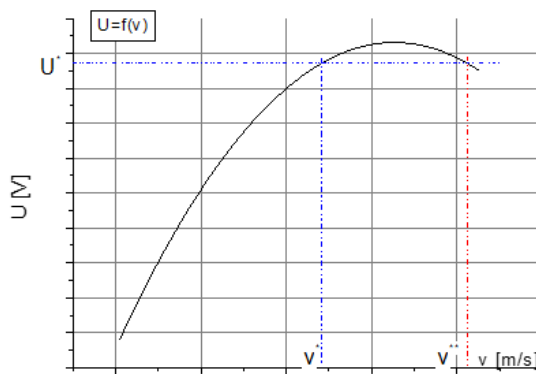


Fig. 9.15: The example of ambiguous approximating curve.

In fact the field of operation for any transducer should be always on the left or on the right side of extremum point (cf. Fig. 9.16a)). Analysing first derivatives of characteristics for the hot wire probe, approximated by means of the 3<sup>rd</sup> order polynomial (Fig. 9.17), we can state, that none of curves passes through zero, however in some points they are close to it (especially curves CTA#2 and CTA#3). Another feature worth analysing is the presence of deflection points. Static characteristics of hot wires are in general free from deflection points, as there is no physical justification of their presence. Deflection point appears when the second derivative of the function is equal to zero. Examining the second derivative of our approximating curve (Fig. 9.18) we can state, that all curves pass through

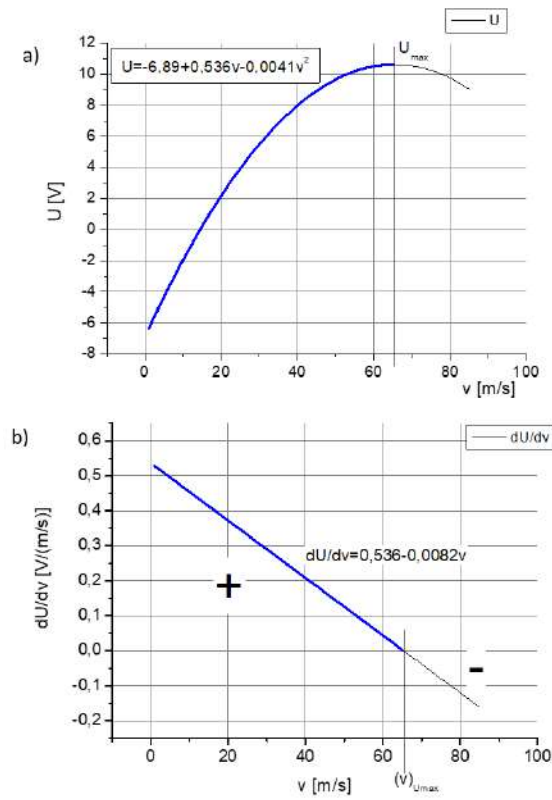


Fig. 9.16: The relationship between ambiguity and the first derivative  $dU/dv$ .

zero, so all of approximating curves will have the deflection point in the range of 3.5 V-5 V.

It makes that the approximation by the 3<sup>rd</sup> order polynomial cannot be considered perfect.

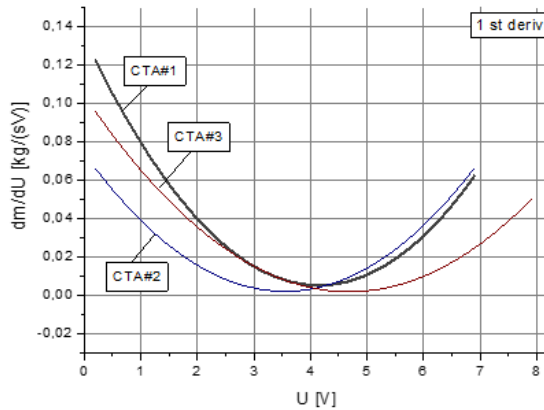


Fig. 9.17: Curves of the first derivative  $dU/dv$  for tested hot wires.

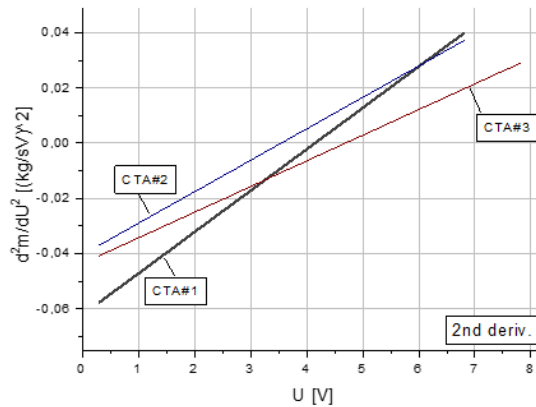


Fig. 9.18: Checking the presence of deflection points – the analysis of the second derivative  $d^2U/dv^2$ .

Manufacturers of hot wire probes [TSI Inc.: *Advantage to the look-up table approach of voltage-velocity conversion in thermal anemometry. Technical note 2007*; <http://www.tsi.com>] recommend the 4th order polynomial as the approximation curve. Let's see the result.

The approximation equation will be:

$$\dot{m} = A_0 + A_1U + A_2U^2 + A_3U^3 + A_4U^4$$

For given set of points, the coefficients will be:

	$A_0$	$A_1$	$A_2$	$A_3$	$A_4$
	$[\frac{kg}{s}]$	$[\frac{kg}{sV}]$	$[\frac{kg}{sV^2}]$	$[\frac{kg}{sV^3}]$	$[\frac{kg}{sV^4}]$
CTA#1	-0.3378	0.2435	-0.0621	0.00631	-0.000174
CTA#2	-0.7686	0.6247	-0.1864	0.02329	-0.00103
CTA#3	0.0696	-0.0578	0.0186	-0.00283	0.000174

The results of approximation are shown in Fig. 9.19.

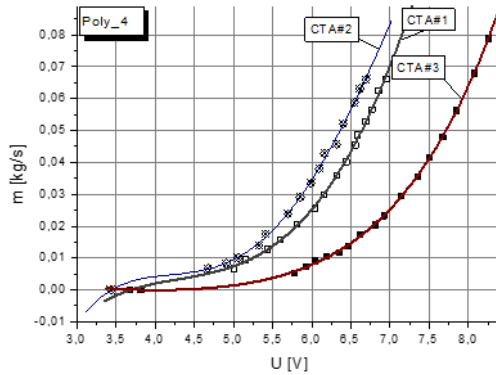


Fig. 9.19: The results of approximation (the 4<sup>th</sup> order polynomial).

Approx. Polynomial 4 <sup>th</sup> order			
	CTA#1	CTA#2	CTA#3
SSE	$1.16 \cdot 10^{-5}$	$5.04 \cdot 10^{-4}$	$5.13 \cdot 10^{-6}$
MSE	$0.72 \cdot 10^{-6}$	$3.15 \cdot 10^{-5}$	$0.30 \cdot 10^{-6}$
RMSE	$0.85 \cdot 10^{-3}$	$5.61 \cdot 10^{-3}$	$0.55 \cdot 10^{-3}$
SST	0.00663	0.00691	0.00869
$R^2$	0.9982	0.9270	0.9994
$\phi^2$	$1.7 \cdot 10^{-3}$	$7.3 \cdot 10^{-3}$	$5.9 \cdot 10^{-3}$

The  $R^2$  values are still very close to 1 for CTA#1 and CTA#3, however slightly worse for CTA#2. But the real problem concerns the shape of approximating curves in initial region  $U \in < 0.5 V >$ .

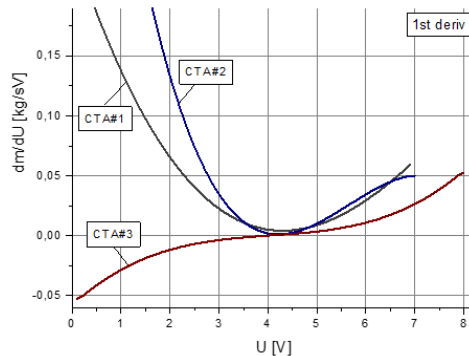


Fig. 9.20: Curves of the 1<sup>st</sup> derivative  $d\dot{m}/dU$ .

The diagram with the first derivative shows, that the CTA#3 curve passes through zero, so this curve will be ambiguous. The curve for CTA#2 passes very close to zero.

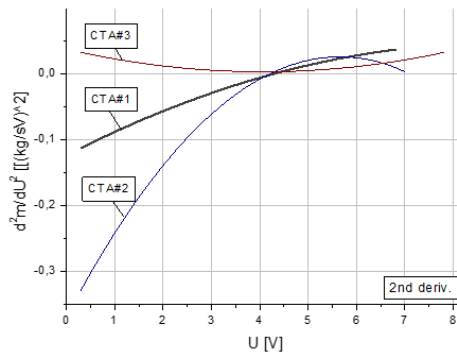


Fig. 9.21: Curves of the 2<sup>nd</sup> derivative  $d^2\dot{m}/dU^2$ .

The diagram with the second derivative shows, that CTA#1 and CTA#2 curves pass through zero, so these curves will have inflection points (the CTA#2 curve will have even 2 of them). Con-

sequently, the results of approximation by means of the 4<sup>th</sup> order polynomial are even worse than in case of the 3<sup>th</sup> order polynomial (and the number of coefficients to be determined is bigger). To avoid the problems with ambiguity and the presence of inflection points it seems reasonable to apply the exponential growth function:

$$\dot{m} = \dot{A}_0 + A_1 e^{\frac{U}{A_2}}$$

The first and the second derivatives of the exponential function are also exponential functions, which never pass through zero. The flaw for such type of function is that coefficients cannot be determined analytically (the set of equations obtained from the least squares method is unresolvable) and a solution must be done iteratively.

The results of the approximation by means of exponential growth function are summarized below:

	$\dot{A}_0$	$A_1$	$A_2$
	$[\frac{kg}{s}]$	$[\frac{kg}{sV}]$	$[V]$
CTA#1	-0.00403	0.00010	1.0590
CTA#2	-0.00534	0.00017	1.1027
CTA#3	-0.00392	0.00008	1.1842

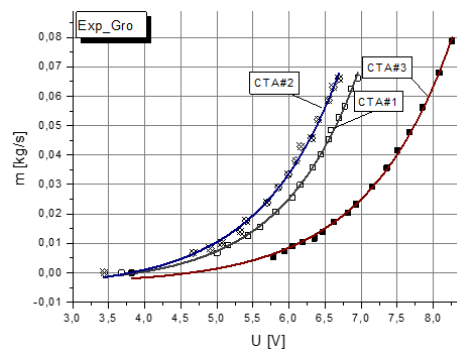


Fig. 9.22: The results of approximation (the exponential function).

Approx. Exponential Grow			
	CTA#1	CTA#2	CTA#3
SSE	$1.6842 \cdot 10^{-5}$	$2.32 \cdot 10^{-5}$	$2.07 \cdot 10^{-5}$
MSE	$1.05 \cdot 10^{-6}$	$1.45 \cdot 10^{-6}$	$1.22 \cdot 10^{-6}$
RMSE	$1.02 \cdot 10^{-3}$	$1.20 \cdot 10^{-3}$	$1.10 \cdot 10^{-3}$
SST	0.00663	0.00691	0.00869
$R^2$	0.9974	0.9966	0.9976
$\phi^2$	$2.5 \cdot 10^{-3}$	$3.4 \cdot 10^{-3}$	$2.4 \cdot 10^{-3}$

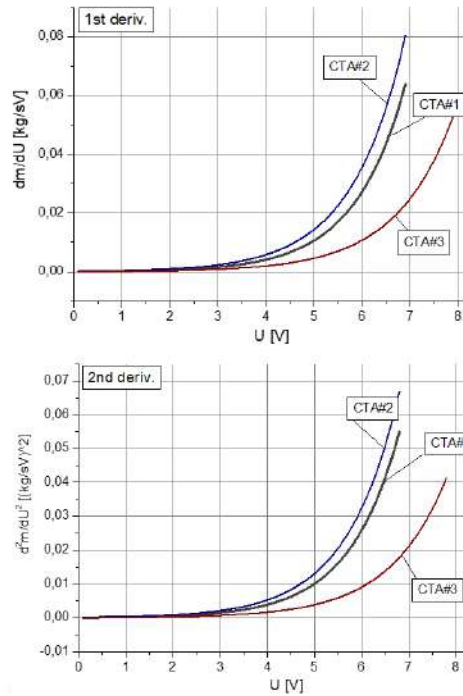


Fig. 9.23: Functions of the 1<sup>st</sup> and the 2<sup>nd</sup> derivative for the exponential growth function.



It's worth noting, that for all three curves, the  $R^2$  is very close to 1. The problem however is, that in the initial region of characteristics (for the lowest voltages) – cf. Fig. 9.22 – the mass flow rates are negative, what is contradictory to the physics of phenomena.

This inconvenience can be removed using modified exponential function in the form called Gompertz function:

$$\dot{m} = A_1 e^{(-A_2(U-A_3))}$$

We can consider it as a double exponential growth.

The results of approximation are given below:

	$\dot{A}_1$	$A_2$	$A_3$
	$[\frac{kg}{s}]$	$[\frac{kg}{sV}]$	$[V]$
CTA#1	1.7905	0.2724	11.7552
CTA#2	0.7796	0.3458	7.9561
CTA#3	1.9993	0.2387	13.1815

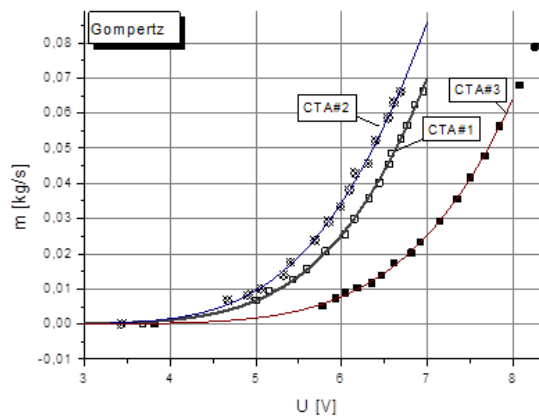


Fig. 9.24: The results of approximation by means of the Gompertz function.

Parameters showing the quality of approximation are summarized below:

Approx. Gompertz function			
	CTA#1	CTA#2	CTA#3
SSE	$7.93 \cdot 10^{-6}$	$1.24 \cdot 10^{-5}$	$2.87 \cdot 10^{-6}$
MSE	$0.50 \cdot 10^{-6}$	$0.78 \cdot 10^{-6}$	$0.17 \cdot 10^{-6}$
RMSE	$0.70 \cdot 10^{-3}$	$0.88 \cdot 10^{-3}$	$0.41 \cdot 10^{-3}$
SST	0.00663	0.00691	0.00869
$R^2$	0.9988	0.9978	0.9997
$\phi^2$	$1.2 \cdot 10^{-3}$	$2.2 \cdot 10^{-3}$	$0.3 \cdot 10^{-3}$

It can be easily seen that Gompertz function give very good quality of approximation (the  $R^2$  differs from 1 only by 0.2% in the worst case – CTA#2) and mass flow rate  $\dot{m}$  values are always positive (cf. Fig. 9.24).

## Chapter 10

# Measurements of fluid flow parameters & experimental data handling

Measurements of fluid flow parameters

## 10.1 Pressure measurements

Pressure is one of the parameters describing the state of a fluid (liquid or gas). On a macroscopic scale, pressure is defined as a force acting per unit area, with the force acting perpendicular to the surface:

$$p = \frac{F_{\perp}}{S}$$

where:

$p$  – pressure,

$F_{\perp}$  – force acting perpendicular to the surface,

$S$  – surface area

Pressure is a scalar quantity and, in the general case, can be a function of spatial coordinates  $x$ ,  $y$ ,  $z$  and time  $t$ :

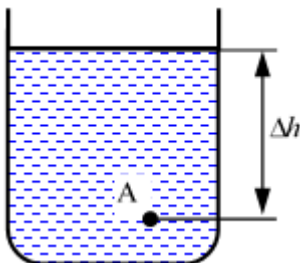
$$p = p(x, y, z, t)$$

The unit of pressure in the SI system is Pascal [Pa]:

$$Pa = \frac{N}{m^2} = \frac{kg\ m}{s^2 m^2} = \frac{kg}{m\ s^2}$$

### *Hydrostatic, static, dynamic and total pressure*

If a fluid of given density  $\rho$  is at rest, there is hydrostatic pressure at level  $h$ , caused by the weight of the fluid above this level (Fig. 10.1).



$$p_A = \rho g \Delta h$$

$\rho$  – fluid density

$g$  – gravity acceleration

$\Delta h$  – depth of the point

A

Fig. 10.1: Pressure interpretation.

If the fluid is in movement with velocity  $v$  we can distinguish 3 pressures (Fig. 10.2):

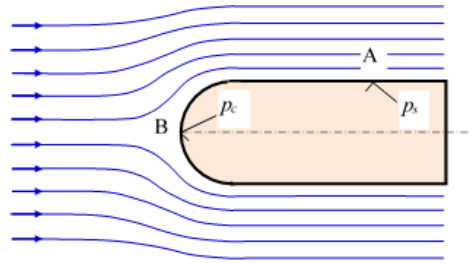


Fig. 10.2: Illustration of the difference between the total and static pressure.

- static pressure  $p$  – the pressure exerted on an object moving with a fluid (point A)
- dynamic pressure  $p_d$ , resulting from the movement of fluid and connected with its kinetic energy:  $p_d = \frac{\rho v^2}{2}$
- total pressure  $p_e$ , being the sum of static and dynamic pressure:  $p_c = p_s + p_d$

Static pressure occurs at surfaces to which the current lines of the moving fluid are parallel, while total pressure occurs at surfaces to which the current lines are perpendicular (Fig. 10.2).

#### *Atmospheric pressure*

Pressure equal to zero exists in a vacuum. The atmosphere surrounding the Earth causes hydrostatic pressure, called atmospheric or barometric pressure. This pressure is caused by the weight of the air and varies with altitude: the higher you go, the smaller the layer of pressing air is and the pressure is lower. In addition, atmospheric pressure strongly depends on local parameters as temperature, humidity or, wind velocity. At sea level, the average pressure is 101325 Pa (this is so called physical atmosphere: 1 atm=101325 Pa).

*Absolute pressure, overpressure, underpressure*

Pressure measurements are usually made using the differential method, comparing the measured pressure value with the reference pressure value. In general atmospheric pressure is used as the reference. We call this differential pressure gauge pressure which can be positive (overpressure) or negative (underpressure) – Fig. 10.3.

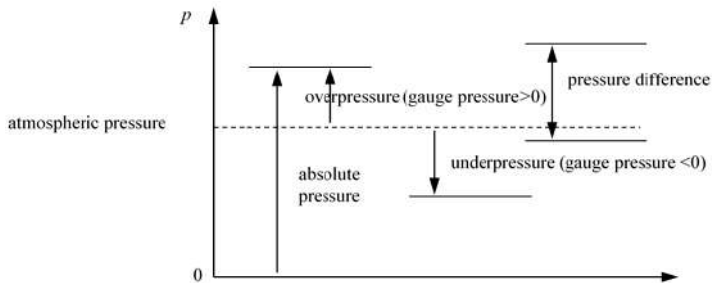


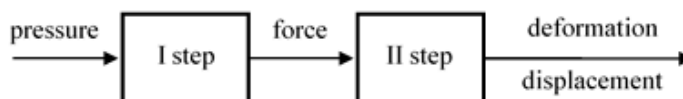
Fig. 10.3: Illustration of the difference between the total and static pressure.

*Pressure measurements*

Basically we can distinguish:

- mechanical pressure transducers
- electrical pressure transducers

## ♣ Mechanical pressure transducers (mechanical manometers)



In these transducers, the inlet pressure signal is converted into a force (I step) and then into a deformation of an elastic element (II step).

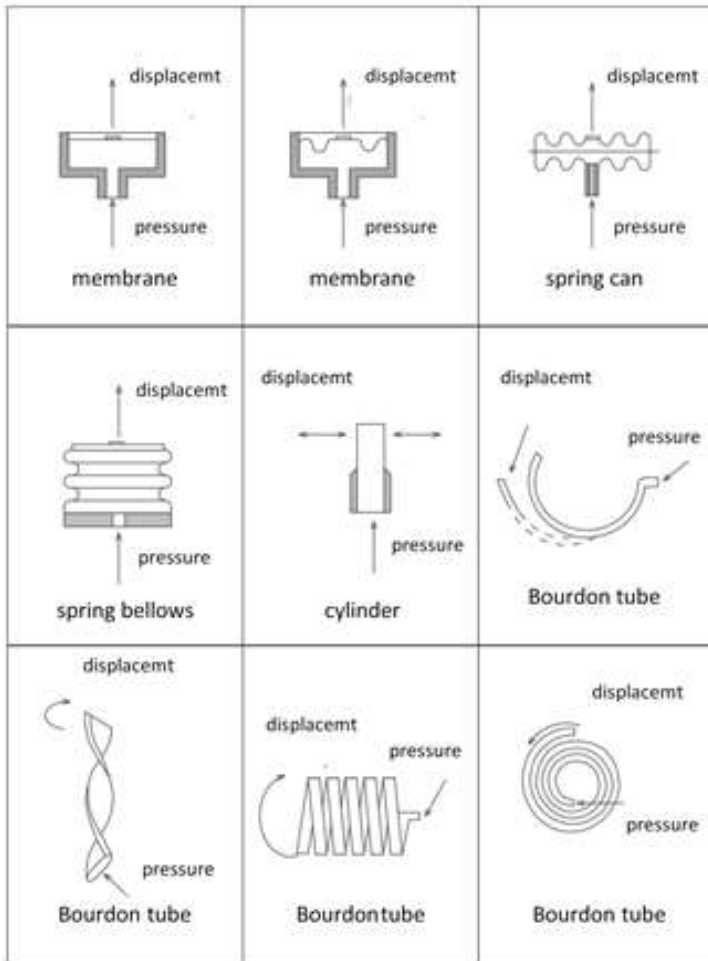


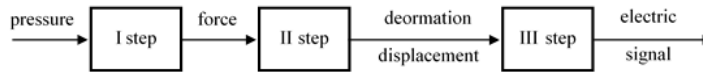
Fig. 10.4: Different types of mechanical manometers.

Mechanical manometers display pressure value on the scale and it can be just read.

In many cases this is not convenient, especially if the measurement is to be carried out on an automatic cycle. In such case we try to obtain electric signal at the transducer output.

### ♣ Electrical pressure transducers

These transducers have electrical signal (voltage or current) at the transducer output.



Within electric pressure transducer we can distinguish in general:

- strain gauge pressure transducers
- capacitive pressure transducers
- strain gauge pressure transducers

A strain gauge is an element that changes its electrical resistance as a result of deformation: elongation or compression. If a strain gauge is glued to a flat membrane, its bending under the influence of the measured pressure changes the resistance of the strain gauge. There are tensile stresses in some parts (and directions) of the deformed flat membrane, and compressive stresses in others. For this reason, strain gauges applied to membranes usually have a so-called rosette shape, as shown in Fig. 10.5.

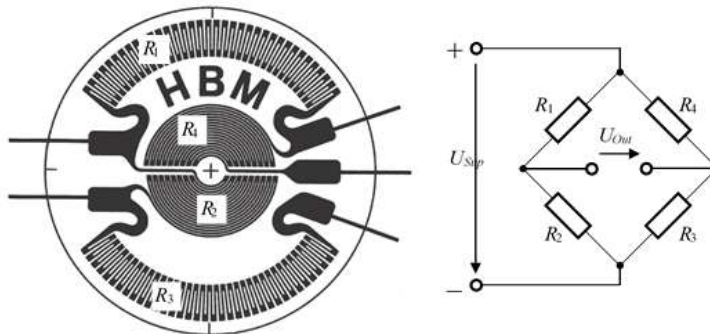


Fig. 10.5: A rosette strain gauge designed to be stuck onto the diaphragm of a pressure transducer and an electric diagram of a Wheatstone bridge.

Strain gauges are combined to form a Wheatstone bridge circuit. The output voltage of the bridge depends on the value of the resis-



tances  $R_1, \dots, R_4$  forming it and is equal to 0 for a balanced bridge, i.e. when the condition occurs:

$$R_1 \cdot R_2 = R_2 \cdot R_4$$

This bridge balance occurs when the diaphragm is undeformed. The deformation of the diaphragm results in resistance changes:

$$R_i = R + \Delta R_i, \Delta R \ll R, \text{ where } i = 1, 2, 3, 4$$

Then an imbalance voltage appears at the output of the bridge:

$$U_{Out} \approx \frac{U_{Sup}}{4R} \cdot (\Delta R_1 + \Delta R_3 - \Delta R_2 - \Delta R_4)$$

Resistance changes in strain gauge sensors are relatively small, which makes them not sensitive enough for typical applications. To increase their sensitivity, strain gauges are made of semiconductors, which exhibit the phenomenon of piezoresistivity. This phenomenon consists of a change in resistivity under mechanical stress, so that the resistivity of such strain gauges, depends not only on a change in their dimensions, but also on changes in the properties of the strain gauge material.

Piezoresistive transducers are complicated semiconducting structures. They are very fragile and must be isolated from the environment by the layer of synthetic oil.

A sample data sheet for the piezoresistive pressure transmitter is shown in Fig. 10.6.

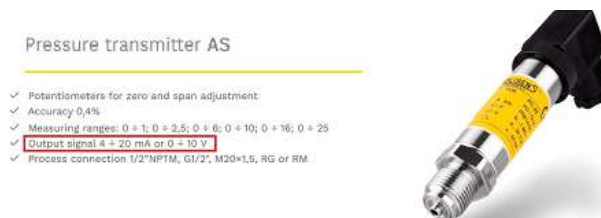


Fig. 10.6: Piezoresistive pressure transducer.

Example

For a pressure transducer given below (Fig. 10.7), determine an equation of its static characteristics and its static sensitivity. What will be the pressure at the transducer inlet if recorded current signal is  $I^*=18.6$  mA.

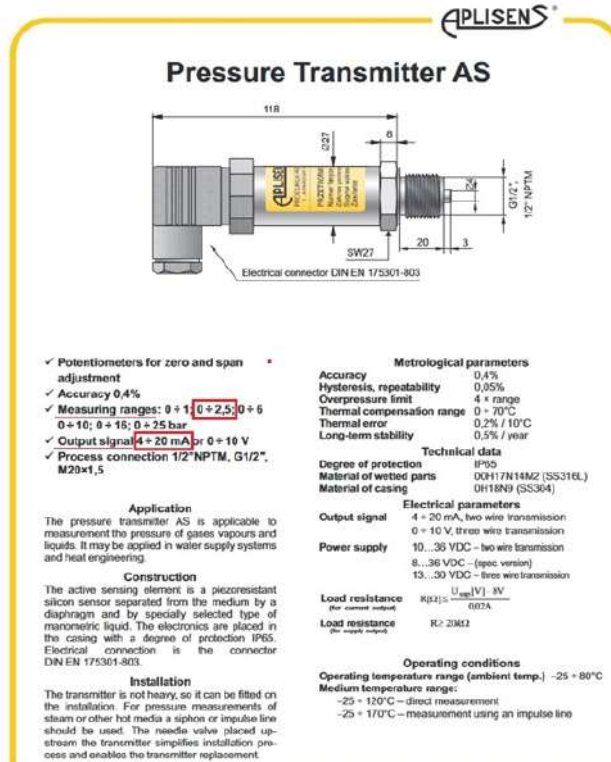
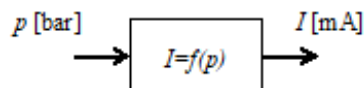


Fig. 10.7: Exemplary data of piezoresistive pressure transducer.

The signal processing scheme is shown in the figure below:



Pressure signal is converted into a current (4 mA-20 mA is the typical standard used in the industry).

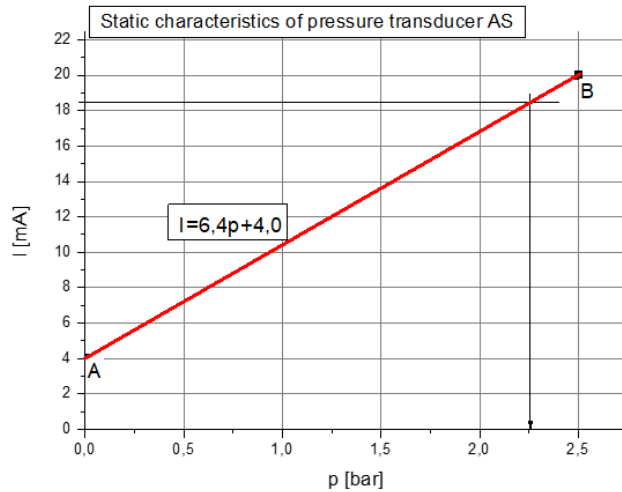
The ranges for input and output signals are as follows:

$$p = \langle 0; 2.5 \text{ bar} \rangle$$

$I = \langle 4.0; 20.0 \text{ mA} \rangle$  The start and end points of the characteristic will have the coordinates:

$$A \Rightarrow p_A = 0 \text{ bar}; I_A = 4.0 \text{ mA}$$

$$B \Rightarrow p_B = 2.5 \text{ bar}; I_B = 20.0 \text{ mA}$$



The equation of static characteristics of the transducer (line A-B):

$$\begin{aligned} I - I_A &= \frac{I_B - I_A}{p_B - p_A} (p - p_A) \\ I - 4.0 &= \frac{20.0 - 4.0}{2.5 - 0} (p - 0) \\ I &= \frac{16.0}{2.5} p + 4.0 \\ I &= 6.4p + 4.0 \end{aligned}$$

Static sensitivity of the transducer is the first derivative of the output signal relative to the input signal:

$$k = \frac{dI}{dp} = \frac{d}{dp} (6.4p - 4.0) = 6.4 \frac{\text{mA}}{\text{bar}}$$

To determine the value of the input signal for a given output current, the inverse static characteristic equation is needed:

$$p = \frac{1}{6.4}(I - 4.0)$$

$$p = 0.156I - 0.625$$

For  $I^* = 18.5$  mA  $\Rightarrow p^* = 0.156 \cdot 18.5 - 0.625 = 2.26$  bar

## 10.2 Flow velocity and flow rate measurements

### Local flow velocity measurements

Local flow velocity can be measured by means of pneumatic probes. The simplest pneumatic probe is the Pitot probe. It can be imagined as a bent tube placed in the flow (Fig. 10.8).

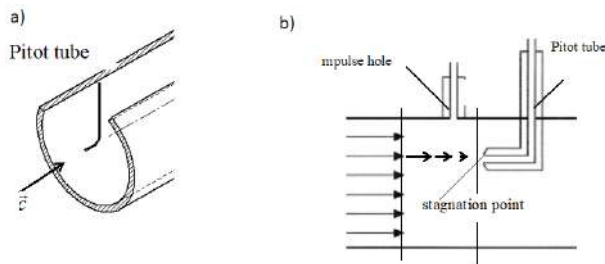


Fig. 10.8: The idea of flow velocity measurement by means of the Pitot tube.

Fig. 10.8 shows the idea of velocity measurement by means of Pitot tube. At some distance from the probe inlet, the jet having velocity  $c$  decelerates and at the probe inlet section it is completely decelerated ( $c=0$  – stagnation point). As the result of this deceleration, the conversion of kinetic energy into potential one (pressure energy) takes place.

Writing Bernoulli equation for sections  $(\infty)$ – $(0)$  we obtain:

$$\rho \frac{c_{\infty}^2}{2} + p_{\infty} = \rho \frac{c_0^2}{2} + p_0$$

where:  $c_\infty=c$  – mean flow velocity in the area undisturbed by the probe  $p_\infty=p$  – static pressure  $c_0=0$  – velocity in the stagnation point.

And we obtain:

$$p_0 = p + \rho \frac{c^2}{2}$$

Pressure  $p_0$  (pressure int stagnation point) is also called total pressure and denoted as  $p_e=p_0$ . It can be expressed as the sum of static pressure  $p$  (this pressure would be recorded by a sensor moving with the fluid at a speed  $c$ ) and dynamic pressure  $p_d=\rho \frac{c^2}{2}$  expressing kinetic energy of the fluid.

So finally we can state that:

$$p_e = p + p_d$$

In practice, to express flow velocity we need the information about two pressures: static  $p$  and total  $p_e$ :

$$c = \sqrt{\frac{2p_d}{\rho}} = \sqrt{\frac{2(p_e - p)}{\rho}}$$

- total pressure  $p_e$  will be measured by a Pitot tube as a stagnation pressure
- static pressure  $p$  can be measured by an impulse hole drilled perpendicularly to the pipe axis (then, no information about the flow velocity is transmitted to the measuring device)

Additionally we must know the fluid density  $\rho$ , that can be expressed from the gas state equation:

$$c\rho = \frac{p}{RT}$$

Where  $R$  is an individual gas constant (for the air  $R=287.15 \frac{J}{kgK}$ ) and  $T$  is gas temperature.

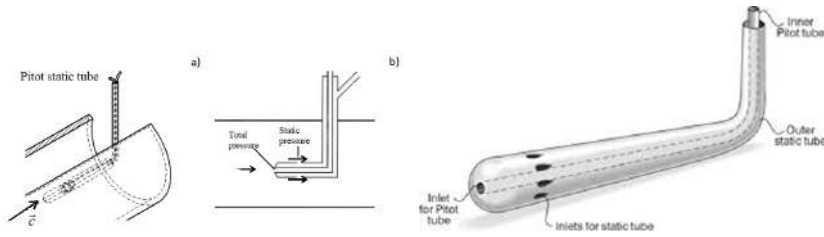


Fig. 10.9: The idea of flow velocity measurement by means of the static Pitot tube and the design of static Pitot tube.

To avoid necessity of drilling impulse hole in the pipe wall, we can apply the Prandtl probe (which is often called Pitot static tube). This probe has an advantage of measuring both static and total pressure Fig. 10.9.

### Flow rate measurements

In general we can distinguish:

- volume flow rate

$$\dot{V} = \frac{V}{\Delta t} \left[ \frac{m^3}{s} \right]$$

- mass flow rate

$$\dot{m} = \frac{m}{\Delta t} \left[ \frac{kg}{s} \right]$$

These two quantities are connected directly with mean flow velocity  $\bar{c}$ :

$$\begin{aligned} \dot{V} &= \bar{c}A \\ \dot{m} &= \rho \bar{c}A \end{aligned}$$

Where  $A$  is a cross sectional area of a duct and  $\rho$  is fluid density.

Flow rate can be determined with use of mean velocity, however it is not common practice as the flow field in the duct can be not uniform and should be determined firstly.

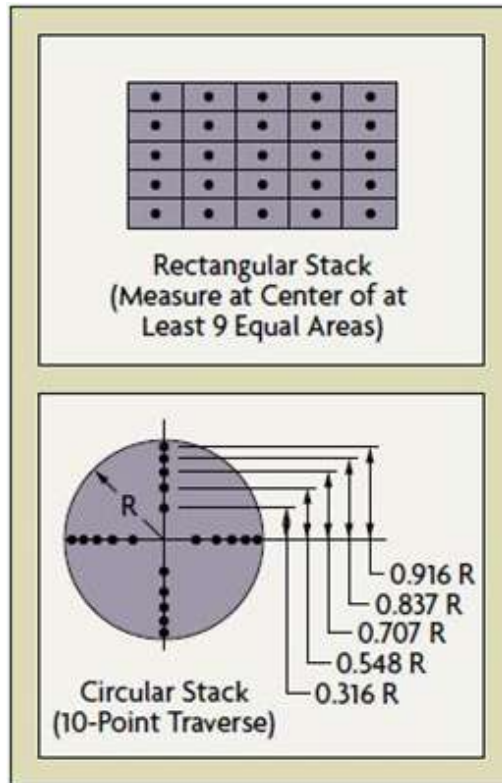


Fig. 10.10: The measurements of local flow velocities – the positions of measuring points.

It can be done with use of pneumatic probes described above (Pitot tube, Pitot static tube or others), making local velocity measurements in different points of the duct, as shown below (Fig. 10.10).

Example of velocity measurement point arrangement for determining the velocity profile in the measurement channel.

In practice, the direct methods of measurement of flow rate are applied.

- Orifice flow meters, measuring nozzles and Venturi nozzles (Fig. 10.11)

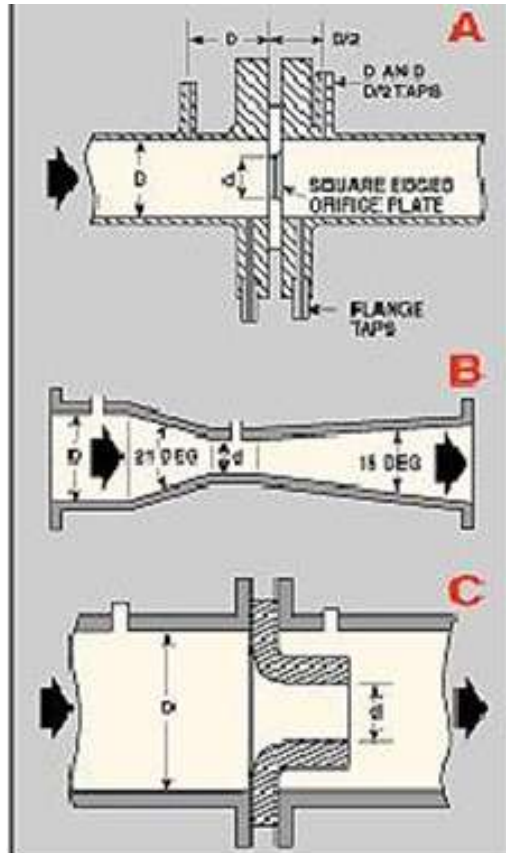


Fig. 10.11: Orifice plate (A), Venturi nozzle (B), measuring nozzle (C).

In all these methods a flow damping element is used. A pressure difference  $\Delta p$  that appears between upstream and downstream of this element is used as the measurement signal as it depends of the flow rate. This relationship is of type:

$$\dot{V} = k\sqrt{\Delta p}$$



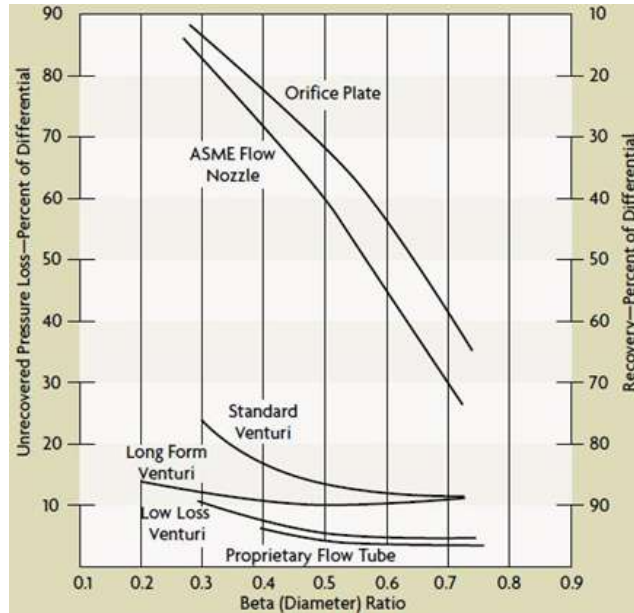


Fig. 10.12: The comparison of pressure losses for different differential flowmeters.

Orifice plate with sharp edges is the simplest solution (from technological point of view), but it introduces the largest flow losses.

Measuring nozzle and Venturi nozzle, thanks to the gentle contouring of the canal shape generate significantly lower flow losses. The principles of measurements of flow rate by means of pressure differential devices are described in the standard ISO 5167-1 1991.

Fig. 10.12 illustrates pressure losses for different types of differential flowmeters.

- Averaging Pitot tubes (Annubar probes)

These flowmeters use the pressure difference occurring on the profile placed in the flow (Fig. 10.13).

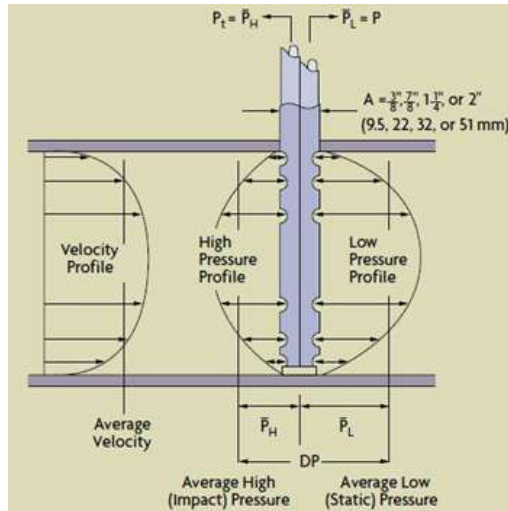


Fig. 10.13: Working principle of averaging Pitot tubes.

If we compare the pressure distribution on different profiles we can notice, that on the inflow side an overpressure zone occurs and on the outflow side an underpressure exists (Fig. 10.14).

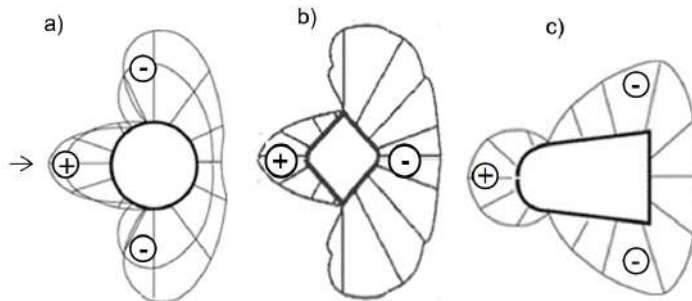


Fig. 10.14: Pressure distribution on different profiles: a) round profile b) diamond shape (Annubar probe), c) airfoil shape (Introbar probe).

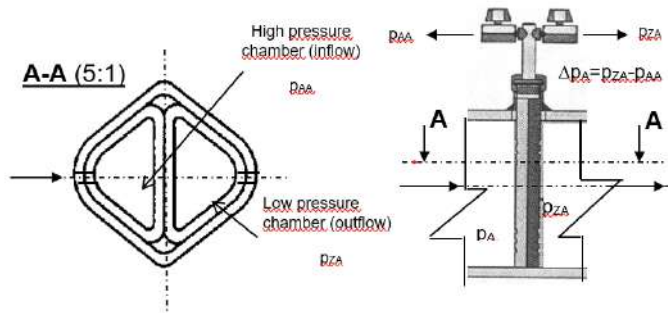


Fig. 10.15: The design and the principle of measurements for diamond shape Annubar probe.

The flow velocity can be expressed as the function of pressure difference between the inflow and outflow pressure.

$$c = K \sqrt{\frac{2\Delta p}{\rho}}$$

The position of microholes (microports) allows for correct recovery of velocity profile (Fig. 10.16).

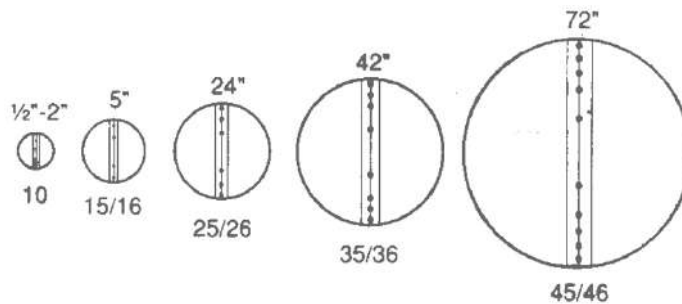


Fig. 10.16: Number and arrangement of impulse holes depending on the diameter of the duct [Dieterich Standard].

Averaging differential probes generate significantly less pressure loss than orifice flowmeters, what is clearly shown on Fig. 10.17.

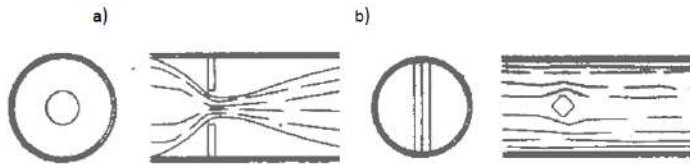


Fig. 10.17: The illustration of difference in pressure losses for the orifice flowmeter and Annubar probe.

- Turbine flowmeters

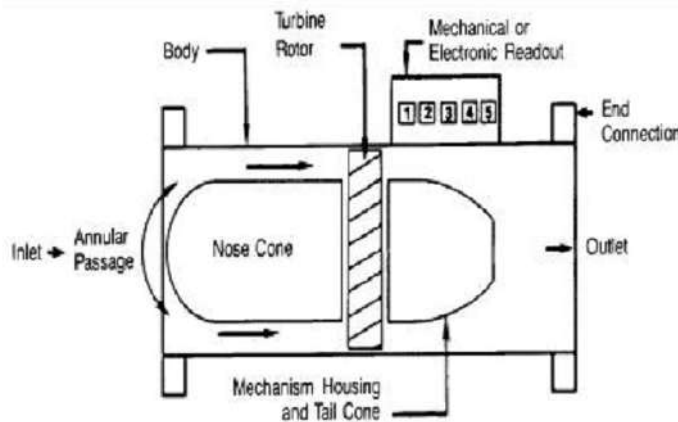


Fig. 10.18: Turbine flowmeter.

The measuring transducer is a turbine driven by the flowing medium (Fig. 10.18). The output signal is the turbine rotational frequency which is proportional to the flow rate.

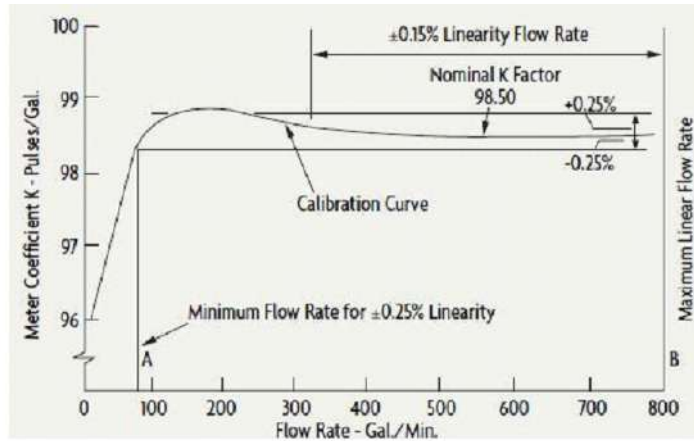


Fig. 10.19: Characteristics of turbine flowmeter.

The characteristics of turbine flowmeters (Fig. 10.19) are linear above a certain flow rate. For lower flow rates, the nonlinearity is very high which causes their poor accuracy in the initial region of the measuring range.

#### - Vortex flowmeters

The principle of their operation is based on a natural phenomenon, the so-called von Karman vortex path, which occurs with the flow of blunt bodies behind which vortex paths are formed (Fig. 10.20).

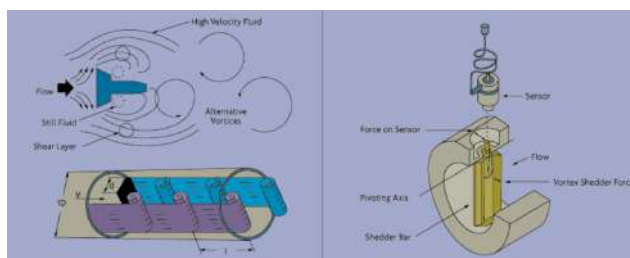


Fig. 10.20: The principle of operation of Vortex flowmeter.

The frequency of these descending vortex paths is proportional to the velocity of the fluid in the channel. The main components of the flow meter are a vortex generator and a transducer that detects

the vortices and generates an electrical output signal proportional to the frequency of the descending vortices. Measurement accuracy is of 1% of the measured value.

- Electromagnetic flowmeters

In an electromagnetic flowmeter, the potential difference created at electrodes placed in a flowing liquid located in a magnetic field perpendicular to the direction of flow is measured (Fig. 10.21).

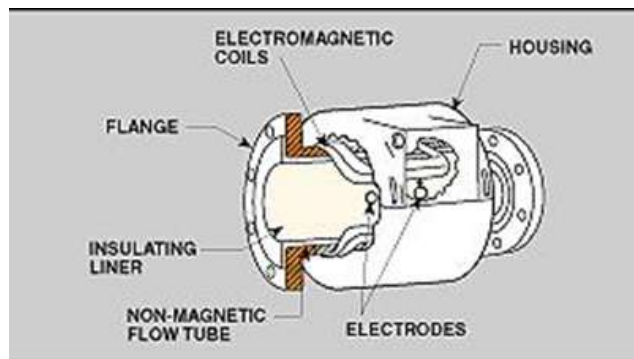


Fig. 10.21: Electromagnetic flowmeter.

The tube-shaped measuring head built into the pipeline has an internal surface lined with a material suitable for the fluid flowing through. Flowmeters of this type are used for a variety of liquids, including chemically aggressive, food-grade and contaminated.

Electromagnetic flowmeters may be used provided that the electrical conductivity of fluid is not less than  $5 \mu\text{S}/\text{cm}$  (in special designs  $1 \mu\text{S}/\text{cm}$ ).

Typical electrical conductivity values for various liquids are given below:

- demineralized water –  $1\text{-}10 \mu\text{S}/\text{cm}$
- drinking tap water –  $200\text{-}1000 \mu\text{S}/\text{cm}$
- seawater –  $1\text{-}10 \mu\text{S}/\text{cm}$
- industrial process water –  $1\text{-}100 \mu\text{S}/\text{cm}$

Measurement uncertainties are at 0.25 to 1% of the range.

- Ultrasonic flowmeters

Ultrasonic flowmeters (Fig. 10.22) allow the non-invasive measurement of the flow rate of various types of liquids. Two phenomena are most commonly used to determine the volume flow rate:

- the phenomenon of changing the speed of an ultrasonic wave propagating in a fluid moving at different speeds (applies to liquids not containing inclusions of solid or gaseous phase)
- Doppler effect (applies to liquids containing inclusions of solid or gaseous phase)

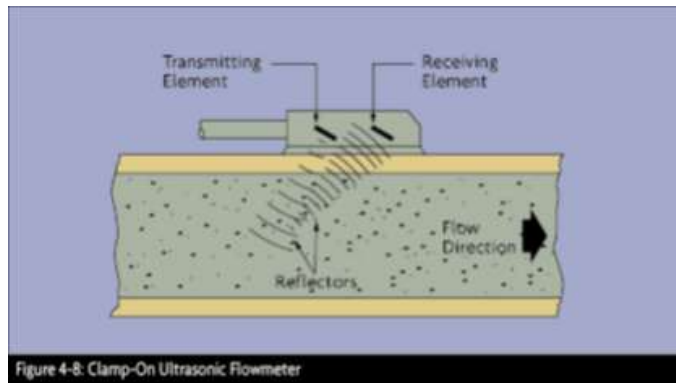


Fig. 10.22: Ultrasonic flowmeter.

In the case of closed channels, the probes are built into the section of pipe inserted into the pipeline. Range of pipe diameters is from a few millimeters to several meters.

Accuracies vary from 1% to 5% of the measuring range.

- Coriolis mass flowmeter

Flowmeters based on the Coriolis force phenomenon measure mass flow rate, they are also appropriate for unsteady flow measurements. They are applied mainly for liquids.

The most common design is a U-tube (Fig. 10.23). The operating principle is as follows: the U-shaped tube oscillates at its own frequency (80 Hz).

The fluid flow makes the U-tube to rotate and a Coriolis force is created. The angle of rotation is directly proportional to the instantaneous mass flow rate. The accuracy is very high: typically 0.1% of the measurement range.

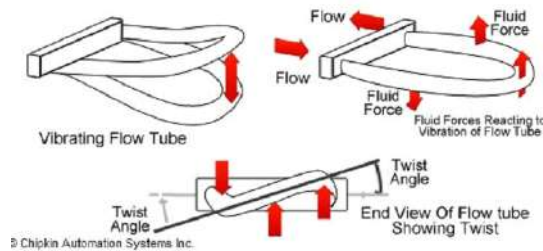


Fig. 10.23: Coriolis flowmeter.

### Temperature measurements

Measurements of flowing fluid temperature in turbomachines are one of the most difficult. This is caused by numerous factors like:

- high (in many cases) velocities of gas
- important temperature gradients in ducts
- very frequent non-stationary flow
- hot or polluted medium

When the flow takes place with higher velocity (as a conventional limit, a speed of approx. 20 m/s is assumed) an additional temperature component  $T_d$ , called dynamic temperature appears and it should be taken into account.  $T_d$  results (as in the case of dynamic pressure) from the deceleration of the flowing medium on the sensor and the conversion of its kinetic energy into thermal energy.

Dynamic temperature (similar to dynamic pressure) is defined:

$$T_d = \frac{c^2}{2c_p}$$

where:  $c_p \left[ \frac{J}{kgK} \right]$  is the specific heat of fluid at constant pressure.



Temperature of flowing fluid  $T_m$  measured by temperature sensor can be expressed as:

$$T_m = T + rT_d$$

where:  $T$  – static temperature

$T_d$  – dynamic temperature

$r$  – recovery coefficient

In the real measurement process, the deceleration of the medium on the sensor surface is never complete, and consequently the measured temperature value  $T_m$  is smaller than the total temperature  $T_e$ :

$$T_e = T + rT_d > T_m = T + rT_d$$

The relationship above shows that the recovery coefficient  $r < 1$ .

For real temperature sensors, the value of the  $r$  coefficient is usually in the range of  $0.6 < r < 0.9$  and it depends on the Mach number (cf. Fig. 10.24).

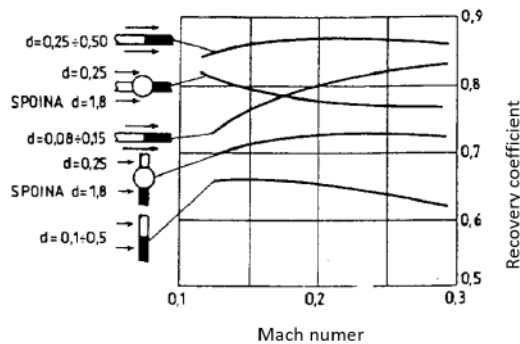


Fig. 10.24: Recovery coefficient for different Mach numbers.

## Thermocouples

Thermocouples are one of the most commonly used temperature sensors. The design of thermocouple is very simple. It is composed of two wires (made of two different metals) welded at one extremity

that creates measuring weld or hot ends. The opposite ends of the wires are called cold or free ends. If there is a temperature difference between the measuring weld and the cold ends, a small voltage, called Seebeck voltage, will develop in the circuit as in Fig. 10.11. The Seebeck voltage is also called the thermoelectric power.

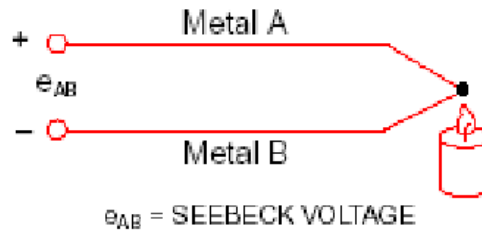


Fig. 10.25: The principle of work of thermocouple.

$$E = e_{AB} = \alpha \Delta T$$

where:  $E$  – thermoelectric power  $e_{AB}$  – Seebeck voltage  $\Delta T$  – temperature difference between hot and cold ends

In fact the relationship between the thermoelectric power and the temperature difference is not fully linear (cf. Fig. 10.26).

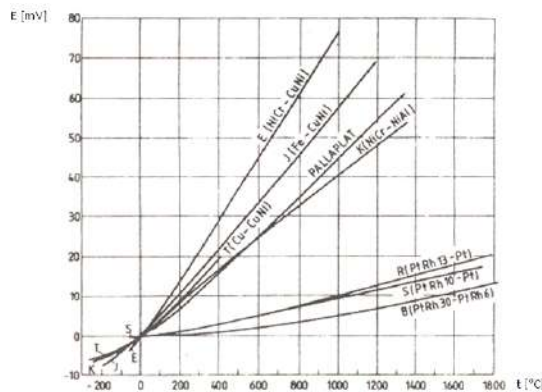


Fig. 10.26: Thermoelectric characteristics of typical thermocouples.

According to the international standard IEC 584 (the Polish equivalent of EN 60584), the thermometric characteristics of thermocouples are standardised:

- Typ **E** (chromel/ constantan)
- Typ **J** (iron/ constantan)
- Typ **K** (chromel/alumel)
- Typ **R** (platinum13%-rod/platinum)
- Typ **S** (platinum10%-rod/platinum)
- Typ **T** (copper/ constantan)
- Typ **B** (platinum6%-rod/platinum30%-rod)

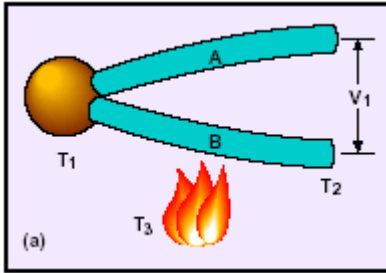
Thermometric characteristics can be presented in tabular form or in polynomial form, which is more convenient. Omega Inc. defines characteristics of their thermocouples in the form of 9th order polynomial:

$$T = a_0 + a_1E + a_2E^2 \dots + a_nE^n$$

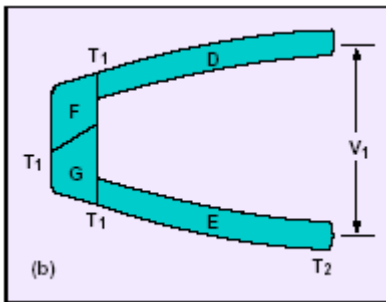
With coefficients of polynomials approximating the thermometric characteristics of the most commonly used thermocouples (according to OMEGA catalogue, 2000) summarized in table below:

	Type E	Type J	Type K	Type R	Type S	Type T
T range [°C ] (min,max)	(-100,1000)	(0,760)	(0,1370)	(0,1000)	(0,1750)	(-160,400)
$a_0$	0.104967248	-0.048868252	0.226584602	0.263632917	0.927763167	0.1008660910
$a_1$	17189.45282	19837.14503	24152.10900	179075.491	169526.5150	25727.94369
$a_2$	-282639.0850	-218614.5353	67233.4248	-48840341.37	-315688363.94	-767345.8295
$a_3$	12695339.5	11569199.78	2210340.682	1.90002· 10 <sup>10</sup>	8990730663	78025595.81
$a_4$	-448703084.6	-264917531.4	-860963914.9	-4. 82704· 10 <sup>12</sup>	-1.63565· 10 <sup>12</sup>	-9247486589
$a_5$	1.10866· 10 <sup>10</sup>	2018441314	4.83506· 10 <sup>10</sup>	7.62091· 10 <sup>14</sup>	1.88027· 10 <sup>14</sup>	6.97688· 10 <sup>11</sup>
$a_6$	-1.76807· 10 <sup>11</sup>		-1.18452· 10 <sup>12</sup>	-7.20026· 10 <sup>16</sup>	-1.37241· 10 <sup>16</sup>	-2.66192· 10 <sup>13</sup>
$a_7$	1.71842· 10 <sup>12</sup>		1.38690· 10 <sup>13</sup>	3.71496· 10 <sup>18</sup>	6.17501· 10 <sup>17</sup>	3.94078· 10 <sup>14</sup>
$a_8$	-9.19278· 10 <sup>12</sup>		-6.33708· 10 <sup>13</sup>	-8.03104· 10 <sup>19</sup>	-1.56105· 10 <sup>19</sup>	
$a_9$	2.06132· 10 <sup>13</sup>				1.69535· 10 <sup>20</sup>	

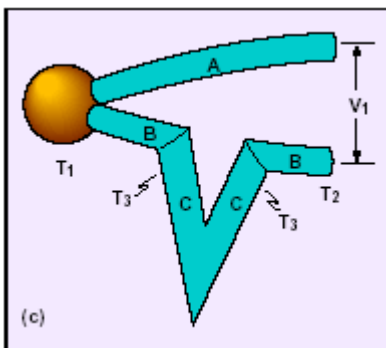
Thermoelectric laws and phenomena occurring in different metals connecting



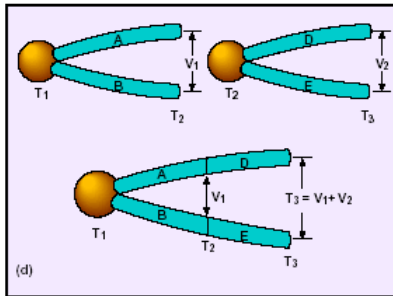
Heating the thermoelectrode along its length does not change the system readings.



The thermocouple readings are not affected by the weld being made of different metals, provided that the temperature is the same throughout the weld.

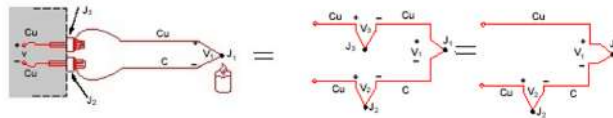


Inserting a section of a different material (C) in the circuit does not change the thermocouple reading, provided that the ends of that section are at the same temperature ( $T_3$ ).



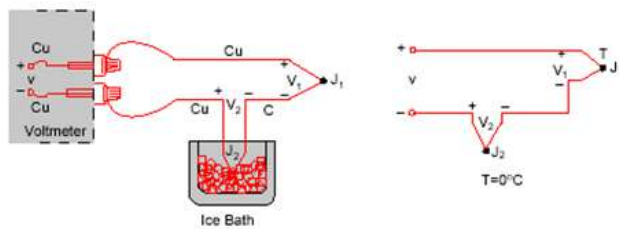
Law of successive metals. The addition of further thermoelectrodes generates an additional voltage (provided there is a temperature difference  $T_1 \neq T_2 \neq T_3$ ).

Thermocouple/ meter interaction – measuring systems



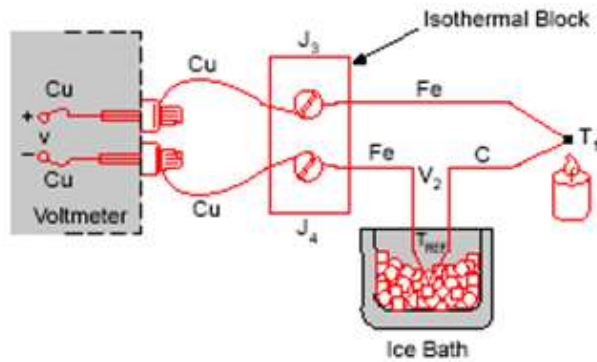
$V_3=0$  – the same metal,  $T_1$  – measured temperature,  $T_2=T_{ref}$  – reference temperature

Copper (Cu) – Constantan (C) thermocouple connection to the meter:  $T_{ref}=T_{amb}$ .

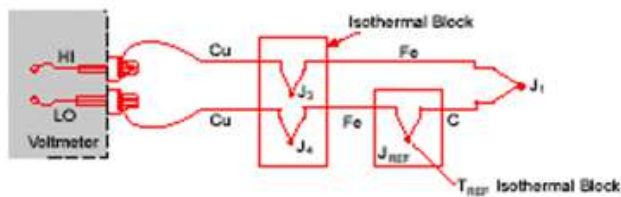


$T_2=T_{ref}=0^\circ\text{C}$  – reference temperature

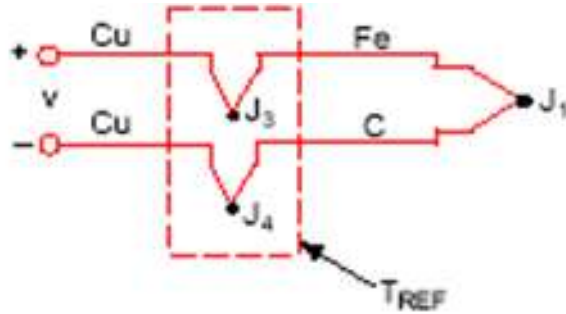
Copper (Cu) - Constantan (C) thermocouple connection to the meter: application of ice bath for the stabilization of cold ends temperature:  $T_2=T_{ref}=0^\circ\text{C}$ .



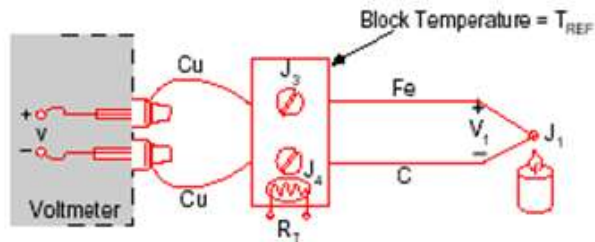
$T_2 = T_{ref} = 0^\circ\text{C}$  – reference temperature,  $T_3 = T_4$  – isothermal block  
 Iron (Fe) - Constantan (C) thermocouple connection to the meter:  
 application of ice bath for the stabilization of cold ends temperature:  
 $T_2 = T_{ref} = 0^\circ\text{C}$ .



Iron (Fe) - Constantan (C) thermocouple connection to the meter:  
 application of isothermal block for stabilization of cold ends and  
 terminals temperature:  $T_2 = T_3 = T_4 = T_{ref}$ .



Iron (Fe) - Constantan (C) thermocouple connection to the meter:  
 application of common isothermal block for cold ends and terminals:  
 $T_2 = T_3 = T_4 = T_{ref}$ .



Iron (Fe) - Constantan (C) thermocouple connection to the meter –  
 correction of cold ends temperature.  $R_T$  – additional thermometer  
 measuring cold ends temperature – meter readings are corrected  
 according to  $R_T$  readings.



## Chapter 11

# Air source heat pumps in single-family homes, overview of solutions

## 11.1 Introduction

Heat pumps are not devices that convert part of the work into heat because they are devices that serve to raise the heat potential, that is, the process of extracting heat from a source with a lower temperature is transferred to a source with a higher temperature. Currently, there are three types of heat pumps that are used in single-family homes, where the difference is due to the lower heat source medium used: ground, water or air. Currently, there are three types of heat pumps that are used in single-family homes, where the difference is due to the lower heat source medium used: ground, water or air. Because ground and water source heat pumps need acceptable conditions of those medium, and they are more expensive in install than air source heat pump, people are looking for this last of mentioned type. So this is this is the reason why this chapter will talk about air source heat pumps (ASHP). They are getting very popular in Western Europe and Poland, because they are cheaper to install and can operate in low temperatures without worrying about freezing lower heat source. The advantages and disadvantages of the heat pump are well known but worth repeating. The main advantages are the low operating cost of the heat pump, its maintenance-free operation, small size, while the disadvantages include high investment cost compared to conventional heat sources, possible inconvenience of operation - noise, a certain temperature range of effective operation. Is it possible to somehow influence the mentioned disadvantages? Unfortunately, current technology does not allow it, but owners of ASHP can and should protect themselves in case of electric power failure, in such a way as to be able to heat the house after the power failure. We are talking about the proper design of the heating system for single-family houses and equipping them with a bivalent source of thermal energy not powered by electricity, such as boilers powered by fossil fuels. This description is intended to present not so much the solutions of individual manufacturers, as issues that are worth paying attention to when selecting an ASHP for the conditions, in which it will work and to indicate why an alternative source of heat energy is recommended in areas where the temperature drops below  $+5^{\circ}\text{C}$ .

## 11.2 Heat pump basics

Heat pump is a device which is transporting heat from a low temperature medium to a high-temperature. Such a device can be any type of an equipment that uses a refrigeration circuit in which we deal with evaporation, compression, condensation and expansion of the refrigerant. This relationship is presented in the p-h diagram shown in Fig. 11.1.

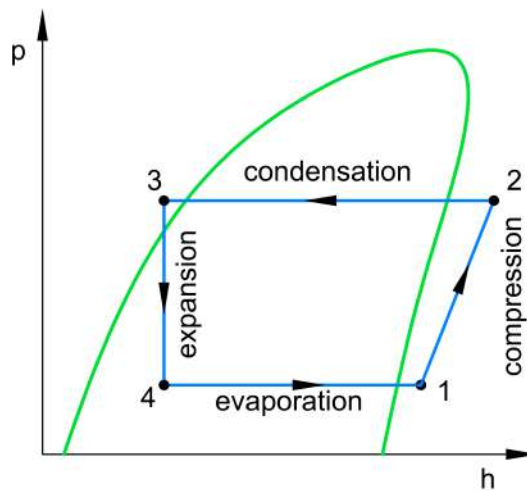


Fig. 11.1: Pressure enthalpy graph for refrigerant cycle.

Its efficiency is described by the formula:

$$COP = \frac{Q_{hp}}{E_{el}}$$

where:

$COP$  – coefficient of performance

$Q_{hp}$  – energy from the heat pump

$E_{el}$  – electric energy used

ASHP efficiency depends on several factors. The first is the proper design of the heat pump, which should feature properly sized heat exchangers, i.e. condenser and evaporator for a specific solution.

ASHP should not be used without determining a criteria of a work for which it is selected. If the size of the condenser, which in the case of ASHP is a water tank equipped with a coil, is incorrectly selected, it may turn out that the heat pump will not turn off at all when the tank is too large, or if the tank is too small it will turn on and off frequently, which may lead to its failure. The second of the important factors responsible for the COP for ASHPs is the proper setting of the so-called bivalent operating point. ASHPs can operate at temperatures below  $+5^{\circ}\text{C}$ , while their efficiency decreases in this range. The problem is frosting of the evaporator, which takes up heat from air that is cool and moist. Frost or ice buildup significantly limits heat transfer, as it is an insulating barrier, in addition, it reduces the hydraulic diameter between the heat exchanger fins, causing considerable resistance to the flow of air pumped by the fan. Adding up these two processes, the efficiency of the system drops to a level that is not cost-effective for the ASHP user, as the amount of energy put into the heat pump approaches the amount of heat obtained, which is similar to heating a house with an electric heater. Therefore, it is important to properly set the temperature bivalent point, which is designed to turn off the heat pump when the outdoor temperature reaches below the value specified by the manufacturer and switch to an alternative source of heat energy, which will show a better economic settlement. The issue presented will be described in detail later in the work. As you can see, the COP is not a fixed parameter and, in addition, it is responsible for the cost of generated heat for a single-family house.

### 11.3 Use of air source heat pumps

Application depends on the environmental conditions at the given location, as the range of effective operation is limited, so the solutions should be tailored. In Poland, the conditions are presented in the Fig. 11.2. From it you can read which regions are exposed to low temperatures in the winter season. Based on it, you should choose not only type of ASHP but also the point of bivalent operation.



Fig. 11.2: Map of climate zones according to EN 12831.

Design outdoor temperature and annual average outdoor temperature is shown table.

Climate zone	Design outdoor temperature [°C]	Average annual outdoor temperature [°C]
I	-16	7.7
II	-18	7.9
III	-20	7.6
IV	-22	6.9
V	-24	5.5

Tab. 11.1: Design outdoor temperature and annual average outdoor temperature.

The values presented for the prevailing conditions in Poland, indicate small difference between zones for average values. On the other hand, given Poland's geographic location, geological, and water structure, highly variable conditions can be expected. Therefore, it is advisable when designing an ASHP to include an emergency heat source that will be able to supply the house with the necessary heat in the event of a power outage or heat pump failure. In the past few years, Polish winters have been among the warmer on record, which does not mean that this trend is likely to change anytime soon. Although the ASHP design allows for operation at low temperature, it should be remembered that in such conditions it requires more electricity than usual, operating at the edge of the operating envelope. Bearing in mind that they are used in single-family homes and often in places with an undeveloped power grid, one can expect a grid to fail due to overloading. Therefore, in recent months, there have been more and more calls among the ASHP research community for single-family homes to be protected against the aforementioned scenarios.

## 11.4 Division of ASHP

The use of air source heat pumps should depend on the surrounding environmental conditions. It is not always possible to use a heat pump whose bottom source is air. This is because an air heat pump needs a stable heat source for the evaporator. Air source heat pumps are cheaper than ground source heat pumps due to the lower investment cost for the construction of the lower heat source. Usually, the decision on the type of heat pump is dictated only by the surrounding thermal conditions in which the heat pump will operate. It is important to remember that the heat pump does not produce heat energy, but transfers it from the lower to the upper heat source, and for this to be possible it is required to determine this source and match it to the power and processing capacity of the heat pump.

ASHP can be divided into two types. The first is monoblock the second is split (Fig. 11.3 and Fig. 11.4).

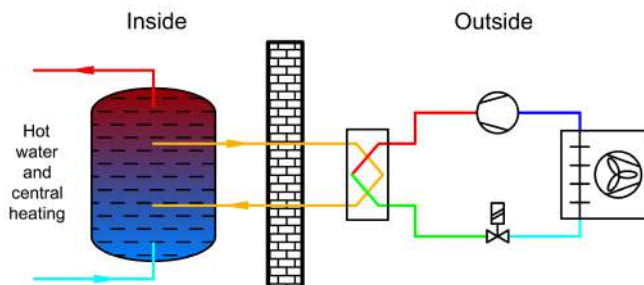


Fig. 11.3: Monoblock.

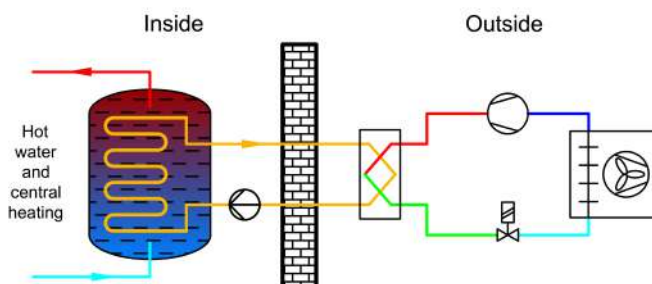


Fig. 11.4: Split.

Monoblocks have the advantage over splits that they are compact structures and the exchangers used in them are contained in a single housing, which is located outside the building. This results in a lower investment cost, because in the case of split systems we have to deal with the transfer of thermal energy through an intermediary substance, which is an aqueous solution of glycol or alcohol. Monoblocks, however, have their limitations due to the temperature range of operation, as they cannot be used in conditions where the temperature drops below  $0^{\circ}\text{C}$  during the day and night. This is related to the possibility of freezing of water from the air on the surface of the evaporator. Such a situation can also occur at temperatures as low as  $+5^{\circ}\text{C}$ , if the dew point is exceeded. When dealing with a split-type heat pump, the problem of low temperatures has been solved by using an intermediate system, the carrier

of which is usually aqueous solutions of glycol or alcohol, as they are adjusted to the range of intended operating temperatures and allow proper operation at low temperatures. Thus, it can be concluded that the decision to use a particular type of air heat pump, is dictated only by the atmospheric conditions in which it will operate. It should also be noted that, for some reasons, monoblocks are more efficient than splits, as there is a better efficiency of this system. This is because the heat carrier in the case of a monobloc is water, while in the case of a split it is an aqueous solution of glycol or alcohol. The difference in conductivity of these two types of liquid is almost three times in favour of water, so monoblocks should be used in the temperature range up to  $+5^{\circ}\text{C}$  because they are more efficient. In the case of air source split heat pumps, there are several issues that affect the efficiency of this system. The main problem with this type of solution is the problem of evaporator icing, which contributes to a reduction in the efficiency of heat extraction from the atmosphere. The ice or frost that forms is a protective insulating layer that prevents effective heat transfer. In addition, the design of the evaporator itself, which, as a rule, is a fin-type heat exchanger with a fairly dense distribution of fins, causes a reduction in the hydraulic cross-section of the flowing air during frosting. This results in an increase in the speed of the fan pumping air through its surface, increasing power consumption, and raises the sound intensity as the air is pumped through very narrow gaps. The solution to the problems in this situation is to use different kinds of systems to de-ice this evaporator, while each system carries different kinds of benefits as well as drawbacks. The main disadvantage of the defrosting system is their energy intensity, which unfortunately significantly affects the efficiency of the heat pump decrease with temperatures from  $+5^{\circ}\text{C}$  to  $-10^{\circ}\text{C}$ . At least four types of de-icing systems are distinguished, which will be described below. In summary, the use of the proper type of heat pump surfaces is solely dictated by the environmental conditions environmental conditions in which it will operate. However, when it comes to conditions prevailing in Poland are generally split type systems due to low temperatures in autumn and spring, which fall below  $+5^{\circ}\text{C}$ .



## 11.5 Refrigerators and EU restrictions

Refrigeration systems run on low-boiling refrigerants, which are currently divided into three groups:

1. Natural – ammonia NH<sub>3</sub>, carbon dioxide CO<sub>2</sub>, propan R290, isobutan R600a
2. HFC – R134a, R404a, R507a, R32, ...
3. HFO – 1234yf, 1234ze, ...

Due to European Union restrictions, manufacturers of refrigeration equipment including AHCPs are obliged in the coming years to limit the use of working agents that affect the Global Warm Potential (GWP). We are referring to Regulation (EU) No 517/2014 on fluorinated refrigerant gases, which gradually introduces increasingly stringent limits that aim to minimise harmful refrigerants from use wherever possible. The above-mentioned groups of agents have their advantages and disadvantages. Natural refrigerants have a low GWP, while they are generally flammable and explosive (R290, R600a) or require high operating pressures (CO<sub>2</sub>). In the case of the second group, these are HFC refrigerants, which have fluorine in their composition, which is considered toxic. For this reason, efforts are being made to dispense with these working agents, even though they have very good properties. The third group is the so-called olefins (HFOs), which are mixtures based on the current working agents, i.e. HFCs and naturals. This group was introduced relatively recently and, due to its properties, has introduced an additional category of working agents. Before it appeared, agents were divided into three categories: non-flammable, flammable and highly flammable (A1, A2, A3, respectively). The new group turned out to be slightly flammable and a group called A2L was introduced. These agents cannot, therefore, be used in areas exposed to fire and in air flow, so they cannot be used, for example, in air handling units because they can cause a fire if they leak. Roadmap is shown in Fig. 11.5.

Flammability	Symbol	Toxicity
No flame	A1	CFC, HCFC, most HFCs
Low	A2L	most HFOs, R32
Flammable	A2	R152
High	A3	hydrocarbones

Tab. 11.2: Refrigerant classes, based on [1].

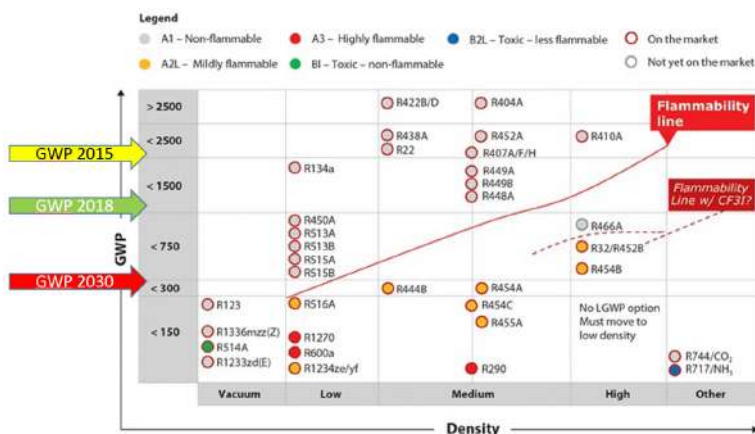


Fig. 11.5: GWP roadmap, based on [1].

An additional problem with the new group was found to be the quite considerable interfacial slip, which affects the quality of operation of refrigeration equipment when the refrigerant leaks. If a leak occurs, a factor that is a mixture should be replaced in its entirety, as it is not known which fraction has escaped into the atmosphere. Previous factors did not have this problem, or it concerned a narrow group of factors. The last and biggest problem with the new factors is their purchase cost, which is certainly felt by owners of cars manufactured after 2018, as the A/C service on those vehicles equipped with R1234yf (HFO) can be 4 to 5 times higher than with the previous refrigerant R134a (HFC). One could reflect in this case on the well-known proverb: better is the enemy of good? In addition, there is a problem with which ASHP and non-ASHP manufacturers

are coming forward. It is the fact that increasingly stringent standards are not being matched by the availability of new refrigerants that meet European Union requirements. One can only guess that they will be developed in the near future, but it is not clear what properties they will have. It will also take some time for manufacturers to switch to the new refrigerants, as it may be advisable to change the seals to be compatible with the new compositions. The next few years will certainly be interesting when it comes to the direction of refrigeration development.

## 11.6 Bivalent point

The bivalent point is a value that determines at what point ASHP should switch to an alternative heat energy source. ASHPs have problems operating at temperatures below  $-7^{\circ}\text{C}$  because their efficiency drops to unity or below unity in relation to the electricity consumed. While they can operate in such conditions, it is economically disadvantageous. When the bivalent temperature specified by the manufacturer is exceeded, or the environmental conditions in which the pump operates, the system switches to an alternative heat source, which guarantees the maintenance of the set temperature in the building. As a standard, ASHP are equipped with electric heaters that allow heating the water in the storage tank to maintain a set temperature to heat the house. This solution is not very efficient in economic terms, while it is very convenient for the end user, because he does not even know that the pump has connected to an alternative energy source. The only downside is the cost of such electric heating, which is much higher than with an ASHP, operating under the optimal conditions for which it is designed. Another way is to use alternative heat sources in the form of heating with fossil fuel or wood boilers. Alternative energy sources should require a developed automatic switching system, which is coupled to the bivalent point adopted by the ASHP manufacturer. Each solution should be tailor-made to achieve the best possible match in terms of heat distribution as well as economically justified. In Poland, there has been an interesting discussion about the market for ASHP in recent months, as there has been a significant increase

in the installation of such pumps in 2022 due to the rising price of fossil fuels including gas, which has influenced the decision of thousands of Poles to supply themselves with this source of heat energy. Unfortunately, this is not a very safe approach, because powering a single-family house with only one source of heat, dependent on electricity, which may be absent in random situations, may affect the temperature in a given building. Such sources may include the aforementioned previously mentioned all kinds of fossil fuel boilers, wood or even wood-burning fireplaces. These problems mainly affect single-family houses, which are located in small towns or far from developed electricity infrastructure, which in the event of an outage can be connected between networks and restored within a few hours. In the case of localities with less power grid coverage, electricity supply can be interrupted even for a whole day or several days, so it is important to protect against such an eventuality. The year 2022 was quite intense when it came to the installation of ASHP in the Polish market, which was affected by the geopolitical situation and inflation. It should also be remembered that Poland lies in a climate with quite variable characteristics, where we are able to have warm winters as well as very cold winters, which can last for several weeks, during which the ASHP may not be able to work. It is important to remember this approach to not to decide solely on one of the sources that may be eliminated due to unfavorable weather conditions. It is also worth mentioning that on the bivalent point of heat pump operation is also largely affected by humidity air, depending on what kind of air we have, the evaporator of our heat pump is exposed to quite strong icing, which reduces the efficiency of the heat exchange. Too frequent activation of the system to de-icing of the evaporator, significantly affects the efficiency of the entire refrigeration system, because, as we mentioned earlier, the use of de-icing carries an additional energy cost, which is later included in the total system for heating. In conclusion, it should be remembered that the estimation of the cost of operating a heat pump concerns not only the operation itself under optimal operating conditions, but also the defrosting system and the properly defined bivalent points, which when poorly set can cause the defrosting system to switch on too often and cause electricity bills to rise. In this

case, it is necessary to tune the ASHP during its operation in order to determine the so-called golden mean, where the operating point should be. In other words, you can say that the system lives a life of its own, which unfortunately must be taken care of if you want to have low electricity bills.

## 11.7 Noise

When deciding on an ASHP, it is also important to remember about its proper location of the outdoor unit. This has a direct bearing not only on the efficiency of the heat pump itself, but also on the amount of noise generated, which can be quite significant in the case of a poorly located outdoor unit.

Distance from wall [m]	Max noise [db]
1	60
4	51
8	45
16	40

Tab. 11.3: Noise near building [1].

In the case of systems that only heat our homes, the outdoor unit should not be located in areas of heavy shade or exposed to strong winds and drafts, because, as mentioned earlier, the heat pump is not used to produce heat energy, but to transfer it from one point to another. Therefore, it is necessary to secure the right conditions for it so that it works optimally. Locating the outdoor unit too close to a wall or in a place where the noise generated by the evaporator fan, as well as the compressor itself, should not bounce between walls because they increase the audible noise. The appropriate location of the outdoor unit should be consulted with the house manager or potential neighbor in such a way as not to make each other miserable.

## 11.8 Methods of defrosting

Defrosting of AHSP applies to split units. It is one of the key problems in conditions where the surface of the heat pump must operate at  $+5^{\circ}\text{C}$  and below because in this range, at a certain humidity, quite severe frosting of the evaporator occurs. Frosting of the surface of this heat exchanger is the same as putting some kind of insulation on the evaporator fins and tubes, thus reducing its efficiency. Several methods are currently in use to de-ice the evaporator, while each of these methods requires additional energy input, so that the efficiency of the air heat pump decreases when the system for de-icing is activated. This is related not only to additional electricity consumption, but also to the fact that the heat pump does not produce heat for the water storage tank during the de-icing, so the time spent on de-icing the evaporator negatively affects the efficiency of the system. The first method is based on the installation of electric heaters under the evaporator in the outdoor unit. As a rule, it is controlled by a temperature sensor or other sensor that determines the formation of a layer of ice on the surface of the evaporator, which sets the signal to start the electric heaters to de-ice the the surface of the heat exchanger. At this point, as a rule, the refrigeration system is turned off because it would adversely affect the de-icing system. As an example to imagine such a solution one can cite the example of a No Frost domestic fridge, where the freezer compartment has an evaporator just equipped with an electric heater. In the refrigerator, the air is distributed by a fan placed above the evaporator, which distributes the cold air partly to the refrigerator chamber and partly to the freezer chamber. Since the evaporator is the coldest component in the refrigerator, condensed moisture from the air settles on the its surface causing reduced heat transfer. Manufacturers equip their refrigerators with an automatic evaporator defrost system, which is controlled either by a temperature sensor or by time where, for example, every 8 hours there is a 10-minute defrost cycle, during which the compressor turns off and a heater with a power similar to that of the compressor turns on. During de-icing, the temperature on the evaporator rises dramatically, causing de-icing of the evaporator surface. The collected water is transported

by gravity outward toward the crankcase of the compressor, where it is used to pre-cool the steam on the compressor discharge. This is quite a smart system using regeneration while it significantly affects the quality of the stored products, since their moisture content is reduced. What would happen if the heater did not switch on? The fridge's compressor would have run continuously, but the products in it would not have been cooled because the evaporator would have been all filled with ice, which would have prevented the supplied air from cooling the warm products. Returning to the air heat pump, it can be said that this system is quite simple, while quite energy-intensive, because during the defrosting the compressor does not work so we do not produce heat that we could use later. The number of defrost cycles depends only on the weather, so it is difficult to compare some of the solutions, especially in the case of year-to-year how such a system affects the overall calculation, since weather conditions are different every year.

The second solution is to use a reverse refrigeration circuit, which is implemented by a four-way valve. This solution is theoretically more efficient, because the heat generated by the compressor in the form of superheated steam, goes instead of the condenser, directly to the evaporator. Thus, it can be said that the efficiency of such a solution is two to four times more effective than in the case of heating with electric heaters (depends on weather conditions), while this solution also has its drawbacks. The heat pump is coupled with a water buffer, which supplies the building with domestic hot water and heat for central heating. When we reverse the refrigeration cycle, we draw heat energy from the water buffer into which heat was just transferred from the outside. The defrost cycle is not long, so the generated loss is not too noticeable if we have a properly sized water storage tank for our needs. The key is again the bivalent source of thermal energy, which would replace the ASHP if necessary. The solution is now commonly used in equipment and also seems to be quite convenient because the end user will not even feel the moment when the defrost system has been switched on.

There are new developments in the scientific literature that have not yet been transferred to production. These are based on heat storage,

which are phase change materials (PCM). The idea, in a nutshell, is to accumulate heat in a separate storage tank, which is connected on a bypass in the line between the discharge of the refrigeration compressor and the expansion valve, where temperatures of up to approximately  $+30^{\circ}\text{C}$  can be used. The stored heat, is to be used to de-ice the flooded evaporator. To do this, the refrigerant vapour is to be pumped through it to transport the heat from the storage to the evaporator. The solution is quite interesting and may have an overall economic benefit, as it makes use of so-called waste heat. However, nothing comes for free in nature, so it is advisable to carry out various types of analyses to confirm the proposed solution. One additional problem is also the transport of oil, which must be ensured at a similar level as it was, since an inadequate heat storage geometry can be a kind of trap in which oil can accumulate and lead to compressor seizure. Nonetheless, the direction to look for a further increase in COP for ASHPs is quite interesting and, over a period of time, may bring the anticipated benefits.

## 11.9 Summary

This paper provides an overview of ASHP used in single-family homes. The division that is used depending on the weather conditions in which it will ultimately operate was presented. The currently used operating factors and the restrictions that apply to the European Union countries in connection with the reduction of carbon dioxide emissions into the environment are presented. The key concepts of the bivalent point were discussed, and the problems to which special attention should be paid when selecting the location of the outdoor unit were presented. Problems that arise at low temperatures, concerning evaporator icing, resulting in reduced ASHP efficiency, are described. Current designs have a number of different types of systems for evaporator de-icing, which are presented and described.

It should be emphasized in conclusion that the use of ASHP for single-family homes is an interesting alternative to current heating systems based on fossil fuels and firewood. However, it is worth



bearing in mind the fact that an ASHP is not a device that produces heat, but only a device that transfers heat using an appropriate refrigerant and thermodynamic circuit. Therefore, the selection of an ASHP should be prepared on the basis of a previously performed audit of the building in question, which should take into account not only the installations in the building but also consider its location in relation to the sun, suitable location in terms of noise generation, and the weather conditions occurring at the site. Using only ASHP as the main source of thermal energy is quite risky, since they are powered by electricity, which may run out for various reasons. This applies mainly to smaller towns and locations far from extensive power grids. It is therefore advisable to use an alternative source of heat energy that will be able to maintain the temperature of the building in cases of power failure and depletion of the water buffer. The selection of a suitable bivalent point is also very important from an economic point of view, as well as the weather conditions in which the outdoor unit is to operate. In the case of locations where we have to deal with humid air (rivers, lakes, ponds in the area), special attention should be paid to the fact of icing of the evaporator. This is important because it is not economically justifiable to de-ice the ASHP frequently when we can use another more efficient heat source, this of course depends on the possibilities and the overall profit and loss calculation for such an approach.

## Part III

# Clean energy







# Introduction

I have a pleasure to present the third part of the e-book for PhD students. It contains materials related to the third school in the subject of '*Clean energy and functional materials*', with a subtitle '**Clean energy**'.

The school was realised in the form of blended learning at IMP PAN in Gdańsk and KEZO in Jabłonna, 21.06-30.06.2023. The presented knowledge is linked with the energy conversion and renewable resources, fluid-solid interaction, complex thermomechanical processes, numerical computational tools based on coupled field mechanics to determine the effective energy conversion of machines and devices, etc.

In the frame of the school the PhD students had also possibilities to visit KEZO that is also shortly presented in the part of the e-book.

I would like to warmly thank the people who co-created this e-book, especially the authors of individual subchapters:

-  Janusz Telega – Chapter 13
-  Artur Andrearczyk & Piotr Klonowicz – Chapter 14
-  Robert Matysko – Chapter 15
-  Alicja Krella – Chapter 16
-  Paulina Rolka & Marcin Lackowski – Chapter 17
-  Patryk Chaja – Chapter 18

Magdalena Mieloszyk, DSc PhD Eng., assoc. prof. IMP PAN  
Director of the Tricity Doctoral School,  
Polish Academy of Sciences

## Chapter 12

# The third School information & statistics

The first school was realised in the blended learning form, in days 21.06.2023 – 30.06.2023.

Hour	Online			Weekend	Hour	at IMP PAN, Gdańsk			at KEZO, Jabłonna				
	Day 1	Day 2	Day 3			Day 4	Day 5	Day 6	Day 7	Day 8			
08:00	08:15	W		Travel to Gdańsk	08:00	09:00	R						
08:15	09:00	L1	L9		L17	09:00	09:45	L1	L11		L21	L31	
09:00	09:45	L2	L10		L18	09:45	10:30	L2	L12		L22	L32	
09:45	10:00	CB	CB		CB	10:30	10:45	CB	CB		CB	CB	
10:00	10:45	L3	L11		L19	10:45	11:30	L3	L13		L23	L33	
10:45	11:30	L4	L12		L20	11:30	12:15	L4	L14		L24	L34	
11:30	11:45	CB	CB		CB	12:15	13:45	LB	LB		LB	LB	
11:45	12:30	L5	L13		L21	13:45	14:30	L5		L15	L25	L35	
12:30	13:15	L6	L14		L22	14:30	15:15	L6		L16	L26	L36	
13:15	14:00	LB	LB		LB	15:15	15:30	CB		CB	CB	CB	
14:00	14:45	L7	L15		L23	15:30	16:15	L7		L17	L27	L37	
14:45	15:30	L8	L16		L24	16:15	17:00	L8		L18	L28	L38	
15:30	15:45		CB		C	17:00	17:15	CB		CB	CB	C	
15:45	18:45		LaP			17:15	18:00	L9		L19	L29		
						18:00	18:45	L10		L20	L30		

W – welcome, C – closing, R – registration, CB – coffee break, LB – lunch break, L – lecture, LaP – lecture about Poland, GT – Gdańsk guided walking tour

The school included lectures:

- ① online
  - 🏠 3 days at own place
  - 📎 24 hours of substantial lessons
  - 📎 3 hours of Polish culture and history
- ② onsite
  - 📍 2 days at IMP PAN, Gdańsk
  - 📍 3 days at KEZO CB Jabłonna, near Warszawa
  - 📎 38 hours of substantial lessons (including laboratory shows)
  - 📎 4 hours of Gdańsk guided walking tour

The lectures were given by lecturers from:

- ✓ 1 person from Bulgaria
- ✓ 1 person from The Netherlands
- ✓ 1 person from Spain
- ✓ 4 persons out of IMP PAN (Kraków, Łódź, Olsztyn, Wrocław)
- ✓ 15 persons from IMP PAN

## Lecturers:

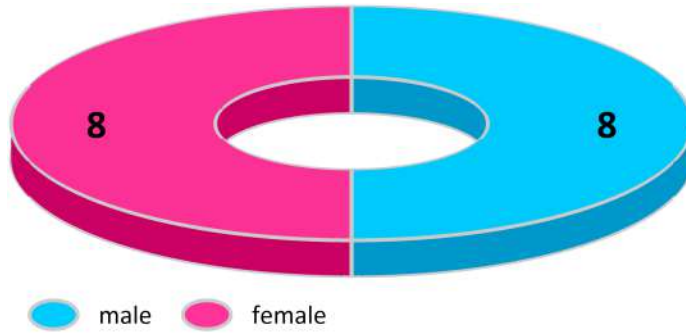
- ◆ prof. ILIYA ILIEV  
University of Ruse, Bulgaria
- ◆ dr inż. ABDALRAHEEM IJJEH  
University of Seville, Spain
- ◆ dr inż. ARTUR POZARLIK  
University of Twente, The Netherlands
- ◆ prof. dr hab. inż. KRZYSZTOF JESIONEK  
Wrocław University of Science and Technology, Poland
- ◆ dr hab. inż. WALDEMAR DUDDA  
Warmia-Masurian University, Olsztyn, Poland
- ◆ dr hab. inż. PAWEŁ MADEJSKI  
AGH University of Science and Technology in Kraków, Poland
- ◆ dr inż. KIRILL KABALYK  
Łódź University of Technology, Poland
- ◆ prof. dr hab. inż. JANUSZ BADUR  
Institute of Fluid-Flow Machinery Polish Academy of Sciences, Poland
- ◆ dr hab. inż. MARIUSZ BANASZKIEWICZ  
Institute of Fluid-Flow Machinery Polish Academy of Sciences, Poland  
General Electric Power, Poland
- ◆ dr hab. inż. TOMASZ OCHRYMIUK  
Institute of Fluid-Flow Machinery Polish Academy of Sciences, Poland
- ◆ dr hab. inż. JANUSZ STELLER  
Institute of Fluid-Flow Machinery Polish Academy of Sciences, Poland
- ◆ dr hab. inż. RYSZARD SZWABA  
Institute of Fluid-Flow Machinery Polish Academy of Sciences, Poland
- ◆ dr hab. inż. JORG VERSTRAETE  
Institute of Fluid-Flow Machinery Polish Academy of Sciences, Poland
- ◆ dr inż. JACEK BISKUPSKI  
Institute of Fluid-Flow Machinery Polish Academy of Sciences, Poland
- ◆ dr inż. ŁUKASZ BREŃKACZ  
Institute of Fluid-Flow Machinery Polish Academy of Sciences, Poland
- ◆ dr inż. PATRYK CHAJA  
Institute of Fluid-Flow Machinery Polish Academy of Sciences, Poland
- ◆ dr inż. ZBIGNIEW KRZEMIANOWSKI  
Institute of Fluid-Flow Machinery Polish Academy of Sciences, Poland

- ❖ dr inż. KSAWERY KULIGOWSKI  
Institute of Fluid-Flow Machinery Polish Academy of Sciences, Poland
- ❖ dr inż. TOMASZ PRZYBYLIŃSKI  
Institute of Fluid-Flow Machinery Polish Academy of Sciences, Poland
- ❖ dr inż. WERONIKA RADZISZEWSKA  
Institute of Fluid-Flow Machinery Polish Academy of Sciences, Poland
- ❖ dr inż. JANUSZ TELEGA  
Institute of Fluid-Flow Machinery Polish Academy of Sciences, Poland
- ❖ mgr inż. PAWEŁ ZAWADZKI  
Institute of Fluid-Flow Machinery Polish Academy of Sciences, Poland

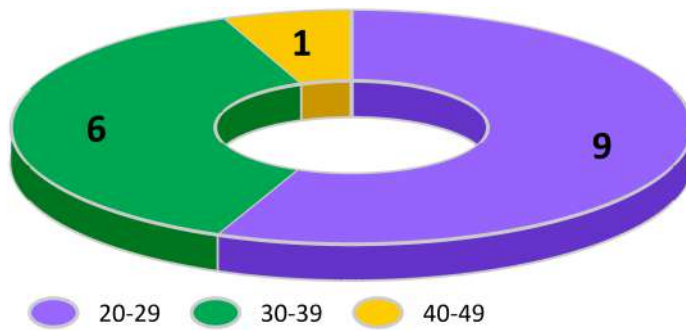


The PhD students, who took a part in the school, at the recruitment stage, filled out an application forms. In the third school edition 16 persons were participating. Based on their submitted application forms, the following statistical data was obtained:

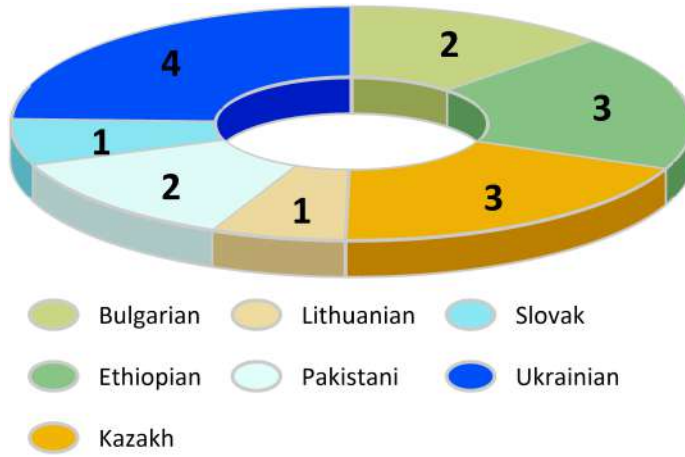
☆ PhD students' gender



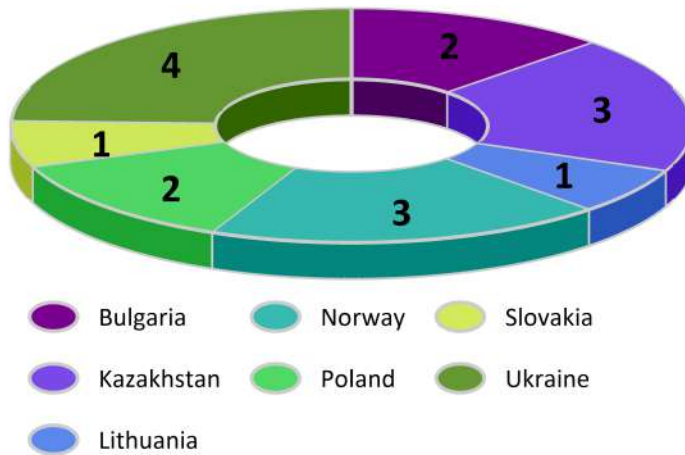
☆ PhD students' age



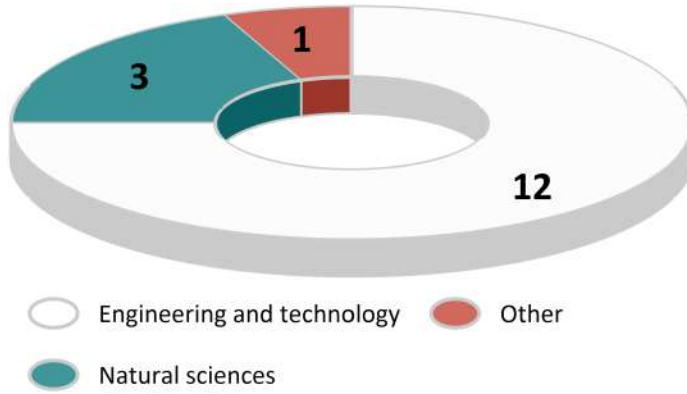
## ☆ PhD students' citizenship



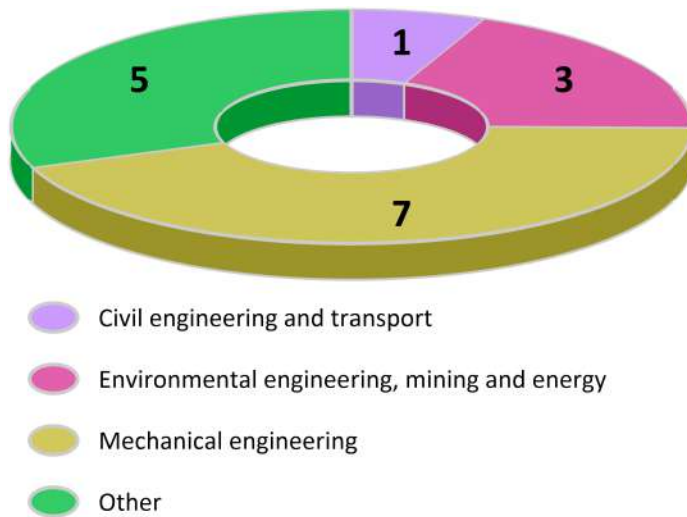
## ☆ PhD students' education country



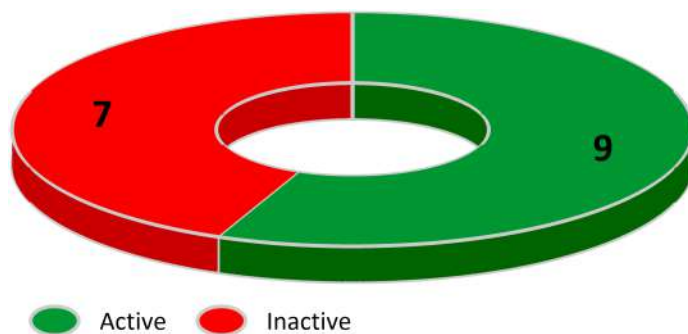
## ☆ PhD students' field of PhD thesis



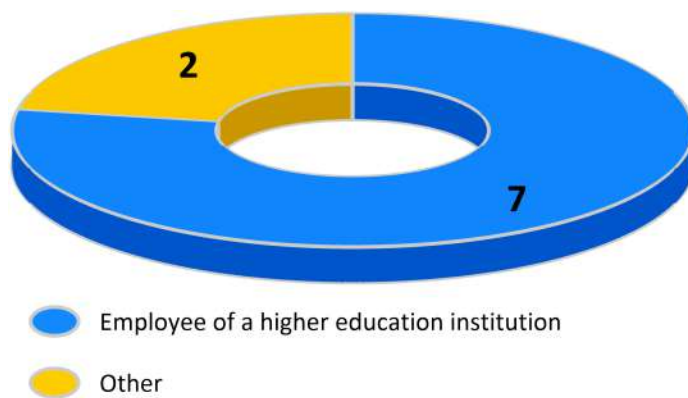
## ☆ PhD students' discipline of PhD thesis



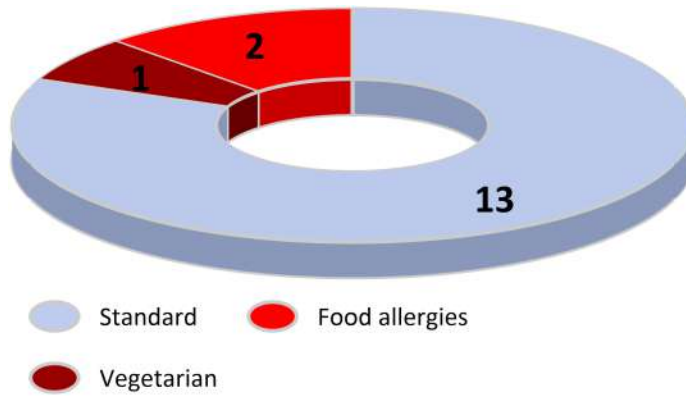
☆ PhD students' status on the labour market



☆ active PhD students' profession



## ☆ PhD students' diet



*Katarzyna Majewska*

## Chapter 13

# A basic supersonic nozzle flow experiment in IMP PAN wind tunnel

The wind tunnel is a device that is an experimental system allowing one to do measurements in 'flow conditions' inside a laboratory. It consists of an actual tunnel and a gas propelling system to generate the flow. The tunnel is usually cylindrical in shape and the propelling system is based on fans or on pressurised or vacuumized tanks. The present form of it is a result of experiments dating back to the mid eighteenth century. It originates from the work of Benjamin Robins (1707 - 1751). He carried out an extensive series of experiments in gunnery, leading him to publish his revolutionary treatise on 'New Principles of Gunnery' in 1742 . The results that he used were obtained using a ballistic pendulum, an apparatus of his invention, that is depicted in Fig. 13.1.



Fig. 13.1: Robins ballistic pendulum.

source: Copied from [https://books.google.pl/books?id=3j8FAAAAMAAJ&printsec=frontcover&client=firefox-a&redir\\_esc=y&hl=pl#v=onepage&q&f=false](https://books.google.pl/books?id=3j8FAAAAMAAJ&printsec=frontcover&client=firefox-a&redir_esc=y&hl=pl#v=onepage&q&f=false)

This is the first time when a device for measuring the influence of the flow on an object has been designed and used in a controlled, scientific manner. It can be called the first ancestor of the modern wind tunnel. There was no real tunnel, the model was travelling through the air to hit the plate of the pendulum. Yet the plate was measuring the overall influence of the travel through gas on the object of interest. It is basically what modern wind tunnels do. There were some disadvantages, like the size of the 'laboratory' whose length was approximately the range of effective rifle shot and the influence of the weather conditions, but the idea has arisen. The one to solve most of the problems of the ballistic pendulum was the inventor of it, Benjamin Robins himself. Four years after his experiments with

the ballistic pendulum, in 1746, feeling a strong need to have more control over the experiments being carried, he designed a device for the task. He invented the whirling arm apparatus in which a weight rotated a drum that carried the test object on an arm of 1.25 m. This design was followed by many aviators, including Maxim, who built his version (depicted in Fig. 13.2) with a propelling motor for his experiments on flight.

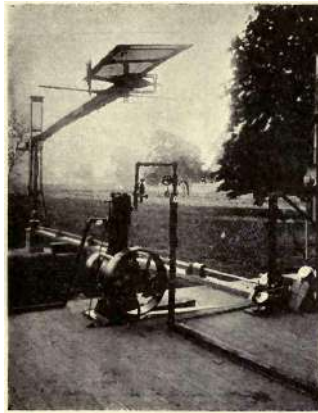


Fig. 13.2: Whirling arm of Maxim.

source: Copied from [http://econterms.net/aero/images/1909\\_-\\_Maxim\\_-\\_arm\\_ready\\_to\\_whirl.png](http://econterms.net/aero/images/1909_-_Maxim_-_arm_ready_to_whirl.png)

The progress was obvious. There was control over the flow velocity, the setup was possible to be installed inside a building, and there was no influence of weather on the test conditions. Still, there were some problems resulting from the rotational movement induced by this setup. The one to emphasise them was Karl Wilhelm Otto Lilienthal (1848 - 1896), the German aviator. He gave an essential contribution for the invention of the wind tunnel as we know and use it today. It was his great contribution, that after doing the measurements using a whirling arm, he made measurements of the forces on stationary aerofoils in the wind over open ground. Because the whirling arm created a swirling motion in the air around it, he had serious doubts about the validity of the data. He stated that his measurements in the natural wind are the more reliable ones. He was aware of the disadvantages of using the whirling arm



apparatus, with the model crossing its own wake and the presence of centrifugal forces in the system. He has led science to the position when it was ready for the invention of wind tunnel. Francis Herbert Wenham (1824 - 1908) was a British marine engineer who studied the problem of human flight. Being a charter member of the Aeronautical Society of Great Britain, he convinced the organisation to raise the funds needed to build a wind tunnel, which was constructed in 1871. It was located at Penn's Marine Engineering Works at Greenwich, England. The tunnel was 12 feet (3.7 m) long and in cross section it was a square of 18 inches edge length (45.7 cm). A steam-powered fan drove the air through a duct to the test section where the model was mounted. The air could travel at a maximum velocity of 40 miles per hour (64.4 km/h). Crude by today's standards, Wenham's wind tunnel set the standards for all aerodynamic research for well over a century. He has invented the tool that is still (over a century later) the essential one for any experimental aerodynamics work.

Nowadays there are two topologies of wind tunnels that are being used. The open (Eiffel – type) and closed return (Prandtl – type). The scheme of open – type is given in Fig. 13.3.

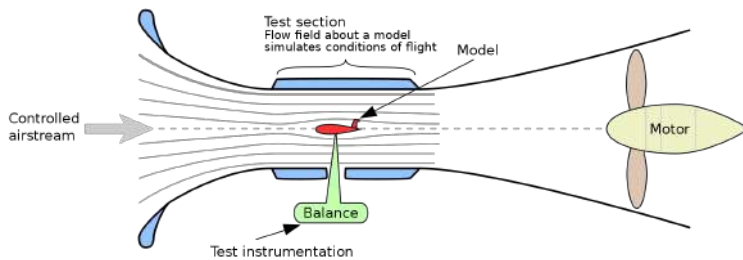


Fig. 13.3: Open return wing tunnel.

source: Copied from [https://en.wikipedia.org/wiki/Subsonic\\_and\\_transonic\\_wind\\_tunnel#/media/File:Windtunnellen.svg](https://en.wikipedia.org/wiki/Subsonic_and_transonic_wind_tunnel#/media/File:Windtunnellen.svg)

The closed return type is given in Fig. 13.4.

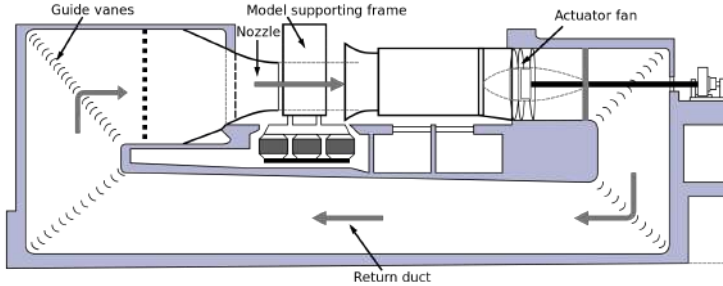


Fig. 13.4: Closed return wing tunnel.

source: Copied from [https://en.wikipedia.org/wiki/Subsonic\\_and\\_transonic\\_wind\\_tunnel#/media/File:Windtunnel3en.svg](https://en.wikipedia.org/wiki/Subsonic_and_transonic_wind_tunnel#/media/File:Windtunnel3en.svg)

Each type has its own advantages and disadvantages, but they serve the very same goal and the general approach on conducting the measurements is similar.

A complete instruction on preparing the tunnel and running an experiment in the IMP PAN supersonic wind tunnel in Gdańsk, Poland will be given hereafter. The scheme of the facility is in Fig. 13.5.

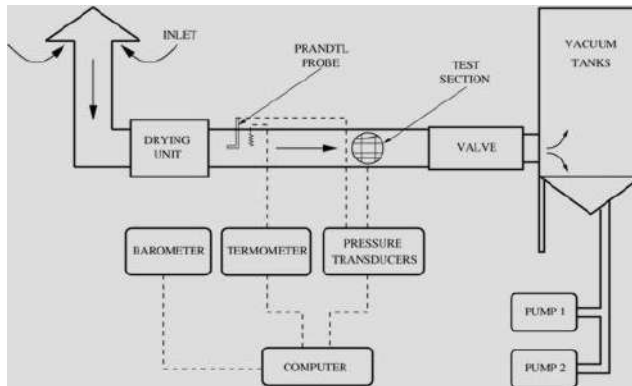


Fig. 13.5: Scheme of IMP PAN wind tunnel.

It is an open return type (Eiffel – type) facility. The flow is propelled by equalizing pressure difference between the tunnel sides and the test section is a part of the duct. The working regime is

intermittent. The time of steady supersonic flow is approximately 20 seconds; it is triggered by opening the main valve that allows the pressure difference to drive the flow. Once the vacuum tanks return to sufficiently high pressure, the flow is to be stopped by closing the main valve. To do every consecutive run, it is necessary to wait 15 minutes. It is the period of pumps evacuating the air from vacuum tanks.

As the initial step of conducting the experiment on supersonic internal flow, one should get familiar with the wind tunnel. Understanding the functions of the components and the principle of operation of the wind tunnel is crucial before conducting any experiments. It is important to do the research prior to entering the laboratory. The main elements of the tunnel are:

- Inlet and air drying unit is depicted in Fig. 13.6.



Fig. 13.6: Inlet with drying unit.

The inlet is an opening to the ambient that is attached on the container containing a deposit of a silica gel. The opening is equipped with a sliding bolt that is equipped with an actuator and end switches. The deposit of silica is used for evacuating the humid-

ity from the air thus securing constant conditions of measurement. It is equipped with a system for drying the gel approximately every 200 blows that consists of three 51 kW electric heaters and auxiliary fan for distributing the hot air inside the deposit. Due to the size and possible working temperature this element is built of steel and for safety reasons it is located outside the building.

- The Prandtl probe is located in the tunnel duct, see Fig. 13.7.



Fig. 13.7: Prandtl probe.

It is a classic Prandtl probe that is placed in the axis of the tunnel duct inside the laboratory room, just prior to the test section. It measures the actual stagnation pressure of the flow entering the nozzle. It is not affected by the stagnation pressure losses due to the flow across the drying unit and the tunnel duct; it is the correct value to be used when calculating Mach number of the flow inside the test section.

- Barometer is depicted in Fig. 13.8.



Fig. 13.8: Barometer.

It is a high precision DRUCK DPI 141 resonant barometer, whose reading gives a very precise view of ambient conditions. It is a value that should be noted along any measurements done on the wind tunnel for future reference.

- Thermometer is depicted in Fig. 13.9.



Fig. 13.9: Thermometer.

The temperature is measured with a K-type thermocouple that is placed very close to the Prandtl probe. The voltage signal is being read by a specialised transducer and together with stagnation pressure it defines the nozzle inlet conditions.

- Pressure transducers.

The stagnation pressure and static pressure from taps located on the object are measured using the INITIUM system depicted in Fig. 13.10.



Fig. 13.10: Pressure transducer.

- Computer that runs all the measurement tasks is depicted in Fig. 13.11.



Fig. 13.11: Laboratory computer.

This device is a desktop PC equipped with versatile digital interfaces, AD cards and LabView software for conducting the experiments.

- Test section is depicted in Fig. 13.12.



Fig. 13.12: Test section.

The test section is a part of the tunnel where the measurement actually takes place. It is rectangular in cross section (100 mm x 500 mm) and both sides can be opened for access during assembling the nozzle or model to be tested.

- Valve is depicted in Fig. 13.13.



Fig. 13.13: Valve.

The valve is mounted on the tunnel duct following the test section downstream. It is used to start and stop the flow by opening or closing the connection between the ambient and the vacuum tanks. It is an electrically controlled, pneumatically propelled device. A ca-

ble remote control is supplied for comfortable operation, depicted in Fig. 13.14.



Fig. 13.14: Valve remote control.

- Vacuum tanks are depicted in Fig. 13.15.



Fig. 13.15: Vacuum tanks.

There are two  $60 \text{ m}^3$  vacuum tanks connected in series with a total capacity of  $120 \text{ m}^3$ . When the air is evacuated and the pressure inside them is about 10 mbar, they allow for approximately 20 sec-



onds of stable flow, with Mach number value of 1.5, with nozzle throat size of 100 mm x 100 mm.

- Vacuum pumps are depicted in Fig. 13.16.



Fig. 13.16: Vacuum pumps.

There are two DEMAG rotary type vacuum pumps (KAESER BSV 100 and KAESER CSV 150) connected in parallel that generate the vacuum in tanks. When both of them are used, a flow can be repeated every ten minutes.

Once you are familiar with the general layout of the wind tunnel, you have to get a deep insight into the safety precautions. The tunnel is a large-scale device. Working with it requires complying with safety regulations. There are many sources of possible accidents involved with it. The one using it can be exposed to:

- Pressure difference capable of causing a very serious harm to a human.
- Electrical voltages that seriously exceed safe levels.
- Extremely high temperatures generated by industrial-power electric heaters (51 kW).
- Heavy metal elements, like tunnel doors or nozzle elements, that have some degrees of freedom and if not secured can cause serious damage.
- Excessive noise that accompanies supersonic flow.

- Possible high torques and powers connected with securely tightening the elements inside the tunnel.
- Probably many more that are alike to take place in a multi-disciplinary workshop.

One has to always have the above in mind. The safety of you and other people is an absolute priority. Prioritize safety training and ensure that all users are familiar with emergency procedures and the location of safety equipment, such as fire extinguishers and first-aid kits. Create a safety checklist and go through it before starting any wind tunnel session. To minimize risks, conduct regular inspections and maintenance of the wind tunnel and its components. Look out for signs of wear and tear, loose connections, or any potential hazards. Any issues or concerns should be promptly reported to the appropriate personnel for resolution. Encourage a strong safety culture within the wind tunnel facility, emphasizing the importance of adhering to safety protocols and looking out for each other's well-being.

- If you do not feel well some day, then do not force it to do the measurement. Next day is a great day for doing experiments in a safe manner.
- If you are going to the laboratory, always inform your supervisor (or a colleague) about it.
- If you do not feel comfortable in the laboratory, ask a colleague to accompany you there.
- If you may need help working in the laboratory, do not hesitate to ask your colleague for assistance.
- Prepare yourself for the working environment:
  - Wear appropriate personal protective equipment (PPE), including safety goggles, gloves, and lab coats.
  - Ensure long hair is tied back, and loose clothing or accessories are removed.
  - Never insert fingers or any objects into the moving parts of the wind tunnel.

- Do not hurry. Plan your measurements reasonably. Do not work under pressure. Once the run starts, it is impossible to stop it immediately. Prior to the run all elements have to be in their positions, securely tightened.
- Never leave a tunnel running unattended.
- If you have any doubts concerning safety matters, discuss it with your supervisor prior to starting the tunnel.

Safety is always a top priority; remember to always care for yourself and other people.

The experimental work starts with positioning the nozzle in the test section. The test object is a curved duct, non-symmetric supersonic nozzle. It is machined of aluminium blocks that form the upper and lower wall of it. In most cases each wall consists of more than one piece, sometimes the number is ten or more. It is a good practice to start with putting the nozzle together outside the tunnel, for example on the floor, to check whether all the elements are there. Such a trial assembly is depicted in Fig. 13.17.



Fig. 13.17: Trial assembly of the nozzle.

Once all the elements are there, the installation in the test section should start. Open both sides of the test section to have easy access to all the fixing elements and mounting holes and install all the elements of the nozzle inside the test section. For now do not tighten the screws, just make sure that the elements are safely mounted with a large freedom to move. Check if the position of the nozzle with respect to the tunnel windows is correct. If yes, close one side

of the test section, so as to have a base surface for the elements. Push the inlet element of one of the nozzle walls (choose the one that is more comfortable for you, it can be either top or bottom one) against the close side wall and tighten the screw fixing it to the bottom (or top) wall of the tunnel. This element is the reference one for mounting the whole nozzle. To position the opposite one use a straight edge of sufficient size, as depicted in Fig. 13.18.



Fig. 13.18: Setting the position of the second inlet element using a straight edge.

The correct way is setting the position, pushing the element against the closed side of the tunnel and gently tightening the screw to fix it to the tunnel. Due to the geometry of the tunnel and the element, there is no access to both ends of the screw. To overcome this issue, special screws are used here, allowing to work with both nut and bolt from outside the tunnel, as it is shown in Fig. 13.19.



Fig. 13.19: A one side screw-nut set.

Once the connection is tight, use the straight edge again, as tightening the screws often causes the element to move. If it is the case, one can try to correct the minor displacement in position using a non-metal machinist hammer, as depicted in Fig. 13.20.



Fig. 13.20: Adjusting the position using non-metal tools.

When both elements are aligned and the screws are tightly fixed it is time to install the central elements. To accomplish it, tighten the screws holding the central element of the nozzle walls. While doing it, they should be pushed against the inlet elements and the side wall; the complete setup is shown in Fig. 13.21.



Fig. 13.21: Nozzle fixed in the test section.

The next step is to connect pressure taps tubes to the pressure scanner. It can be done in any order, as the position of each tap can be freely defined in the application that does the pressure measurement. However, it is a rule of the thumb to do it in a way that corresponds to the actual shape of the system. One of good solutions is to use channels of separate modules for the top wall and for the bottom wall. It is essential to include a clear information on the assignment of channels to pressure taps with the measurement results. An image like in Fig. 13.22 is very informative.

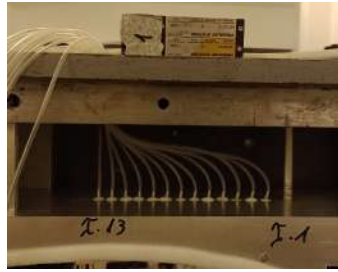


Fig. 13.22: Pressure channels assignment.

Looking at it explains that the top wall is measured by module "T", and the channels are connected consequently and going upstream from channel number "1". The tubes are lead outside the tunnel through holes in the top and bottom wall. After connecting the tubes, these holes (with tubes going through them) have to be sealed using a "Play-Dough" mass; the sealing should be made on both sides of the each hole, like in Fig. 13.23.



Fig. 13.23: Sealing the tubing leading hole with Play-Dough.

The remaining mounting holes that are not used for either screws or tubing have to be closed and sealed. It is done using a plate of PCV placed over the hole with a double-sided adhesive tape and covered with a duck tape from outside, like in Fig. 13.24.



Fig. 13.24: Mounting holes closed and sealed.

Now the tunnel can be closed and sealed with paper tape placed on all the interfaces of the plates, like in Fig. 13.25.



Fig. 13.25: Test section closed and sealed.

To switch on the tunnel, one should turn on the side switch on the control panel and press the 'Otwieranie automatyczne' button. It will cause the inlet to open, which takes about four minutes, and allow for operating the main valve. This state is indicated with the panel looking like in Fig. 13.26.



Fig. 13.26: Control panel in 'Ready-to-work' state.

Now the vacuum pumps can be switched on to evacuate air from vacuum tanks. The pressure in the tanks is displayed in real-time mode on the LED display depicted in Fig. 13.27.

When the pressure, on the display, reaches approximately 10, the system is ready for measurement.



Fig. 13.27: Vacuum tanks pressure and stagnation temperature displays.

The pressure is measured (and archived) using a LabView application with GUI depicted in Fig. 13.28.





Fig. 13.28: Pressure measurement application GUI.

The measured results are saved as text and comma separated values files. Now the tunnel can be started and the measured can be taken. After the experiment is done, one should turn off the vacuum pumps, open the valve allowing the tanks to reach the ambient pressure, close the valve and turn off the control panel.

*all photographs source: own materials*

## Chapter 14

# Introduction to thermal turbines and their applications

## 14.1 Introduction

This chapter is about the principles, design, and applications of thermal turbines, which are devices that transform the energy of a fluid into mechanical work. Thermal turbines are a type of engine that belong to the class of turbomachines, which have the following characteristics:

- they have continuity of parameters, such as flow and work, throughout the process,
- they involve kinetic energy as an intermediate stage of the process
- they contain a rotor (usually with blades) that interacts dynamically with the fluid; the word turbine comes from the Latin word *turbo*, meaning 'that which spins'

Thermal turbines are different from other types of turbines, such as water turbines or wind turbines, because they operate in the range of compressible working fluids, such as air, steam, or hydrogen. This means that the fluid undergoes a significant change in temperature, pressure, and density across the turbine stages. Therefore, thermal turbines require special considerations for thermodynamics, aerodynamics, heat transfer, and structural mechanics.

There are various types of thermal turbines, depending on the working fluid and the application. The most common ones are gas turbines and steam turbines. Gas turbines use air as the working fluid and combust fuel to increase its temperature and pressure. Gas turbines are used in jet engines, gas turbine power plants, and combined cycle power plants. Steam turbines use water as the working fluid and heat it up to produce steam in a boiler. Steam turbines are used in steam power plants, nuclear power plants, and geothermal power plants.

Another type of thermal turbine is the organic Rankine cycle (ORC) turbine, which uses vapors of other working fluids (such as refrigerants, hydrocarbons, siloxanes) instead of water. ORC turbines have the advantage of being able to recover heat from lower-temperature sources, such as industrial waste heat, solar ponds,

geothermal sources, etc. ORC turbines in general have lower operating temperatures and pressures than steam or gas turbines. ORC turbines are also more flexible in terms of design and optimization than steam or gas turbines.

In this chapter, you will learn about the basic components of thermal turbines, such as nozzles, blades, rotors, stators, and casings. You will also learn about the performance parameters of thermal turbines, such as power output, efficiency, pressure ratio, and specific work. You will study the thermodynamic cycles of thermal turbines, such as Brayton cycle for gas turbines and Rankine cycle for steam and ORC turbines. You will also learn about the design methods and optimization techniques for thermal turbines, such as blade geometry, stage loading, flow angle distribution, and blade cooling.

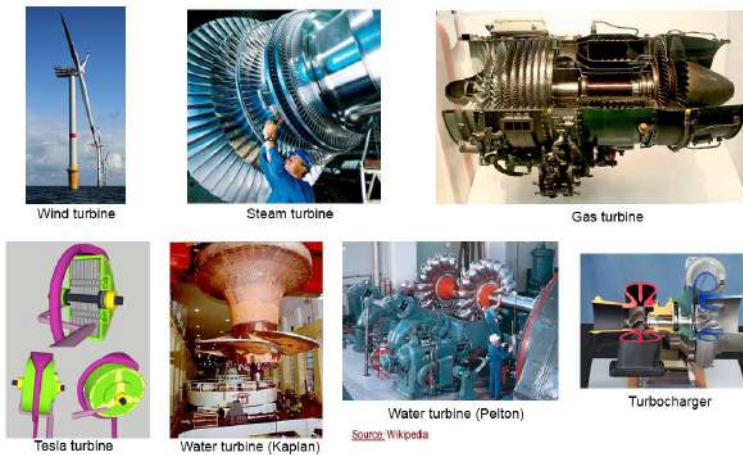


Fig. 14.1: Types of thermal turbines [2].

## 14.2 Turbine cycles – basics

The Brayton cycle and Rankine cycle are foundational thermodynamic processes underlying the operations of gas turbines and steam power plants, respectively. While the Brayton cycle harnesses the properties of gases, especially air, for applications like jet

propulsion, the Rankine cycle capitalizes on phase changes of water to produce electricity in many of the world's power stations. Both have been instrumental in shaping modern industry, transportation, and energy production, serving as testaments to the power of thermodynamic principles in practical applications.

### 14.2.1 Brayton cycle (gas turbine cycle)

The Brayton cycle represents the operation of a gas turbine engine, most commonly used in jet engines and power plants. Basic Brayton cycle diagram is presented in Fig. 14.2(a). The cycle consists of three primary processes: compression, combustion, and expansion.

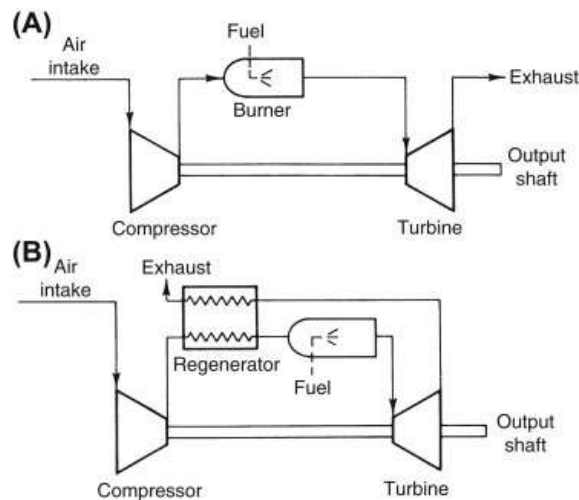


Fig. 14.2: Brayton cycle operational diagram [114]: (a) basic, (b) with recuperation.

**Compression:** Ambient air is drawn into a compressor where its pressure is increased. This results in an increase in the temperature of the air due to the work done on it.

**Combustion:** The high-pressure air enters a combustion chamber, where it's mixed with fuel and ignited. This results in a significant increase in temperature and volume. The pressure may remain almost constant.

Expansion: The high-temperature, high-pressure gas then expands in a turbine, producing work. This work drives the compressor and may also drive other components, like an electrical generator. The temperature and pressure of the gas decrease during this phase. Above mentioned processes are presented in the Fig. 14.3 in two representations.

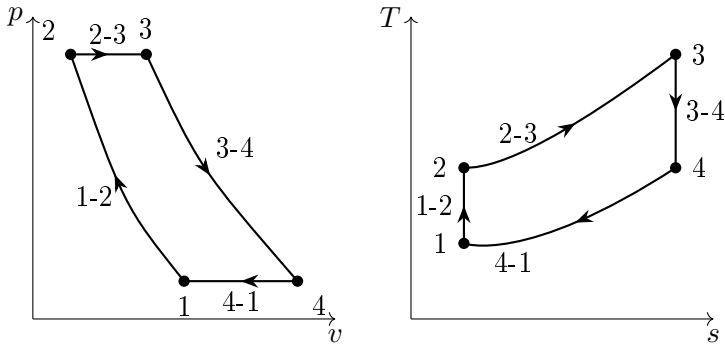


Fig. 14.3: Brayton cycle at pressure-volume (on the left) and temperature-entropy (on the right) diagrams.

Where:

1. **Process 1-2:** Isentropic compression in the compressor. Air is compressed from state 1 to state 2.
2. **Process 2-3:** Constant pressure heat addition in the combustion chamber. Energy is added, and the air expands from state 2 to state 3.
3. **Process 3-4:** Isentropic expansion in the turbine. The high-temperature air from the combustion chamber expands to produce work from state 3 to state 4.
4. **Process 4-1:** The cycle then returns to state 1 to complete the cycle. In an open Brayton cycle, there isn't a traditional 'return' process as fresh air is continuously taken in.

The efficiency of the Brayton cycle under ideal conditions is given by the relation:

$$\eta = 1 - \left( \frac{p_2}{p_1} \right)^{\frac{\gamma - 1}{\gamma}} \quad (14.1)$$

Where:  $\eta$  is the thermal efficiency of the cycle,  $p_1$  is the pressure of the air before compression,  $p_2$  is the pressure of the air after compression,  $\gamma$  is the ratio of specific heats; for air under ideal conditions, this value is typically taken as 1.4.

It's worth noting that in real-world scenarios, there are additional losses and factors that may affect the cycle's efficiency, making it lower than the ideal value. One of the important characteristics of the Brayton cycle is the compression ratio. This pressure ratio ( $\Pi$ ) in the Brayton cycle is the ratio of the compressor discharge pressure to the inlet pressure. It significantly impacts the cycle's efficiency. Generally, an increased pressure ratio elevates the cycle's thermal efficiency, as the temperature difference between the high and low temperatures in the cycle widens. However, there's an optimum range: excessively high pressure ratios can introduce engineering challenges, such as the need for advanced cooling techniques and materials to withstand increased temperatures. Thus, while a higher pressure ratio can boost efficiency, practical considerations can limit its feasible range in real-world applications. The efficiency of the Brayton cycle can be improved by increasing the compression ratio and the maximum temperature in the cycle. In practical systems, intercooling, reheating, and regeneration are techniques employed to improve efficiency.

A Brayton cycle with recuperation (see Fig. 14.2(b)) captures some of the waste heat from the turbine exhaust to preheat the air before it enters the combustion chamber. This increases the thermal efficiency by reducing the fuel required.

Processes with recuperation:

1. air is first compressed in the compressor
2. the compressed air is then preheated in the recuperator using waste heat from the turbine exhaust
3. preheated air enters the combustion chamber where fuel is added and burned

4. the high-temperature gas from the combustion chamber expands in the turbine to produce work
5. the turbine exhaust passes through the recuperator to preheat the incoming air before being expelled

The recuperation process significantly enhances the efficiency of the Brayton cycle by reducing the fuel consumption for a given turbine inlet temperature.

### 14.2.2 Clausius-Rankine cycle (steam turbine cycle)

The Clausius-Rankine cycle is the fundamental thermodynamic cycle for steam power plants. Layout of Rankine cycle diagram is presented in Fig. 14.4.

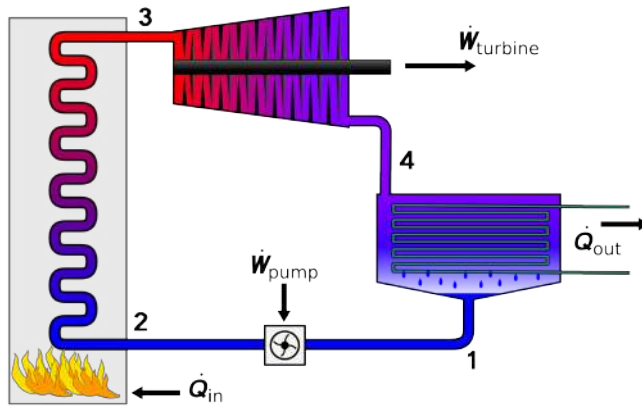


Fig. 14.4: Rankine cycle operational diagram [3].

It involves phase changes of water (from liquid to steam and vice versa) and typically consists of four processes:

**Pumping:** Liquid water (often referred to as feedwater) is pumped from low to high pressure, typically using a feedwater pump. This process requires a relatively small amount of work due to the incompressible nature of the liquid.

**Boiling and Superheating:** The high-pressure liquid enters a boiler where it's heated at constant pressure until it becomes saturated



steam. It can then be further heated to become superheated steam.

**Expansion:** The high-temperature, high-pressure steam expands in a turbine, producing work. The steam loses temperature and pressure in this process, and depending on the design, it might exit as wet steam (with some liquid droplets) or dry/superheated steam.

**Condensation:** The steam passes through a condenser where it is cooled at a nearly constant pressure by a secondary cooling medium (e.g., cooling water) until it condenses back into a liquid state.

The T-s diagram with marked processes is showed in Fig. 14.5.

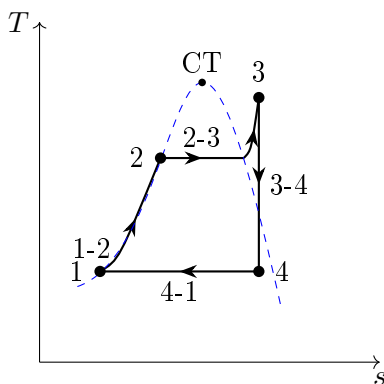


Fig. 14.5: The Clausius-Rankin cycle at temperature-entropy diagram. CT – critical temperature.

Where:

1. **Process 1-2:** Isentropic compression in the pump. Liquid water is compressed from state 1 to state 2.
2. **Process 2-3:** Constant pressure heat addition in the boiler. Water is boiled and converted to steam, going from state 2 to state 3.
3. **Process 3-4:** Isentropic expansion in the turbine. Steam expands, producing work, from state 3 to state 4.
4. **Process 4-1:** Constant pressure heat rejection in the condenser. Steam is condensed back into water, moving from state 4 back to state 1.

The efficiency of the Rankine cycle under ideal conditions is defined by:

$$\eta = 1 - \frac{h_3 - h_4}{h_3 - h_2} \quad (14.2)$$

Where:  $\eta$  is the thermal efficiency of the cycle,  $h_1$ ,  $h_2$  is the specific enthalpy of the fluid at the beginning, and at the end of the isentropic compression, respectively,  $h_3$  is the specific enthalpy at the end of the constant pressure heat addition,  $h_4$  is the specific enthalpy at the end of the isentropic expansion.

Similar to the Brayton cycle, real-world conditions introduce inefficiencies, losses, and thus, the actual efficiency of power plants operating on the Rankine cycle is typically lower than the ideal value.

The efficiency of the Clausius-Rankine cycle can be enhanced by superheating the steam to higher temperatures, increasing the boiler pressure, or by using regenerative feedwater heaters. Variations like the supercritical Rankine cycle are also used for even greater efficiency. These methods in more detail are described below:

**Superheating** – Steam is heated above its boiling point in the boiler to increase its enthalpy and reduce moisture content in the turbine.

**Reheat Cycle** – Steam, after partial expansion in the turbine, is returned to the boiler for reheating.

**Regeneration** – As depicted by the dashed lines, a portion of the steam is extracted from the turbine and used to preheat the water entering the boiler via feedwater heaters.

These modifications aim to bring the Rankine cycle closer to the Carnot cycle, thereby increasing its efficiency.

While both cycles are utilized for power generation, the Brayton cycle primarily uses gas (like air) throughout the process, and the Clausius-Rankine cycle employs a working fluid (like water) that undergoes phase changes. The selection between these cycles for specific applications depends on the available heat source, desired power output, and efficiency requirements.

### 14.3 Turbine stage – basics

A turbine stage is a combination of a stator and a rotor, which are sets of blades that are either stationary or rotating, respectively. The stator blades are used to accelerate the fluid and to give it a significant circumferential velocity component, while the rotor blades are used to extract work from the fluid and to transfer it to the load. The load can be either an electric generator, a compressor or any other device that requires a drive. A turbine stage processes a certain pressure (or enthalpy) drop, which is the difference in fluid pressure (or enthalpy) between the inlet and the outlet of the stage. The enthalpy drop represents the amount of thermal energy that is converted into mechanical work by the turbine stage.

The enthalpy drop that can be processed in one stage is limited by several factors, such as:

- The blade speed limitation: The blade speed (also called the peripheral speed) is the tangential velocity of the blade tip relative to the stationary frame. It depends on the rotational speed of the shaft and the radius of the rotor. The blade speed is limited by the stress and strain that the blade material can withstand due to centrifugal forces and fluid forces. If the blade speed is too high, the blade may break or deform.
- The stage type: The stage type refers to the way that the fluid pressure (or enthalpy) drop is distributed between the stator and the rotor blades. There are three main types of stages: impulse, reaction, and velocity-compound. In an impulse stage, all the pressure drop occurs in the stator blades, and the rotor blades only change the direction of the fluid flow. In a reaction stage, part of the pressure drop occurs in both the stator and the rotor blades, and both sets of blades change both the direction and the magnitude of the fluid velocity. In a velocity-compound stage, a single set of stator blades is followed by two sets of rotor blades with an intermediate set of stationary blades between them. The intermediate blades redirect the fluid flow so that it can enter the second set of rotor blades at an optimal angle.

For very large enthalpy drops (for example, in steam turbines), it is impossible to process all of it in a single stage. Therefore, multistage machines are used, which consist of several turbine stages arranged in series. Each stage processes a fraction of the total enthalpy drop, and the fluid expands gradually as it passes through each stage.

The Fig. 14.6 shows an example of a single-stage axial turbine, which is a type of turbine where the fluid flows parallel to the axis of rotation. The figure illustrates how the stator and rotor blades are positioned with respect to each other. You can also see that both sets of blades have a curved profile, which deflects the fluid flow at an angle. This creates a tangential force on the blades, which causes torque on the shaft.

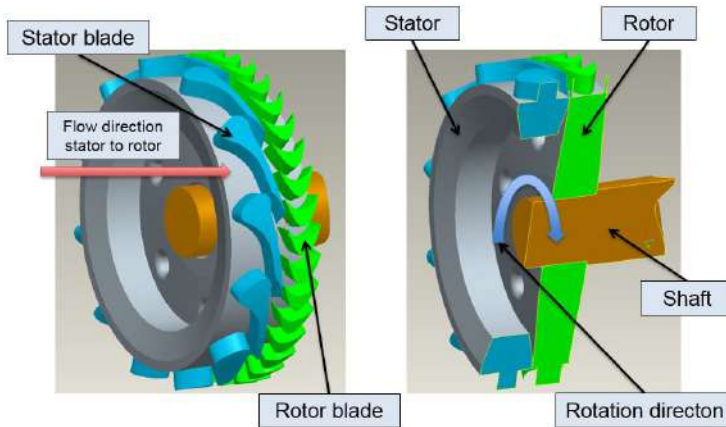


Fig. 14.6: Example of an axial stage of turbine.

A common way to represent a turbine or a turbine stage is to use a section that cuts through the axis of rotation. This is called the 'normal view' or 'normal projection'. In this view, the blades are also sliced by the section plane. However, many sources prefer to show the blades as if they were projected along the circumference, without cutting them (see Fig. 14.7). This type of section is usually called the 'meridional view'.

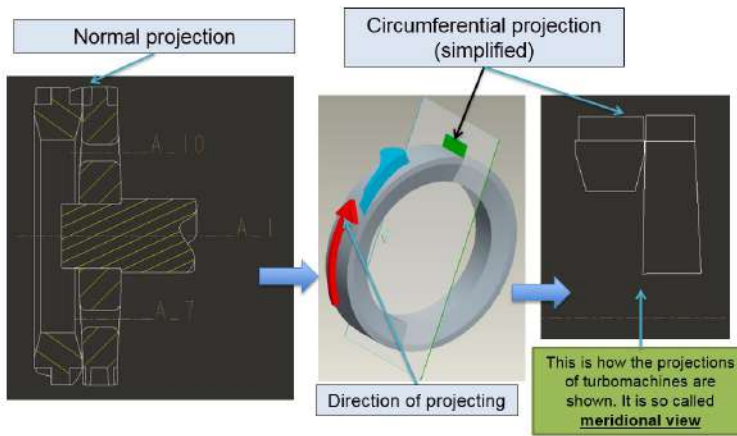


Fig. 14.7: View and projection conventions (section through the axis).

There are different ways to show the blades and the channels between them. But we usually use the 'blade-to-blade view' to show the blade cascade. This is a view that unfolds the blades and shows them in a flat plane (Fig. 14.8). Another figure (Fig. 14.9) shows how the turbines are shown in the literature.

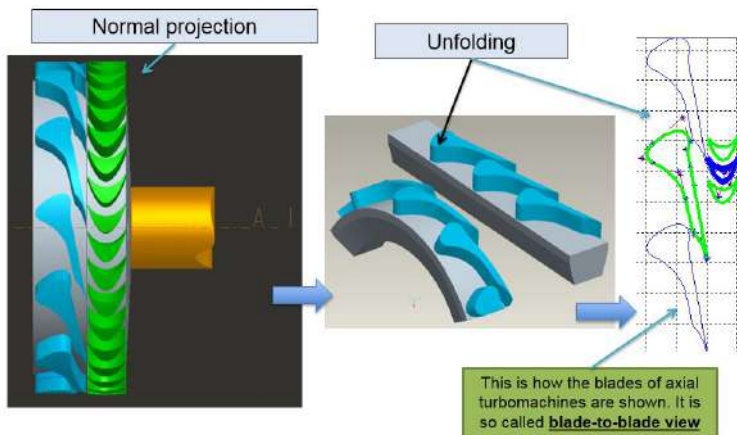


Fig. 14.8: View and projection conventions (view of the blades).

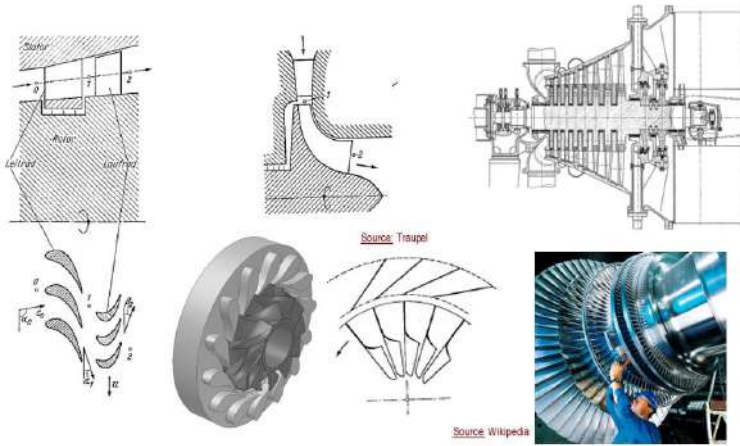


Fig. 14.9: View and projection conventions [2, 112].

## 14.4 Classification of turbines

### 14.4.1 Flow direction

Depending on the characteristics of the fluid and the desired output, different types of turbines can be used. One way to categorize turbines is based on the direction of the main (meridional) flow. We can therefore divide the turbines into:

- axial turbines, where the flow is parallel to the axis of rotation,
- radial turbines, where the flow is perpendicular to the axis of rotation:
  - centrifugal turbines, where the flow moves away from the axis of rotation (also known as radial outflow turbines),
  - centripetal turbines, where the flow moves towards the axis of rotation (also known as cantilever turbines),
- mixed flow turbines, where the flow has both radial and axial components:
  - radial-axial turbines, where the flow enters radially and exits axially (also known as radial inflow turbines or sim-

ply radial turbines - this is a very common type of single stage turbine),

- diagonal turbines, where the flow has an oblique angle to the axis of rotation (this is a rare type of turbine).

Cross section view of turbines types depends on this classification is shown in Fig. 14.10.

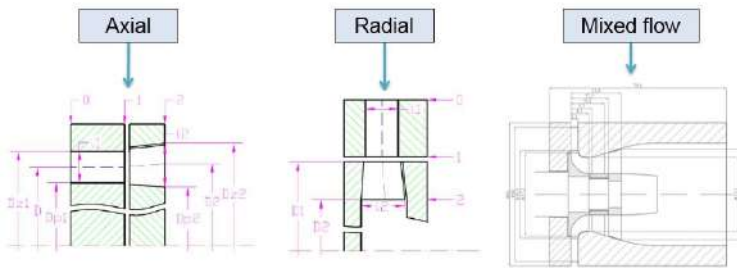


Fig. 14.10: Classification of Turbines by flow direction.

#### 14.4.2 Compressibility

As we have mentioned before, thermal turbines are characterized by significant changes in temperature across the stages, which implies that the working fluid is compressible. Compressibility is a property of a fluid that describes how its density changes with pressure. In general, a fluid is considered compressible when its density change due to pressure is not negligible compared to its density change due to temperature. This usually happens when the fluid velocity or the Mach number (the ratio of the fluid velocity to the speed of sound) exceeds a certain value (for example, 0.2 but this is not a strict value) [4].

Compressible flow (or gas dynamics) is the branch of fluid mechanics that deals with flows having significant changes in fluid density. Compressible flow is relevant to high-speed aircraft, jet engines, rocket motors, high-speed entry into a planetary atmosphere, gas pipelines, and many other fields [98].

The study of compressible flow in thermal turbines is important for

understanding the thermodynamic cycles, the aerodynamic forces, the shock waves, and the losses that occur in these devices. The classification dependent of compressibility is shown in Fig. 14.11.

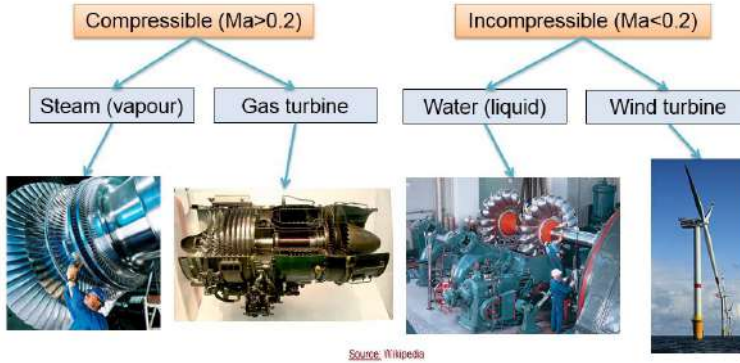


Fig. 14.11: Classification of turbines by working medium or compressibility [2].

### 14.4.3 Number of stages

In general, we can classify the turbines into single stage and multi-stage (Fig. 14.12), depending on the number of rows of blades that the working fluid passes through. Turbocharger turbines are usually single stage, because they operate at high rotational speeds and low pressure ratios, which require a small enthalpy drop per stage. Steam turbines are usually multistage, because they operate at low rotational speeds and high pressure ratios, which require a large enthalpy drop per stage. The reason that the expansion in certain turbines must be divided into stages is following:

- The total enthalpy drop within the turbine is defined by the inlet pressure and temperature, outlet pressure and the fluid properties, such as the specific heat ratio and the gas constant. The enthalpy drop represents the amount of thermal energy that is converted into mechanical work by the turbine.
- The enthalpy drop in a stage is mainly limited by the peripheral speed, which is the tangential velocity of the blade tip



relative to the stationary frame. It depends on the rotational speed of the shaft and the radius of the blade. The peripheral speed is limited by the stress and strain that the blade material can withstand due to centrifugal forces and fluid forces. If the peripheral speed is too high, the blade may break or deform.

- The total enthalpy drop does not have to be divided equally across the stages, but it depends on the design conditions. For example, in a gas turbine, it is desirable to have a higher enthalpy drop in the first stage than in the last stage, because this increases the overall efficiency and reduces the cooling requirements. In a steam turbine, it is desirable to have a lower enthalpy drop in the first stage than in the last stage, because this reduces the moisture content and erosion of the blades.

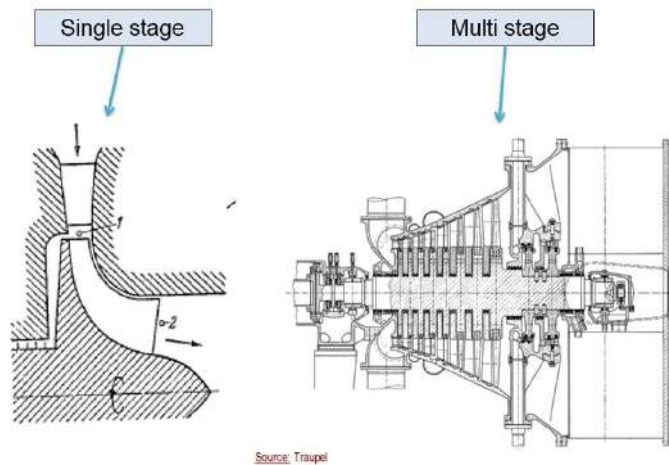


Fig. 14.12: Classification of turbines by number of stages [112].

#### 14.4.4 Steam turbines classification

Steam turbines are essential components in power generation and industrial processes, converting thermal energy from high-pressure steam into mechanical energy through expansion. This mechanical energy is then harnessed to drive electrical generators or other ma-

chinery. In this chapter, we explore three primary types of steam turbines – condensing turbines, back-pressure turbines, and extraction turbines – discussing their operating conditions, applications, and limitations. Their main graphical classification is presented in Fig. 14.13.

Condensing turbines are primarily designed for efficient electricity generation. They expand steam through the turbine and exhaust it into a condenser, where it is condensed back into water and returned to the boiler for reheating and reuse. The condenser operates at very low pressure, creating a significant pressure difference across the turbine and maximizing work extraction from the steam. Condensing turbines are commonly used in large power plants where the main objective is efficient electricity generation. However, their major drawback is the need for a cooling system, such as a cooling tower or water body, to dissipate the heat generated during the condensation process.

Back-pressure turbines, on the other hand, are designed for applications that require both electricity and heat. They expand steam through the turbine and exhaust it at a relatively high pressure for use in other processes, such as heating or industrial applications. The exhaust pressure is determined by the requirements of the downstream process and is generally much higher than the pressure in a condenser. This results in a smaller pressure difference across the turbine, leading to reduced work extraction compared to condensing turbines. Back-pressure turbines are often employed in cogeneration plants, where both electricity and useful heat are produced simultaneously.

Extraction turbines offer a combination of the features of both condensing and back-pressure turbines. They allow for the extraction of steam at one or more intermediate points during the expansion process. The extracted steam can be used for various applications, such as heating or process steam, while the remaining steam continues to expand through the turbine to generate electricity. Extraction turbines provide controlled steam extraction and extraction pressure, making them ideal for situations requiring both electricity and process steam or heat, such as specific industrial plants or district

heating systems.

In conclusion, the choice of steam turbine type depends on the specific requirements of the application, whether it is electricity generation, process steam, or heating. Condensing turbines are optimized for efficient electricity generation, back-pressure turbines are well-suited for cogeneration applications, and extraction turbines offer flexibility in steam extraction for diverse uses. Each type of turbine has its unique operating conditions, applications, and limitations, making them suitable for different scenarios in power generation and industrial processes.

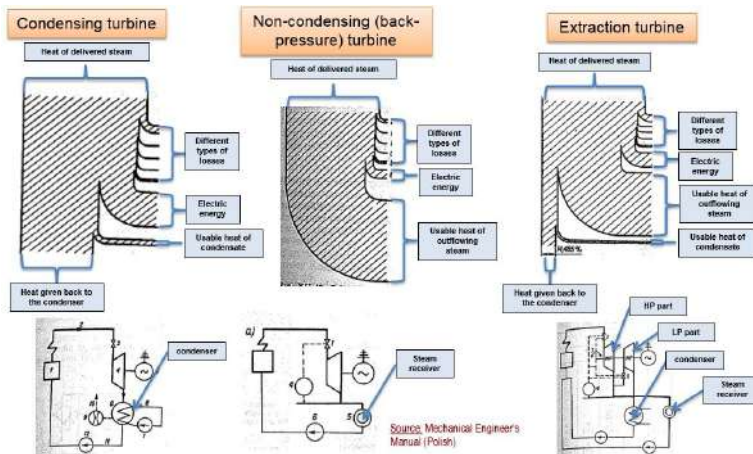


Fig. 14.13: Classification of steam turbines by operational mode [29].

#### 14.4.5 Steam turbine classification based on size

Steam turbines come in various sizes, catering to different power output requirements (Fig. 14.14). In this chapter, we categorize steam turbines into small, middle power, and big turbines based on their power output. It is essential to note that this classification is somewhat blurred and not strictly adhered to, as different factors such as manufacturer specifications, application, or geographical region can influence the categorization.

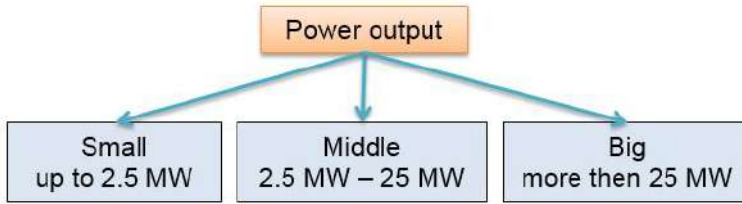


Fig. 14.14: Classification of steam turbines by size.

Small steam turbines, with a power output of up to 2.5 MW, are compact and versatile. They are well-suited for decentralized energy systems, industrial processes, and cogeneration plants, fitting seamlessly into applications with limited space and specific power requirements. Industries such as food processing, chemical, pharmaceutical, and paper manufacturing often employ these turbines to meet their energy needs. Their ability to generate power for small communities or facilities makes them ideal for decentralized energy systems.

Middle power steam turbines, with a power output ranging from 2.5 MW to 50 MW, occupy a larger space compared to small turbines and cater to higher power generation capacities. They find applications in medium-scale power plants and district heating systems, providing both electricity and heat for residential and commercial buildings. Some large industrial facilities with considerable power and steam demands may also utilize middle power turbines to satisfy their energy requirements.

Big steam turbines, with a power output of above 50 MW, are large-scale machines designed to meet high power generation demands. They are primarily used in large power plants, including coal-fired, nuclear, or combined-cycle plants, where they often operate alongside gas turbines. These turbines play a crucial role in supplying electricity to the grid, meeting the energy demands of cities, regions, or even entire countries.

In conclusion, steam turbines' classification based on size and power output is not strictly defined, and the divisions can be blurred. Nev-

ertheless, small, middle power, and big steam turbines each have their unique applications and advantages, making them suitable for different scenarios and requirements in the energy and industrial sectors. Regardless of their size, steam turbines remain a vital component in power generation and industrial processes, offering efficient and versatile solutions for various energy needs.

#### 14.4.6 Other classification methods

Thermal turbines can be categorized into high-speed and low-speed turbines based on their rotational speed. High-speed turbines typically operate at rotational speeds above 3,600 RPM, while low-speed turbines operate below this threshold. High-speed turbines are usually used in smaller applications with limited space, such as industrial processes or decentralized power generation. In contrast, low-speed turbines are preferred for large-scale power generation, as they offer higher power output and efficiency.

Turbines can also be classified as single-shaft or multi-shaft turbines depending on the number of shafts used in their design. Single-shaft turbines have one shaft connecting the turbine and generator, while multi-shaft turbines use multiple shafts, each driving a separate generator. Multi-shaft turbines are ideal for applications requiring higher power outputs or increased operational flexibility, as they can operate independently or simultaneously for better load management and efficiency.

Another classification criterion is the number of casings used in the turbine construction. Turbines can be categorized as single-casing or multi-casing. Single-casing turbines have one casing housing all the turbine stages, while multi-casing turbines use multiple casings, each housing one or more stages. Multi-casing turbines are commonly used in high-pressure, high-temperature applications, where steam or gas conditions can vary significantly across the turbine stages. Separate casings allow each stage to be optimized for specific conditions, enhancing efficiency and performance.

Thermal turbines can also be classified based on whether they use a gearbox. Turbines with a gearbox employ a set of gears to increase

or decrease the generator's rotational speed, optimizing the speed for the specific application. Direct-drive turbines, without a gearbox, connect the turbine shaft directly to the generator. Gearboxes are often utilized in high-speed turbines to reduce the generator speed, making it more suitable for electricity generation. Direct-drive turbines offer simplicity and efficiency but may require larger generators due to higher rotational speeds.

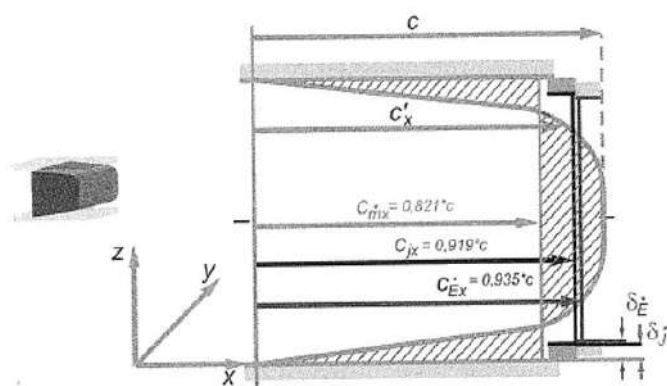
Finally, thermal turbines can be classified based on their application or destination, such as energy, industrial, aircraft, automotive, and others. Energy turbines are used in power plants for electricity generation. Industrial turbines serve various industries, providing process heat, mechanical drives, or cogeneration. Aircraft turbines, used in jet engines, provide thrust for propulsion. Automotive turbines can be found in some vehicles for propulsion or auxiliary power. Each application has specific requirements and constraints that influence the design and operation of the turbines.

In conclusion, thermal turbines can be classified based on various criteria, including speed, number of shafts, casings, whether they use a gearbox, and their specific application or destination. Each classification method has implications for the turbine's design, operation, and usage, making them suitable for different scenarios and requirements. Thermal turbines remain integral components in power generation, industrial processes, transportation, and more, offering efficient and versatile solutions for diverse energy needs.

## 14.5 Engineering approach to modelling flow in turbines

Real fluid flow in turbines is inherently complex due to the numerous physical phenomena at play, including turbulence, boundary layer effects, heat transfer, and fluid-solid interactions. Engineers working on turbine designs must grapple with these complexities to optimize turbine performance. However, simulating real fluid flow in 3D can be computationally intensive, making it impractical for some design and analysis tasks. Instead, engineers often resort to using simplified flow models, especially in the preliminary design stages, to gain

insights into the fluid dynamics and make informed design decisions. Simplifying a 3D flow model into a 1D model involves reducing the flow's spatial complexity, transforming the velocity and other parameters from distributions across the channel into averaged values. This simplification enables engineers to focus on the overall flow behavior, ignoring the intricate velocity variations that occur within the channel. An example of simplifying a 3D flow model into 1D is shown in Fig. 14.15.



Source: Gundlach (Polish)

Fig. 14.15: Simplifying a 3D flow model into a 1D model [31].

In a real-world 3D flow, the velocity distribution in the channel is not constant. It varies due to factors such as turbulence, boundary layer effects, and geometrical constraints, changing from zero at the walls (due to the no-slip condition) to a maximal value,  $c$ , in the free stream region. Engineers can average the velocity across the channel to determine the velocity of an equivalent 1D stream.

The value of the averaged velocity vector depends on the chosen method of averaging. Common approaches include averaging across the area, mass flow averaging, and momentum averaging. Area averaging considers the flow's cross-sectional area, dividing the sum of all velocity components by the total area. Mass flow averaging calculates the average velocity based on the flow's mass, considering the flow density. Momentum averaging involves the flow's mo-

mentum, accounting for both mass and velocity, and is particularly useful where the flow's momentum significantly impacts the overall system behavior. Apart from the velocity, other parameters such as pressure, temperature, enthalpy, and entropy can also be averaged and assigned to the so-called mean line or 1D stream (Fig. 14.16). These parameters play a vital role in determining the turbine's performance, and simplifying them into a 1D model enables easier analysis and prediction of the turbine's behavior. In conclusion, simplifying a 3D flow model into a 1D model is a common practice in turbine applications, particularly during the preliminary design stages. The process involves averaging various parameters, such as velocity, pressure, temperature, and enthalpy, across the flow channel. Different methods of averaging, including area, mass flow, and momentum averaging, can be employed, each affecting the resulting averaged values. The 1D flow model, represented by the mean line stream, provides a practical approach for analyzing and predicting the turbine's performance.

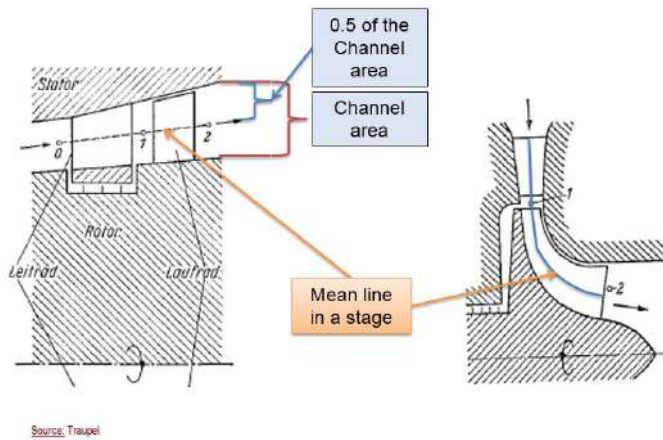


Fig. 14.16: Equivalent 1D mean line in a turbine stage [112].

## 14.6 Principle of operation of a turbine stage

A turbine stage functions by converting the potential energy of a fluid into kinetic energy, which is then transformed into useful



mechanical work. This process involves multiple components, including the stator and rotor, which interact with the fluid to produce the desired energy conversion.

The energy conversion process begins when a high-pressure fluid, such as steam or gas, enters the turbine stage with a substantial amount of potential energy. This potential energy arises from the fluid's pressure and temperature, which have been increased by an external source, such as a boiler or compressor.

As the fluid enters the stator, it undergoes expansion, which leads to an increase in its kinetic energy. The stator's primary function is to accelerate the fluid and introduce a circumferential velocity component, effectively directing the flow onto the rotor at the optimal angle. This acceleration process converts the fluid's potential energy into kinetic energy, which manifests as an increase in velocity.

Once the fluid exits the stator, it encounters the rotor, where the kinetic energy is extracted and transformed into work. In an impulse stage, the rotor blades are driven primarily by the fluid's kinetic energy (see figure 14.17). The fluid impinges on the rotor blades, transferring its momentum and causing the rotor to rotate. As the fluid's velocity decreases, its pressure and temperature drop, leading to a reduction in its kinetic energy.

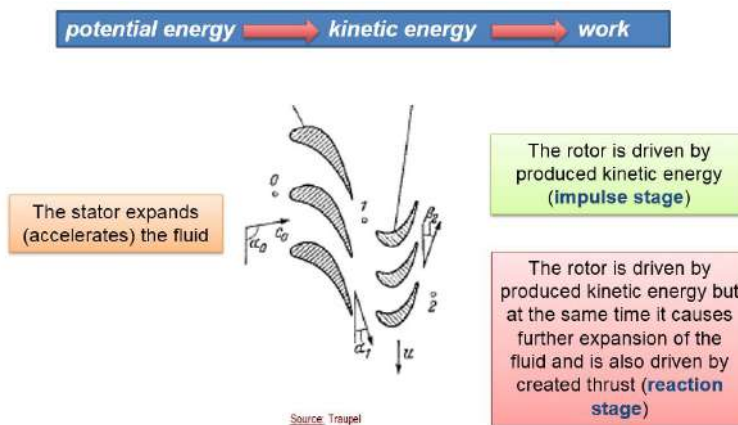


Fig. 14.17: Energy conversion process in thermal turbines [112].

In a reaction stage, the rotor blades not only extract energy from the fluid's kinetic energy but also cause further expansion of the fluid. As the fluid flows through the rotor blades, it continues to expand, leading to a drop in pressure and an increase in velocity. This expansion generates additional thrust, which contributes to driving the rotor. The reaction stage combines the principles of both impulse and reaction to extract energy from the fluid.

During the design and analysis phase of a turbine, engineers often use the  $h$ - $s$  (Mollier) diagram and velocity triangles diagram. The Mollier diagram (Fig. 14.18), also known as the enthalpy-entropy diagram, provides a graphical representation of the fluid's thermodynamic properties, such as enthalpy, entropy, pressure, and temperature. This diagram allows engineers to visualize the energy conversion process within the turbine stage and assess its efficiency.

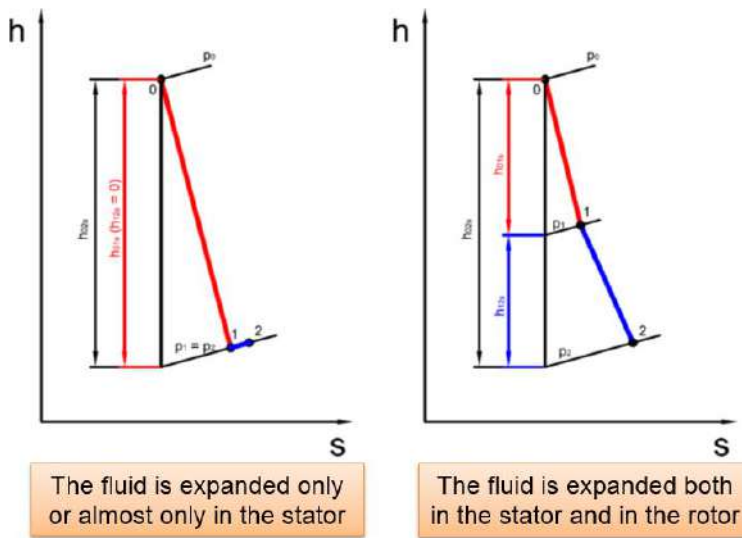


Fig. 14.18: Expansion in impulse and reaction stage on  $h$ - $s$  (Mollier) diagram.

Velocity triangles, on the other hand, offer insights into the fluid's velocity components at the rotor's inlet and outlet. These diagrams help engineers analyze the fluid's behavior as it interacts with the ro-

tor blades, aiding in the design of the rotor's geometry and orientation to maximize energy extraction. Example of these parameters is shown in Fig. 14.19.

In conclusion, a turbine stage operates by converting the potential energy of a fluid into kinetic energy, which is then transformed into mechanical work. The stator accelerates the fluid and introduces a circumferential velocity component, while the rotor extracts energy from the fluid's kinetic energy and further expansion in the reaction stage. During the design and analysis phase, the h-s (Mollier) diagram and velocity triangles diagram provide valuable tools for understanding the fluid's behavior and optimizing the turbine stage's performance.

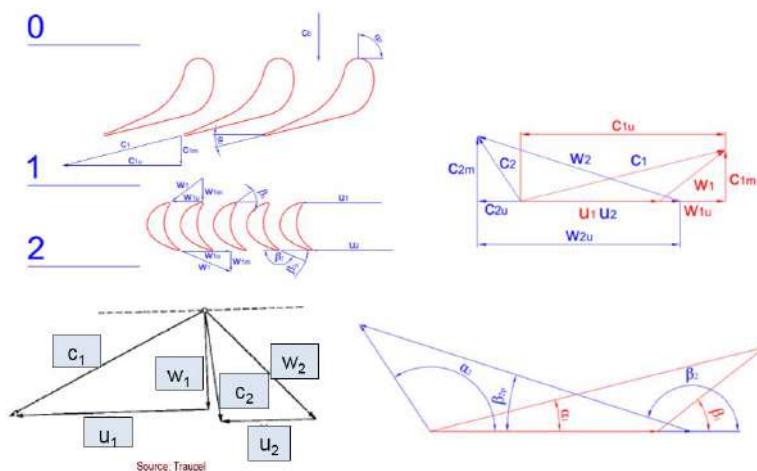


Fig. 14.19: Velocity components and triangles [112].

The Euler equation is a foundational concept in the field of turbomachinery. It describes the energy exchange between a fluid and a rotor and applies to a wide range of turbomachines, including turbines, pumps, and compressors. The equation was formulated by the Swiss mathematician and physicist Leonhard Euler and is essential for analyzing and designing turbomachines. The specific energy exchanged in a rotor (Eq. 14.3), denoted as  $e_u$ , represents the difference in the product of the fluid's circumferential velocity

component and the rotor's tangential velocity at the inlet and outlet of the rotor. This energy exchange is central to the operation of turbomachines.

$$e_u = (c_{1u} \cdot u_1 - c_{2u} \cdot u_2) \quad (14.3)$$

Similarly, the power exchanged in a rotor (Eq. 14.4),  $P_u$ , is the product of the fluid's mass flow rate and the specific energy exchanged in the rotor. For a turbine rotor, this power is the mechanical power produced, whereas, for compressors and pumps, it is the power input required to increase the fluid's pressure or head.

$$P_u = m(c_{1u} \cdot u_1 - c_{2u} \cdot u_2) \quad (14.4)$$

In addition to the basic form of the Euler equation, there is also a kinetic form that is useful for a more detailed analysis of a turbine stage (Eq. 14.5). It is derived from velocity triangles and describes the specific energy exchange in terms of the fluid's absolute and relative velocities and the rotor's tangential velocities at the inlet and outlet of the rotor.

$$e_u = \frac{c_1^2}{2} - \frac{c_2^2}{2} + \frac{u_1^2}{2} - \frac{u_2^2}{2} + \frac{w_2^2}{2} - \frac{w_1^2}{2} \quad (14.5)$$

Furthermore, energy conservation in a turbine stage can be expressed through several equations:

- The total fluid enthalpy at the stage inlet must be equal to the total outlet enthalpy plus the energy given to the rotor

$$h_{e0} = h_{e2} + e_u \quad (14.6)$$

- The breakdown of the total enthalpy into static and dynamic parts

$$h_0 + \frac{c_0^2}{2} = h_2 + \frac{c_2^2}{2} + e_u \quad (14.7)$$

- The energy conservation in the stator

$$h_0 + \frac{c_0^2}{2} = h_1 + \frac{c_1^2}{2} \quad (14.8)$$

- The static enthalpy drop in the stator

$$h_{01} = h_0 - h_1 = \frac{c_1^2}{2} - \frac{c_0^2}{2} \quad (14.9)$$

- Combining equations Eq. 14.7, Eq. 14.8, and the kinetic form of the Euler equation

$$h_1 + \frac{c_1^2}{2} = h_2 + \frac{c_2^2}{2} + \frac{c_1^2}{2} - \frac{c_2^2}{2} + \frac{u_1^2}{2} - \frac{u_2^2}{2} + \frac{w_2^2}{2} - \frac{w_1^2}{2} \quad (14.10)$$

- Rearranging Eq. 14.10 gives the relation for the static enthalpy drop in the rotor.

$$h_{12} = \frac{w_2^2}{2} - \frac{w_1^2}{2} + \frac{u_1^2}{2} - \frac{u_2^2}{2} \quad (14.11)$$

These equations play a key role in the process of designing turbines. They help us determine the main dimensions of each stage, as well as the angles of the blades. This information is then used to create the detailed design of the blade geometry. While a complete guide to the turbine design process is beyond the scope of these introductory notes, those who are interested can find more information in additional literature [24, 32, 38, 88, 112].

## 14.7 Industrial applications of thermal turbines – examples

Thermal turbines, fundamental to the power generation sector, have found their applications in numerous industries due to their ability to convert thermal energy into mechanical energy. This conversion enables driving various processes and operations. The prominence of thermal turbines in modern industry is marked by their efficiency, the diverse energy sources they can employ, and the substantial power they can produce.

### 14.7.1 Power generation

**Coal-fired power plants:** As one of the longstanding methods of electricity generation, coal-fired power plants once held the lion's

share in the power sector [19]. The process involves combusting coal to generate high-pressure steam, which drives a turbine, subsequently producing electricity. Although their contribution to greenhouse gas emissions has led to growing environmental concerns and a shift towards greener alternatives, they have been, for a significant period, the backbone of electricity generation in many countries.

**Combined cycle power plants:** These technologically advanced systems combine the Brayton cycle (high-temperature gas cycle) and the Rankine cycle (steam turbine cycle) to push the boundaries of efficiency. The primary stage involves gas turbines generating electricity. Subsequently, the waste heat generated is harnessed to produce steam, which powers another turbine, resulting in additional electricity generation. This 'combined' approach can reach efficiency levels upwards of 60%, making them a preferable choice for new power plants [46].

### 14.7.2 Co-generation or combined heat and power

Combined heat and power (CHP) systems represent a paradigm shift in how we view energy production. Instead of the traditional approach where electricity and heat are produced separately, CHP systems simultaneously generate electricity and useful thermal energy from a single energy source, markedly reducing energy waste.

**Industrial heating systems:** Industries such as paper mills, chemical plants, and refineries require colossal amounts of heat for their processes [99]. Instead of separate systems for heating and power, industries are turning to CHP. For instance, a paper mill might harness the waste heat from power generation to dry paper, streamlining energy use and significantly reducing operational costs.

### 14.7.3 Waste-to-energy plants

**Municipal waste treatment:** These plants are at the intersection of waste management and energy production [12]. Municipal waste, which would traditionally be destined for landfills, is incinerated. The heat generated is used to produce steam, which powers a turbine, resulting in electricity generation. Such plants not only

help cities manage waste but also produce energy, making them a two-pronged solution to modern urban challenges.

#### 14.7.4 Renewable energy integration

**Solar thermal power plants:** Concentrated solar power (CSP) plants are a shining example of how renewables are leveraging thermal turbines [58]. Mirrors or lenses concentrate sunlight onto a targeted area to produce heat. This heat is then used to generate steam, which drives a thermal turbine, leading to electricity production.

**Geothermal power:** The Earth's natural heat, in the form of steam or hot water, is tapped into to produce electricity [125]. Geothermal power plants extract this steam from the Earth's crust, using it to power thermal turbines.

#### 14.7.5 Conclusion

Thermal turbines' footprint in modern industry is expansive and growing. Their adaptability and efficiency continue to make them a preferred choice across sectors. As industries globally pivot towards sustainability and efficiency, thermal turbines, whether used in traditional settings or integrated with renewable sources, are poised to play an even more pivotal role.

## Chapter 15

# Thermodynamic analysis and optimization of ORC cycle



## 15.1 Introduction

The chapter presents the general equations describing the thermodynamic parameters of thermal cycles. Calculations of an ORC cycle are presented, along with its optimization process with respect to the objective function, which is the exergetic efficiency. The optimization was related to maximizing the objective function. The optimization was conducted to determine the heat exchange surface of the ORC cycle evaporator and the working fluid's vaporization temperature. Energy, entropy, and exergy balance calculations for the proposed technical solution are demonstrated. The calculations are based on the methodology outlined in reference [21, 22, 68].

## 15.2 Energy balance

The general equations describing the cycle according to the first law of thermodynamics can be expressed in a general form:

$$\begin{aligned} \frac{dE}{dt} = & \sum (\dot{m}_{in}h_{in}) + \sum \dot{Q}_{in} + \sum \dot{W}_{in} \\ & - \sum (\dot{m}_{out}h_{out}) - \sum \dot{Q}_{out} - \sum \dot{W}_{out} \end{aligned} \quad (15.1)$$

For a steady state, it can be written as:

$$\begin{aligned} & \sum (\dot{m}_{in}h_{in}) + \sum \dot{Q}_{in} + \sum \dot{W}_{in} = \\ & = \sum (\dot{m}_{out}h_{out}) + \sum \dot{Q}_{out} + \sum \dot{W}_{out} \end{aligned} \quad (15.2)$$

For a steady state, the generalized mass balance equation is:

$$\frac{d\dot{m}}{dt} = \sum \dot{m}_{in} - \sum \dot{m}_{out} \quad (15.3)$$

For steady-state conditions, the generalized mass balance equation takes the form:

$$\sum \dot{m}_{in} = \sum \dot{m}_{out} \quad (15.4)$$

### 15.3 Entropy balance

Below is the generalized equation for entropy balance.

$$\sum \dot{S}_{in} + \dot{S}_{gen} = \sum \dot{S}_{out} + \frac{dS_{sys}}{dt} \quad (15.5)$$

where  $\frac{dS_{sys}}{dt}$  – the change in total entropy of a system over time

$\sum \dot{S}_{out}$  – the total entropy flux leaving the system

$\sum \dot{S}_{in}$  – the total entropy flux entering the system

$\dot{S}_{gen}$  – the generated total entropy flux

Entropy can be transferred through mass or heat fluxes but not through work. The exchange of heat through a wall causes the transport of entropy according to the equation:

$$dQ = TdS \quad (15.6)$$

Since:

$$dS = \frac{dQ}{T} \quad (15.7)$$

It can be written as:

$$S_{1-2} = \int_1^2 \frac{dQ}{T} \quad (15.8)$$

For a closed system where there is no mass transfer across its boundaries, entropy is only transferred through heat exchange. In this case, the entropy balance equation can be expressed as:

$$\sum_{in} \left( \int \frac{d\dot{Q}}{T} \right) + \dot{S}_{gen} = \frac{dS_{sys}}{dt} + \sum_{out} \left( \int \frac{d\dot{Q}}{T} \right) \quad (15.9)$$

When the closed system is adiabatic, meaning there is no mass or heat transfer, the entropy balance simplifies to:

$$\dot{S}_{gen} = \frac{dS_{sys}}{dt} \quad (15.10)$$

When  $dS_{sys} = d(ms)$  and as a result  $\Delta S_{sys} = m_2 s_2 - m_1 s_1$

For an open system (within a control volume, CV), the entropy balance equation can be written as:

$$\begin{aligned} \sum_{in} \left( \int \frac{d\dot{Q}}{T} \right) + \sum_{in} (\dot{m}s) + \dot{S}_{gen} &= \\ = \frac{dS_{CV}}{dt} + \sum_{out} \left( \int \frac{d\dot{Q}}{T} \right) + \sum_{out} (\dot{m}s) & \quad (15.11) \end{aligned}$$

For steady flow in time when the mass enclosed within the control volume and the specific entropy of the same volume are constant (which means  $S_{CV} = m_{CV}s_{CV} = const$ ) the entropy balance can be expressed in the form of a general equation:

$$\sum_{in} \left( \int \frac{d\dot{Q}}{T} \right) + \sum_{in} (\dot{m}s) + \dot{S}_{gen} = \sum_{out} \left( \int \frac{d\dot{Q}}{T} \right) + \sum_{out} (\dot{m}s) \quad (15.12)$$

For example, for a flow with two inlet mass streams, one outlet mass stream, and a heat stream being dissipated from the system Fig.15.1, the above equation can be expressed in a form that allows for the determination of the generated entropy in the form of an equation:

$$\frac{\dot{Q}}{T_{sys}} + \dot{m}_1 s_1 + \dot{m}_2 s_2 + \dot{S}_{gen} = (\dot{m}_1 + \dot{m}_2) s_s + \frac{\dot{Q}}{T_o} \quad (15.13)$$

So the generated entropy of the system is:

$$\dot{S}_{gen} = (\dot{m}_1 + \dot{m}_2) s_s + \frac{\dot{Q}}{T_o} - \frac{\dot{Q}}{T_{sys}} - \dot{m}_1 s_1 - \dot{m}_2 s_2 \quad (15.14)$$

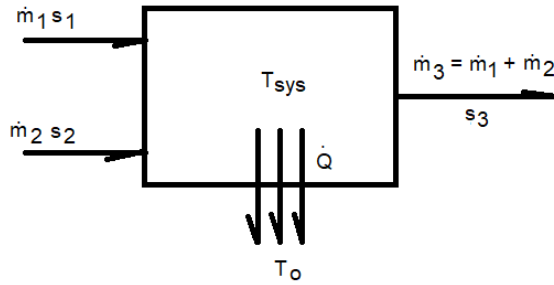


Fig. 15.1: Example of entropy stream flow.

### 15.3.1 Exergy Balance

The exergy balance is related to the second law of thermodynamics. The exergy balance introduces the concept of exergy destruction, which represents the maximum potential work that is impossible to recover due to the irreversibility of processes. The most important relationship is between exergy destruction, entropy generation, and reference temperature, which can be expressed by the equation:

$$Ex_d = T_o \dot{S}_{gen} \quad (15.15)$$

In general, it can also be written that:

$$\sum \dot{Ex}_{in} = \frac{dEx_{sys}}{dt} + \sum \dot{Ex}_{out} + \dot{Ex}_d \quad (15.16)$$

Where

$\sum \dot{Ex}_{in}$  – sum of the total exergy streams entering the system

$\dot{Ex}_d$  – total exergy destruction

$\frac{dEx_{sys}}{dt}$  – change in system exergy over time

$\sum \dot{Ex}_{out}$  – sum of the total exergy streams leaving the system

The equation describing the exergy balance for thermo-flow systems can be written as:

$$\begin{aligned} \sum_{in} \left[ \dot{W} + \dot{m}\varphi + \left(1 - \frac{T_o}{T}\right) \dot{Q} \right] &= \\ &= \frac{dEx}{dt} + \sum_{out} \left[ \dot{W} + \dot{m}\varphi + \left(1 - \frac{T_o}{T}\right) \dot{Q} \right] - P_o \frac{dV_{CV}}{dt} + \dot{Ex}_d \end{aligned} \quad (15.17)$$

Where the total specific exergy is given by:

$$\varphi = \left( (h - h_o) + T_o(s - s_o) + \frac{1}{2}v^2 + g(z - z_o) + ex^{ch} \right) \quad (15.18)$$

For steady-state conditions, the equation can be written as:

$$\begin{aligned} \sum_{in} \left[ \dot{W} + \dot{m}\varphi + \left(1 - \frac{T_o}{T}\right) \dot{Q} \right] &= \\ &= \sum_{out} \left[ \dot{W} + \dot{m}\varphi + \left(1 - \frac{T_o}{T}\right) \dot{Q} \right] + \dot{Ex}_d \end{aligned} \quad (15.19)$$

For individual streams at the inlet and outlet, it can be written as:

$$\dot{Ex}_d = \dot{W}_1 + \dot{m}_1\varphi_1 + \left(1 - \frac{T_o}{T}\right) \dot{Q}_1 - \dot{W}_2 - \dot{m}_2\varphi_2 - \left(1 - \frac{T_o}{T}\right) \dot{Q}_2 \quad (15.20)$$

If we assume  $\dot{Q} = \sum_{in} \dot{Q} - \sum_{out} \dot{Q}$ ,  $\dot{W} = \sum_{out} \dot{W} - \sum_{in} \dot{W}$ ,  $\dot{m} = \dot{m}_1 = \dot{m}_2$  and there is no energy destruction  $\dot{Ex}_d = 0$  the equation describing *reversible* work can be written as:

$$\dot{W}_{rev} = \dot{m}(\varphi_1 - \varphi_2) + \sum \left(1 - \frac{T_o}{T}\right) \dot{Q} \quad (15.21)$$

According to the definition, exergy represents the maximum potential of the system to perform work, so:

$$\dot{Ex}^w = W \quad (15.22)$$

When dealing with work and moving walls (e.g. piston engine)

$$\dot{E}x^w = W - P_o(V - V_o) \quad (15.23)$$

When dealing with mass flow

$$\dot{E}x^m = \dot{m}\varphi \quad (15.24)$$

The exergy associated with heat flow through a partition is related to the equation:

$$\dot{E}x^Q = \int \left(1 - \frac{T_o}{T}\right) dQ \quad (15.25)$$

Where  $T_o$ ,  $p_o$ ,  $z_o, V_o$  are reference values (e.g. initial values of the process – ambient temperature, initial pressure, etc.).

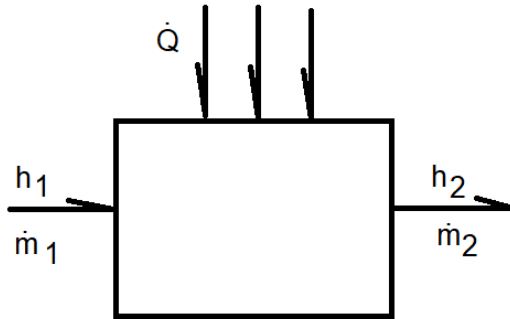


Fig. 15.2: Mass and heat streams supplied to the system.

When analysing exergetic efficiency, two definitions of efficiency are used. Efficiency, similar to the energy balance equation, can be referred to according to the principle of effect-to-input ratio using the equation Fig. 15.2:

$$\eta = \frac{\dot{m}_2 h_2 - \dot{m}_1 h_1}{\dot{Q}} \quad (15.26)$$

Efficiency can also be defined according to the principle of useful output effect (stream) in relation to input effects (streams) Fig. 15.2:

$$\eta = \frac{\dot{m}_2 h_2}{\dot{Q} + \dot{m}_1 h_1} \quad (15.27)$$

In this case, exergetic efficiency can be defined similarly using the relationships presented below:

$$\psi = \frac{\dot{m}_2 ex_2 - \dot{m}_1 ex_1}{\dot{Q} \left(1 - \frac{T_0}{T}\right)} \quad (15.28)$$

or:

$$\psi = \frac{\dot{m}_2 ex_2}{\dot{Q} \left(1 - \frac{T_0}{T}\right) + \dot{m}_1 ex_1} \quad (15.29)$$

Both of these definitions of efficiency based on the first and second laws of thermodynamics [21] are applied in this work.

### 15.3.2 Detailed calculations and optimisation of the ORC cycle

Fig. 15.3 presents the analyzed ORC cycle.

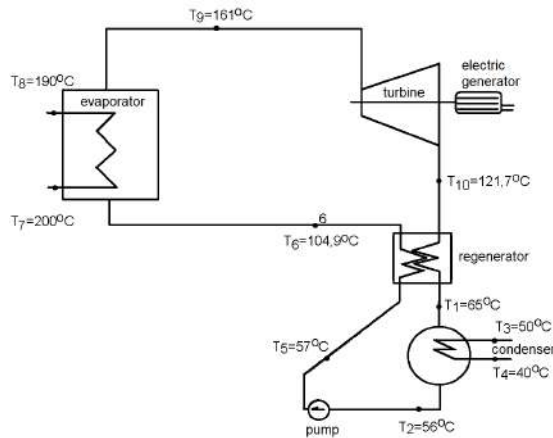


Fig. 15.3: Optimized ORC Cycle.

The analysis of this cycle was carried out in terms of entropy generation within individual power plant components. Fig. 15.3 also depicts the operational parameters adopted for the optimization of the ORC system [22, 68].

In the cogeneration cycle, the heat absorbed by the condenser and the power obtained in the turbine are the final outcomes dependent on the operational parameters present in various subsystems. Below, our proprietary model describing the optimized ORC cycle is presented:

- a) Equations describing the exergy flow at characteristic points of the ORC cycle:

$$\dot{S}_1 = \dot{m}_{hfe} (h_1 - h_{hfe,ot}) - \dot{m}_{hfe} T_{ot} (S_1 - S_{hfe,ot}) \quad (15.30)$$

$$\dot{S}_2 = \dot{m}_{hfe} (h_2 - h_{hfe,ot}) - \dot{m}_{hfe} T_{ot} (S_2 - S_{hfe,ot}) \quad (15.31)$$

$$\dot{S}_3 = \dot{m}_{hfe} (h_3 - h_{hfe,ot}) - \dot{m}_{hfe} T_{ot} (S_3 - S_{hfe,ot}) \quad (15.32)$$

$$\dot{S}_4 = \dot{m}_{woda} (h_4 - h_{woda,ot}) - \dot{m}_{hfe} T_{ot} (S_4 - S_{woda,ot}) \quad (15.33)$$

$$\dot{S}_5 = \dot{m}_{woda} (h_5 - h_{woda,ot}) - \dot{m}_{hfe} T_{ot} (S_5 - S_{woda,ot}) \quad (15.34)$$

$$\dot{S}_6 = \dot{m}_{hfe} (h_6 - h_{hfe,ot}) - \dot{m}_{hfe} T_{ot} (S_6 - S_{hfe,ot}) \quad (15.35)$$

$$\dot{S}_7 = \dot{m}_{hfe} (h_7 - h_{hfe,ot}) - \dot{m}_{hfe} T_{ot} (S_7 - S_{hfe,ot}) \quad (15.36)$$

$$\dot{S}_8 = \dot{m}_{hfe} (h_8 - h_{hfe,ot}) - \dot{m}_{hfe} T_{ot} (S_8 - S_{hfe,ot}) \quad (15.37)$$

$$\dot{S}_9 = \dot{m}_{hfe} (h_9 - h_{hfe,ot}) - \dot{m}_{hfe} T_{ot} (S_9 - S_{hfe,ot}) \quad (15.38)$$

$$\dot{S}_{10} = \dot{m}_{hfe} (h_{10} - h_{hfe,ot}) - \dot{m}_{hfe} T_{ot} (S_{10} - S_{hfe,ot}) \quad (15.39)$$

where:  $\dot{m}_{hfe}$  – the mass flow rate of the HFE7100 working fluid,  $h_{hfe,ot}$  – enthalpy of the HFE7100 working fluid for ambient conditions,  $h_1 \div h_{10}$  – enthalpies for nominal conditions at various points of the thermal cycle,  $T_{ot}$  – ambient temperature,  $s_1 \div s_{10}$  – specific entropy for nominal conditions at various points of the cycle ORC,  $S_{hfe,ot}$  – calculated entropy for ambient conditions.



b) Exergy balance in the ORC cycle:

$$\Delta\dot{S}_{los,skr} = \dot{S}_1 + \dot{S}_4 - \dot{S}_2 - \dot{S}_3 \quad (15.40)$$

$$\Delta\dot{S}_{los,kot} = \dot{S}_7 + \dot{S}_6 - \dot{S}_9 - \dot{S}_8 \quad (15.41)$$

$$\Delta\dot{S}_{los,turb} = \dot{S}_9 - W_{turbina} - \dot{S}_{10} \quad (15.42)$$

$$\Delta\dot{S}_{los,pompa} = W_{pompa} + \dot{S}_2 - \dot{S}_5 \quad (15.43)$$

where:  $\Delta\dot{S}_{los,skr}$  – change in exergy in the condenser,  $\Delta\dot{S}_{los,kot}$  – change in exergy in the boiler,  $\Delta\dot{S}_{los,turb}$  – change in exergy in the turbine,  $\Delta\dot{S}_{los,pompa}$  – change in exergy in the pump,  $W_{pompa}$  – pump work,  $W_{turbina}$  – power generated in the turbine.

c) Heat balances in the ORC cycle:

- condenser

$$\dot{m}_{hfe} (h_1 - h_2) = k_{skr} A_{skr} \frac{(T_1 - T_3) - (T_2 - T_4)}{\ln \frac{(T_1 - T_3)}{(T_2 - T_4)}} \quad (15.44)$$

where:  $k_{skr}$  – heat transfer coefficient in the condenser,  $A_{skr}$  – heat exchange surface area in the condenser,  $T_1 \div T_4$  – temperatures at characteristic points of the ORC cycle.

- pump

$$W_{pompa} = \dot{m}_{hfe} (h_5 - h_2) \quad (15.45)$$

- evaporator

$$\dot{m}_{hfe} (h_9 - h_6) = k_{kot} A_{kot} \frac{(T_7 - T_6) - (T_8 - T_9)}{\ln \frac{(T_7 - T_6)}{(T_8 - T_9)}} \quad (15.46)$$

where:  $k_{kot}$  – heat transfer coefficient in the boiler,  $A_{kot}$  – heat exchange surface area in the boiler,  $T_6 \div T_9$  – temperatures at characteristic points of the ORC cycle.

- turbine

$$W_{turbina} = 0.7 \dot{m}_{hfe} (h_9 - h_{10}) \quad (15.47)$$

d) Equations describing the efficiency of the cogenerative ORC cycle:

- energy efficiency

$$\eta_{en} = \frac{\dot{Q}_{skr} + (W_{turbina} - W_{pompa})}{\dot{Q}_{kot}} \quad (15.48)$$

where:  $\dot{Q}_{skr}$  – heat transfer rate in the condenser,  $\dot{Q}_{kot}$  – heat transfer rate supplied in the boiler.

- exergetic efficiency (objective function)

$$\eta_{egz} = \frac{\dot{S}_7 - \dot{S}_8 - \Delta\dot{S}_{los,skr} - \Delta\dot{S}_{turb} - \Delta\dot{S}_{pompa}}{\dot{S}_7 - \dot{S}_8} \rightarrow max \quad (15.49)$$

During the calculations, it was assumed that the heat transfer rate discharged in the condenser is constant. Values for the condenser temperature rise and its heat exchange surface were also held constant:

$$\dot{Q}_{skr} = const; \quad \Delta T_{log,skr} = const; \quad A_{skr} = const$$

Heat transfer coefficients were assumed to be the same for boiling and condensation in the ORC cycle.

$$k_{skr} = 400 \frac{W}{m^2 K} \quad i \quad k_{kot} = 400 \frac{W}{m^2 K}$$

Boiling temperature and evaporator surface area were selected as state variables. The range of variation for these parameters was defined within the following range:

$$1m^2 \leq A_{par} \leq 10m^2 \quad (15.50)$$

$$150^\circ C \leq T_{par} \leq 180^\circ C \quad (15.51)$$

Fig. 15.4 and Fig. 15.5 depict the calculated energy and exergetic efficiency of the ORC system as a function of the selected state variables.

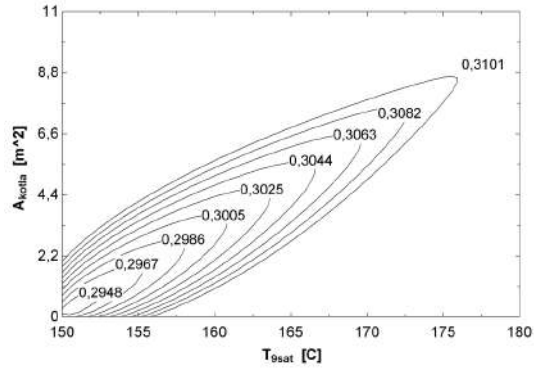


Fig. 15.4: Exergetic efficiency contours of the ORC system as a function of the evaporator heat exchange surface area and boiling process temperature.

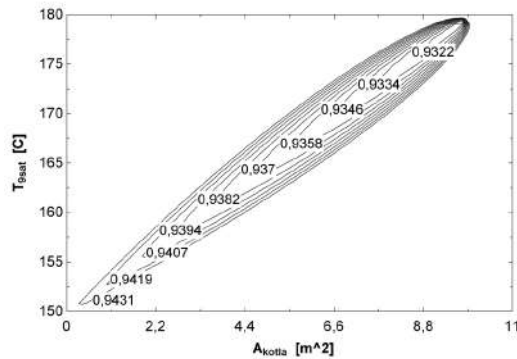


Fig. 15.5: Energy efficiency contours of the ORC system as a function of the evaporator heat exchange surface area and boiling process temperature.

Fig. 15.6 to Fig. 15.10 illustrate the results of calculations for the optimized ORC power plant parameters. Fig. 15.6 presents the profile of the average boiler logarithmic temperature difference as a function of the boiler surface area.

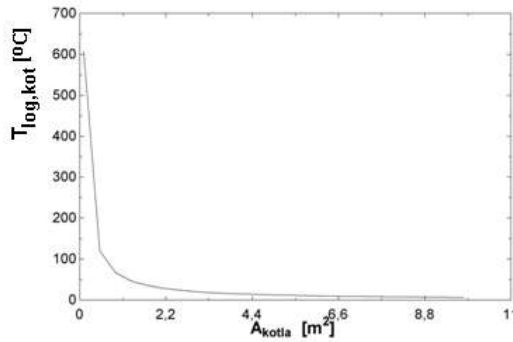


Fig. 15.6: Increase in the average logarithmic temperature difference in the evaporator of the ORC cycle as a function of the evaporator surface area.

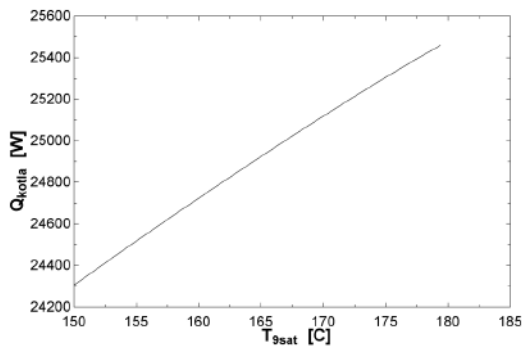


Fig. 15.7: Change in the heat transfer rate supplied to the ORC cycle as a function of the boiling temperature.

Fig. 15.7 illustrates the change in the heat transfer rate supplied to the ORC cycle as a function of the boiling temperature. It is evident that the higher the boiling temperature, the greater the heat transfer rate delivered to the vaporization process in the system.

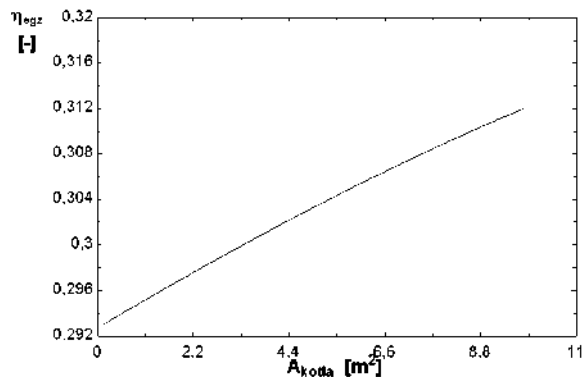


Fig. 15.8: Exergetic efficiency as a function of the evaporator surface area in the ORC cycle.

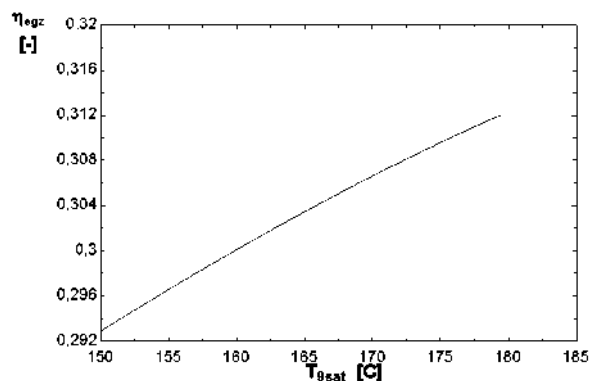


Fig. 15.9: Exergetic efficiency of the evaporator as a function of the boiling temperature in the ORC cycle.

The exergetic efficiency plot of the ORC cycle as a function of the boiler surface area is shown in Fig. 15.8. A larger boiler surface area enables the transfer of a greater heat flow, contributing to an increase in exergetic efficiency. Exergetic efficiency also rises for higher boiling temperatures (Fig. 15.9). An increase in the boiling temperature leads to an elevation in the power generated by the ORC turbine (Fig. 15.10).

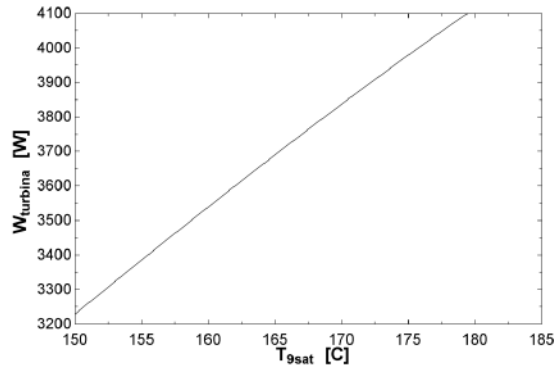


Fig. 15.10: Turbine power as a function of boiling temperature.

The presented calculation results concern the issues of designing an ORC cycle considering exergetic losses. Correctly solved design problems for an ORC power plant are of great importance for its subsequent operation. Therefore, it is valuable to use the definition of exergetic efficiency as it allows for selecting optimal operating parameters that reduce the overall operating cost of the entire co-generative ORC power plant cycle.

## 15.4 Summary

In thermodynamic systems, several global optimization objectives are commonly used for both steady-state and transient processes, all of which hold significant importance for technological operations. These optimization objectives include:

- A. For steady-state process optimization:
  - Installation dimensions – seeking a minimum. To minimize material costs, efforts are made to reduce the dimensions of the installation.
  - Thermodynamic efficiency, exergetic efficiency – seeking a maximum. Optimal thermodynamic parameters are selected for the entire system or its key components to achieve the highest possible efficiency within given constraints. Efficiency often

depends on minimizing entropy generation in the thermodynamic system.

- Heat flows – seeking a maximum. Many processes in installations require specific heat flows. The maximum heat flow is often sought in systems where size reduction is necessary, such as micro-ORC systems.
  - Economic expenses – seeking a minimum. Installations operated at high process costs lack economic justification due to excessively long payback periods.
- B. For transient process parameter optimization, the most important criteria include:
- Controller settings for closed-loop control systems (e.g., time constants, proportional, derivative, and integral gains in a PID controller). Controller settings are tuned to minimize control error and minimize the rise time of the system's response to a unit step change.
  - Minimum inertia for open-loop control systems. In open-loop systems, inertia determines the rise time of the system's response to specified parameters. This aims to achieve appropriate extrema for parameters like specific weight, specific heat, and installation volume, which influence the system's overall inertia.

During the optimization of an ORC cycle, the objective function was the maximum exergetic efficiency, with the design parameters being the geometric and thermodynamic variables associated with the installation's nominal conditions. It is important to note that constraints arising from factors like working fluid properties impact the final results of the objective function, in this case, the maximum exergetic efficiency. Often, optimization processes halt due to constraints associated with optimization itself.

Exergetic efficiency is a measure of the effectiveness of converting supplied energy into useful work in a given process. For engines and energy systems, it is the ratio of the output exergy (useful work) to the input exergy (supplied energy). In short, exergetic efficiency reflects how efficiently and effectively a given machine or system

converts the supplied energy into desired work or beneficial output.

In practice, exergy analysis and exergetic efficiency assessment aid in identifying areas of energy loss, optimizing processes, and designing more efficient energy systems, including ones like ORC systems, which are often used for heat recovery and power generation from low- to medium-temperature heat sources.

The provided information revolves around the analysis and optimization of an Organic Rankine Cycle (ORC) system, considering exergetic factors. The design of an ORC system holds significant importance for its efficient operation, making use of exergetic efficiency definitions to fine-tune operational parameters and minimize long-term operational costs in the context of a cogenerative ORC power plant cycle. This analysis involves key factors such as heat transfer, temperature variations, and efficiency curves, all of which are vital for achieving optimal performance and energy conversion.



## Chapter 16

# An effect of hydrogen on material properties

## 16.1 Introduction

With the increase in energy consumption, the interest in hydrogen as an alternative fuel to fossil fuels has increased. Hydrogen is the fuel whose mass unit has the highest calorific value (120 MJ/kg) and heat of combustion (141.9 MJ/kg) in relation to weight. Due to its energy potential and minimal emissions, hydrogen is a key element considered a new source of electricity generation [84].

The hydrogen atom (H) has the simplest structure consisting of one proton and one electron. Its atomic weight is 1.00794u, and its density is 0.082 kg/m<sup>3</sup>. It is most commonly found in compounds such as natural gases (methane) or volcanic gases and forms numerous natural compounds such as water, proteins, hydrocarbons, and sugars. The reaction of metals with water or acids leads to the formation of hydrogen in the molecular form H<sub>2</sub> and also the atomic form H, which is a colourless, odourless, tasteless, non-toxic gas. Another feature of hydrogen, especially atomic hydrogen, is its flammability. Its diffusion into the metal structure leads to a decrease in ductile and strength properties and accelerated cracking. This process of degradation of the material was called "hydrogen embrittlement" [57, 85, 92]. Also, the term "hydrogen-induced failure" which is nowadays more and more common is used [63, 110, 119]. The term change is because the phenomenon of destruction caused by hydrogen is very complex, and embrittlement is one of its symptoms. In [59], there was stated that hydrogen embrittlement is the result of the synergism of several mechanisms, such as local hydrogen-enhanced plasticity, hydrogen-enhanced decohesion, hydrogen adsorption-induced dislocation emission, and stress-induced vacancy. The presence of hydrogen in material structure enhances corrosion processes [65, 86, 106]. Starting from 2000 year, the number of publications concerning the problem of material degradation caused by hydrogen published in Elsevier journals is continuously increasing (Fig. 16.1).

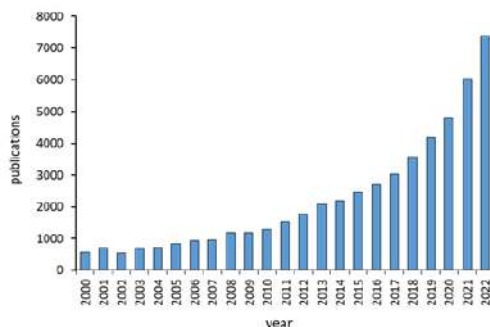


Fig. 16.1: Number of publications on hydrogen-induced failure in Elsevier.

## 16.2 Diffusion

The very small size of atomic hydrogen ( $31 \pm 5$  pm/ $0.03 \text{ \AA}$ ) allows its relatively easy penetration into the gaps in the crystallographic structures of materials. The size of the gaps depends on the crystallographic structure, the degree of filling, i.e. atomic packing factor (APF), and the size of the atoms of the elements.

The atomic packing factor, also so-called packing efficiency, or packing fraction is the fraction of volume in a crystal structure that is occupied by constituent particles. The APF is calculated by assuming that all the atoms are identical rigid spheres, with a radius large enough that each sphere abuts the next atoms (Fig. 16.2).

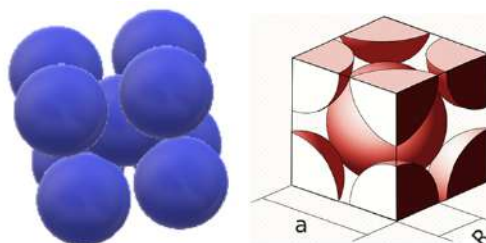


Fig. 16.2: Model of a body-centered-cubic (BCC) crystallographic unit cell (a) with dimensions used for APF calculation.

The radius of the spheres is taken to be the maximum value such that the atoms do not overlap.

$$APF = \frac{N_{particle} V_{particle}}{V_{unitcell}} \quad (16.1)$$

where  $N_{particle}$  is the number of particles in the unit cell,  $V_{particle}$  is the volume of each particle, and  $V_{unitcell}$  is the volume occupied by the unit cell.

In structural materials, the lowest APF (APF=0.64) is found in metals or alloys with a regular body-centered-cubic (BCC) crystallographic structure. The highest degree of packing is found in materials with a regular face-centered-cubic and hexagonal close-packed structure (APF=0.74). It means that materials with such structure have smaller interstitial sites (also called holes or voids).

In a crystallographic unit cell, there are two types of interstitial voids in the crystallographic lattice: tetrahedral voids surrounded by 4 contacting atoms of the main element, and octahedral voids surrounded by 6 contacting atoms. In a BCC unit cell, there are 6 octahedral voids located at the center of each face of the unit cell, which  $c$ , and 12 further ones located at the midpoint of each edge of the same cell, for a total of 6 net octahedral voids. Additionally, there are 24 tetrahedral voids located in a square spacing around each octahedral void, for a total of twelve net tetrahedral voids. In FCC and HPC close-packed structures there are 4 octahedral voids (1:1 ratio) and 8 tetrahedral voids (1:2 ratio) per unit cell. The tetrahedral void is smaller in size and could fit an atom with a radius  $0.225 \times R$  (radius of the atoms making up the lattice). An octahedral void could fit an atom with a radius  $0.441 \times R$ . An atom that fills this empty space could be larger than this ideal radius ratio, which would lead to a distorted lattice due to pushing out the surrounding atoms, but it cannot be smaller than this ratio. This shows that the radius of the atom of the main metal in an alloy is very important. In the case of iron, the size of the tetrahedral and octahedral voids is 31.5 pm and 57.4 pm, respectively. In steels, these voids are filled by carbon atoms. The atomic radius of carbon is 70 (67) pm, so only larger octahedral voids can be filled, causing

deformation of the crystallographic lattice. The maximum solubility of carbon in  $\gamma$ -Fe iron (austenite, FCC) reaches about 2% C. The size of smaller voids is the size of hydrogen.

Due to the number of voids in the crystallographic lattice, hydrogen diffusion is easier in the BCC structure compared to FCC structure. However, the difference is mainly in mobility. The diffusion is described by:

$$D = D_0 \exp\left(\frac{-Q}{RT}\right) \quad (16.2)$$

where  $D_0$  is the temperature-independent constant,  $Q$  is the activation energy for diffusion,  $R$  is the gas constant, and  $T$  is the temperature in  $K$ . According to Ref. [83], the lattice hydrogen diffusion relationships are:

$$D_\alpha = 2.3 \times 10^{-3} \exp\left(\frac{-6.680}{RT}\right) \quad (16.3)$$

for  $\alpha$  ferrite and BCC structure, and

$$D_\gamma = 2.7 \times 10^{-2} \exp\left(\frac{-54.400}{RT}\right) \quad (16.4)$$

for  $\gamma$  austenite and FCC structure.

This causes the values of the hydrogen diffusion coefficient in austenitic steel to be several orders of magnitude lower than in ferritic steel. In [53], there is shown that diffusivities at room temperature are about  $5.8 \times 10^{-10}$  cm<sup>2</sup>/s and  $7.37 \times 10^{-16}$  cm<sup>2</sup>/s for ferrite (pure iron) and austenite (304 steel), respectively. For multi-phase steels, diffusion coefficients range from  $2.19 \times 10^{-10}$  cm<sup>2</sup>/s for steels containing ferrite and carbides to  $3.0 \times 10^{-15}$  cm<sup>2</sup>/s for steels containing ferrite and austenite. In the case of steels composed of martensite and bainite, the hydrogen diffusion coefficient is  $4.43 \times 10^{-11}$  cm<sup>2</sup>/s, while for steels containing martensite and NiAl precipitates, it is  $9.42 \times 10^{-12}$  cm<sup>2</sup>/s. This shows that structure plays a key role in the resistance to hydrogen diffusion. Eq. 16.3 and Eq. 16.4 show that temperature also strongly affects the diffusion coefficient. At

200°C, diffusivities are about  $4 \times 10^{-4}$  cm<sup>2</sup>/s and  $3 \times 10^{-8}$  cm<sup>2</sup>/s for ferrite and austenite, respectively [83, 105]. Thus the increase is 6 orders of magnitude for iron, and 8 orders of magnitude for austenite. For temperatures below 100°C, the diffusion coefficient of pure iron decreases exponentially [103]. In the case of temperatures ranging from 75°C to 5°C, the diffusion coefficient can be described by the following equation:

$$D_{\alpha} = (5.12 \pm 0.61) \times 10^{-4} \exp\left(\frac{-4.15}{RT}\right) \quad (16.5)$$

Thus, both the temperature-independent constant and activation energy for diffusion changed. Despite crystallographic lattice, diffusion occurs along grain boundaries. This indicates that grain size also affects diffusion. Another factor affecting hydrogen solubility is the alloying elements. For example, the addition of Ni, Cr (in the range from 0.2 to 0.7%) or Cu (>0.02%) to carbon steel reduces hydrogen solubility [90]. In the case of high-strength 42CrNiMoV steel, the addition of 0.03wt% Nb causes significant grain refinement and the reduction of hydrogen diffusion coefficient by ~39% [126]. Investigations of X80 pipeline steel showed that the hydrogen diffusion coefficient, in addition to temperature, depends on heat treatment (annealing) [128]. In the case of the as-received state, the hydrogen diffusion coefficient was from  $9.1 \times 10^{-6}$  cm<sup>2</sup>/s at 25°C to  $17.1 \times 10^{-6}$  cm<sup>2</sup>/s at 45°C. Annealing this steel at 200°C for 12h caused an increase in the hydrogen diffusion coefficient from  $1.5 \times 10^{-5}$  cm<sup>2</sup>/s at 25°C to  $2.7 \times 10^{-5}$  cm<sup>2</sup>/s at 45°C.

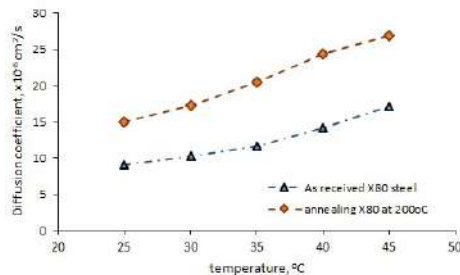


Fig. 16.3: Hydrogen diffusion coefficient of X80 steel, based on [128].

Fig. 16.3 shows that increasing temperature increased the difference in diffusion coefficients.

The penetration of hydrogen into the crystallographic lattice takes place through the so-called trapping, i.e. hydrogen falls into lattice imperfections, e.g. dislocations that capture hydrogen. These traps play a role in hydrogen embrittlement.

Regardless of the temperature, the mobility and solubility of hydrogen also depend on the applied stress, especially tensile [57]. As the stress increases, the dislocations begin to move, creating new hydrogen traps. As a consequence, hydrogen moves faster and over greater distances than is implied by diffusion caused by concentration gradients. Another consequence is the blockage of dislocation movement and the formation of dislocation pile-ups at hydrogen penetration sites. This leads to a decrease in dislocation mobility and plasticity, causing the so-called hydrogen embrittlement.

### 16.3 Effect of hydrogen on ductility

Many studies have dealt with the negative effect of hydrogen on the plasticity of steel. Refs [57, 83, 85, 105] are review publications that present the problem holistically. However, they were published in the 1970s and 1980s. This fact indicates that the problem of the influence of hydrogen on the properties of materials, including steel, was dealt with much earlier before the idea of using hydrogen energy was introduced [37, 84].

Investigations of the influence of hydrogen on the ductility (reduction in area, elongation in tensile test) showed that elongation decreased by 46.4% (from 56% to 30%) for 21Cr-6Ni-9Mn stainless steel, but no effect was noted for Cu and Al [57].

In the case of Fe-0.22C-1.40Si-1.80Mn (wt%) steel, the decrease in ductility depended on the steel treatment and charging time [129]. Cold-rolled steel prepared by a quenching and partitioning treated steel, to precipitate  $\epsilon$ -carbide in martensite had better elongation than this steel after additional tempering at 200°C for 2h when tested without hydrogen charging. However, a 1-minute charging

showed an opposite relation. In addition, tempered steel did not lose its ductility compared to the uncharged state. Nevertheless, 5-minute charging drastically decreased elongation, by about 90% and 80%, respectively for steel without and after treatment had slightly better elongation). Microscopic studies using transmission electron microscopy (TEM) revealed a small amount of hydrogen around the  $\varepsilon$ -carbide indicating that carbides were the traps for hydrogen atoms.

Precipitation-hardened Ni-based superalloys (Alloy 718 and Alloy 725, which are widely used in the oil and gas industries) showed approx. 66% and 87% decrease in elongation, respectively, after hydrogen charging [59]. Similar to Fe-0.22C-1.40Si-1.80Mn (wt%) steel, hydrogen was trapped at precipitates, i.e. (Nb,Ti)C, (Nb,Ti)(C,N), (Nb,Ti)N, Al<sub>2</sub>O<sub>3</sub>, (Cr,Mo)-rich precipitate, and also  $\gamma'$  (Ni,Nb,Ti), especially at carbides and precipitates located along grain boundaries (GBs).

Analysis of data from Refs [57, 59, 128, 129] indicates that hydrogen caused from 35% to even 90% reduction in plasticity (Fig. 16.4).

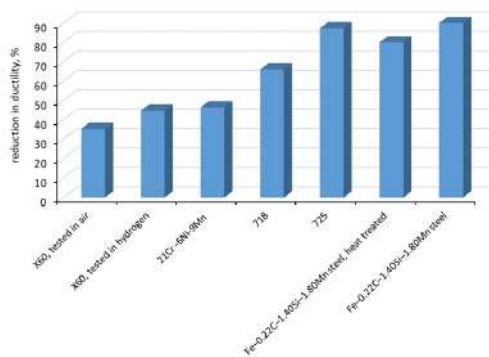


Fig. 16.4: Reduction in ductility, based on Refs [57, 59, 128, 129].

An effect of environment and strain rate on the resistance to ductility reduction was studied in Ref. [128]. Hydrogen charging X80 pipeline steel tested in air at a slow strain rate ( $2 \times 10^{-5}$ ) caused a 35% reduction in elongation. In the case of the hydrogen environment, the reduction in elongation was nearly 45%. Also, a large



reduction of ductility caused by the hydrogen environment was shown in [27]. However, an increase in strain rate from  $2 \times 10^{-5}$  to  $2 \times 10^{-4}$  caused an improvement in the elongation of X80 steel [128]. Hydrogen-charged X80 steel tested in the air had elongation equalled 11.5% and 16%, respectively for slow and high strain rates. In the case of the hydrogen environment, elongation was 2.1% and 3.6%, respectively. Thus, at the high strain rate, elongation was improved by 40% and 71%, respectively for testing in air and hydrogen. The influence of the hydrogen environment on the reduction of steel elongation was nearly 82% for testing at a slow strain rate and 77.6% for a high strain rate.

The reduction of ductility also depends on the strength of the material (the greater the strength of the uncharged material, the greater the reduction in ductility) and the saturation of steel with hydrogen (the greater the degree of saturation, the greater the reduction in ductility) [56]. The increase in densities of vacancies caused by hydrogen is an additional factor [82].

## 16.4 Effect of hydrogen on tensile strength

The influence of hydrogen on mechanical properties was mainly carried out by two test methods: by comparing the test results performed in the air and hydrogen environments or by using materials initially charged with hydrogen (so-called pre-charged materials) and without hydrogen charging. However, in some papers, results were presented where the material was tested in an air and hydrogen environment and was without and with pre-charge, so the presented results are more complex. As in the case of ductility, reductions in yield strength (YS) and ultimate tensile strength (UTS) have often been reported as a result of the presence of hydrogen on the material structure.

A commercial-grade pure iron tested by using repeated stress relaxation tests under simultaneous cathodic hydrogen charging showed a decrease in YS by 8.5% (from 179.25 MPa to 163.94 MPa) [119]. A decrease in YS was also noted in testing API Grade 60 steel [86]. There was also shown the effect of grain size: the smaller the grains

size the smaller the reduction in YS. According to [86], both YS and UTS decreased for testing in a hydrogen environment. The reduction of YS was from 0.32% to 2% for the grain size of 14  $\mu\text{m}$  and 35  $\mu\text{m}$ , respectively. In the case of UTS, the reduction was from 9% to 19.7%, respectively. A decrease in UTS was also obtained in testing martensitic steel containing 11.2wt% Cr and 11.3wt% Ni [123]. The heat treatment affecting the volume fraction of the austenitic phase resulted in the reduction of UTS. The largest decrease was observed for steels with an austenite phase below 10% by volume. Also, [59] reported a decrease in YS and UTS. However, an opposite effect of hydrogen on YS, i.e. an increase in YS, is shown in [10, 57]. In Ref. [47, 50] is shown that the reduction or improvement in YS and UTS depends on many factors, e.g. steel grade, the method of steel production, heat treatment, grain size, temperature, saturation of steel with hydrogen and many others. The final effect (reduction or improvement) is a synergy of the mentioned factors. Fig. 16.5 shows that the reduction of tensile strength more often concerns UTS than YS.

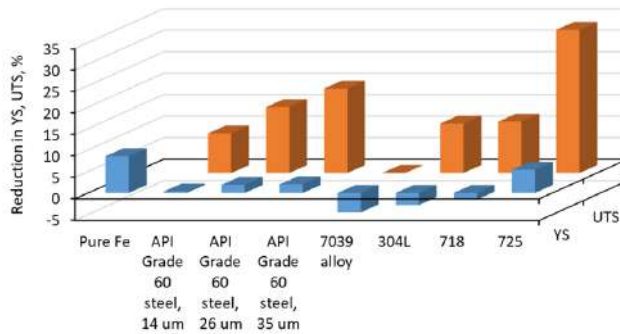


Fig. 16.5: Reduction of YS, UTS caused by hydrogen, based on Refs [57, 59, 128, 129].

Besides the reduction of UTS, hydrogen also affected the fracture strength and time to fracture [40, 126]. Tests of three steels with different Ni content showed that the increase in Ni content was accompanied by an increase in bainite in the steel structure and fracture strength in the conditions of hydrogen corrosion [40]. This

confirmed the high effect of structure on the resistance to hydrogen degradation.

## 16.5 Effect of hydrogen on a damage behaviour

As mentioned in the previous sections, microscopic studies proved that in most cases hydrogen is trapped at precipitates, especially those located along grain boundaries (GBs). The hydrogen preferable location at precipitates is consistent with the increase in the diffusion coefficient, as shown in the first section. Fig. 16.6 shows that grain boundaries, which are an area with more disorder and larger voids than grains are the places of privileged hydrogen location. In addition, the hydrogen absorption can differ depending on the arrangement of grains relative to each other.

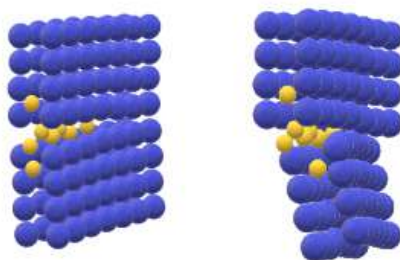


Fig. 16.6: Two examples of grain boundaries with different arrangements, blue are metal atoms, yellow are hydrogen atoms.

The other places of hydrogen trapping were any structure defects, including crack tips [53, 110, 116]. In the case of S13Cr steel [33], such places are martensite lath boundaries, prior austenite boundaries and precipitated austenite as well as newly formed martensite [33]. Trapping hydrogen at precipitates facilitated brittle fracture and caused a mixed ductile-brittle failure mode. Such degradation was observed in testing Ni-based superalloys (Alloy 718 and Alloy 725) [59], and S13Cr steel [33]. There was shown that hydrogenated alloys fractured in a mixed failure mode combining both brittle and ductile failures. Transgranular brittle failure in the form

of river patterns, ridges, and steps was observed, as well as intergranular cracking along GBs.

In the case of iron not charged with hydrogen [119], the fracture surface was ductile with microvoids present along the edges. In contrast, damage to the hydrogen-charged material shows that it has progressed to an intercrystalline fracture. The surface shows traces of secondary cracking, grain boundary yawning and micropores. Due to the absence of slip marks on the facets, Wang et al. concluded that the degree of plasticity was minimal during this failure.

Investigations of additively and conventionally manufactured 304L austenitic stainless steel [50] showed that the fracture surface of hydrogen-charged specimens consists of two regions: the central one with dimples and the outermost region with quasi-cleavage fracture. The outermost region was a region, where the material was exposed to hydrogen charging. Surface cracks propagated perpendicular to the tensile axis. The depth of the brittle region, i.e. the hydrogen-affected zone, in samples fabricated by laser powder-bed-fusion (LPBF) and 304 steel after annealing and hot-rolling at 1000°C to a thickness reduction of 50% and subsequently homogenized at 1150°C for 18h in Ar atmosphere (AHT) is significantly shallower ( $\sim 20\text{-}50\ \mu\text{m}$ ) than that in the annealed sample without hot-rolling and homogenization (A) that was  $\sim 140\text{-}180\ \mu\text{m}$ . Also, the depth of cracks is much shallower in the LPBF and AHT samples compared with the A sample. However, the majority of cracks observed were nucleated and propagated along the  $\gamma\text{-}\alpha'$  interface ( $\gamma\text{-}\alpha'$  interface crack) as well as within  $\alpha'$  ( $\alpha'$  crack). In investigations of ferrite-perlite steel the dominant hydrogen transport path is through the ferrite because pearlite blocks the effects on the permeation of hydrogen [120]. Brittle intercrystalline cracks were initiated at ferrite grains and triple junctions.

## 16.6 Summary

An effect of hydrogen action on the material was presented. Hydrogen as the smallest atom can easily penetrate the microstructure and

crystallographic structure leading to accelerated failure. The most simple way of hydrogen penetration is along the grain boundaries. Other places for trapping hydrogen atoms are vacancies, precipitates, and triple junctions. The reduction in plasticity can reach even 90%. The reduction in YS and UTS depends on the method of steel production, phase composition, grain size, heat treatment, testing temperature and environment, strain rate, the level of saturation of steel with hydrogen and many others. The final effect (reduction or improvement) is a synergy of the mentioned factors. In some cases, an increase in YS was observed, but not in UTS. Despite tensile strength properties, hydrogen decreases the time to failure. This means shortening the life of devices exposed to hydrogen. Therefore, the development of the hydrogen economy, including hydrogen energy, requires the development of new materials and coatings that will protect against or reduce the destructive effects of hydrogen.

## Chapter 17

Accumulation of heat and cold using latent heat storage materials – phase change materials (PCMs)

## 17.1 Introduction

Environmentally harmful human activity and ensuring energy independence make it necessary to transform the energy sector towards renewable energy sources. Still, for the energy transformation to be possible, it requires the use of energy storage facilities on a large scale for two reasons: due to the periodic availability of renewable energy sources (e.g. solar radiation, wind) in a given place and time, and due to the time-varying demand for energy. This means that if energy production occurs at a different time than the demand for it, it is necessary to store energy. There are different ways to store energy. Electricity generated by e.g. photovoltaic or wind installations can be stored directly in the electric and magnetic field (e.g. using supercapacitors, superconductors) or by converting this energy into: electrochemical energy (e.g. using accumulators/batteries), mechanical energy (e.g. pumped hydro systems, compressed air storage technologies), chemical energy (e.g. hydrogen production), thermal energy (e.g. water storage, latent heat thermal energy storage, thermochemical storage). However, the conversion of energy from one form to another causes conversion losses, so it is preferable to store the energy in the form required for consumption.

In the building sector, where energy consumption accounts for 40% of global consumption and is responsible for 36% of greenhouse gas emissions into the atmosphere, a significant part of this energy consumption is due to the heating and cooling needs of residential and non-residential buildings [95]. Only in Europe, half of the total energy consumption is used to heating and cooling buildings, of which around 84% comes from fossil fuels [95]. This indicates that buildings need retrofits, which would allow the reduction of energy consumption by buildings (e.g. by better insulation of buildings, replacement of low-effectives devices) and increase the use of renewable energy sources and their storage systems in heating and cooling installations of buildings. Heat and cold used for heating and cooling can be obtained directly from renewable energy sources (e.g. from solar collector installations, from cool night air in the summer, from free-cooling), or from waste heat recovery (e.g. from industrial processes, server rooms). However, heat and cold must be

stored by thermal energy storage (TES), where the energy will be stored and delivered in the same form, and the storage efficiency will be high due to the lack of conversion losses and the occurrence of only losses resulting from the heat transfer from the storage system to the environment.

Thermal energy storage (heat or cold accumulation) can be achieved in three ways:

- using sensible heat (specific heat)
- latent heat
- thermochemical processes

**Energy storage in sensible heat** is based on the use of the specific heat of a substance/material in a liquid or solid state (e.g. water, sand, gravel). Heat or cold is stored in the accumulation material as a result of its temperature changes during heating or cooling processes. The stored energy is proportional to changes in the temperature of the accumulating material, and its amount also depends on the amount and type of accumulating material. Thermal energy storage using sensible heat can be implemented by using the heat capacity of water, natural deposits (rocks, sand) and soil. The choice of accumulation material depends on the temperature of the process and the desired efficiency. Water is most often used due to its high heat capacity, price, easy availability and the possibility of using it for domestic purposes, e.g. as domestic hot water. Energy storage using sensible heat is characterized by achieving low energy storage densities, which has a significant impact on the size and volume of the storage.

**Latent heat thermal energy storage (LHTES)** is based on the use of the heat of phase transitions when material that can change phase from one to another at a specific temperature (or specific temperature range), is heated or cooled. This material is called the phase change material (PCM). During a phase transition (a change of physical state of material), energy in the form of heat or cold can be absorbed or released. Latent heat thermal energy storage allows for relatively high energy densities, higher than using sensible heat (see Fig. 17.1).



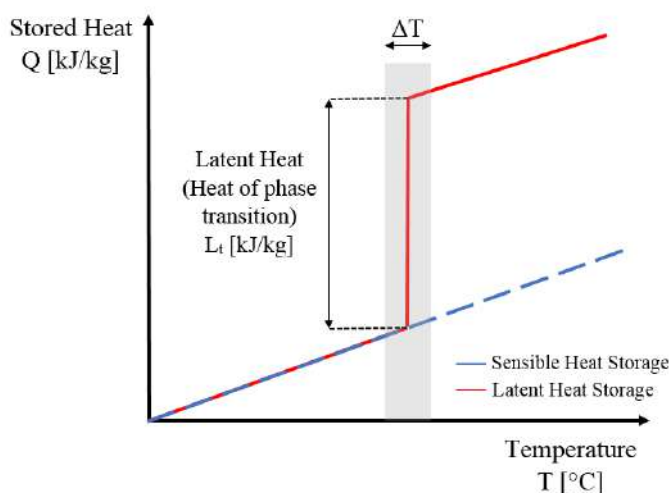


Fig. 17.1: Comparison of sensible and latent heat storage.

However, the highest thermal energy storage densities are achieved in **thermochemical processes** using the thermal effects of sorption processes and reversible endotherm/exotherm chemical reactions. In these processes, as a result of the supply of heat, an endothermic reaction takes place in which heat is absorbed and stored for some time. On the other hand, the release of the accumulated heat occurs during the reversal of the reaction - exothermic transformations. The heat of sorption processes is several times higher than the heat of phase transitions, and the heat of chemical reaction is even an order of magnitude higher. In addition, it allows to store energy without loss to the environment. However, the operation of thermochemical storage facilities is more difficult and complicated, because it requires special reactors, separation of reaction products and the use of specialized technologies for storing reaction products (especially those in the gaseous state), and most processes require high temperatures [18].

For these reasons, latent heat thermal energy storage and the use of phase change materials (PCMs), are becoming more and more popular. The use of latent heat allows to achieve higher energy storage

densities (resulting in the smaller size of tank), and better temperature characteristics of heat medium during its collection compared to the use of sensible heat storage, and on the other hand, it causes moderate operational problems in relation to the technology using thermochemical processes [18].

## 17.2 Phase Change Materials (PCMs) – definition, properties and types

Phase Change Materials (in short: PCMs) are chemical compounds that can absorb or release energy during a phase change from one phase to another. The phase transition can occur:

- from a solid to a liquid state (and vice versa), during melting or solidification processes
- from the liquid to gas (and vice versa), during evaporation or condensation processes
- from gas to solid (and vice versa), in the processes of sublimation and resublimation
- as a result of transformations taking place in a solid (from solid state to solid state)

During a phase transition at specific temperature or temperatures range, there is a thermal effect that causes a change in enthalpy without a relatively large change in temperature (see Fig. 17.1). The difference between the enthalpy before and after the phase change is called the latent heat, which determines the amount of energy stored during the phase change.

Transitions to the gas have the greatest latent heat, then melting/solidification processes and solid-solid transitions. In practice, phase transitions into gas are rarely used due to the problem of a large volume changes (even up to three orders of magnitude) [18]. Therefore, latent heat thermal energy storage is mainly based on melting/solidification processes, where the volume change is relatively small (usually up to 10% [70]).

**How is heat or cold stored during melting/solidification processes?**

During the melting/solidification process, the solid-liquid/liquid-solid phase change occurs in three stages (see Fig. 17.2). To melt solid (e.g. ice) it is necessary to supply heat. By providing heat, the material heats up and increases its temperature up to the melting point – the beginning of the phase transition (points A – B). The heat supplied in the first stage is accumulated using sensible heat (specific heat). After reaching the melting point, a solid-liquid phase change occurs (e.g. melting of ice into water) during which heat is absorbed and the temperature of the material increases slightly or remains constant for some time (points B – C). At this point, the energy in the form of heat is absorbed by the phase change material, which stores it with latent heat. After the melting is completed (the final phase transition temperature is reached), the third stage begins, in which, due to further heating, the temperature of the material continues to increase until thermal equilibrium is reached (points C – D). In the third stage, heat is also accumulated as the results of sensible heat. The heat stored by the phase change material at the melting point can be released by the reverse process – in this case, in the solidification process. In order to solidify the molten material, it must be cooled. By cooling the material (e.g. water), we lower its temperature up to the phase transition temperature (points D – C). Then solidification occurs (change of state from liquid to solid, e.g. from water to ice). At this point, the phase change material releases (gives off) the accumulated heat, and its temperature remains constant or decreases slightly for some time (points C – B). After reaching the solidification temperature and completing the phase transition, the temperature again starts to decrease significantly (points B – A), which is due to the sensible heat transfer taking place in the already solid material. Once thermal equilibrium is established, the temperature of the material remains unchanged.

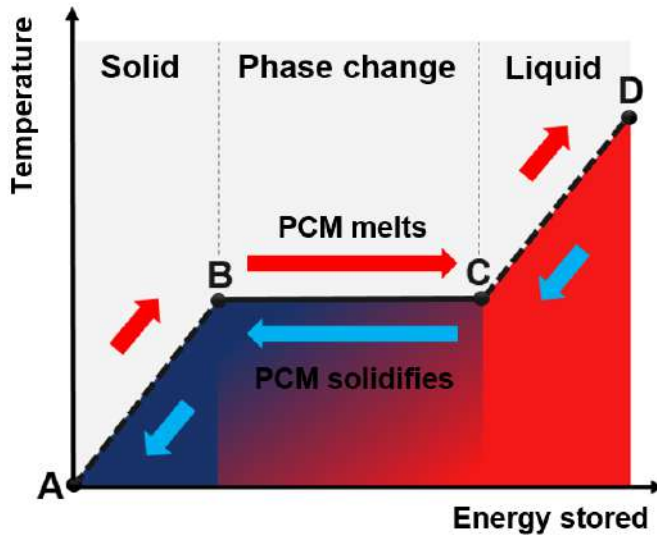


Fig. 17.2: Energy storage (heat/cold storage) mechanism of phase change materials with solid – liquid phase transition.

The amount of energy (heat or cold) stored by the phase change material during the melting or solidification process can be determined according to Eq. 17.1:

$$Q_{PCM} = mcp_s(T_m - T_1) + mL_t + mcp_l(T_2 - T_m) \quad (17.1)$$

where  $m$  – material mass,  $cp_l$ ,  $cp_s$  – liquid, solid specific heat, respectively,  $T_m$  – phase change temperature,  $T_1$ ,  $T_2$  – the temperature of the material at the start and end of the heating/cooling process, respectively,  $L_t$  – latent heat.

In Eq. 17.1, the first and last terms refer to heat/cold storage based on the specific heat of the material and the middle term expresses latent heat thermal energy storage.

The ability to store a certain amount of energy (in the form of heat or cold) and the dynamics of energy absorption or release are depend on the individual properties of phase change materials.

**PCMs have the following properties [43, 94, 96]***Thermophysical properties:*

- a. Phase change temperature; it is a specific material property that determines at what constant temperature or range of temperatures a phase transition occurs during which energy is absorbed or released.
- b. Heat capacity; determining the amount of energy stored by the PCM in a specific temperature range. The heat capacity consists of the latent heat and the specific heat of the material in both states. Latent heat mainly determines the PCM's ability to store heat or cold. From a practical point of view, the specific heat of materials is important because, together with the latent heat, it determines the total heat capacity over the entire operating temperature range.
- c. Thermal conductivity; which affects the intensity of heat exchange, and thus the time of transferring and receiving energy (heat or cold) from the environment
- d. Density; which together with the heat capacity affects the determination of the amount of heat or cold storage material and the target size of the heat or cold storage (accumulator)
- e. Volume changes during the phase transition
- f. Absence or presence of supercooling effect upon solidification; the occurrence of the supercooling effect consists in the fact that the solidification process does not start at the phase change temperature, but only after the temperature is lowered from a few to even several dozen degrees below the phase change temperature, until the first nuclei of the solid phase appear [18], after which the temperature in the entire volume increases to the phase transition temperature and a phase transition occurs. When supercooling occurs, it can make it difficult to release stored energy, prevent the material from solidifying, and retain stored heat.

*Chemical properties:*

- a. Stability of materials in many cycles of phase changes; maintaining the stability of the material is important in terms of ensuring the durability of the material and maintaining its properties. Sometimes the chemical stability of PCMs is not maintained, e.g. in the phase transition of some salt hydrates, where during non-congruent melting phase separation occurs (decomposition into water and less hydrated salt) as a result of the difference in density. The occurrence of phase separation leads to changes in the thermophysical properties of PCMs.
- b. Material compatibility; PCMs can interact with other materials - metals or plastics, due to their placement in tanks, encapsulation or placing in plastic packaging. Some PCMs can degrade some plastics or corrode some metals. Determining the material compatibility of PCM with other materials provides knowledge on the selection of the appropriate material to which the PCM can be placed or from which the tank or storage can be made [94].
- c. Flammability
- d. Explosiveness
- e. Toxicity

Based on the above properties, it can be concluded that an **ideal PCM for heat or cold storage should be characterized by:** high heat capacity (high latent heat and specific heat), high density, low volume change during phase transition, low viscosity, chemically and thermally stable during many cycles of phase transitions, do not show the effect of supercooling, have appropriate thermal conductivity, be compatible with other materials and safe for humans (non-toxic, non-flammable, non-explosive). In addition, the PCM should have a phase change temperature range adapted to the operating temperatures of the installation and heat/cold sources in order to be able to accumulate heat or cold. For ecological reasons, it should be biodegradable, and for economic reasons it should be cheap, easily available in large quantities and long-lived (have as many cycles of phase transitions as possible, several thousand cy-

cles and more) [43].

In fact, chemical compounds that are phase change materials do not meet all properties that define an ideal PCM. However, individual groups of chemical compounds, which are **PCM**, **have common properties, hence PCMs, due to its chemical composition, can be classified into:**

- organic materials; which are paraffins (e.g. octadecane, hexacosan) , fatty acids (e.g. capric acid, stearic acid), alcohols (e.g. xylitol, erythritol), ethylene glycol polymers, esters and other hydrocarbon derivatives
- inorganic materials; which are water, salts (e.g. sodium chloride  $\text{NaCl}_2$ ), salt hydrates (e.g. calcium chloride hexahydrate  $\text{CaCl}_2 \cdot \text{H}_2\text{O}$ , potassium fluoride tetrahydrate  $\text{KF} \cdot 4\text{H}_2\text{O}$ )
- eutectic mixtures; they are mixtures of inorganic or organic substances

Tab. 17.1 and Tab. 17.2 present a comparison of properties characterizing organic and inorganic PCMs with an indication of their advantages and disadvantages.

Tab. 17.1: Advantages and disadvantages of organic PCMs.

Advantages	Disadvantages
high latent heat (usually in the range of 130 - 260 kJ/kg, and even above 260 kJ/kg for some sugar alcohols)	low thermal conductivity (in the range of 0.1 - 0.3 W/mK, with the exception of sugar alcohols, whose thermal conductivity is in the range of 0.4 - 0.8 W/mK)
narrow melting temperature range (homogeneous substances)	large volume changes in the melting process
chemically and thermally stable	flammable (usually eliminated by adding flame retardants)
rare supercooling effect	lower density and specific heat compared to inorganic materials
chemically neutral	possible incompatibility with plastics (like LDPE and PP), in case of fatty acids possible incompatibility with some metals
usually compatible with other materials	expensive

where: LDPE – Low-density polyethylene, PP – Polypropylene



Tab. 17.2: Advantages and disadvantages of inorganic PCMs.

Advantages	Disadvantages
high volume storage capacity	problems of thermal and chemical stability (the occurrence of phase separation – mainly in salt hydrates)
high latent heat (higher than organic materials, typically in the range of 150 - 300 kJ/kg and even above 300 kJ/kg for some salts)	occurrence of the supercooling effect (eliminated by use of nucleating additives)
cheap and easily available	corrosive to most metals
narrow melting temperature range	
higher thermal conductivity than organic materials (in the range of 0.5 - 1.2 W/mK)	
non-flammable	

### 17.3 Applications of PCMs for the accumulation of heat and cold

A phase change material, can be classification due to chemical composition or considered by its phase change temperature (temperature range of phase transitions) to:

- low-temperature materials (from  $-20^{\circ}\text{C}$  to  $+5^{\circ}\text{C}$ ) where PCMs are typically used in refrigeration or cooling systems
- medium-low temperature materials (from  $+5^{\circ}\text{C}$  to  $+40^{\circ}\text{C}$ ), where PCMs are used in building heating and cooling systems, or other heating/cooling applications
- medium-temperature materials (from  $+40^{\circ}\text{C}$  to  $+80^{\circ}\text{C}$ ), where PCMs are used in heating systems, domestic hot water systems, electronic applications
- high-temperature materials (above  $+80^{\circ}\text{C}$ ), where PCMs are used for absorption devices, waste heat recovery, solar thermal electricity generation (Concentrated Solar Power, CPS) [25]

Phase change materials can be used in two ways: to maintain temperature (passively) or to accumulate heat or cold as a thermal energy storage (actively).

During a phase transition, phase change materials show no temperature change (or slightly temperature change) over time despite heating or cooling, which means that they can be used to prevent temperature fluctuations. The heat or cold previously accumulated by the material is transferred in an unforced way, and the heat exchange takes place as a result of natural convection.

Therefore, in practice, PCMs in passive ways are used as follows [18, 70, 96, 97]:

- to maintain the temperature of food products above or below a specific temperature; e.g. during their transport using cartridges filled with PCM, using special transport containers (boxes) with PCM, using backpacks or bags with PCM
- for the transport medicines, vaccines, blood and internal organs

- in medicine to induce therapeutic hypothermia in newborns suffering from birth asphyxia
- in the textile industry in astronaut suits, protective clothing for firefighters, outerwear and sportswear
- to prevent overheating; to cooling photovoltaic modules (in order to prevent the reduction of their efficiency), cooling electronics, e.g. processors, cooling electric car batteries
- to improve the thermal comfort of buildings; where PCM can be one of the components of building materials (e.g. cement, gypsum, insulating materials) or be placed in free spaces of buildings (e.g. suspended ceilings, walls, roofs)

The ability of PCMs to accumulate and deliver large amounts of heat/cold at a relatively small temperature difference (during a phase transition) means that these materials can be used as an accumulation material in thermal energy storage. In active systems, there is a forced heat exchange between the PCM and the heat transfer fluid (HTF) which allows to control the energy supplied to or released from the PCM accumulator.

Latent heat thermal energy storage in active systems can be used for [18, 70, 95–97, 107]:

- accumulation of solar energy; which can be implemented by storing heat from solar collector installations or electricity from photovoltaic installations as a result of its conversion into heat, and then using it for the heating building or for domestic hot water
- accumulation of heat/cold surpluses, e.g. storing waste heat from industrial processes, from server rooms
- to support district heating networks
- increasing the energy efficiency of heating/cooling systems with air-source heat pumps, as a result of accumulating heat (or cold) generated by the air-source heat pump in periods with higher efficiency of device, and then using it in periods of unfavorable weather conditions
- accumulation of cold in the summer as a result of night air

ventilation in heating, ventilation, air conditioning (HVAC) systems and its use during the sunny days

- accumulation of heat/cold in transitional periods (e.g. spring, early autumn) in buildings with HVAC systems (e.g. office buildings) in order to maintain thermal comfort and reduce energy consumption
- in order to reduce the costs of heating or cooling, as a result of storing electricity in the form of heat or cold in periods with tariffs with lower prices for electricity consumption

Different applications of LHTES cause that they may differ from each other in terms of construction. Latent heat thermal energy storage (PCM accumulator) in which liquids are heat transfer fluid (e.g. water, water glycol solutions) have various designs. The heat/cold accumulators with PCM have the following design:

- A storage tank with an internal heat exchange surface; they usually consist of a tank inside which there is a heat exchanger immersed in a phase change material (see Fig. 17.3a)). The HTF flowing through the exchanger, exchanges heat with the accumulation material – PCM. In this solution the amount of PCM in the tank is large, and the dynamics of storage tank loading and unloading depends on the heat exchange surface – the type of heat exchanger used. In this type of storage tank, heat exchangers are used, such as: shell and tube heat exchangers, fin-and-tube heat exchangers, coil heat exchangers, heat exchangers with capillary tube bundles.
- A storage tank with macro-encapsulated PCM (packed bed LHTES); it is a tank filled with closed capsules in which PCM is applied in a way as to ensure free change of volume during the phase transition (see Fig. 17.3b)). PCM capsules can have different shapes – they can be a spherical, rectangular, cylindrical or elliptical. Heat exchange in a tank with macro-encapsulated PCM occurs as a result of direct contact of the HTF with the outer wall of the PCM capsule, during the flow of HTF in the tank. The disadvantage of this design is the limited amount of PCM used in the tank.

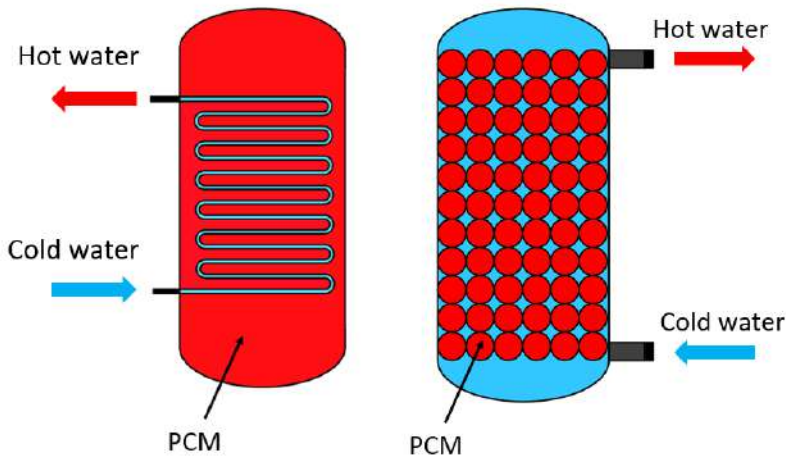


Fig. 17.3: An example of a LHTES construction: a) a storage tank with an internal heat exchange surface, b) a storage tank with macro-encapsulated PCM (with spherical capsules).

- Heat accumulators with direct contact; it is a storage tanks where there is no physical separation between PCM and HTF, and forced convective heat transfer is the dominant heat exchange mechanism in the storage. The supply and removal of heat is done by "pumping" HTF (usually thermal oil) and mixing it with the phase change material. The PCM used in this solution cannot be soluble in HTF and there must be a large density difference between PCM and HTF to ensure separation of these substances due to buoyancy effect during heat transfer.

Accumulation of heat or cold can also take place in a latent heat accumulator in which air is HTF. Usually these heat accumulators consist of rectangular boxes with a cross-section similar to the cross-section of ventilation ducts. Inside the boxes there are shelves on which aluminum plates or bags filled with PCM are placed (see Fig. 17.4). In this solution, the supply or release of heat/cold occurs as a result of air flow between the rows of shelves. These heat accumulators are built into ventilation/air-conditioning

installations, allowing to improve the thermal comfort of the building and reduce energy consumption, especially in summer, taking advantage of the possibility of accumulating cold at night and using it during the day, or in transitional periods (spring, autumn) when they can accumulate heat (or cold) and use it to improve thermal comfort, e.g. in office rooms.

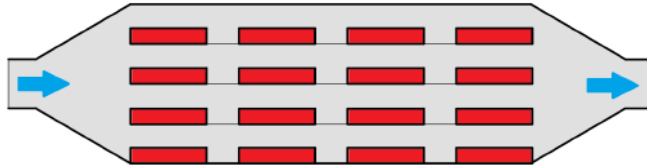


Fig. 17.4: An example of a LHTES dedicated to ventilation and HVAC systems.

## 17.4 Summary – limitations of PCMs and research trends

Phase change materials, thanks to their ability to store energy in the form of heat or cold, have found many applications in everyday life. In the context of their use to reduce energy consumption and greenhouse gas emissions, their use in the construction and energy sectors plays a special role, where they allow to regulate daily temperature fluctuations in rooms or can store (and then use) energy from renewable sources or waste heat. However, despite many research works on PCMs and the implementation of LHTES for cooperation with heating or cooling installations, there are still limitations such as: the problem of stability of inorganic compounds, low thermal conductivity (mainly of organic compounds) and the cost, which makes that this technology is constantly being developed. Therefore, current research works are focused on the search for new PCMs (with high heat capacity, stable, natural origin and cheap) or solutions improving thermal conductivity and increasing the intensification of heat exchange.

## Chapter 18

# Research Center of the Polish Academy of Sciences – Energy Conversion and Renewable Resources

The Research Center of the Polish Academy of Sciences – Energy Conversion and Renewable Resources, located in Jabłonna, small town, in Legionowo County (ca. 20 km from Warsaw) was established in 2016. The Research Center is a part of the Institute of Fluid Flow Machinery, the Polish Academy of Sciences (IMP PAN) located in Gdańsk.

Nowadays, the Research Center is one of the largest scientific and research complexes dedicated to topics related to renewable energy sources (RES) and equipped with the most modern, top-class research equipment in Europe. In recent years, a new scientific specialisation, the so-called – small-scale distributed energy based on RES, was developed at IMP PAN. Researchers of the Institute actively work in several research fields related to: designing new co-generation systems, ecological boilers with low exhaust emissions, production of biogas and syngas, obtaining energy from the sun or wind, energy storage (electric, thermal). The laboratory base in Jabłonna is a place that allows conducting the above-mentioned works. It is worth mentioning, that the Research Centre laboratories cover a total area of 2.788 m<sup>2</sup>.



Research Center of the Polish Academy of Sciences – Energy Conversion and Renewable Resources – Institute of Fluid Flow Machinery off-site research centre.

source: Own materials.



In the Research Centre it is possible to distinguish five thematically coherent internal research laboratories:

- laboratory of solar techniques
- laboratory of micro-power plants
- wind energy laboratory
- energy safety engineering laboratory
- integrated energy plus laboratory

and external (field) research laboratories:

- photovoltaic stands
- tracker
- solar collectors and photovoltaic panels
- wind turbines

that allow performing tests in real environmental conditions.



Energy Conversion and Renewable Resources laboratories.

source: Own materials.

Scientific research conducted at the Research Center is determined by the following strategic goals:

- commercialisation and dissemination of new, alternative technologies for electricity and heat generation
- promoting small-scale distributed energy in the context of Energy Clusters

- cogeneration of various forms of energy obtained from different sources
- development of measurement methods in distributed energy
- methods of certification of devices for the production of energy from renewable sources, optimisation of energy consumption
- development of smart-grid systems for smart houses and autonomous energy regions (energy islands)
- integration of various energy sources (sun, wind, biomass combustion, heat pumps, fuel cells) in the construction of small-scale combined heat and power plants
- optimisation and control of energy conversion from sources based on smart-grid systems
- integration of RES technologies in distributed energy
- promotion and development of small-scale, distributed prosumer energy

A short description of the five internal laboratories is presented.

#### *Laboratory of solar techniques*

Laboratory is divided into two parts related to exploitation tests of photovoltaic cells and solar collectors as well as testing operational parameters of heat pumps.

The first part of the laboratory is designed to testing individual photovoltaic cells as well as entire solar panels and solar-thermal systems (collectors) in the presence of radiation produced by a solar simulator. The laboratory is equipped with a high-quality solar simulator (class AAA), a device for measuring quantum efficiency and a system for simulating photodegradation in the presence of UV radiation. The large-area solar simulator provided by Eternal Sun is the first simulator of this type in Poland and one of several in Europe that generates continuous and homogeneous radiation identical to the natural solar spectrum. This system allows to measure the third generation cells, which are characterized by the so-called effect of saturation of the electric charge.

Also, the equipment possessed by the laboratory allow to perform tests on hybrid photovoltaic-thermal PVT systems cooperating with a heat pump as their lower source. The stand allows for comprehensive testing of refrigeration, air-conditioning and heat pump systems in stationary conditions and for dynamic loads for a wide range of operating parameters. Due to its specificity, the stand is particularly suitable for any research work aimed at multi-criteria optimization of devices. The stand has a precisely regulated heat load, which enables achieving high accuracy and stability of measurement parameters. The thermal loads have a separate accurate measurement system for determining the thermal performance.

#### *Laboratory of micro-power plants*

The laboratory contains equipment for analysing phase change materials and heat storage, thermal and flow phenomena related to co-generation power plants, installations for the production of energy from renewable energy sources, small-size, high-speed rotors and bearings applied in various types of machines used in distributed energy as well as the development of ecological, innovative energy conversion technologies based on biomass and biodegradable waste.

The laboratory for testing phase change materials (PCMs) offers the possibility of research on heat storages with PCMs. The laboratory is equipped with a universal test stand for testing thermal energy storage with phase change (dedicated to systems using RES). The stand also includes 6 different structures of heat storages with PCM and sets of thermal loads for storages. Thermal load systems with a power of up to 32 kW allow the storage to be supplied with a liquid at a temperature of up to 310°C and to receive heat at a temperature of up to 310°C with the use of high-temperature thermal oil or with a water glycol solution to work at lower parameters from -20°C to 90°C. The system is also equipped with a dedicated cooling system with a thermal power of 60 kW. The stand has a control system that allows for precise regulation of the characteristics of power supply and heat collection parameters from the energy storage, and thus a thorough analysis of its loading and unloading. The laboratory carries out research in the field of thermal energy storage using

phase change materials in a comprehensive manner – in the form of cold, i.e. below  $0^{\circ}\text{C}$ , and in the form of high-temperature heat, i.e. up to  $300^{\circ}\text{C}$ .

The laboratory for presentation and research on cogeneration power plants is equipped with extensive technical facilities and high-quality research equipment that allows for precise testing of thermal and flow phenomena, various configurations of thermal cycles and devices. The laboratory has several expositions and research stands: a stand for testing the prototype of the ORC micro-cogeneration plant, a stand for testing microturbines and cooperation with an energy storage, and a stand for testing thermodynamic cycles. There is an efficient source of heat in the form of a boiler with high-temperature oil with a capacity of 300 kWt and a temperature of max.  $350^{\circ}\text{C}$  with precision temperature control and three delivery points. The collection of heat from the research systems is ensured by cooling installations allow the use of heat for heating purposes or supplying heat storage facilities. The laboratory uses the infrastructure of solar collectors, heat storage and cold production.

Research works carries out in the laboratory of environmental diagnostics and analysis are related to the broadly understood diagnostics of installations for the production of energy from renewable energy sources as well as other industrial installations. The laboratory's equipment includes a set of high-class thermal imaging cameras, as well as a drone adapted to carry cameras to conduct analyses of large areas (e.g. photovoltaic farms). The laboratory enables research and development work on small-size, high-speed rotors and bearings that are applied in various types of machines used in distributed energy (including steam and gas microturbines).

The research concerns both the optimization of the structure, material issues and operational aspects. New, unconventional methods of bearings can be developed using the existing test stands and measuring equipment. The laboratory enables the development of new solutions and technologies dedicated to modern energy microturbines and other flow machines used in cogeneration systems. Laboratory equipment includes: five test stands enabling testing of various expansion machines (including: steam and gas microtur-

bines and the Stirling engine), microelectric power generators and multi-support rotors. The equipment also includes: a multi-channel measurement system, portable devices for assessing the technical condition of machines, an ultra-fast camera and high-speed rotor balancers. This equipment enables research and development of various types of rotating machines.

The laboratory of thermal biomass and biofuel processing enables research aimed at the development of ecological, innovative energy conversion technologies based on biomass and biodegradable waste, while maintaining environmental protection requirements. The equipment includes e.g. devices for the production of biofuels and systems for the production of heat and electricity, which are to be used for research in the area of:

- issues of pyrolysis, gasification and combustion, ranging from a single particle to a bed of particles characteristic of technical devices
- aspects of biomass and waste utilization for energy purposes, taking into account chemical analyses of substrates and products
- methods of cleaning the generator gas from tars and solid particles
- design and optimization of energy generation system equipment (pyrolysis reactors, gasifiers, boilers, syngas purification installations)
- designing high-temperature heat exchangers

#### *Wind energy laboratory*

The laboratory is equipped with an open low-speed wind tunnel containing two independent measurement chambers; one of them is adapted for testing small wind turbines or models of large wind turbines. The tunnel operates in a suction mode and reaches a flow velocity in the measuring chamber of up to 30 m/s. The measuring chamber is 4 meters long with a square cross-section of 2 by 2 meters.

The measuring chamber of the tunnel is equipped with the following measuring systems:

- measurement of the velocity field – a sliding row of hot-wire anemometric sensors
- forces and moments – Stewart platform with optical strain gauge
- deformations – a system of optical measurement of deformation of wind turbine blades under the influence of aerodynamic forces
- noise – a portable acoustic camera for measuring the intensity and location of the noise source
- measurement of generator characteristics

The laboratory has systems dedicated to wind turbines for measuring windmill characteristics (torques, forces, mechanical power, electric power, rotational speed, velocity field distribution, deformation of rotor elements, noise). In addition, the research team performs numerical simulations in the field of wind energy and aerodynamics.

#### *Energy safety engineering laboratory*

The laboratory was established in cooperation with the Institute of Fundamental Technological Research of the Polish Academy of Sciences in Warsaw. The work in the laboratory is focused on testing devices related to clean air, applications of additive manufacturing techniques to develop solutions related to the security of energy and transport systems as well as production and characterisation of functional materials dedicated to use in devices for energy conversion and storage.

The gas purification laboratory is focused on testing devices related to clean air, i.e. protection of the atmosphere against pollution. Both devices that contribute to reducing the emission of harmful substances into the atmosphere (e.g. dielectric barrier discharge (DBD) plasma actuators) and devices used to purify polluted gases, in particular dust removal (e.g. electrostatic precipitators), are tested. The laboratory is equipped with a system for laser vi-

sualization of flows and measurement of flow velocity fields using the Particle Image Velocimetry (PIV) method. The system uses e.g. Nd:YAG laser and two fast CMOS cameras. Thanks to this, it is possible to simultaneously measure all three components of the flow velocity field in the laser plane. The laboratory is also equipped with apparatus for measuring gas parameters, including the measurement of dust density (measurement divided into fractions of various sizes in the range from 10 nm to 32  $\mu\text{m}$ ). In addition, the laboratory is equipped with a function generator and a high-voltage amplifier that enable powering various devices with almost any type of high voltage (from -30 kV to +30 kV) and equipment to monitor electrical parameters.

The combination of additive manufacturing and research equipment allows conducting comprehensive research on solutions that increase the security of energy and transport systems. The research team of the laboratory has experience in modelling and designing structural diagnostic systems, energy dissipation systems and professional electronic systems for industrial applications. The laboratory has equipment that allows for professional design and production of advanced electronic devices, application of tracks and thin layers of materials on surfaces in three dimensions using the *Aerosol Jet Printing* technology and conducting research on the production of complex metal elements using the selective laser sintering technique.

The laboratory of functional materials carries out work on the production and characterization of functional materials applied in devices for energy conversion and storage. The laboratory is equipped with a scanning electron microscope, a mechanical profilometer and a high-vacuum magnetron sputtering machine. The mechanical profilometer allows for repeatable and accurate surface characteristics, e.g. standard roughness measurement and local height measurements. The high-vacuum magnetron sputtering machine equipped with a turbomolecular pump allows for the production of thin layers of oxidizing and non-oxidizing metals as well as layers of metal oxides (e.g. tin-doped indium oxide) on selected substrates. The built-in quartz microbalance ensures precise control of the thickness of the sputtered layer.

*Integrated energy plus laboratory*

The laboratory consists two main parts: presentations and operational tests on micro-cogeneration systems and building energy monitoring.

The cogeneration systems laboratory is used for presentation and operational tests of the latest technologies for generating heat and electricity. The laboratory equipment includes mCHP cogeneration units with a capacity of approx. 1 kWe and 20 kWt to approx. 30 kWe and 80 kWt, manufactured in various technologies. These are systems based on: gas piston engines, external combustion engines (Stirling engines), gas microturbine, fuel cell. The scope of its work of the laboratory also includes a heating system using a gas and biomass boiler, a 120 kWe gas turbine cooperating with an ORC system with a capacity of approx. 20 kWe using low-temperature heat, a cogeneration system with a piston engine powered by syn-gas from a biomass gasifier, solar collectors and waste heat, heat pumps and heat storage; The above systems are controlled by a local management system that controls the production, distribution and consumption of electricity throughout the facility.

The building energy monitoring and management laboratory operates on the basis of the so-called an extended Building Management System (BMS) located in the Research Centre building and specialized software for work dedicated to the search for the optimal energy balance for various RES devices operating in one power grid. This laboratory also includes a set of Internet of Things (IoT) network that allow communication and control of devices located in a statistical household.

Below, closer look into a particular laboratories location.





Production of electricity – equipment and its locations.  
 source: Own materials.



Heat and cold production – equipment and its locations.

source: Own materials.



Electricity, heat, and cold storages together with production applying cogeneration – equipment and its locations.

source: Own materials.

Part IV

Other

## Chapter 19

# Life during PhD and beyond: A researcher's perspective

## 19.1 Introduction

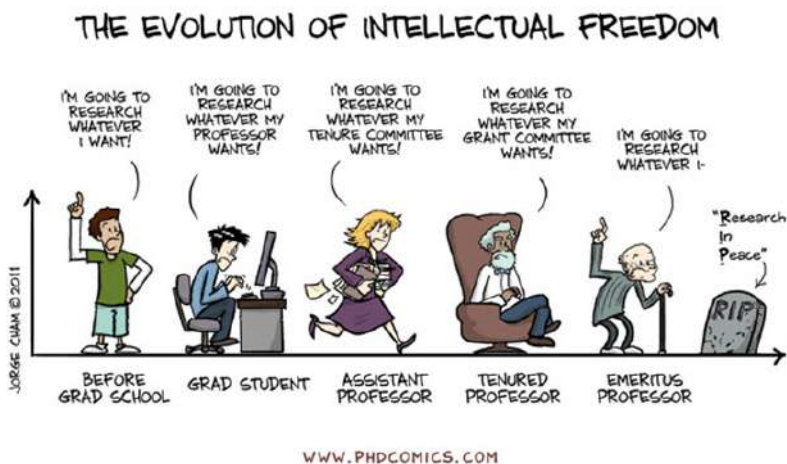
In general a PhD is the often a minimum requirement for academic teaching at the university level. According to some historians the first doctorate was bestowed in the year 1150 and over its almost millennia long history it has meant different things at different times and in different regions. In spite of the changing perceptions of the PhD it has always been associated with academic excellence and its relevance remains even today. So the endeavour to get a PhD will put you in the top 1% of the people in the world [6].

This career path makes particular sense in the so-called western world which have research-based economies as their guiding and organizing principle. Having built this historic background of the globally accepted highest academic degree, the chapter embarks upon sharing the experience that the author has developed over the last decade in academia. The chapter is neither supposed to be a know-all handbook of what to expect in the journey nor is it a quick-fix to the problems that you might encounter. The chapter is aimed at giving a flavour of life in academia for motivating people to embark upon this demanding yet satisfying journey. Also, the chapter is a way to remind the people who have already embarked on the quest of knowledge, that whatever they might be feeling, they are not alone, there are hundreds if not thousands of researchers who are going through the same.

The rest of the chapter is organized as follows: the next section gives an overview in life of an academic in the sense of the roles or tasks that are encountered at different stages of the career. This will allow firstly to manage expectations of the prospective researchers and also give perspective to doctoral students by walking in the proverbial other person's shoes. The section 3 identifies the common mistakes early stage researchers (ESRs) commit and how to avoid those including a discussion on mental health which has only recently been noticed and discussed. The conclusion focusses on the key take-aways from the chapter and there emphasis on self awareness and open communication.

## 19.2 Academic life

Just as the perception of PhD varies in time and based on your location, academic job titles have changed over time and do differ from country to country. Also, job titles do get lost in translation from local languages to English. But typically in an academic setting, there is a research track, teaching track and an administrative track. Most people will have a bit of duties in all of this track but there is always an illusion of choice on the academic in these roles. So the most common career progression in academia particularly teaching jobs is a doctoral student who graduates and takes up a post-doctoral position. These post-doctoral positions are often project specific and time bound. Typically after few years of gaining post-doctoral experience, the researchers may be offered (but not always) a tenure track position. The assistant professors progress to associate professors and after a few years of distinguished service may be promoted to full professors.



Illusion of intellectual freedom [14].

source: Copied from [https://phdcomics.com/comics/archive\\_print.php?comid=1436](https://phdcomics.com/comics/archive_print.php?comid=1436)

A tenure is a very interesting and polarizing aspect of life in academia. The tenure is an indefinite appointment that can be cut short only for a just cause or under extraordinary circumstances. The tenure

was aimed at maintaining academic freedom for the researchers to pursue research and innovation and draw evidence-based conclusions without corporate, religious or political pressure. Although it was successful to do this to a certain level, political and corporate wills do determine funding levels and often indirectly affect research although not through direct censorship. A fun comic, presented above, by Jorge Cham does illustrate this.

On an individual level tenure does give the researcher stability and allows a more long term view which in general helps big picture research. The main opponents of the tenure system although state that tenure system breeds laziness. Personally, the long term position has indeed allowed me to focus on long term research goals and build my research profile. It has also allowed me enough stability to put together a lot of research equipment that makes my lab competitive. On the downside, having job security albeit on an average salary took away the motivation to actively look for some better career prospects. This topic has been highly debated, an excellent discussion on its societal and inclusivity repercussions may be found here [34, 93].

Although in the current rapidly changing world a lot of the research roles have evolved, the essential tasks have remained same. Typical PhD student is expected to dedicate almost all time to research. Research tasks may change from field of interest as well as even type of work. But will typically including collecting data, analysing the data, and organizing it to test the hypothesis. In most cases, the PhD student will have some teaching and supervision duties.

The post-doctoral researcher typically is looked at as an apprenticeship of research profession. The responsibilities for this role will include mostly research tasks with some day-to-day supervision of doctoral and master students and even a little project management. At this stage more involved teaching experience is also to be acquired.

The assistant professor will have similar responsibilities as the post-doctoral researcher but will be more involved in administrative duties at the university as well as project levels. Typically they will dedicate around 40% time doing actual research.



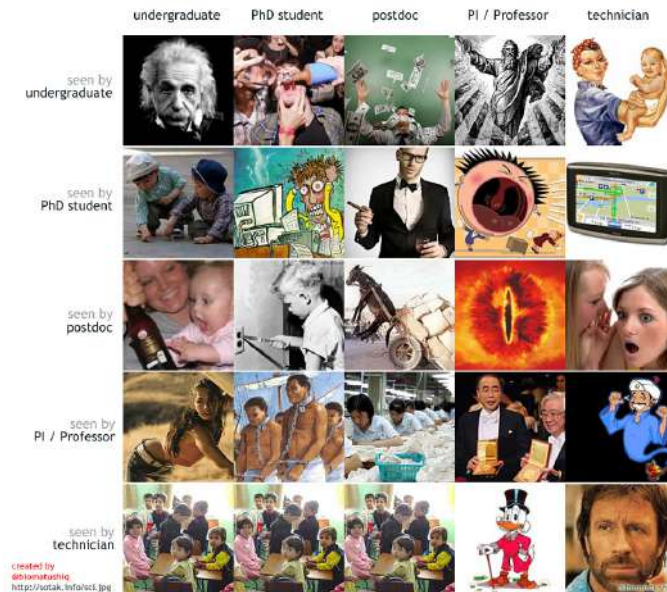
The associate professors will be more involved in defining research agendas and will typically involve around 20-25% of time to research. They are expected to be involved with funding acquisition, project management and running a team of researchers.

The full professors are involved with more defining policies and serve in various committees at the university as well as societies and funding bodies. Full professors typically spend very little time doing active research but are heavily involved in securing sponsorship and higher levels of funding and endowments.

Of course depending on the nature of the field and teaching and research background as well as personal inclinations these roles might change a bit. But often the academic system expects and gives incentives to adhere to these roles and time distribution. Beyond research in academic field there are several research roles in private industry which also can be monetarily much more rewarding. In addition to doing active research there are full-time teaching positions which might be of interest to people who wish to shape the young minds. Beyond these traditional roles there are opportunities also opening up in research management, grant proposal writing and assessment, academia-industry liaison as well as policy determination in national and international bodies. Most of these roles value the skills gathered in the field during the PhD but may need some additional training in specific fields. An excellent overview has been given in [26, 64]. There are also several examples of researchers monetizing their research through spin-offs. Of course entrepreneurship needs a completely different sets of skills which often doctoral programs are not known to prioritize. So it is important to be made aware of the prospects that one might have in the future and gather the required skills for excelling in the particular career option.

There is a fun comic by Matus Sotak [67] which emphasizes how different people in academia view each other and drives the point on how each one perceives the other. Of course this does not reflect complete truth is an attempt at humor and is included in jest.

### How people in science see each other



Roles in academia as seen by each other all.

source: Copied from <http://sotak.info/sci.jpg> (with permission of the author)

### 19.3 Dos and Don'ts of your doctoral journey

The research towards your doctoral degree has innumerable highs and lows. The ups and downs of this journey keep it interesting but also causes a large amount of stress and around 50% of the candidates do not finish the journey. To quote, Leo Tolstoy, 'all happy families are alike but each unhappy family is unique in its own special way'. Something similar can be said of the PhD journey. On closer inspection though, the primary factors can be broadly classified under three heads:

- a) lack of understanding,
- b) lack of preparation,
- c) lack of resources.

Within these heads there are innumerable problems which makes each of the failures of which there are many unique. For instance, the lack of understanding might stem from the cultural differences between the supervisor and the student, or lack of understanding of the research topic. But it can also stem from lack of understanding of what is expected from the candidate as well as the supervisor. The lack of preparation too can manifest in a variety of ways, for instance the schooling system including undergraduate and graduate studies do not prepare the candidates for the technical know-how as well as the problem solving skills needed in the PhD journey. The education systems in some countries value back breaking hard-work but not creative thinking while in some countries they do encourage creative thinking but do not inculcate strong work ethics. As a result only a few people are really geared for the hard and smart work needed during the doctoral studies. On the supervisor side, it is only now that some training on man management and human resource management is being offered to the supervisors. Until recently they were expected to learn on the job, and most supervisors themselves were not prepared for shouldering the responsibility of supervision. For successful PhD in addition to human efforts, other resources such as time, equipment, funding, motivation, and creative thinking to name a few are needed. A lack of any one of them results in an unfinished journey. Each of the factor themselves has multiple facets, for instance lack of time may be on the part of the supervisor who is involved in several different tasks and does not guide the candidate, or the candidate is at a place in his personal life where the uncertainty associated with the PhD journey is not ideal and has to move on to more stable jobs or just that the research work is no longer novel enough as the idea was either scooped by someone else, or is no longer relevant due to some other breakthrough. Some of these factors are beyond anyone's control (personal circumstances) or one person's control (the academic system) but most of the factors can be understood and remedied or mitigated through proper planning, clear communication and managing expectations.

The planning of the doctoral journey is very important. The career development plan (CDP) can be an excellent starting point for this.

The CDP should be looked at as a document which is continuously evolving based on the needs of the project and based on feedback from peers and other external factors. At the same time it should have SMART (specific, measurable, attainable, realistic and time bound) objectives and milestones. The plan should also include timelines and scope for dissemination which is agreed upon by all stake holders. This document may also outline the steps needed to achieve the final goal, as it allows better risk management.

Also, it is very important to identify a mentor (different from your supervisor). Ideally the mentor should be someone who knows your field but is not working in the same general area to avoid any conflict of interests. The mentor is ideal to voice concerns and bounce ideas without having repercussions or judgment. This really allows helps you to gain the big picture, give perspective and sometimes see the light at end of the tunnel.

Another important aspect is self-awareness. It is extremely important on the candidate to be honest to oneself, be clear in their mind and be convinced on what and why they are doing the PhD. This clarity can not only motivate you and allow you to focus. As self-drive and self discipline are extremely important for the timely completion of the research.

Based on multiple academic sources [7, 115] the most common cause of PhD students quitting is poor/non existent supervision or conflicts with the supervisor. Supervision is extremely influential factor on the outcome. As highlighted the challenge at times is the lack of training on the part of the supervisor but also a lack of clear communication and often background differences. In my experience the kind of supervision needs to be tailored based on the personality of the student, the stage of the research etc. For instance, personally having an open door policy, worked for me the best as I could really focus on my research rather than focusing on the reporting. But I have known a few people who were not keen to take initiative or were too shy to approach for help. Hence there is no one size fits all solution for this aspect, but honesty and clear communication will ensure that the best course of action is chosen.

I will also like to highlight the common mistakes ESRs commit, firstly they have unrealistic expectations as the outcome of their research work, and the speed of progress they will make. The research towards a PhD is about pushing the boundaries of knowledge and improving the understanding of the subject matter. Only a fraction of doctoral works have a paradigm changing effects. Hence not managing expectations only sets one up for disappointment. Secondly about the progress, the first year or so is about getting to know the subject matter, understanding the state of the art, identifying the problem and equipping oneself for the tools which will be needed for tackling the problem. In this day and age we have the power of the internet at our finger tips, so it is often a misconception that one can access the information on the fly, although it is true for basic fact checking, the understanding of the concepts do takes time, and only after understanding they can be applied effectively to your problem. Another commonly made mistake is underestimating the execution problems and time needed for designing the experiments and realizing them. Although a task which is done countless number of times, a new experimental campaign always throws new issues. I have had personally been stuck with the setup for several weeks. Hence these are issues which need to be understood in order to prepare oneself and not get overwhelmed when these things do happen.

During the realization of my PhD topic I often realized how our ability to understand time is warped. Seemingly far-off planned things have a tendency to approach quickly, while the waiting of seemingly a few days such as results of processing, or the decision making process of the manuscript or a project which is expected in a short time feels like it is taking forever. At such points having a clear perspective and time based plans allows us to focus on the bigger picture than delve on the small aspects. So the time factor should be looked as a resource and at the same time positive motivator.

There is a growing stereotype of academically inclined people often lack the social or presentation skills. This although true to a few people, is a vast exaggeration. The stereotype applies to a tiny percentage of the people who are qualified geniuses and often excused

from social niceties. In most cases, good science needs to be backed by excellent people skills. These skills can manifest in the form of writing which is clear, concise and easy to grasp for all readers or through presentation skills where the audience are able to pick the crux of the matter and provide insights/feedback to the work. So indeed presentation skills are important and will be indirectly tested at the time of peer review, as well as the doctoral defence. These skills are not innate but need to be developed and groomed through practice. Also these social skills will help in the networking which is also a key part of life in academia. The networking is important as this is the place where you will possibly find your next job, collaborator or even the next big idea. Hence efforts are indeed needed on this front. Also having good social skills will allow you to easily communicate and collaborate with other researchers. I do believe that collaboration multiplies the research output and make the research more rounded and robust. The collaboration efforts should come from you as an ESR with backing from your supervisor. I was blessed to have a world leader in the field as my supervisor, furthermore, the supervisor was extremely supportive of collaborations. Hence, I never had issues to collaborate with other groups and that indeed helped my PhD. But mind, you the doors opened by your supervisor need to be reciprocated with efforts on your end. Delivering results in a timely manner is a must as it reinforces the faith of your supervisor and the collaborator.

Lastly I will like to highlight some of the darker sides of research. The academic field seems to have a systematic problem, where there is a concentration of power at the top. For an ESR it might seem that challenging the system is futile. Although it might feel that way, it is not always the case. In order to protect yourself knowing the correct procedure and means of addressing the issues in an unbiased is important. Almost all major institutions and employees have strict human resource practices which are in place to protect you. Hence knowing them is of utmost importance. Also, there are several other checks and balances such as editorial boards of journals, and funding bodies where transgressions can be reported anonymously without any repercussions. I hope none of them have to use this but having the knowledge empowers you and will give

you a piece of mind which is necessary.

Indeed mental health issues have sprung up a lot in the society in the last few years, and there is an even higher occurrence among ESRs. The primary factors is the pressures ESRs face in terms of performance and the financials. Also unhealthy working conditions, and the helplessness felt by the researchers is a very significant contributing factor. There is no one solution that fits all. But having a support system is one of the best ways to overcome this. There are several initiatives such as the COST action (CA19117) ReMO which covers the relevant topics in detail.

Although these lists of dos and don'ts is highly personal based on my experience. These points have been noted by several other bloggers and researchers [23, 66].

## 19.4 Conclusion

Personally, I believe that the journey of PhD is as much about self-discovery as much as it is about science. The aim of the PhD is not only discovering or inventing something new. But more of understanding the scientific process which includes, understanding the problem, suggesting solutions and analysing to determine the best solution. The sets of skills you will learn are coveted in all walks of life. I do not know a single person who regrets doing a PhD, and I encourage you to fight out through the hard times.

Having support and good dynamic with your supervisor will be the single biggest factor determining the outcome of the whole process. In order to give it a best chance a strong work ethic and good open communication with your supervisor is a must. A discussion about the supervision which allows you to thrive is a must.

Also having a development plan a vision with both short term and long term goals gives motivation and provides a documented track for assessment of your journey at any time. The document also helps you to time the big steps in your PhD journey. For instance, in many cases the transition between the end of your PhD and the next job is quite rough. The transition is complicated not only due to

the uncertainty but other administrative issues such as visa status, funding availability etc. So in this case, the completion may be planned to make the ESR eligible for some funding schemes, or recruitment times etc. The plan also ensures that the supervisor and student team is best able to manage the risks and ensure timely execution.

Hence, bear in mind that the challenges will be arduous but through a sincere effort the challenges can be overcome. Furthermore, you should note that you are not alone and be willing to ask for help, as asking for help is not a sign of weakness but a sign of self awareness which is important in this journey.

*Rohan Soman*



## Chapter 20

# Polish history and culture

Poland is a country in Central Europe. Over the centuries this location created very unique culture, where influences from the West and from the East coexist (Sławomir Mrożek used to say: *I'm from west of the East and east of the West*). What is western in Poland, that is, for example, popular culture, Catholic Church and Latin alphabet, while one can trace many more eastern accents in Polish cuisine, language (belonging to Slavic group) and appearance.



Author's graphic presenting eastern and western influences on present Poland.

source: Own materials.

Polish history is very rich and complicated also because of its location in the centre of the European map – in centre of many phenomena, processes and events. It is very difficult to tell this history shortly, therefore one can follow the choice of Polish National Bank presenting silhouettes of the most important Polish rulers on banknotes. The first presented leader is Mieszko I (10 PLN) and during his rules origins of Polish statehood and Baptism of Poland in 966 (or rather the prince and his court). The next character is his son – the first king of Poland – Bolesław Chrobry (20 PLN) and story about his relationship with the first Patron Saint of Poland, St. Adalbert (św. Wojciech). Number three that is Kazimierz Wielki (50 PLN) called 'The Great' referring to his tallness but first of all achievements in modernization of the country and construction of line of fortification called *The trail of Eagles' Nests* (Szlak Orlich Gniazd). The fourth king that can be seen on 100 PLN banknote is Władysław Jagiełło, prince from Lithuanian dynasty crowned

as the king of Poland, from whom the union between Poland and Lithuania starts and who defeated Teutonic Knights under Grunwald in 1410. Number five is Zygmunt Stary (200 PLN) who dealt with Teutonic Knights and reinforced Italian influences on Polish culture, especially in Cracow (Kraków). The last and the most appreciated King of The Polish and Lithuanian Commonwealth is Jan III Sobieski the victor from Vienna, from 1683.



*The Battle of Grunwald*, Jan Matejko. The painting and the date in history - 15.07.1410, that all the Poles know.

source: Wikimedia Commons

After rules of leaders from banknotes Poland faced many problems concerning its economy and also threats from the side of its neighbours. It all resulted in three next partitions – annexation of Polish territory by Russia, Prussia and Austria. In 1795 Poland finally disappears from the map for over century. However this period was very tragically in Polish history, it created vision of patriotism demanding sacrifices and inspired many artists through the 19th century to create really unique pieces of art. In the field of literature it is Adam Mickiewicz and his *Pan Tadeusz* – Polish national epopee and Henryk Sienkiewicz's *Trylogia* written 'to com-



Jan Matejko, *selfportrait*.

source: Wikimedia Commons

to com-

*fort hearts'* – book that created among Poles collective imagination about 17th century Polish and Lithuanian Commonwealth, honor and patriotism. When it comes to music Poland can be proud of the world famous pianist and composer Fryderyk Chopin, who made career mainly in Paris because like many other Poles had to flee after one of uprisings in partitioned Poland in November 1831. Another field that played huge part in creating image of Polish history and enhancing patriotic feelings that is painting and its most known, in Poland, representative – Jan Matejko. He is the creator of Polish collective imagination about how our rulers and the most important moments in Polish history looked like.



Author's collage presenting the most important moments of Polish history in 20th and 21st centuries.

photos source: Wikimedia Commons

Although 20th century starts for Poland with a great success – regaining independence on the 11<sup>th</sup> of November 1918, the whole

century turned out to be the most tragic in the country's history. After the First World War (WWI) ending in not over for Poles, because brand new country was attacked by Bolshevik Russia. Battle of Warsaw on the 15<sup>th</sup> of August 1920 that stopped the invasion became a legend. Nineteen years later the biggest catastrophe in Polish history starts on the 1<sup>st</sup> of September 1939 at 4:48 a.m. – Schleswig-Holstein (German Battleship) opened fire to the Polish Military Transit Depot at Westerplatte. On the same day starts the first Blitzkrieg (when Polish-German border is attacked by German troops on its whole length) in history and symbolically the Second World War (WWII). Six years of this conflict and both occupations – German and Soviet, brought to Poles the worst tragedies: Holocaust, concentration camps, massacres of civilians, Katyń Murder and deportations Poles to Syberia. At the end of the war Poland was in ruin and lost its independence getting under influence on the Union of Soviet Socialist Republics (USSR).

The next chapter of Polish history, that is the period of the People's Republic of Poland (PRL) 1944-1989. Injustice of the communist system and permanent economic crisis led to revolts and strikes – not legal in totalitarian regime, so ended by authority in very brutal way. Until in 1980 one very successful strike started – the Solidarity Strike in the Shipyard of Gdańsk led by Lech Wałęsa. It was the strike that changed the history of the whole region and brought independence to Poland in 1989 after the first democratic (although not entirely free) elections on the 4<sup>th</sup> of June. In next years Poland changed vectors in its foreign affairs and joined NATO (1999) and EU (2004).

Another interesting side of Poland are touristic attractions in Poland. Starting from the North, the Main Town in Gdańsk, the Wooden Pier in Sopot and Teutonic Castle in Malbork. Then lets move to the East, where Primeval Forest of Białowieża and Polish Bisons attract attention of tourists. Next is Warsaw – the capital of Poland, very interesting though completely destroyed during the WWII and rebuild afterwards. The most popular touristic attraction in Poland is Cracow, really picturesque city with famous university, also close to Tatra Mountains and beautiful mountain resort – Zakopane.



Author's graphic presenting attractions in one of regions of Poland.  
 photos source: Wikimedia Commons.

Other big cities with important universities are Poznań, Wrocław, Lublin and Olsztyn.

Referring to the introduction, although Poland was in the area of Soviet influences after the WWII, western culture was the most appreciated and desired. Western symbols, such as Coca Cola, Rock&Roll or comics, were presented as dangerous creations of 'rotten' West. This propaganda did not succeed – especially since The Thaw in 1956, three years after the death of Stalin, slightly modified western patterns in architecture, music, cinematography were implemented in Poland. Examples that have been presented earlier are two historic films in Hollywood style *Krzyżacy* by Aleksander Ford 1960 and *Potop* by Jerzy Hoffman 1974. The great stars of Polish song were Czesław Niemen and Kalina Jedrusik, called also Polish Marilyn Monroe. Today concerts of Dawid Podsiadło and Korteż gather thousands of fans.

Polish cuisine is also an important part of culture. It is also worth to mention a significance of food in post communist countries mentioning coupons for products at moments of most severe crisis, long queues in front of almost empty shops and specific 'culture' of milk bars (traditional canteens with satirical visualization from comedy *Miś* by Bareja). Today the most popular traditional dishes as dumplings, *żurek*, *bigos* can be found both in traditional canteens, called milk bars, and restaurants. The most popular pastries

are apple pie, yeast cake and cheesecake. It is also important to mention, that Poles are open to new tastes and experiments so in bigger cities one may find, without any problem, Italian, Turkish, Mexican, Chinese, etc. restaurants. And in this way once again influences from both – East and West coexist in Polish culture.

*Sandra Wodzyńska-Goc*

## Chapter 21

### A few words about Gdańsk



Gdańsk is a city on the Baltic coast in northern Poland. Gdańsk is the capital and largest city of the Pomeranian Voivodeship. It is the main seaport in Poland and the fourth largest metropolitan area in the country.

The city lies at the southern end of the Gulf of Gdańsk, close to Gdynia and the resort of Sopot – all three cities together are called as the Tri-City (Polish: Trójmiasto). Gdańsk lies at the mouth of the Motława River, connected to the Leniwka River, a branch in the Vistula delta that connects Gdańsk to Poland's capital, Warsaw.

It is a city with over a thousand years of history, whose identity has been shaped over the centuries by the influence of different cultures. The two most interesting periods of the city of Gdańsk are presented below.

## 21.1 Golden Gdańsk

Gdańsk (Fot. 12) is the city with the history which goes back to the tenth century. First settlement was mentioned in writing thanks to a missionary St. Adalbert who baptized inhabitants of Gdańsk in year 997. Gdańsk obtained city rights in the 13th century. In 1308 Gdańsk was captured by Teutonic Knights and stayed under their rule till 1454 (Fot. 18). At that time the city became a member of the Union of Hanseatic Towns. After defeat of Teutonic Order King Casimir the Jagiellonian incorporated Gdańsk into the Crown. It was the beginning of the "golden age" in Gdańsk history. Thanks to numerous privileges which Gdańsk merchants obtained from the king, the city became the richest one in Poland in 16th century. It was called the granary of Poland as it were mostly grains being sold in the harbour on Motława river (Fot. 13, Fot. 14, Fot. 15). Partitions of Poland brought the end of Gdańsk's heyday. Gdańsk was annexed by Prussia in year 1793. After the First World War, under the Versailles Treaty Gdańsk became a Free City supervised by the League of Nations. It was here that the Second World War began. In March 1945 Gdańsk was destroyed in about 90% (<http://dziedzictwo-gdansk.pl/>, Thematic collection: Fotografia, Fotografia subcollections: Zniszczenia i odbudowa). It is taking years

to rebuild it though the reconstruction has already started just after the war. Gdańsk museums can be visited using the website <https://wirtualne.muzeumgdansk.pl/oddzialy/>. It is possible to walk inside the Main Town Hall (fot.16). It used to be the seat of the city authorities from 15th century up to the year 1921. In the Red Chamber one can see a marvellous fireplace and original paintings from the beginning of 17th century (Fot. 10, Fot. 11). In the tower of Town Hall there is a carillon which consists of 37 new bells (Fot. 9). The tradition of carillon music came to Gdańsk from the Netherlands. It is also possible to visit the Uphagen's House which is a museum showing day-to-day life of a rich merchant Johan Uphagen who lived in Gdańsk in 18th century (Fot. 6, Fot. 7, Fot. 8). Another interesting place is the Artus Court. It served as the seat of the brotherhoods of rich patricians (Fot. 5). Another interesting historic building is St. Mary Church which is the biggest one built from bricks in Europe (Fot. 3). The website <https://bazylikamariacka.gdansk.pl/wirtualny-spacer/> allows to admire some of masterpieces like the Astronomical Clock from 15th century (Fot. 1, Fot. 2).

## 21.2 Gdańsk in 21th century

The first shots of Second World War were fired by German battleship Schleswig-Holstein on 1<sup>st</sup> of September 1939 (Fot. 19, Fot. 20, Fot. 21, Fot. 22) where occurred at the place called Westerplatte. There is only one original guardhouse from that time, possible to see using the website <https://wirtualne.muzeumgdansk.pl/oddzialy/>. Since the year 2016 archaeological excavation have been conducted on Westerplatte. There is a new cemetery of Polish soldiers whose remains were found in the year 2019 (Fot. 23). The meaning of Westerplatte – it is a symbol of self-determination, honour and bravery, because it was defended by 7 days by Polish soldiers. However it was not only Westerplatte that was attacked on the 1<sup>st</sup> of September 1939 in Gdańsk. Another interesting place is a building of Polish Post Office situated in the centre of Gdańsk (Fot. 34). Its defenders fate was tragic because they were sentenced to death after the surrender. A group of 38 Poles were shot on 5<sup>th</sup> of October 1939. There

is a monument devoted to them on the Square of Defenders of Polish Post Office in Gdańsk (Fot. 33). Another part of this chapter is concentrated on history of the Solidarity Trade Union (Fot. 28) which came into being in Gdańsk Shipyard in August 1980 (Fot. 32). Near by is the Solidarity Square with a famous monument devoted to workers who were killed during strike in December 1970 (Fot. 29, Fot. 30). There is a modern building next to it which hosts European Solidarity Centre (Fot. 24, Fot. 31). There is an exhibition telling the history of strike in August 1980 and the struggle of Polish society against the communists (Fot. 25, Fot. 26, Fot. 27). It allows to understand that this place is a symbol of the fall of communism in Europe.

*Marta Szagzdowicz*  
*all photographs source: own materials*



Fot. 1



Fot. 2



Fot. 3



Fot. 4



Fot. 5



Fot. 6



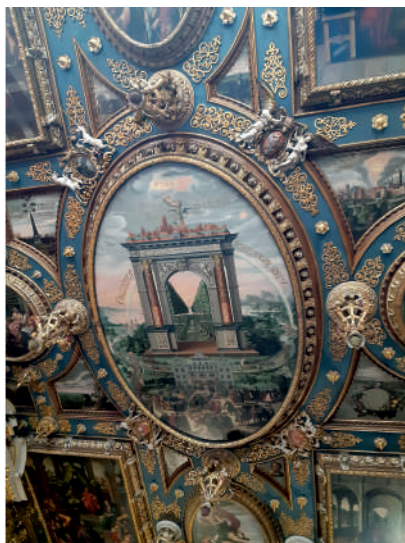
Fot. 7



Fot. 8



Fot. 9



Fot. 10



Fot. 11



Fot. 12



Fot. 13



Fot. 14



Fot. 15



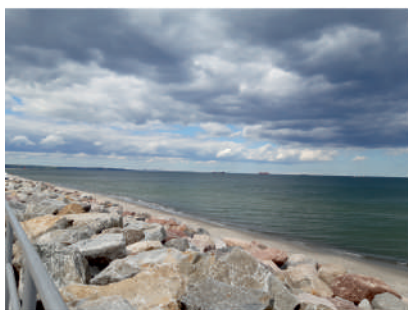
Fot. 16



Fot. 17



Fot. 18



Fot. 19



Fot. 20





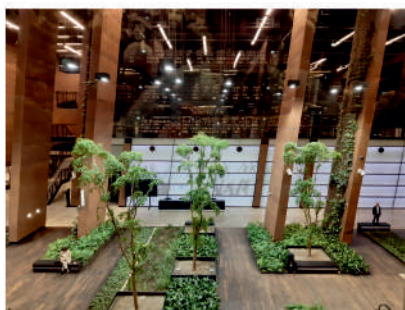
Fot. 21



Fot. 22



Fot. 23



Fot. 24



Fot. 25



Fot. 26



Fot. 27



Fot. 28



Fot. 29



Fot. 30



Fot. 31



Fot. 32



Fot. 33



Fot. 34

## Chapter 22

# Schools in numbers

The project was implemented under the program of the Polish National Agency for Academic Exchange – SPINAKER – Intensive International Education Programs. The program is financed from the non-competition project No. **POWR.03.03.00-00-PN16/18** *Supporting the institutional capacity of Polish universities through the creation and implementation of international study programs* under the Knowledge Education Development Operational Program.

Polish National Agency for Academic Exchange (NAWA), as part of the SPINAKER programme – Intensive International Curricula, awarded the Institute of Fluid Flow Machinery Polish Academy of Sciences (IMP PAN) with funding for the project **CenMAT** *Clean energy and functional materials* with European Funds Contribution: **PLN 487 046.00**.





logo

website <https://cenmateu.wordpress.com/>

A short, in numbers, summary of the schools organized within **CenMAT** project.


①  total number of schools – **3**

 Summer – **2**


 Winter – **1**


- ② 📅 total number of training days – **21**
  - 📶 online days – **11**
  - 🏠 onsite days – **10**
    - 📖 total number of onsite locations – **2**
      - 📍 IMP PAN, Gdańsk
      - 📍 KEZO CB, Jabłonna
- ③ ⌚ total number of hours of substantial lectures – **158**
  - 📶 online hours – **88**
  - 🏠 onsite hours (incl. lab shows) – **70**
- ④ 🖼️ total number of hours of other activities – **28**
  - 🚗 trip to Lubań Living Laboratory – **8**
  - 🗣️ talks about Polish history and culture – **3x3**
    - 📍 Gdańsk guided tour: 📶 online (2x1.5) and 🏠 onsite (2x4)
- ⑤ 👤 total number of lecturers – **37**
  - 📖 out of Poland – **6**
    - 🇵🇹 Bulgaria
    - 🇱🇹 Lithuania
    - 🇪🇸 Spain
    - 🇳🇱 The Netherlands
  - 📖 out of IMP PAN – **7**
    - 🇵🇱 Kraków
    - 🇵🇱 Łódź
    - 🇵🇱 Olsztyn
    - 🇵🇱 Warszawa
    - 🇵🇱 Wrocław
  - 📖 from IMP PAN – **24**
- ⑥ 🎓 total number of PhD students – **46**


A short, in percentage, summary of the application forms filled out by participating PhD students.


 total number of filled out application forms – **46**


 participants' gender


 female **33%**


 male **67%**


 participants' age

 20-29 years **46%**

 30-39 years **43%**


 40-49 years **9%**


 50-59 years **2%**


 participants' citizenship


 Bangladeshi **2%**

 Bulgarian **9%**


 Ethiopian **7%**


 Indian **11%**


 Indonesian **4%**

 Iranian **13%**


 Italian **2%**

 Ivorian **2%**


 Kazakh **11%**


 Lithuanian **2%**

 Pakistani **9%**


 Peruvian **2%**












 Slovak **2%**


 Spanish **4%**




 Ukrainian **20%**









 participants' education country

-  Bulgaria **9%**
-  China **2%**
-  France **2%**
-  India **2%**
-  Kazakhstan **9%**
-  Lithuania **2%**
-  Norway **7%**
-  Poland **41%**
-  Slovakia **2%**
-  Spain **4%**
-  Ukraine **20%**

 participants' field of PhD thesis

-  engineering and technology **76%**
-  natural sciences **15%**
-  other **9%**

 participants' discipline of PhD thesis

-  biomedical engineering **2%**
-  civil engineering and transport **2%**
-  environmental engineering, mining and energy **13%**
-  material engineering **7%**
-  mechanical engineering **50%**
-  other **26%**

- ☐ participants' status on labour market
  - active **61%**
  - inactive **39%**
- active participants' profession
  - 📖 employee of a higher education institution **79%**
  - 📖 other **21%**
- ☐ participants' diet
  - 🍴 dairy and gluten free **2%**
  - 🍴 dairy free **2%**
  - 🍴 gluten free **0%**
  - 🍴 standard **54%**
  - 🍴 vegan **0%**
  - 🍴 vegetarian **11%**
  - 🍴 food allergies **4%**
  - 🍴 not stated **26%**

*Katarzyna Majewska*

## Acknowledgments

The project is implemented under the program of the Polish National Agency for Academic Exchange (NAWA) - Intensive International Education Programs (SPINAKER).

The program is financed from the non-competition project No. POWR.03.03.00-00-PN16/18 'Supporting the institutional capacity of Polish universities through the creation and implementation of international study programs' under the Knowledge Education Development Operational Program.

**Clean energy and functional material (CenMAT).**



# Bibliography

- [1] <https://www.danfoss.com/>.
- [2] <https://en.wikipedia.org/wiki/Turbine>.
- [3] [https://en.wikipedia.org/wiki/Rankine\\_cycle](https://en.wikipedia.org/wiki/Rankine_cycle).
- [4] [https://en.wikipedia.org/wiki/Compressible\\_flow](https://en.wikipedia.org/wiki/Compressible_flow).
- [5] A. T. Alavie, R. Maaskant, M. M. Ohn, S. E. Karr, S. Y. Huang, D. J. Glennie, C. Wade, A. Guha-Thakurta, G. Tadros, S. Rizkalla, et al. Multiplexed bragg grating laser sensors for civil engineering. In *Distributed and Multiplexed Fiber Optic Sensors III*, volume 2071, pages 21–29. SPIE, 1993.
- [6] Alice Clubbs Coldron. How rare (or common) is it to have a phd? <https://www.findaphd.com/blog/5403/how-rare-or-common-is-it-to-have-a-phd>. 10/07/2023.
- [7] C. R. Bair and J. G. Haworth. Doctoral student attrition and persistence: A meta-synthesis of research. *Higher education: Handbook of theory and research*, pages 481–534, 2005.
- [8] J. Baird. An improved method and means of producing optical images. *British patent*, page 285.738, 1928.
- [9] M. Benounis and N. Jaffrezic-Renault. Elaboration of an optical fibre corrosion sensor for aircraft applications. *Sensors and Actuators B: chemical*, 100(1-2):1–8, 2004.

- [10] K. Bertsch, A. Nagao, B. Rankouhi, B. Kuehl, and D. Thoma. Hydrogen embrittlement of additively manufactured austenitic stainless steel 316 l. *Corrosion Science*, 192:109790, 2021.
- [11] P. Biswas, S. Bandyopadhyay, K. Kesavan, S. Parivallal, B. A. Sundaram, K. Ravisankar, and K. Dasgupta. Investigation on packages of fiber bragg grating for use as embeddable strain sensor in concrete structure. *Sensors and Actuators A: Physical*, 157(1):77–83, 2010.
- [12] R. A. M. Boloy, A. da Cunha Reis, E. M. Rios, J. de Araújo Santos Martins, L. O. Soares, V. A. de Sá Machado, and D. R. de Moraes. Waste-to-energy technologies towards circular economy: a systematic literature review and bibliometric analysis. *Water, Air, & Soil Pollution*, 232(7):306, 2021.
- [13] C. D. Butter and G. Hocker. Fiber optics strain gauge. *Applied optics*, 17(18):2867–2869, 1978.
- [14] J. ChamB. *Piled higher and deeper*. ISBN: 97809721695-0-9, p. 1445.
- [15] A. R. Chambers, M. C. Mowlem, and L. Dokos. Evaluating impact damage in cfrp using fibre optic sensors. *Composites science and technology*, 67(6):1235–1242, 2007.
- [16] T. H. Chan, L. Yu, H.-Y. Tam, Y.-Q. Ni, S. Liu, W. Chung, and L. Cheng. Fiber bragg grating sensors for structural health monitoring of tsing ma bridge: Background and experimental observation. *Engineering structures*, 28(5):648–659, 2006.
- [17] J. Chen, J. Wang, X. Li, L. Sun, S. Li, and A. Ding. Monitoring of temperature and cure-induced strain gradient in laminated composite plate with fbg sensors. *Composite Structures*, 242:112168, 2020.
- [18] D. Chwieduk and M. Jaworski. *Renewable energy in construction. Energy storage*. PWN, 2018.

- [19] W. E. Council. World energy resources 2016. *World Energy Council, London, UK*, 2016.
- [20] F. Cucinotta, E. Guglielmino, and F. Sfravara. Life cycle assessment in yacht industry: A case study of comparison between hand lay-up and vacuum infusion. *Journal of Cleaner Production*, 142:3822–3833, 2017.
- [21] Y. Dai, J. Wang, and L. Gao. Parametric optimization and comparative study of organic rankine cycle (orc) for low grade waste heat recovery. *Energy conversion and management*, 50(3):576–582, 2009.
- [22] İ. Dincer and C. Zamfirescu. *Advanced power generation systems*. Elsevier, 2014.
- [23] Dissertation Genius. The six laws of phd failure. <https://dissertationgenius.com/the-six-laws-of-phd-failure/>. 28/06/2023.
- [24] S. L. Dixon and C. Hall. *Fluid mechanics and thermodynamics of turbomachinery*. Butterworth-Heinemann, 2013.
- [25] K. Du, J. Calautit, Z. Wang, Y. Wu, and H. Liu. A review of the applications of phase change materials in cooling, heating and power generation in different temperature ranges. *Applied energy*, 220:242–273, 2018.
- [26] Elizabeth Stivison. Overview of academic research, teaching and other positions. <https://www.asbmb.org/asbmb-today/careers/020720/overview-of-academic-research-positions>. 28/06/2023.
- [27] Y. Fan, B. Zhang, H. Yi, G. Hao, Y. Sun, J. Wang, E.-H. Han, and W. Ke. The role of reversed austenite in hydrogen embrittlement fracture of s41500 martensitic stainless steel. *Acta Materialia*, 139:188–195, 2017.
- [28] P. Ferreira, E. Caetano, and P. Pinto. Real-time flying shape detection of yacht sails based on strain measurements. *Ocean Engineering*, 131:48–56, 2017.

- [29] U. Fischer, J. Potrykus, Z. Smalec, and E. Wnuczak. *Poradnik mechanika*. REA, 2008.
- [30] Y. Gebremichael, W. Li, W. Boyle, B. Meggitt, K. Grattan, B. McKinley, G. Fernando, G. Kister, D. Winter, L. Canning, et al. Integration and assessment of fibre bragg grating sensors in an all-fibre reinforced polymer composite road bridge. *Sensors and Actuators A: Physical*, 118(1):78–85, 2005.
- [31] W. Gundlach and A. Olczyk. Droga od cieplnych maszyn objętościowych do przepływowych, do ich symbiozy i dalej... *Zeszyty Naukowe. Ciepłne Maszyny Przepływowe-Turbomachinery/Politechnika Łódzka*, (121):35–53, 2002.
- [32] W. R. Gundlach. *Podstawy maszyn przepływowych i ich systemów energetycznych*. Wydawnictwa Naukowo-Techniczne, 2008.
- [33] J. He, L. Chen, X. Tao, S. Antonov, Y. Zhong, and Y. Su. Hydrogen embrittlement behavior of 13cr-5ni-2mo supermartensitic stainless steel. *Corrosion Science*, 176:109046, 2020.
- [34] Henry Reichman. Eight myths about tenure. <https://www.aaup.org/article/eight-myths-about-tenure>. 28/06/2023.
- [35] K. Hill, Y. Fujii, D. C. Johnson, and B. Kawasaki. Photosensitivity in optical fiber waveguides: Application to reflection filter fabrication. *Applied physics letters*, 32(10):647–649, 1978.
- [36] D. Hondros and P. Debye. Elektromagnetische wellen an dielektrischen drähten. *Annalen der Physik*, 337(8):465–476, 1910.
- [37] M. K. i Środowiska. Polska strategia wodorowa do roku 2030 z perspektywą do 2040 r. *Załącznik do uchwały*, (149), 2021.
- [38] D. Japikse and N. C. Baines. Introduction to turbomachinery. (*No Title*), 1994.

- [39] A. Jensen, H. Torkildsen, C. Wines, G. Sagvolden, and S. Lovseth. Resultater fra fullskala verifikasjon av globale laster ved maling av kontrollert endring av stille vannsmoment. *Forsvarets forskningsinstitutt (FFI), Norway*, 2008.
- [40] J. W. Jo, H. J. Seo, B.-I. Jung, S. Choi, and C. S. Lee. Effect of bainite fraction on hydrogen embrittlement of bainite/martensite steel. *Materials Science and Engineering: A*, 814:141226, 2021.
- [41] Z. Kaczmarek. *Światłowodowe czujniki i przetworniki pomiarowe*. Agenda Wydawnicza PAK, 2006.
- [42] G. C. Kahandawa, J. Epaarachchi, H. Wang, and K. Lau. Use of fbg sensors for shm in aerospace structures. *Photonic Sensors*, 2(3):203–214, 2012.
- [43] P. Kapica and J. Karwacki. Review and criterions of selecting the phase-change materials that can be used to collaborate within refrigeration plants. In *Conference Proceedings of 50 Days of Refrigeration. Current trends in technical solutions for refrigeration, air-conditioning, ventilation and heat pump devices and systems.*, pages 121–132. SYSTHERM, 2018.
- [44] J. Kiddy, C. Baldwin, and T. Salter. Hydrostatic testing of a manned underwater vehicle using fiber optic sensors. In *Proceedings of OCEANS 2005 MTS/IEEE*, pages 1876–1881. IEEE, 2005.
- [45] G. Kister, D. Winter, R. Badcock, Y. Gebremichael, W. Boyle, B. Meggitt, K. Grattan, and G. Fernando. Structural health monitoring of a composite bridge using bragg grating sensors. part 1: Evaluation of adhesives and protection systems for the optical sensors. *Engineering Structures*, 29(3):440–448, 2007.
- [46] J. Kotowicz and M. Brzęczek. Analysis of increasing efficiency of modern combined cycle power plant: A case study. *Energy*, 153:90–99, 2018.



- [47] M. Koyama, E. Akiyama, Y.-K. Lee, D. Raabe, and K. Tsuzaki. Overview of hydrogen embrittlement in high-mn steels. *international journal of hydrogen energy*, 42(17):12706–12723, 2017.
- [48] K. Kuang, R. Kenny, M. Whelan, W. Cantwell, and P. Chalker. Embedded fibre bragg grating sensors in advanced composite materials. *Composites Science and Technology*, 61(10):1379–1387, 2001.
- [49] K.-t. Lau, L. Yuan, L.-m. Zhou, J. Wu, and C.-h. Woo. Strain monitoring in frp laminates and concrete beams using fbg sensors. *Composite structures*, 51(1):9–20, 2001.
- [50] D.-H. Lee, B. Sun, S. Lee, D. Ponge, E. A. Jäggle, and D. Raabe. Comparative study of hydrogen embrittlement resistance between additively and conventionally manufactured 304l austenitic stainless steels. *Materials Science and Engineering: A*, 803:140499, 2021.
- [51] D. Li, Z. Zhou, and J. Ou. Dynamic behavior monitoring and damage evaluation for arch bridge suspender using gfrp optical fiber bragg grating sensors. *Optics & Laser Technology*, 44(4):1031–1038, 2012.
- [52] H.-N. Li, D.-S. Li, and G.-B. Song. Recent applications of fiber optic sensors to health monitoring in civil engineering. *Engineering structures*, 26(11):1647–1657, 2004.
- [53] X. Li, X. Ma, J. Zhang, E. Akiyama, Y. Wang, and X. Song. Review of hydrogen embrittlement in metals: hydrogen diffusion, hydrogen characterization, hydrogen embrittlement mechanism and prevention. *Acta Metallurgica Sinica (English Letters)*, 33:759–773, 2020.
- [54] H. F. Lima, R. da Silva Vicente, R. N. Nogueira, I. Abe, P. S. de Brito Andre, C. Fernandes, H. Rodrigues, H. Varum, H. J. Kalinowski, A. Costa, et al. Structural health monitoring of the church of santa casa da misericórdia of aveiro using fbg sensors. *IEEE Sensors Journal*, 8(7):1236–1242, 2008.

- [55] Z. Liu, X. Liu, S.-P. Zhu, P. Zhu, W. Liu, J. A. Correia, and A. M. De Jesus. Reliability assessment of measurement accuracy for fbg sensors used in structural tests of the wind turbine blades based on strain transfer laws. *Engineering Failure Analysis*, 112:104506, 2020.
- [56] M. Louthan. Hydrogen embrittlement of metals: a primer for the failure analyst. *Journal of Failure Analysis and Prevention*, 8:289–307, 2008.
- [57] M. Louthan Jr, G. Caskey Jr, J. Donovan, and D. Rawl Jr. Hydrogen embrittlement of metals. *Materials Science and Engineering*, 10:357–368, 1972.
- [58] K. Lovegrove and W. Stein. Introduction to concentrating solar power technology. In *Concentrating Solar Power Technology*, pages 3–17. Elsevier, 2021.
- [59] X. Lu, Y. Ma, and D. Wang. On the hydrogen embrittlement behavior of nickel-based alloys: alloys 718 and 725. *Materials Science and Engineering: A*, 792:139785, 2020.
- [60] K. Majewska, M. Mieloszyk, W. Ostachowicz, and A. Król. Experimental method of strain/stress measurements on tall sailing ships using fibre bragg grating sensors. *Applied Ocean Research*, 47:270–283, 2014.
- [61] A. Majewski. *Podstawy techniki Światłowodowej: zagadnienia wybrane*. 1997.
- [62] M. Majumder, T. K. Gangopadhyay, A. K. Chakraborty, K. Dasgupta, and D. K. Bhattacharya. Fibre bragg gratings in structural health monitoring—present status and applications. *Sensors and Actuators A: Physical*, 147(1):150–164, 2008.
- [63] M. Martin, B. Somerday, R. Ritchie, P. Sofronis, and I. Robertson. Hydrogen-induced intergranular failure in nickel revisited. *Acta Materialia*, 60(6-7):2739–2745, 2012.

- [64] Martina G. Efeyini. The other side of research. <https://www.asbmb.org/asbmb-today/careers/011020/the-other-side-of-research>. 28/06/2023.
- [65] E. Martínez-Pañeda, Z. D. Harris, S. Fuentes-Alonso, J. R. Scully, and J. T. Burns. On the suitability of slow strain rate tensile testing for assessing hydrogen embrittlement susceptibility. *Corrosion Science*, 163:108291, 2020.
- [66] Matt Might. 10 easy ways to fail a ph.d. <https://matt.might.net/articles/ways-to-fail-a-phd/>. 28/06/2023.
- [67] Matus Sotak. How people in science see each other. <http://sotak.info/sci.jpg>. 28/06/2023.
- [68] R. Matysko and H. Strońska. *Modelowanie systemów cieplno-przepływowch. Część I i Część II*. Wydawnictwo IMP PAN, 2018.
- [69] R. M. Measures. Fiber optics, bragg grating sensors. *Encyclopedia of Smart Materials*, 2002.
- [70] H. Mehling and L. F. Cabeza. Heat and cold storage with pcm. *Heat and mass transfer*, 2008.
- [71] G. Meltz, W. W. Morey, and W. H. Glenn. Formation of bragg gratings in optical fibers by a transverse holographic method. *Optics letters*, 14(15):823–825, 1989.
- [72] M. Mieloszyk, A. Andrearczyk, K. Majewska, M. Jurek, and W. Ostachowicz. Polymeric structure with embedded fiber bragg grating sensor manufactured using multi-jet printing method. *Measurement*, 166:108229, 2020.
- [73] M. Mieloszyk, M. Jurek, K. Majewska, and W. Ostachowicz. Terahertz time domain spectroscopy and imaging application for analysis of sandwich panel with embedded fibre bragg grating sensors and piezoelectric transducers. *Optics and Lasers in Engineering*, 134:106226, 2020.

- [74] M. Mieloszyk, K. Majewska, and W. Ostachowicz. Thz spectroscopy application for detection and localisation of water inclusion in glass composite. *Composite Structures*, 192:537–544, 2018.
- [75] M. Mieloszyk, K. Majewska, and W. Ostachowicz. Application of thz spectroscopy for localisation of fibre optics embedded into glass fibre reinforced composite. *Composite Structures*, 209:548–560, 2019.
- [76] M. Mieloszyk, K. Majewska, and W. Ostachowicz. Studies of fibre reinforced polymer samples with embedded fbg sensors. In *Proceedings of the 13th International Conference on Damage Assessment of Structures: DAMAS 2019, 9-10 July 2019, Porto, Portugal*, pages 926–936. Springer, 2020.
- [77] M. Mieloszyk, K. Majewska, and W. Ostachowicz. Application of embedded fibre bragg grating sensors for structural health monitoring of complex composite structures for marine applications. *Marine Structures*, 76:102903, 2021.
- [78] M. Mieloszyk and W. Ostachowicz. An application of structural health monitoring system based on fbg sensors to offshore wind turbine support structure model. *Marine Structures*, 51:65–86, 2017.
- [79] M. Mieloszyk and W. Ostachowicz. An application of structural health monitoring system based on fbg sensors to offshore wind turbine support structure model. *Marine Structures*, 51:65–86, 2017.
- [80] D. Mittleman. *Sensing with terahertz radiation*, volume 85. Springer, 2013.
- [81] N. Nagai and R. Fukasawa. Abnormal dispersion of polymer films in the thz frequency region. *Chemical Physics Letters*, 388(4-6):479–482, 2004.
- [82] M. Nagumo and K. Takai. The predominant role of strain-induced vacancies in hydrogen embrittlement of steels: Overview. *Acta Materialia*, 165:722–733, 2019.

- [83] H. G. Nelson. Hydrogen embrittlement. In *Treatise on Materials Science & Technology*, volume 25, pages 275–359. Elsevier, 1983.
- [84] H. Nowakowska, J. Mizeraczyk, and J. Janke. Energetyka wodorowa. 2007.
- [85] R. Oriani. Hydrogen embrittlement of steels. *Annual review of materials science*, 8(1):327–357, 1978.
- [86] C. Park, N. Kang, and S. Liu. Effect of grain size on the resistance to hydrogen embrittlement of api 2w grade 60 steels using in situ slow-strain-rate testing. *Corrosion Science*, 128:33–41, 2017.
- [87] M. Peccianti, R. Fastampa, A. M. Conte, O. Pulci, C. Violante, J. Łojewska, M. Clerici, R. Morandotti, and M. Messori. Terahertz absorption by cellulose: Application to ancient paper artifacts. *Physical Review Applied*, 7(6):064019, 2017.
- [88] S. Perycz. *Turbiny parowe i gazowe*. Zakład Narodowy im. Ossolińskich, 1992.
- [89] K. Peters. Fiber-optic sensor principles. *Encyclopedia of Structural Health Monitoring*, 2009.
- [90] I. Pietkun-Greber and R. M. Janka. Oddziaływanie wodoru na metale i stopy. *Proceedings of ECOpole*, 4, 2010.
- [91] L. Ren, H.-N. Li, J. Zhou, D.-S. Li, and L. Sun. Health monitoring system for offshore platform with fiber bragg grating sensors. *Optical Engineering*, 45(8):084401–084401, 2006.
- [92] I. M. Robertson, P. Sofronis, A. Nagao, M. L. Martin, S. Wang, D. Gross, and K. Nygren. Hydrogen embrittlement understood. *Metallurgical and materials transactions A*, 46:2323–2341, 2015.
- [93] Roger Pielke Jr. is-it-time-to-retire-academic-tenure. <https://rogerpielkejr.substack.com/p/is-it-time-to-retire-academic-tenure>. 28/06/2023.

- [94] P. Rolka, J. Karwacki, and M. Jaworski. Compatibility tests between three commercially available organic pcms and metals typically used in fin-and-tube heat exchangers. *Materials*, 14(18):5172, 2021.
- [95] P. Rolka, R. Kwidzinski, T. Przybylinski, and A. Tomaszewski. Thermal characterization of medium-temperature phase change materials (pcms) for thermal energy storage using the t-history method. *Materials*, 14(23):7371, 2021.
- [96] P. Rolka, T. Przybylinski, R. Kwidzinski, and M. Lackowski. The heat capacity of low-temperature phase change materials (pcm) applied in thermal energy storage systems. *Renewable Energy*, 172:541–550, 2021.
- [97] P. Rolka, T. Przybylinski, R. Kwidzinski, and M. Lackowski. Thermal properties of rt22 hc and rt28 hc phase change materials proposed to reduce energy consumption in heating and cooling systems. *Renewable Energy*, 197:462–471, 2022.
- [98] A. Romei, D. Vimercati, G. Persico, and A. Guardone. Non-ideal compressible flows in supersonic turbine cascades. *Journal of Fluid Mechanics*, 882:A12, 2020.
- [99] M. A. Rosen. Energy-and exergy-based comparison of coal-fired and nuclear steam power plants. *Exergy, An International Journal*, 1(3):180–192, 2001.
- [100] C.-H. Ryu, S.-H. Park, D.-H. Kim, K.-Y. Jhang, and H.-S. Kim. Nondestructive evaluation of hidden multi-delamination in a glass-fiber-reinforced plastic composite using terahertz spectroscopy. *Composite Structures*, 156:338–347, 2016.
- [101] M. F. Sá, L. Guerreiro, A. M. Gomes, J. R. Correia, and N. Silvestre. Dynamic behaviour of a gfrp-steel hybrid pedestrian bridge in serviceability conditions. part 1: Experimental study. *Thin-Walled Structures*, 117:332–342, 2017.

- [102] K. Schroeder, W. Ecke, J. Apitz, E. Lembke, and G. Lenschow. A fibre bragg grating sensor system monitors operational load in a wind turbine rotor blade. *Measurement science and technology*, 17(5):1167, 2006.
- [103] Z. Shirband, M. R. Shishesaz, and A. Ashrafi. Hydrogen degradation of steels and its related parameters, a review. *Phase Transitions*, 84(11-12):924–943, 2011.
- [104] R. N. Soman, K. Majewska, M. Mieloszyk, and W. Ostachowicz. Damage assessment in composite beam using infrared thermography, optical sensors, and terahertz technique. *Journal of Nondestructive Evaluation, Diagnostics and Prognostics of Engineering Systems*, 1(3):031001, 2018.
- [105] M. Sozańska. *Niszczenie wodorowe typu "rybie oczy" wybranych stali dla energetyki*. Wydawnictwo Politechniki Śląskiej, 2006.
- [106] B. Surowska. *Wybrane zagadnienia z korozji i ochrony przed korozją*. Wydaw. PL, 2002.
- [107] A. Szczęśniak, W. Bujalski, A. Grzebielec, K. Futyma, J. Karwacki, and P. Rolka. A hybrid district heating substation with an adsorption chiller and pcm storage units: a concept and preliminary study. In *E3S Web of Conferences*, volume 321, page 02009. EDP Sciences, 2021.
- [108] M. Szustakowski. *Elementy techniki światłowodowej*. Wydawnictwa Naukowo-Techniczne, 1992.
- [109] S. Takeda, Y. Aoki, T. Ishikawa, N. Takeda, and H. Kikukawa. Structural health monitoring of composite wing structure during durability test. *Composite structures*, 79(1):133–139, 2007.
- [110] A. Tehranchi, X. Zhou, and W. Curtin. A decohesion pathway for hydrogen embrittlement in nickel: Mechanism and quantitative prediction. *Acta Materialia*, 185:98–109, 2020.

- [111] H. E. Torkildsen, A. Grovlen, A. Skaugen, G. Wang, A. E. Jensen, K. Pran, and G. Sagvolden. Development and applications of full-scale ship hull health monitoring systems for the royal norwegian navy. In *Recent developments in non-intrusive measurement technology for military application on model-and full-scale vehicles*, number 22, page 114. Meeting Proceedings RTO-MP-AVT-124, Paper 22., 2005 Neuilly-sur-Seine, 2005.
- [112] W. Traupel. Thermal turbomachinery. vol. 2. thermische turbomaschinen. bd. 2. geaenderte betriebsbedingungen, regelung, mechanische probleme, temperaturprobleme. 1982.
- [113] E. Udd and W. B. Spillman Jr. *Fiber optic sensors: an introduction for engineers and scientists*. John Wiley & Sons, 2011.
- [114] D. Vallero. Chapter 31 - controlling air pollution from sources. In D. Vallero, editor, *Fundamentals of Air Pollution (Fifth Edition)*, pages 881–925. Academic Press, Boston, fifth edition edition, 2014.
- [115] E. van Rooij, M. Fokkens-Bruinsma, and E. Jansen. Factors that influence phd candidates? success: the importance of phd project characteristics. *Studies in Continuing Education*, 43(1):48–67, 2021.
- [116] L. Wan, W. T. Geng, A. Ishii, J.-P. Du, Q. Mei, N. Ishikawa, H. Kimizuka, and S. Ogata. Hydrogen embrittlement controlled by reaction of dislocation with grain boundary in alpha-iron. *International Journal of Plasticity*, 112:206–219, 2019.
- [117] G. Wang, K. Pran, G. Sagvolden, G. Havsgård, A. Jensen, G. Johnson, and S. Vohra. Ship hull structure monitoring using fibre optic sensors. *Smart materials and structures*, 10(3):472, 2001.
- [118] G. Wang, K. Pran, G. Sagvolden, G. Havsgård, A. Jensen, G. Johnson, and S. Vohra. Ship hull structure monitoring



- using fibre optic sensors. *Smart materials and structures*, 10(3):472, 2001.
- [119] S. Wang, M. L. Martin, P. Sofronis, S. Ohnuki, N. Hashimoto, and I. M. Robertson. Hydrogen-induced intergranular failure of iron. *Acta Materialia*, 69:275–282, 2014.
- [120] M. Wasim and M. B. Djukic. Hydrogen embrittlement of low carbon structural steel at macro-, micro- and nano-levels. *International Journal of Hydrogen Energy*, 45(3):2145–2156, 2020.
- [121] R. M. Woodward, B. E. Cole, V. P. Wallace, R. J. Pye, D. D. Arnone, E. H. Linfield, and M. Pepper. Terahertz pulse imaging in reflection geometry of human skin cancer and skin tissue. *Physics in medicine and biology*, 47(21):3853, 2002.
- [122] B. Wu, G. Wu, and C. Yang. Parametric study of a rapid bridge assessment method using distributed macro-strain influence envelope line. *Mechanical Systems and Signal Processing*, 120:642–663, 2019.
- [123] Z. Yang, Z. Liu, J. Liang, J. Su, Z. Yang, B. Zhang, and G. Sheng. Correlation between the microstructure and hydrogen embrittlement resistance in a precipitation-hardened martensitic stainless steel. *Corrosion Science*, 182:109260, 2021.
- [124] C. Yeh. Elliptical dielectric guides. *Journal of Applied Physics*, 33:3225–3243, 1962.
- [125] S. J. Zarrouk and H. Moon. Efficiency of geothermal power plants: A worldwide review. *Geothermics*, 51:142–153, 2014.
- [126] C. Zhang, W. Hui, X. Zhao, Y. Zhang, and X. Zhao. The potential significance of microalloying with Nb in enhancing the resistance to hydrogen-induced delayed fracture of 1300-mpa-grade high-strength bolt steel. *Engineering Failure Analysis*, 135:106144, 2022.

- [127] J. Zhang, J. Wang, X. Han, H.-L. Cui, C. Shi, J. Zhang, and Y. Shen. Noncontact detection of teflon inclusions in glass-fiber-reinforced polymer composites using terahertz imaging. *Applied Optics*, 55(36):10215–10222, 2016.
- [128] C. Zhou, B. Ye, Y. Song, T. Cui, P. Xu, and L. Zhang. Effects of internal hydrogen and surface-absorbed hydrogen on the hydrogen embrittlement of x80 pipeline steel. *International Journal of Hydrogen Energy*, 44(40):22547–22558, 2019.
- [129] X. Zhu, W. Li, T. Hsu, S. Zhou, L. Wang, and X. Jin. Improved resistance to hydrogen embrittlement in a high-strength steel by quenching–partitioning–tempering treatment. *Scripta Materialia*, 97:21–24, 2015.